Characterisation of Emissions and Combustion Stability of a Port Fuelled Spark Ignition Engine

Nicholas M Brown, BSc, MSc.

Thesis submitted to the University of Nottingham for the degree of Doctor of Philosophy

March 2009

Table of Contents

Abstract

"Characterisation of Emissions and Combustion Stability of a Port Fuelled Spark Ignition Engine"

The chemical and physical limits of cycle-to-cycle combustion variability and engine out emissions of a gasoline port fuelled spark ignition engine have been investigated. The experimental investigations were carried out on a V8 engine with port fuel injection and variable intake valve timing.

The chemical limits of stable combustion have been shown to be a function of burned gas, fuel and air mixture. The widest limit, gas fuel ratio of <24, burned gas fraction <0.27 and AFR >9 was found at maximum brake torque spark timing. Retarding the spark timing by 10°CA caused a small reduction in the stable area, 20°CA retard reduced the stable combustion area significantly, whereby stable combustion occurred within an area of gas fuel ratio of <19, burned gas fraction <0.2 and AFR >10.

Burn rate analysis indicated increased variability in both the flame development and rapid burn period. The increase in variability in the rapid burn period is greater than that associated with the flame development. The variability is magnified from flame development through the rapid burn phase. This finding was consistent for unstable combustion caused by exceeding chemical and physical limits.

Engine out emissions were investigated and characterised using engine global state parameters, for example AFR, burned gas fraction, for both stable and unstable

combustion conditions. Carbon monoxide and oxides of nitrogen emissions correlations were unaffected by the presence of unstable combustion events whereas hydrocarbon emissions showed a significant increase. The incorporation of these findings were implemented into an engine simulation (Nu-SIM V8) investigating the impact for the New European Drive Cycle condition.

Acknowledgements

Firstly I would like to thank Professor Paul Shayler, my supervisor at the Engines Research group. His help, guidance and support throughout the course of researching and writing this thesis. Thanks is also given to the technical staff of the Engine Research group, Geoff Fryer and Paul Haywood, for ensuring that the test facility was kept in top notch working order, and especially John McGhee, for all his advice and encouragement. All my friends and former colleagues within the department are also thanked, particularly Adam for helping, advising and supporting during much of the research.

Thanks also to the Ford Motor Company, the commercial partners of the Engines Research group, for the provision of the test engine and financial backing.

Finally, I would like to thank my family support and especially my wife, Liz, for all her help, support, encouragement and, most of all, patience.

Nomenclature

$\overline{c_v}$	Average heat capacity	[kJ/kg K]
B	Bore	[m]
x_b	Burned gas mass fraction	[-]
r_c	Compression ratio	[-]
R^2	Correlation coefficient	[-]
θ	Crank angle	[degs]
V_s	Cylinder swept volume	[m³]
V_s	Cylinder swept volume	[m³]
η_{cyl}	Cylinder volumetric efficiency	[-]
Δ or d	Difference	[-]
p_e	Exhaust manifold gas pressure	[Pa]
T_e	Exhaust manifold gas temperature	[K]
EVO_{loss}	Exhaust valve opening mean effective pressure loss	[kPa or bar]
Q	Heat release or transfer	[J]
h_c	Heat transfer coefficient	[W/m²K]
ICW_{loss}	Incremental compression mean effective pressure loss	[kPa or bar]
ρ_m	Intake manifold gas density	[kg/m³]
p_m	Intake manifold gas pressure	[Pa]
T_m	Intake manifold gas temperature	[K]
S_u	Laminar burning velocity	[m/s]
$\dot{m}_a$	Mass flow rate of air induced	[kg/s]
$\dot{m}_f$	Mass flow rate of fuel induced	[kg/s]
m_f	Mass of fuel in cylinder charge	[kg]
mep	Mean effective pressure	[kPa or bar]
$\overline{S}_p$	Mean piston speed	[m/s]
A	Measured and calculated oxygen-containing species to measured carbon	[-]

	containing species	
$\tilde{x}_i^*$	Mole fraction of species indicated on a dry basis	[-]
$\tilde{x}_i$	Mole fraction of species indicated on a wet basis	[-]
A_{ring}	Orifice area facilitating cylinder blowby	[m^2]
n	Polytropic index/ Wiebe form factor	[-]
p	Pressure	[bar or Pa]
x_r	Residual gas mass fraction	[-]
R	Specific gas constant	[J/kg K]
σ_{IMEP}	Standard deviation of indicated mean effective pressure	[kPa or bar]
m_a	Trapped cylinder air mass	[kg]
m_b	Trapped cylinder burned mass	[kg]
m_f	Trapped cylinder fuel mass	[kg]
m_{EGR}	Trapped external exhaust gas recirculated	[kg]
m_i	Trapped intake charge mass	[kg]
K	Water gas equilibrium constant (3.5)	[-]
a	Wiebe efficiency factor	[-]
W_c	Work per cycle	[J]

General subscripts

0-10%	0-10% mass fraction burned
10-90%	10-90% mass fraction burned
bby	Blowby
c	Compression
d	Delay
e	Expansion
f	N:C ratio in a given fuel
g	Gross
ht	Heat transfer
i	Internal
id	Ignition delay
max	Maximum value
n	Net
s	Spark
y	H:C ratio in a given fuel
z	O:C ratio in a given fuel

Abbreviations

AFR	Air Fuel Ratio
BDC	Bottom Dead Centre
CA	Crank Angle
CAE	Computer Aided Engineering
CCV	Cycle to Cycle Variation
CO	Carbon Monoxide
CO_2	Carbon Dioxide
COV	Coefficient of Variance
COV_{IMEP}	Coefficient of Variance of IMEP
ECU	Engine Control Unit
EDC	European Drive Cycle
EGR	Exhaust Gas Recirculation
EMS	Engine Management System
EOC	End of Combustion
EVO	Exhaust valve opening
FID	Flame Ionisation Detector
FTP75	Federal Test Procedure 75
GDI	Gasoline Direct Injection
GFR	Gas Fuel Ratio
HC	Unburned Hydrocarbon
HCs	Unburned Hydrocarbons
HEGO	Heated Exhaust Gas Oxygen sensor
IC	Internal Combustion
IMEP	Indicated Mean Effective Pressure
IMPR	Inlet manifold pressure referencing
IVC	Intake valve closing
MAF	Mass Air Flow
MAP	Manifold Absolute Pressure
MBT	Maximum Brake Torque
MBT^*	Minimum Spark Advance for Best Torque
NDIR	Nondispersive - Infrared Analysers
NEDC	New European Drive Cycle
NO	Nitric Oxide
NO_2	Nitrogen Dioxide

NO$_x$	Oxides of Nitrogen
Nu-SIM	Nottingham University Simulation
NVH	Noise Vibration and Harshness
O$_2$	Oxygen
OBD	Onboard Diagnostics
PFI	Port Fuel Injected
PIPR	Polytropic index pressure referencing
PMEP	Pumping mean effective pressure
PW	Pulse Width
rpm	Revolutions per minute
SI	Spark Ignition
TDC	Top Dead Centre
UEGO	Universal Exhaust Gas Oxygen sensor
VCT	Variable Cam Timing
VO	Valve Overlap
VVT	Variable Valve Timing
VVTi	Variable Intake Valve Timing
WOT	Wide Open Throttle

CHAPTER 1

Introduction

1.1 Background

This thesis contains two main areas of research both related to gasoline fuelled spark ignition (SI) engines. Firstly, evaluating the combustion process and causes of cycle to cycle variability (CCV) and secondly characterising feedgas emissions. The experimental work was carried out on a modern port fuel injected (PFI) gasoline engine with variable intake valve timing (VVTi). The application of variable valve technologies is becoming commonplace amongst the new generation of SI engines, for reasons which include raising power output, extending the working range of engine speed and reducing part-load throttling losses. Yet there exists interactions between valve events and the combustion process that need to be more fully understood. The aim of the combustion study is to investigate these interactions, the limits of stable operation and the causes of CCV. Directly linked to this study is the characterisation of emissions using measurable or easily determinable factors of engine state and what physics of behaviour underpins the connection of these. The emissions studies are more generally used to understand engine performance.

The number of cars globally exceeds 550 million with an estimated rate of production of 45 million cars per year [1]. The market share of diesel powered passenger cars has increased substantially in Western Europe from 28 to 49% in the last 6 years [2], in the US the SI engine still remains the power plant of choice with a significant proportion powered by large capacity V8 engines. The V8 designs are regarded as having good noise, vibration and harshness (NVH) characteristics associated with high power at full load, meaning that these engines tend to be lightly loaded at most in-service operating conditions. The consequence of operating at light load is that fuel economy and engine-out pollutant emissions are inherently greater, predominantly due to high throttling losses. Applications of the V8 engine

in Europe are mainly found in the luxury vehicle market. Due in part to the higher profit to cost ratio and customer expectations, electronic throttle control and variable valve timing first emerge in the same market.

The scope to raise the efficiency of the SI engine through design improvements has reduced as key parameters such as compression ratio and combustion chamber design have evolved towards their best achievable values or designs. Modern SI engines typically have compression ratios between $9 - 11$, with pentroof, 4 valve per cylinder combustion chamber design. These advancements affect the efficiency of the engine across the entire operating range, yet the diverse nature of the operating range means there still exists compromises between design variables. Optimisation of the gas exchange process throughout the operating range by the use of variable valve timing (VVT) has potential to improve volumetric, mechanical and thermal efficiencies therefore reducing fuel consumption and emissions. Systems used on engines vary in complexity that generally fall into two categories variable phase systems and variable event timing systems, with the ability in either case to add variable lift.

Application of VVT systems coupled with advances in aftertreatment systems has increased the interest in the operation of SI engines with lean, dilute mixtures. This is a potentially more fuel efficient and less polluting mode of operation compared to traditional SI engines that are required to operate within a close bound around stoichiometric. One significant problem associated with lean and or dilute mixture preparation is that the combustion process is likely to be less stable cycle by cycle. The development of limiting physical and chemical parameters is necessary so engines can operate in areas that are not associated with increasing cyclic variability. This can result in a rapid increase in hydrocarbon (HC) emissions and a noticeable decrease in engine work output.

The move from mechanical to electronic control of the engine has been of significant importance. Both modern SI and diesel vehicles being controlled by an engine management system (EMS) embedded in the engine control unit (ECU). The complexity of the EMS has increased due to more sensors and actuators embedded in the engine, coupled with increasingly stringent legislation. Particularly important

on SI engines is the use of oxygen sensors (commonly known as heated exhaust gas oxygen sensor (HEGO) and universal heated exhaust gas oxygen sensor (UEGO)). These sensors are integral in maintaining closed loop fuelling and therefore high conversion efficiencies of the exhaust aftertreatment system, vital in adhering to legislation.

The use of computer aided engineering (CAE) has become commonplace in the automotive industry with models of different complexities being used throughout the design procedure to reduce development time and optimise the final product. The drive cycle defined in standard legislative test procedures, the new European drive cycle (NEDC) in Europe, federal test procedure 75 (FTP75) in North America, for example are used to simulate operating conditions arising in vehicle service. Driving vehicles through these standard cycles allows a standardised comparison of emissions and fuel economy of different vehicles. Development of vehicle models that predict engine performance over the drive cycle, off cycle and steady state conditions enables evaluation of important system interactions that effect emissions and fuel economy. The models can be used in the development stages of the vehicle allowing evaluation of strategy and calibration changes. Importantly the model can be used to evaluate the effect of sensor failure or degradation on emissions and the resulting consequences on the aftertreatment system over the vehicle lifetime, on a legislative perspective, 80,000km or 5 years (Euro III), from January 2005 (Euro IV) 100,000km or 5 years [3].

1.2 Research Objectives

Specific tasks undertaken include:

- Investigate the chemical (air/fuel/residual fractions) and physical (spark timing) limits of stable work output of a V8 SI engine with VVTi.

- Investigate, evaluate and utilise the most robust method for calculating the mass fraction burned rates from the measured cylinder pressure data.

- Determine the instability of which part of the combustion event, flame development or rapid burn causes unstable work output.

- Develop a set of emissions generic functions, describing CO, HC and NOx emissions across the full operating range of the V8 engine.

- Incorporate and assess the influence of the emissions generic functions developed over the NEDC in Nottingham University Simulation (Nu-SIM) V8

- Compare and contrast the generic functions with physical based emissions models.

The investigations reported in this thesis are primarily concerned with the combustion process and emissions from a PFI SI engine with VVTi. Previous work [4] established combustion stability limits based on variability in the work output of an I4 engine both at fully warm and cold operation. The transition from stable to unstable operation at a range of engine speeds and loads was characterised using the mixture gas fuel ratio (GFR). It was found that at fully warm conditions a rapid decay in combustion stability consistently occurred at a GFR of 25:1. This study only investigated the variations in work output, no analysis of the combustion was provided. Further work by Lai [5] used experimental data to develop boundaries of stable work output based on chemical factors, namely, GFR, burned gas fraction (x_b) and air fuel ratio (AFR), with minimal investigation on the influence of spark timing, using similar methodology to that of [4]. Analysis of the combustion was provided using software developed by the author, where overall, variations in work output were caused as the burn progresses through the charge with little pre-conditions from the early stages of flame development. The aim of the current work was to further investigate the limits on stable operation including a detailed study of the influence of spark retard, since this is routinely used as a method of reducing catalyst light off times by increasing the burned gas temperature. The cause of the variation in work output is investigated by calculating and correlating burn rates and key burn parameters. Specifically investigating the correlation between variability in the flame development and rapid burn angle. Additional to this work is a comparison with alternative methods of defining mixture limits on stable

operation that have been applied to PFI gasoline engines operating on a mixture of liquid and hydrogen fuel [6].

Previous work [7] showed that emissions of carbon monoxide (CO), oxides of nitrogen (NO_x combination of nitric oxide (NO) and nitrogen dioxide(NO_2)) and unburned hydrocarbons (HCs) from three fixed valve timing SI engines were all very similar and could be represented using 'generic functions' based on measured engine parameters. These functions have been applied to a data set from the V8, with particular emphasis on the influence of variable valve timing which has not been previously investigated. The effect of unstable combustion conditions on emissions is characterised separately. The emissions data is used to calculate combustion efficiency, highlighting the importance of determining stable operating limits, which are particularly important when variable valve strategies are available. Finally in some cases, previously developed physical models are compared with the results from the 'generic functions'

The findings from the experimental work have been used to develop feature models that have been used in a V8 version of Nu-SIM, the initial Nu-SIM V8 was developed by Harbor [8] for which the author contributed a significant amount of engine data to which sub models were fitted. These models have been further reviewed and updated in light of the findings from the combustion and emissions study, incorporating the combustion efficiency calculations allowing the influence of unstable combustion cycles to be accurately represented by a representative drop in work output. Results from Nu-SIM are presented over the NEDC assessing the effect of the new emissions models.

1.3 Layout of Thesis

The investigations in this thesis include further development of mixture limits on combustion stability, characterisation of emissions and development and implementation of feature models in Nu-SIM V8. In Chapter 2, relevant literature is

reviewed in relation to the combustion process, included is a historical and current review of European legislation relating to motor vehicles.

In Chapter 3, a review of the engine test facility is presented. This includes an overview of the hardware and software used to capture the engine data. Methods used to calculate key experimental variables are presented. Of key importance the method and results from the in-cylinder gas sampling system, used to characterise the influence of variable valve timing on the residual gas fraction.

In Chapter 4, methods of determining mass fraction burned parameters are assessed. These are the Rassweiler and Withrow method and the traditional first law of thermodynamics approach. Results from the two methods as the combustion process becomes unstable are compared. Critically, the number of cycles required to accurately calculate burned mass fraction values is defined.

In Chapter 5, the chemical and physical limits on combustion stability in terms of a limit on cyclic variability of indicated mean effective pressure (IMEP) are defined. The data used was taken from sweeps carried out in three different ways: either constant fuelling, air charge or load at engine speeds and loads typical of the V8 engine.

Chapter 6 develops the causes of CCV by establishing the link between the variation of IMEP with burned mass fraction data.

Chapter 7 uses the functional form of the previously developed 'generic functions' [7] to fit the emissions data from the V8 engine. The influence of VVTi is taken into account by adding new functions; an assessment of an alternative method for determining relative spark timing and variations in combustion efficiency is also presented. The influence of the newly developed emissions and combustion models on vehicle performance are shown by comparing outputs from the V8 version of Nu-Sim. Chapter 8 reviews literature related to the emissions work developed in Chapter 7, where applicable the 'generic functions' are underpinned using previously developed physical models. In the case of HC emissions the functions are broken down into two parts, emissions resulting from normal combustion process and those from unstable operating conditions.

Chapter 9 is used to revisit the stability investigation. A simple heat release model is used to investigate the relationship between variability in the flame development and the rapid burn periods, where the variations in heat release was produced by manipulating the Wiebe function.

Discussions and conclusion are provided in chapter 10.

CHAPTER 2

Literature Review

2.1 Introduction

Relevant literature and background to the work presented in this thesis are reviewed in this chapter, although specific literature relating to emission formation mechanisms is reviewed in the relevant chapter. Firstly, European legislation relating to SI motor vehicles are described in detail from its inception to the current standards, with reference to Onboard Diagnostics (OBD). An overview of the combustion process is provided, discussing previous work that has described the causes of cycle to cycle variability. Methods of extending stability limits and emerging gasoline technology that are capable of utilizing these technologies are also discussed. VVT strategies are introduced, with both the types and effects of each system being reviewed.

2.2 Legislation the European perspective

This section focuses on the development of emissions legislation relating to motor vehicles within the European Community, Figure 1 provides an overview of the emissions limits imposed and the associated percentage reduction of each emission from the first legislation. The first legislation came into force in 1970 [9] this legislation only related to spark ignition engines, imposing limits on emissions of HCs and CO. The legislation comprised three separate tests. The type 1 test, known as the European Drive Cycle (EDC) shown in Figure 2 was designed to mimic conditions of urban journeys from an initial cold engine start. The test lasting thirteen minutes comprised four cycles that were carried out without interruption, each cycle containing 15 phases (idling, acceleration, steady speed, deceleration,

etc). The vehicle was soaked prior to the test for a period of six hours at between 20 to 30°C, the actual test start, when exhaust gas collection began, was 40 second after the initial attempt to start the engine. The mass of CO and HCs had to be less than the legislative limit, where the limits varied with vehicle reference weight as indicated by the error bars. Conformity of production for a series of vehicles was also described, where CO and HC limits had to be no greater than 20% and 30% higher than the legislative limits respectively. Test types 2 and 3 limited CO emissions at idle and HC crankcase emissions respectively. Emissions of NOx were not included in the legislation until 1976[1]. The conflicting engine strategies required to reduce NOx and HC emissions simultaneously was reflected in the legislation when a further refinement in 1983[2] combined these two emissions into one limit, thus allowing engine manufacturers to pursue strategies to lower NOx or HC emissions. The new legislation also applied to diesel powered vehicles, due essentially to the increased market share. Although further legislation altered vehicle categorisation and introduced limits on particulates, significant changes to the vehicle testing procedure occurred with the introduction of what is commonly known as Euro I legislation [9][3].

The Euro I legislation altered test type 1 (the EDC) by introducing an extra urban cycle proceeding the four elementary urban cycles as shown in Figure 2, with the new drive cycle known as the new EDC (NEDC). The issues of fuel economy were raised whereby in the future measures to curb carbon dioxide (CO_2) emissions would be proposed. Euro I legislation for spark ignition engines was only achievable with exhaust after treatment systems; these systems require specific operating conditions to maintain high conversion efficiencies [10]. The emissions recorded for the type 1

---

[1] Date of legislation, type approval required from 01/10/77, prohibit the entry into service of vehicles from 1/10/80.

[2] Date of legislation, type approval required from 01/10/84, prohibit the entry into service of vehicles from 1/10/86.

[3] Date of legislation, type approval required from 01/7/92, prohibit entry into service of vehicles from 31/12/92.

test were therefore multiplied by a deterioration factor, supplied by the manufacturer, based on experimental data, or specified in the legislation, the aim that the aftertreatment system was robust enough to meet the standards for 80,000km. Euro I also introduced limits on evaporative emissions. To increase the rate of development of cleaner vehicles that would meet new legislation earlier, provisions for tax incentives were put in place to equal the expenditure on the aftertreatment costs. Euro II further reduced the emissions limits.

Euro III and IV legislation were introduced together in 1998[4], with different implementation dates, allowing engine manufacturers to better plan the engine and aftertreatment system developments required to meet the future standards and take full advantage of the tax incentives available if they met the standards early. Along with the further reduction in the emissions levels significant changes to the vehicle tests were made. Emissions were sampled from key on for the NEDC and a new test was introduced to specifically legislate against cold start emissions, namely CO (15 g/km) and HCs (1.8 g/km), where the vehicle was driven over the EDC with the ambient temperature maintained at -7°C.

The issues of maintaining highly efficient emissions control systems over the vehicle lifetime were further addressed with the introduction of OBD for emissions control systems. "Emissions control systems" were defined as the EMS and any emission-related component in the exhaust or evaporative system which supplies an input or receives an output from the EMS. The OBD system must have the capability to record in the EMS any malfunction of an emission-related component or system that would result in emissions exceeding the limits. Specifically related to SI engines, it was necessary to be able to detect and log engine misfire either caused by poor fuel metering or the absence of spark, if the occurrence of misfire exceeded a certain threshold then fuelling was disabled to the misfiring cylinder. Oxygen sensors (HEGO and/or UEGO) needed to be checked for continuity and fuelling

---

[4] Date of legislation, Euro III type approval required from 01/01/00, prohibit entry into service from 1/01/02, Euro IV type approval from 01/01/05, prohibit entry into service from 01/01/06

perturbation strategies needed to be included as part of the EMS to check for failing catalysts. The OBD test in the legislation required manufacturers to supply faulty components that needed to flag errors when the vehicle was driven over the NEDC. The direct impact on the consumer was that the vehicle is fitted with an OBD dash light, that illuminates when OBD faults are registered, this indicates the EMS has moved into a limp home or emergency start-up strategy and requires the fault to be diagnosed and remedied. Finally, the move from Euro III to IV requires the increased robustness of the emission control system with conformity of in service vehicles required for 100,000km compared to 80,000km previously.

Significant reductions in vehicle out emissions have been achieved since the introduction of legislation, although much of the reduction has been achieved with aftertreatment systems, which necessitates, in SI engines for the combustion system to be operating at a relatively stable condition, namely stoichiometric. The drive for lower CO_2 emissions both from the customer and governments needs advancements in the combustion system so as to achieve the minimum fuel consumption. These necessary changes are likely to move the combustion process towards less stable regimes, which need to be fully understood before a successful design can be productionised.

2.3 SI combustion process and factors affecting combustion stability

In a PFI spark ignition engine in which fuel and air are inducted together, forming a relatively homogeneous mixture, it is plausible to divide the combustion process of this mixture into four distinct phases: (1) spark ignition; (2) early flame development; (3) flame propagation; and (4) flame termination. It is widely accepted [11,12,13,14] that significant improvements in fuel economy can be achieved by operating with lean or dilute mixtures. Three factors are predominant in causing the improvement in fuel economy: (1) reduced pumping work at constant break load (with dilute mixtures because fuel and air remain constant; hence intake pressure

increases, with lean mixtures because the air is increased; hence intake pressure increases); (2) reduced heat transfer to the walls because the burned gas temperature is decreased significantly; and (3) a reduction in the degree of dissociation in the high-temperature burned gases which allows more of the fuel's chemical energy to be converted to sensible energy near TDC. The first two of these are comparable in magnitude and each is about twice as important as the third. The problem associated with lean and dilute mixtures is that the combustion process is significantly less robust. The mixture is harder to ignite and flame propagation is slower with a greater susceptibility for partial burning, a combination of these factors leads to an unacceptable increase in cyclic variability limiting the range of operating conditions. The next sections provide a review of each phase of combustion discussing techniques used to reduce cyclic variability therefore extending the stable operating range.

2.3.1 Spark ignition and flame initiation

The ignition energy required to ignite quiescent stoichiometric gasoline and air mixture is about 0.2mJ. Conventional ignition system delivers a spark with 30 to 50mJ where spark durations are greater than 0.5ms [14]. In a typical spark discharge there are a number of important phases, namely the breakdown, electrical arc and glow discharge phases. The first two phases establish the ignition plasma; it is during the glow discharge phase that self sustaining propagation of the flame kernel begins. The successful development of a flame kernel depends on a large number of parameters such as ignition energy, plasma volume and location, chemical reactions, mean flow field and turbulence around the spark plug location [15]. Even if successful propagation of the flame kernel occurs fluctuations in any of the factors mentioned contribute to CCV. A number of researchers have investigated methods of enhancing the flame ignition. A comprehensive study of different ignition systems by Geiger et al [16] showed that transistorized coil ignition systems lead to better flame initiation of lean mixtures than a capacity-discharge ignition system. In the same study, spark plugs with thin electrodes and extended electrode gaps were found to extend the lean limit for stable combustion which was

corroborated by the findings of [17-20]. The study by Rivin et al [19] using a disc-shape high swirl combustion chamber operating on lean methane mixtures investigated the spark plug orientation and flow velocity through the spark gap. Enhanced spark discharge characteristics (80mJ spark energy) were able to achieve reliable ignition of ultra lean mixtures (equivalence ratios of between 0.62 to 0.64). The spark plug orientation was found to have no influence on the lean misfire limit. At high flow velocities past the spark gap (8.6m/s) no reliable combustion of the mixtures with an equivalence ratio of 0.66 could be achieved, even with the enhanced spark discharge system. This failure to ignite is likely to be caused by excessive stretching of the flame kernel [21]. Many engine based studies [22-24] however, have highlighted that increasing the mean flow velocity and the turbulence using a variety of different mechanisms extends the lean operating limit by reducing the onset of excessively high cycle to cycle variations.

2.3.2 Early flame development

The early flame development period is typically defined by the period between spark and a specified mass fraction burned, although the criteria used varies between different researchers. Early research by Hires et al [24] referred to the flame development stage as the initiation stage, or 'ignition delay', which was the period from spark to one percent mass fraction burned. Although this was an arbitrary point it represented a state where significant energy release began and a fully developed flame front had been established. This period has been used by other researchers [25-27] to help understand the causes of cyclic variability and lean operating limits. Alternatively 2 percent mass fraction period [28] and the 10 percent mass fraction period [22,29] have been used when establishing causes of cyclic variability. In most cases no reasons are provided as to the choice of period, the choice simply being arbitrary, others [30] however state that the earliest period that can be investigated is dependent on the noise in the pressure measurements and heat release calculations. Because researchers have used various different periods, establishing how variability in the early flame development period

influences the overall combustion process and therefore variability in work output is hard to ascertain.

Work by Holmstrom and Denbratt [31] presented a limited number of experimental results where the variability in the 0-2, 0-10, 0-50 and 0-90 percent mass fraction were provided. The same variability was found in each period, indicating how variability in the early flame development period is maintained throughout the rest of the burn. A model was developed specifically investigating the contribution to cyclic variability of random walk of the flame kernel; 0-1 percent mass fraction burned period. Comparing with the experimental results showed that the model predicted only 25 percent of the standard deviation of the combustion duration, IMEP, maximum pressure and location of maximum pressure. It was suggested that additional variability observed could be attributed to flow field fluctuations causing variations in the wrinkling and stretching of the flame kernel during the initial flame development exacerbated by variations in mixing between the fuel, air and residual gas.

2.3.3 Flame propagation

In this phase the flame is assumed to be fully turbulent and is when the main portion of in-cylinder charge is burned, commonly referred to as the rapid burn period. Again this period is defined differently by researchers due to the different definitions for the flame development period. In all modern SI engines the spark plug location is in the centre of the combustion chamber and in the absence of a directed mean flow the flame propagates spherically out from the spark. The rate of propagation is strongly dependent on the active flame front area and the physical and chemical properties embodied in the laminar burning velocity, which is solely a function of mixture composition, temperature and pressure [32]. The development of the flame kernel directly influences the active flame front of the propagating flame; therefore cyclic variability will be manifested in the flame propagation period. The contribution to overall cyclic variability from only the flame propagation period is therefore complex to resolve from experimental work.

2.3.4 Flame termination

Flame termination is characterised, typically as the period of 90 to 100 percent mass fraction burned. In this period the flame impinges on the cylinder walls, locally quenching the flame and significantly slowing the rate of burn. Cyclic variability in this period is likely to have been manifested by variability in the flame development and rapid burn period. Comparisons of calculated mass fraction burned profiles and Schlieren images of the propagating flame indicate that even when essentially 100 percent of the mass has been burned there is still the presence of burning charge [33].

2.4 Measures of cyclic variability

The most important factor with regard to engine performance characteristics is the CCV in IMEP, the most commonly used term used to define the variability is the coefficient of variation (COV_{IMEP}) in IMEP (COV is defined as the standard deviation divided by the mean). IMEP is related to the in-cylinder pressure history and is therefore influenced by various factors such as the rate of heat release from the combustion, heat losses to the cylinder walls and cylinder volume change due to piston motion. It has been shown [34,14] that COV_{IMEP} in the order of 10 percent can result in vehicle driveability problems. Although in the past different thresholds have been used; 6 percent [35], 7 percent [36], 13 percent [37] and 36 percent [38]. More recent work by Hill [39] suggested the COV_{IMEP} limit should be set to 5 percent, the limit was set more conservatively than other researchers to allow some room for overshoot on controllers thus ensuring driveability would not be compromised. Work using a single cylinder engine [17] looking at methods to extend the lean misfire limit used COV_{IMEP} of 2 percent as the threshold value. The limit used will be dependent on experimental equipment. For example factors such as engine cylinder number, number of cylinders monitored and data acquisition system will affect the limit.

Researchers have in the past used a number of other factors to identify cyclic variability. A literature review by Ozdor et al [40] identified parameters that had been used by researchers. There were four distinct areas. Firstly pressure related parameters, in cylinder peak pressure (p_{max}), in cylinder peak pressure location ($\theta_{p_{max}}$), maximum rate of pressure rise ($(dp/d\theta)_{max}$), maximum rate of pressure rise location ($\theta_{(dp/d\theta_{max})}$), IMEP of individual cycles and COV_{IMEP}. Secondly combustion related parameters, maximum rate of heat release ($(dQ/d\theta)_{max}$), maximum burning mass rate ($(dx_b/d\theta)_{max}$), ignition delay ($\Delta\theta_{id}$), combustion duration ($\Delta\theta_d$) and time in crank angles elapsed from ignition to a moment at which a certain mass fraction is burnt ($\Delta\theta_{x_b}$). Fourthly flame front related parameters and fifthly exhaust gas related parameters, although both these parameters are used to a lesser extent.

One of the easiest parameters to calculate is p_{max} since no engine position measurements are required, yet variations in this parameter have been shown [36] to initially increase as the lean limit was approached, in a similar fashion to COV_{IMEP}. Once COV_{IMEP} exceeded 5 percent variations in p_{max} were found to actually decrease. This can be explained by the fact that near the misfire limit the pressure due to combustion is negligible therefore p_{max} will simply reflect the compression pressure which is constant for a given load therefore variability will decrease. This would also apply, therefore to variability in $\theta_{p_{max}}$. A study by Brown et al [12] came to similar conclusions where COV_{IMEP} and $COV_{p_{max}}$ showed no correlation when the ignition timing was varied.

The heat release profile is calculated using the first law of thermodynamics which can also be used to calculate the mass fraction burned profiles, although it is more usual to calculate burn parameters using the Rassweiler and Withrow method. Typically the approach adopted by researchers [17], in recent times is to use COV_{IMEP} as the key variable to determine cyclic variability and analyse the causes of the COV_{IMEP} from calculated burn parameters. These typically include the use of different burn durations, for example 0-10 percent mass fraction burned (flame development angle ($(\Delta\theta_{0-10\%})$)) and 10-90 percent (rapid burn angle ($(\Delta\theta_{10-90\%})$)).

The variation of researchers' approaches to investigate CCV makes it difficult to compare results and establish definitive reasons for the causes of the variability. It is though necessary to investigate both the variability in work output from the engine, namely *IMEP* and to understand the root causes of this variability, analyse the burn rates, simply investigating pressure related parameters are unlikely to provide significant information to understand the variations.

2.5 Variable Valve Timing

The manipulation of valve timings provides the ability to overcome some constraints that are implicit with an SI automotive engine design, since typically a compromise between valve timings to maintain stable idle combustion and wide open throttle (WOT) maximum power needs to be adopted [41].

VVT can be used to describe variable phasing mechanisms, where the valves open and close at different times in the cycle, where on simple systems phasing the intake valve is preferred, with more complex systems phasing both the intake and exhaust. Some systems also utilise variable valve lift along with phasing where typically two or three settings are available, finally the most complex of systems utilise both intake and exhaust valve phasing and lift where the lift can be different for each intake or exhaust valves. Many mechanisms have been investigated to implement VVT. Work by Moriya et al [42] tabulated the merits of many different designs during the description of the development of a continuously variable intake cam phasing system, as with many systems the one offering the most independence and therefore the greatest of possible benefits, electromagnetic controlled valves is also the most complex and hardest to implement. Although comparing the deliverables namely, increased power, torque, fuel economy and a reduction in emissions against the number of additional parts cam phasing was described as being the most cost effective.

Variable intake cam phasing has been investigated by a number of researchers [43-45]. Leone et al [43] showed that a significant benefit of advancing the intake valve

timing at part load was that the residual gas fraction (x_r) substantially increased, this resulted in a direct reduction in NOx and HC emissions, pumping work is also reduced due to the increased internal residual recirculation therefore a higher manifold absolute pressure (MAP) is required to maintain a given load. The results were compared with dual equal and exhaust only valve phasing where dual equal was found to provide the greatest fuel economy benefit and exhaust only greatest NOx reduction, concerns were also raised with the intake only strategy since this increased the probability for engine knock. Duckworth and Barker [44] included port throttling investigations alongside variable intake cam phasing, benefits were found from both systems. Specifically from the variable valve phasing improved idle stability, peak power and fuel consumption was demonstrated; specific reference was made to the ability to replace external exhaust gas recirculation (EGR) systems with the internal EGR created by changing the valve timing.

CHAPTER 3

Test Facilities and Key Experimental Variables

3.1 Introduction

This chapter describes the engine test facility, data acquisition system and how key experimental variables were determined, namely, AFR, burned gas fraction (x_b), minimum spark advance for best torque (θ_{MBT^*}), $IMEP$ and COV_{IMEP}. The test engine was a production Jaguar AJ27; naturally aspirated PFI 4.0l V8. The engine was equipped with an electronically controlled throttle and variable intake cam phasing. An in-line automatic transmission was used to couple the engine to a dynamometer. The engine was instrumented to allow data acquisition while software provided by Jaguar was used to interrogate and adapt calibration settings of the EMS. The test facility and software for data acquisition were designed and implemented by Harbor [8] and Lai [5], and only a brief description is provided here. The experimental procedure used to determine key variables is described highlighting the effect of changes in valve overlap (VO) on x_b and the particular problems associated with determining AFR when experimenting at unstable operating conditions.

3.2 Power Plant Description

The AJ27 is a 90º V8, quad cam, 32 valve engine with an aluminium structure that has been in production since 1996; Table 1 provides engine specifications as defined by Szczupak et al [46]. Of particular importance to this study was that the intake valve timing could be phased over 42ºCA, while maintaining a constant opening

duration of 230ºCA, the exhaust cam timing was fixed, as shown in Figure 3. The full range of cam phasing was only available above 1000rpm.

The engine was coupled via a production automatic gear box to a 250kW Froude Consine eddy current dynamometer, the controller of which could run in one of three modes; constant brake torque, speed or power. The 5 speed gear box was locked in 4th gear corresponding to a gear ratio of 1:1. Fuel was pumped to the engine from the original vehicle fuel tank by an external fuel pump, the fuel supplied was standard pump 95 octane ultra low sulphur unleaded petrol complying with BS EN 22B; additional specifications are shown in Table 2. A cooling tower was installed to provide cooling for the engine and dynamometer via different cooling circuits. An automatic cooling replenishing system was used for directly cooling the dynamometer, while the engine was cooled indirectly via a heat exchanger coupled to the engine coolant circuit. An extra heat exchanger was used to cool the engine oil. The exhaust system was again taken from a production vehicle and was installed on the test bed with minimal modifications including catalysts and silencers, allowing representative measurements to be made.

3.3 Engine control and data acquisition

The engine was controlled with a 16bit dual processor production EMS. Calibration parameters such as spark timing, cam phasing and fuelling could be interrogated and altered using software provided by Jaguar. The system also allowed 16 EMS variables to be logged. An independently controlled stepper motor was used to actuate the pedal position and hence control the electronic throttle.

Data acquisition was achieved using hardware and software (LabVIEW) from National Instruments. Two data acquisition systems were developed in LabVIEW. The first, 'time based', where steady state measurements such as temperatures, inlet and exhaust manifold pressures were recorded, the system had the capability to record from 32 differential analog input channels at typically a rate of 5 Hz. Table 3 shows the variables recorded and relevant location of all the variables logged using

the time based data acquisition system. The second 'triggered based', was used to acquire high speed data, primarily for the acquisition of in-cylinder pressure, 8 differential analog input channels could be recorded up a rate of 500kHz, more than adequate for the range of engine speeds investigated.

3.4   Test Equipment

All thermocouples used were K type with accuracy of $\pm 1^{\circ}C$ across the operating range. Supplementary AFR sensors (Horiba MEXA-700) were installed on both exhaust lines (one for each bank). The intake and exhaust manifold pressure were measured using Kulite sensors. Either feed gas or post catalyst emissions could be sampled using an emissions stack capable of measuring NO_x, HC, CO, CO_2 and oxygen (O_2). NO_x was measured on a wet basis (exhaust gas directly sampled) using a chemiluminescent gas analyser, HCs were also measured on a wet basis using a flame ionisation detector (FID) gas analyser, CO and CO_2 were measured on a dry basis using nondispersive - infrared analysers (NDIR) and O_2 was measured on a dry basis using a paramagnetic analyser [47]. All analysers were calibrated following the manufacturers guidelines before each testing session and recalibrated at the end of the testing period to check for drift.

In-cylinder pressure was measured in two cylinders, one from each cylinder bank, with Kistler piezoelectric 6052A high speed pressure transducers flush mounted in the cylinder head, the signal from the transducer was amplified using Kistler 5011 charge amplifier. The Kistler 6052A is reported [48] to be robust to the intermittent exposure to the combustion event in an internal combustion (IC) engine which can result in thermal shock. This is the contraction and expansion of its diaphragm due to the temperature difference, causing the force applied to the quartz crystal to be different for a given cylinder pressure. Thermal shock causes errors in pressure measurements with notable errors in the calculated values of $IMEP$. The work by Rai et al [48] has characterised the effect of thermal shock on $IMEP$ using reference water cooled sensors as a baseline, thermal shock was shown to be dependent on sensor type, engine speed and peak in-cylinder pressure, with the

greatest effects being at low engine speed, high loads and advanced ignition timings. Results for the Kistler 6052A show $IMEP$ errors due to thermal shock are less than -1%, with the sensor completely recovering from the effects of thermal shock by the end of the expansion stroke.

The in-cylinder pressure is logged with reference to the engine crank angle (CA); CA was measured using a Hohner shaft encoder that was coupled to the crank shaft. The encoder gave a Top Dead Centre (TDC) pulse and a pulse every 0.5 degrees crank angle (°CA). Significant errors in calculated values of $IMEP$ can occur when the cylinder volume is phased incorrectly with the in cylinder pressure, that results from the cylinder pressure being referenced incorrectly with the crank angle. Previous work by Brunt [49] has shown that for a 1°CA TDC phasing error, the associated error in calculated $IMEP$ can be up to 6% for a SI engine operating from idle to full load. Two methods for determining TDC to accuracies greater than 1°CA are available, analytical determination based on motored traces or a capacitance probe. Nilsson and Eriksson [50] have analytically investigated 4 methods of determining TDC from simulated pressure traces with the most robust method determining TDC within 0.1°CA, but the methods are sensitive to errors in geometry and heat transfer information. The benefit of the capacitance probe is that it is mounted in the engine and can be used under fired and motored conditions, the probe outputs a continuous signal based on the proximity of the piston to the probe and therefore allows direct comparison with the TDC signal from the shaft encoder as shown in Figure **4**. The capacitance probe was successfully used in the engine to determine TDC to ±0.2°CA, acceptable here since this study focuses on the variability of $IMEP$ rather than absolute values.

3.5 Determination of Key Experimental Variables

The work presented here relies on the determination and calculation of key experimental variables. The choice of method used is dependent on the engine operating condition. The methods are described in the following subsections.

3.5.1 Determination of relative spark timing

Spark timing determines the start of combustion. If it is too early, work transfer from the piston to the gases in the cylinder at the end of the compression stroke is too large and high rates of heat release may result in engine knock. Contrastingly if combustion starts to late indicated thermal efficiency is penalised, peak cylinder pressure is reduced and the expansion stroke work transfer from the gas to the piston decreases as shown in Figure 5. At a fixed speed, mixture composition and flow rate there exists a spark timing that gives maximum engine torque, known as maximum brake torque (θ_{MBT}), this timing also gives maximum brake power and minimum brake specific fuel consumption. The maximum in each brake torque curve is quite flat particularly at low load as shown in Figure 6, therefore accurate determination of θ_{MBT} is relatively uncertain. An alternative definition is used throughout this work which defines the minimum advance spark timing for best torque (θ_{MBT^*}) corresponding to a spark timing retarded to give a 1 percent reduction in torque from the maximum value.

Minimum advance spark timing for best torque is determined at each steady state condition by conducting a spark sweep from significantly retarded timings to the knock limit or once the torque has significantly reduced from the peak, a 2nd order polynomial is fitted to the data from which θ_{MBT} and θ_{MBT^*} are determined. Adopting this method, for most operating conditions the average correlation coefficient, (R^2) is >0.95, although this reduces to R^2 > 0.84 for operating conditions at the partial burn/misfire limit. The reduction is caused by increased fluctuations in torque at each given spark timing. Over a wide range of speeds and loads the difference between θ_{MBT} and θ_{MBT^*} varied from 3ºCA to 5ºCA. For a given operating condition the spark timing relative to MBT* is defined as

$$\theta_{\Delta MBT} = \theta_{MBT^*} - \theta_s \qquad (1)$$

where θ_s is the absolute spark timing. A value of zero $\theta_{\Delta MBT}$ corresponds to MBT* and a positive $\theta_{\Delta MBT}$ refers to spark timings retarded from MBT*.

3.5.2 AFR calculation and determination

The definition of AFR is:

$$AFR = \frac{\dot{m}_a}{\dot{m}_f} \tag{2}$$

where, $\dot{m}_a$ is the air mass flow rate (kg/s) and $\dot{m}_f$ the fuel mass flow rate (kg/s). Three typical methods are used to determine AFR, the first given by equation 2, the second using an exhaust oxygen sensor, in this case a UEGO referred to as AFR_{UEGO} and the third, based on exhaust gas emissions referred to as $AFR_{emissions}$. In principle, AFR can be determined from measurements of the induced flow rates of fuel and air. Calibration of the fuel injectors based on the demanded pulse-width from the EMS was carried out by Harbor [8] the fuel delivered was a linear function of fuel pulse width (PW), given by

$$m_f = 2.815 \times 10^{-9} \times PW + 0.849 \times 10^{-7} \tag{3}$$

where m_f is the mass of fuel injected per cylinder (kg) and PW is in milliseconds (ms), directly measured by the EMS. Reliable measurements of air mass flow rate ($\dot{m}_a$) using the engine mass air flow rate (MAF) sensor proved difficult, however, and was abandoned when the AFR from equation 2 was found to be inconsistent with AFR_{UEGO} and $AFR_{emissions}$.

Several methods of calculating AFR based on measured exhaust gas emissions have been proposed [51-54]. An assessment of different methods was carried out by Lynch and Smith [55], the findings showed that the methods used by Urban and Sharp [54] and Fukui et al [52] were essentially identical and more accurate than other methods because fewer simplifying assumptions were made. The method of Urban and Sharp [54] was therefore applied and is briefly outlined, for a generalised fuel which can be described as $CH_y O_z N_f$:

$$AFR_{emissions} = \frac{A \times 4.773 \times 28.96}{12.011 + 1.008\,y + 15.999\,z + 14.008\,f} \tag{4}$$

A is the measured ratio of oxygen-containing species to measured carbon containing species, y is the H:C ratio assumed to be 1.85, with both z and f being zero for standard pump grade gasoline. A is given by:

$$A = \frac{y}{4} - \frac{z}{2} + \frac{\left(\tilde{x}_{CO_2} + \tilde{x}_{O_2} + \tilde{x}_{NO_2} \frac{(\tilde{x}_{CO} + \tilde{x}_{NO})}{2} + \tilde{x}_{HC}\left(\frac{z}{2} - \frac{y}{4} \right) - \frac{y\tilde{x}_{CO}(\tilde{x}_{CO} + \tilde{x}_{CO_2})}{4(Kx_{CO_2} + \tilde{x}_{CO})} \right)}{\left(\tilde{x}_{HC} + \tilde{x}_{CO} + \tilde{x}_{CO_2} \right)} \tag{5}$$

K, the water gas equilibrium constant is assumed to be 3.5, with all species, $\tilde{x}_i$ measured as mole fractions with the same background moisture, in this case wet. The $\tilde{x}_{NO}$ and $\tilde{x}_{NO_2}$ are measured as a combined $\tilde{x}_{NO_x}$ the ratio of $\tilde{x}_{NO} : \tilde{x}_{NO_2}$ was set to be constant across all operating conditions as 10:1.

The oxygen concentration was measured using a paramagnetic analyser, the measured oxygen concentration is affected by other paramagnetic gases, namely

$\tilde{x}_{NO}$, $\tilde{x}_{CO}$ and $\tilde{x}_{CO_2}$. A correction to the $\tilde{x}_{O_2}$ accounting for $\tilde{x}_{NO}$, $\tilde{x}_{CO}$ and $\tilde{x}_{CO_2}$ is made based on values given in [56], where the correct oxygen concentration used in the $AFR_{emissions}$ calculation is given by:

$$\tilde{x}_{O_2(corrected)} = \tilde{x}_{O_2(measured)} - 0.442\tilde{x}_{NO} + 0.00623\tilde{x}_{CO} + 0.00354\tilde{x}_{CO_2} \quad (6)$$

The exhaust gas emissions are measured directly on a percentage molar volume basis, $\tilde{x}_{CO_2}^*$, $\tilde{x}_{CO}^*$ and $\tilde{x}_{O_2}^*$ are measured on a dry basis whereas $\tilde{x}_{HC}$ and $\tilde{x}_{NO}$ are measured on a wet basis. The relationship between wet and dry species is given by:

$$\tilde{x}_i = (1 - \tilde{x}_{H_2O})\tilde{x}_i^* \quad (7)$$

where:

$$\tilde{x}_{H_2O} = \frac{y}{2} \frac{\tilde{x}_{CO}^* + \tilde{x}_{CO_2}^*}{[1 + \tilde{x}_{CO}^*/(K\tilde{x}_{CO_2}^*) + (y/2)(\tilde{x}_{CO}^* + \tilde{x}_{CO_2}^*)]} \quad (8)$$

The Horiba MEXA-700λ UEGO sensors are quoted to have an accuracy to within ±0.3 AFR in the range of 9.5-20 AFR, and within ±2.0 AFR for the rest of the lean operating range [57]. UEGO sensors all operate on the Nernst principle, basically, by applying a pump voltage, oxygen from the exhaust gas is pumped through a diffusion barrier into or out of a diffusion gap that remains at stoichiometric. The pump current is proportional to the exhaust-gas oxygen concentration and this is a non-linear measure for AFR [58]. Figure 7 shows the difference in $AFR_{emissions}$ and AFR_{UEGO}. For the range shown the difference between $AFR_{emissions}$ and AFR_{UHEGO} is within the 10% error, although as indicated by the trendline once the AFR is greater than 20 the AFR_{UEGO} measures leaner than that determined from the emissions. This phenomenon is essentially caused by the occurrence of partial and

misfiring cycles at those very lean operating conditions, significantly increasing the HC emissions that results in inaccuracies in measurements from the UEGO and emissions to different degrees. Winborn [4] highlighted these problems experimenting at partial burning/misfiring conditions where the AFR_{UEGO} was found to measure leaner than the mixture ratio supplied. The work involved operating the engine at a constant throttle angle, engine speed and temperature; it can therefore be assumed the air charge is constant. The fuel flow rate is therefore directly proportional to changes in the injector fuel pulse width. Comparing the instantaneous fuel injected with the fuel injected of a stable AFR at the given operating condition allows determination of a corrected exhaust gas AFR_c during unstable operating conditions, where:

$$AFR_c = \frac{AFR_{emissions\_stable} m_{f\,stable}}{m_{f\,unstable\_condition}}$$

(9)

m_f is determined in both cases from equation 3. Figure 8 compares the inaccuracy of AFR_{UEGO} and $AFR_{emissions}$. It is apparent that AFR_{UEGO} predicts substantially leaner than the AFR_c, although the error associated with using $AFR_{emissions}$ is less than the AFR_{UEGO} in the worst case scenario the error difference can be as high as 20%. Based on these findings, at stable operating conditions $AFR_{emissions}$ was used, for unstable operating conditions the AFR was calculated from equation 9.

3.5.3 Influence of Valve overlap on the residual gas fraction

VVT is known to affect the in-cylinder residual gas fraction (x_r). Many researchers [45, 59-61] have investigated the effect of different VVT mechanisms on the burned gas fraction, emissions and other engine performance parameters. A comparative study by Leone et al [43] investigating four variable camshaft timing (VCT) strategies at part load has described the predominant effects of variable intake cam phasing. Significant advancement of the intake events extends the VO period into

the exhaust stroke, since the intake manifold is at a lower pressure exhaust gas back-flows from the exhaust port and cylinder into the intake port. This exhaust gas is then drawn back into the cylinder on the subsequent stroke. Thus increasing the intake manifold pressure, reducing pumping work and increasing the x_r resulting in a reduction in NOx and HC emissions.

Accurate knowledge of the x_r is required for modelling purposes and understanding combustion and emissions characteristics, for this reason an experimental test facility was developed to sample in cylinder gases that enabled direct calculation of the x_r. The experimental method and apparatus adopted is similar to that used by Toda et al [59].

The experimental apparatus and control circuitry was designed and validated previously [62] although the author aided in adapting the design for application to the AJ27, therefore a brief summary is given here. A conventional spark plug was modified to accommodate a 1.2mm capillary tube; this tube was connected to a E7T05071 Mitsubishi gasoline direct injection (GDI) fuel injector which acted as the sample valve. Initial design of the apparatus mounted the injector on the engine to minimise the capillary volume, this design was found to be susceptible to failure due to high frequency oscillations of the injector, causing the capillary tube to fracture. A more robust system was implemented where the injector body was mounted away from the engine but resulted in increased capillary volume hence longer sample periods.

The sample period was determined indirectly from the ignition timing and once started was actuated every cycle. The sampling system was designed to ensure that the injector opened only when in-cylinder pressure was greater than atmospheric. The end of the sample period was set at 10°CA before sparking, this value was chosen so as to minimise the effects of the sampling process on combustion. The sampled in-cylinder gas was directly feed into a CO_2 gas analyser. A limiting factor for the experimental set up was that the CO_2 analyser required a minimum flow rate of 0.3l/min, this was achieved for every test condition by retarding the spark timing where necessary, hence increasing the sample period and pressure differential. Operating under these optimised conditions meant there was a time delay of

approximately 30s from the start of sampling before the analyser settled to a constant output representative of the operating condition.

The x_r was calculated from the following:

$$x_r = \frac{\tilde{x}_{CO_{2_c}} - \tilde{x}_{CO_{2_i}}}{\tilde{x}_{CO_{2_e}} - \tilde{x}_{CO_{2_i}}} \qquad (10)$$

where the subscripts c, i and e are measured dry in-cylinder, intake manifold and exhaust CO_2 mole fractions, because CO_2 mole fractions are measured on a dry basis. A correction factor Z,

$$Z = \frac{(\tilde{x}_i)_{wet}}{(\tilde{x}_i)_{dry}} = \frac{1}{1 + 0.5[y(\tilde{x}^*_{CO_2} + \tilde{x}^*_{CO}) - 0.74\tilde{x}^*_{CO}]} \qquad (11)$$

is used to convert the dry mole fraction measurements to wet.

The sampling period was determined by the spark timing, under light load operating conditions the spark timing needed to be retarded from MBT* to produce a sufficient flow rate. Figure 9 shows that changes in relative spark timing have negligible effects on the measured x_r. The effect of VO on the measure x_r is shown in Figure 10a-c. The change in x_r is non linear and is only significant for VOs of greater than 20ºCA with the x_r more than doubling for a VO change of 42ºCA at 1500rpm. The effect of volumetric efficiency is shown by the different load points at each engine speed, where at higher loads and therefore higher volumetric efficiency the x_r is smaller at all VOs. The x_r is influenced by engine speed at a given VO, reducing engine speed results in increased x_r essentially because there is greater time for exhaust gases to backflow into the cylinder and intake port. The measured results were used to produce a model of x_r using the model based calibration

(MBC) toolbox in MATLAB. Engine speed, inlet manifold pressure and VO were the input factors, contour plots shown in Figure 11, indicate as with the measured results the highest x_r will occur at the lowest engine speed, lightest load and largest VO. In this case due to the limitations of the cam phasing mechanism the highest x_r of 0.35 was attainable at 1000rpm, 0.44bar inlet manifold pressure and 42°CA VO.

3.5.4 Comparison of theoretical and measured residual gas fraction

Previous work [4] derived a method to determine the GFR and the x_r. This derivation is shown here. The GFR is defined as the total trapped mass in the cylinder divided by the trapped fuel mass, which can be expressed in terms of AFR and the burned gas fraction (x_b) in the unburned mixture during compression:

$$x_b = \frac{m_b}{m_a + m_f + m_b} \tag{12}$$

where m_b is the trapped burned mass, m_a is the trapped air mass and m_f is the trapped fuel mass, from which

$$m_b = \frac{(m_a + m_f)x_b}{1 - x_b} \tag{13}$$

The GFR is therefore given by

$$GFR = \frac{m_a + m_f + m_b}{m_f} = \frac{AFR+1}{1-x_b} \tag{14}$$

The burned gas fraction comprises both residual gases from the preceding cycle and exhaust gas recirculated externally (EGR) which is defined as

$$EGR = \frac{m_{EGR}}{m_a + m_{EGR}} \tag{15}$$

The residual gas fraction is defined as

$$x_r = \frac{m_r}{m_i + m_r} \tag{16}$$

where the trapped intake charge (m_i) includes the recirculated gas:

$$m_i = m_a + m_{EGR} + m_f \tag{17}$$

and

$$m_b = m_{EGR} + m_r \tag{18}$$

Using equations (14) to (18), the burned gas fraction given by (13) can be expressed in the form

$$x_b = x_r + \frac{(1 - x_r)AFR.EGR}{AFR + 1 - EGR} \qquad (19)$$

A simple method for estimating the x_r was established. Where x_r is related to compression ratio and volumetric efficiency. The use of volumetric efficiency implicitly accounts for changes in engine speed, throttle angle and the effects of different intake and exhaust systems. Combining the definition given by equation (15) and (17),

$$m_i = \frac{(m_a + m_{EGR})(AFR + 1 - EGR)}{AFR} \qquad (20)$$

and using volumetric efficiency to define the cylinder volumetric efficiency as based on the intake mass of normal gaseous components,

$$m_a + m_{EGR} = \rho_m V_s \eta_{cyl} \qquad (21)$$

where V_s is the engine swept volume, η_{cyl} is the volumetric efficiency from manifold to cylinder and ρ_m is the density of the air and recirculated gas mixture in the intake port, treated as a perfect gas mixture,

$$m_i = \frac{V_s \eta_{cyl}(AFR + 1 - EGR)p_m}{RT_m AFR} \qquad (22)$$

where p_m is the intake manifold pressure, T_m is the intake manifold temperature and R is the specific gas constant. If the x_r is proportional to the clearance volume and gas state at the end of the exhaust stroke on the preceding cycle, then

$$\frac{m_i}{m_r} = Y\left(\frac{T_e}{T_m}\right)\left(\frac{p_m}{p_e}\right)(r_c - 1)\eta_{cyl}\left(\frac{AFR + 1 - EGR}{AFR}\right) \tag{23}$$

where T_e is the exhaust gas temperature, p_e is the exhaust gas pressure and r_c is the engine compression ratio, the product of the proportionality constant Y and the temperature ratio T_e/T_m are typically close to 2, therefore substituting equation (23) into equation (16), gives

$$x_r = \frac{1}{1 + 2(p_m/p_e)(r_c - 1)\eta_{cyl}(AFR + 1 - EGR)/AFR} \tag{24}$$

Equation (24) has been shown [4] to produce values that are consistent with literature, in these cases only engines with fixed standard valve timing arrangements were compared. The error ratio between the measured x_r and the predicted x_r (equation 24) is shown in Figure 12. The error ratio in all the cases increases with larger VOs, the increase being non linear. The error ratio starts to increase from approximately 10 - 15°CA, with a slight dependence on engine speed. The error ratio is unaffected by load changes at the three engine speeds since the change in the x_r is accounted for by the volumetric efficiency term in equation (24).

Lai [5] investigated a method of correcting the predicted x_r based on equation (19) by introducing a fictitious 'internal' (EGR$_i$) term, where x_r was the value predicted by equation (24) and x_b was the measured residual gas fraction. This is equivalent to the burned gas fraction in this case since the AJ27 had no external EGR system.

It was found, to a good approximation that the mass of EGR$_i$ was a simple polynomial function of VO.

$$m_{iegr} = \frac{120}{N} \times (2.555e^{-7} \times (VO)^2 - 7.1105e^{-7} \times (VO) - 5.1014e^{-5}) \quad (25)$$

Substituting the value from equation (25) into equation (15)

$$EGR_i = \frac{m_{iegr}}{m_a + m_{iegr}} \quad (26)$$

and finally calculating the actual residual gas fraction:

$$x_{r\_corrected} = x_r + \frac{(1-x_r)AFR.EGR_i}{AFR + 1 - EGR_i}$$

(27)

The correlation between the measured and predicted $x_{r\_corrected}$ is shown in Figure 13, the empirical trend follows the overall trend from the measured results, with particularly good performance at the highest measured x_r. Although an attempt was made to apply a semi-physical model described by [63] it was found that this model under predicted the x_r at high VOs. Throughout this work, values for the x_r are calculated from equation 27 ($x_{r\_corrected}$).

3.5.5 IMEP and COV_IMEP

The in-cylinder pressure data can be used to calculate the work transfer from the gas to the piston per cycle per unit swept volume:

$$mep = \frac{W_c}{V_s} \tag{28}$$

where W_c is the work delivered per cycle and V_s is the swept volume of one cylinder. For this work, the engine output is measured in terms of the IMEP. There are two definitions of IMEP, firstly net IMEP ($IMEP_n$) which includes all four strokes

$$IMEP_n = \frac{1}{V_s} \int_0^{720} p dV \tag{29}$$

and gross IMEP ($IMEP_g$) which includes only the compression and expansion strokes

$$IMEP_n = \frac{1}{V_s} \int_{180}^{540} p dV \tag{30}$$

The difference between $IMEP_n$ and $IMEP_g$ is termed the pumping mean effective pressure (PMEP):

$$PMEP = IMEP_n - IMEP_g \tag{31}$$

In the case of the AJ27 the intake cam can be phased, for a conventional engine with fixed intake cam timing, intake valve closing (IVC) is a trade-off between low speed torque and high speed power [64]. Phasing the intake cam is in part used to decrease PMEP, where advancing the intake cam at part load increases the VO and as has been shown the x_r, therefore a higher MAP is required to maintain the load. The convention described by equations (29) and (30) assumes that the work associated with exchanging the exhaust gas with fresh charge occurs only during the exhaust and intake strokes with no impact on the indicated work. Previous work [65] showed that this method did not allow a valid comparison of the PMEP work reducing strategies since the convention did not take into account valve timing effects occurring during the expansion and compression stroke. The method is described and applied here to clarify the effect of the intake cam phasing on the work output from the AJ27.

Firstly a calculation is made to account for the expansion work loss by opening the exhaust valve before bottom dead centre (BDC). This is achieved by extrapolating the expansion pressure from exhaust valve opening (EVO) to BDC using a curve fitted to PV^{n_e} where n_e is based on the measured expansion stroke data prior to EVO. The difference between the two areas from EVO to BDC is normalised by the swept volume as is termed the EVO expansion loss (EVO_{loss}),

$$EVO_{loss} = \frac{1}{V_s} \int\limits_{EVO}^{BDC} (p_{extrapolated} - p_{measured}) dV \qquad (32)$$

A similar correction is made for the effects of early or late IVC. With early IVC, the intake MAP must increase to maintain the same torque. Late IVC allows nearly the complete elimination of the intake stroke pumping work but results in a large increase of work during the first part of the compression stroke. This increased work is termed incremental compression work (ICW_{loss}) and is quantified in a similar way to the method adopted to determine the EVO_{loss}. The compression stroke pressure is extrapolated to BDC based on pV^{n_c} with n_c determined over an interval where

pV^{n_c} is approximately linear. The difference between the two areas from BDC to IVC is normalised by the swept volume and is termed the ICW_{loss}:

$$ICW_{loss} = \frac{1}{V_s} \int_{BDC}^{IVC} (p_{extrapolated} - p_{measured}) dV \tag{33}$$

The work related to the gas exchange process is therefore defined as:

$$PMEP_{adj} = PMEP + ICW_{loss} + EVO_{loss} \tag{34}$$

and the adjusted $IMEP_g$ is given by:

$$IMEP_{g\_adj} = IMEP_g + ICW_{loss} + EVO_{loss} \tag{35}$$

in both cases ICW_{loss} and EVO_{loss} are expressed as positive numbers. Finally the adjusted $IMEP_{n\_adj}$ is given by:

$$IMEP_{n\_adj} = IMEP_{g\_adj} - PMEP_{adj} \tag{36}$$

Both n_c and n_e should be close to a value of 1.3. The calculation in both cases is based on a linear fit to the measured data over 10°CA before spark timing for n_c and 10°CA after the end of combustion for n_e. The resulting range of n_c and n_e by applying this method was 1.3±0.04 and 1.3±0.03 respectively. An example of the extrapolated data is shown in Figure 14 with the intake cam fully retarded (late

IVC). The method was applied to a set of data comprising both fully advanced and retarded IVC timings at two loads and three engine speeds. The torque was held constant for both valve timings. The effect of the change in the IVC timing on calculated EVO_{loss} and ICW_{loss} is shown in Figure 15 at each engine speed and load. The change in the calculated EVO_{loss} for the two valve timings is minimal compared to the change in ICW_{loss}, which is a result of the fixed EVO. The difference between $IMEP_g$ and $IMEP_{g\_adj}$ is shown in Figure 16, with Figure 17 showing the difference between $PMEP$ and $PMEP_{adj}$. In both cases the effect of including EVO_{loss} and ICW_{loss} on the PMEP and $IMEP_g$ calculations is insignificant when compared to the traditional integral method. In light of these results all calculations of work related parameters ($IMEP_n$, $IMEP_g$ and PMEP) are made using the conventional integral method.

A significant amount of work presented in later chapters focuses on combustion stability and although many parameters exist to quantify combustion stability, COV_{IMEP} is often used since this provides a direct correlation between variability in combustion and deterioration in vehicle driveability [14, 34]. The definition is given by:

$$COV_{IMEP} = \frac{\sigma_{IMEP}}{mean(IMEP)} \qquad (37)$$

Being that the calculation involves average and standard deviation values, COV_{IMEP} will be dependent on the sample size. The required sample size for a representative value of COV_{IMEP} was investigated for both stable and unstable operating conditions. Figure 18 shows the effect of cycle number on the calculated value of COV_{IMEP_n} for stable operating conditions, after 100 samples the COV_{IMEP_n} can be regarded as being representative of the operating condition with any increase in sample size, up to 1000 cycles resulting in a change in COV_{IMEP_n} of less than ±0.1. These findings are similar to those of Hill [39] where for operating conditions

where COV_{IMEP} was less than 5, sample sizes as low as 10 or 20 could give a good estimation of COV_{IMEP}. The influence of cycle number during unstable operating conditions is shown in Figure 19, in this case it is necessary to use a sample size of 500 to gain a representative value of COV_{IMEP_n}, the use of 1000 cycles results in a change in COV_{IMEP_n} of less than ±0.2. This sample size is less than that adopted by Shayler et al [66] where a sample size of 2000 was used, although the effect of sample size was not investigated on the value of COV_{IMEP}. More recent work [6] investigating stability limits used 400 cycles to calculate COV_{IMEP}. An evaluation of IMEP calculation routines and analysis errors by Brunt and Emtage [49] suggested that the minimum number of cycles to gain a representative mean IMEP value was 150, it was suggested for best practice that 300 should be used. Although it is apparent that variable sample sizes could be used to calculate an accurate COV_{IMEP}, dependent on operating condition, throughout this work a sample size of 500 is used.

3.6 Discussion and Summary

The test facilities have been described. The features of the AJ27 engine used in the experimental elements of the research have been introduced. A PC-based data acquisition system was used in conjunction with a Jaguar EMS and software used to interrogate and manipulate engine variables. The additional engine instrumentation has been described enabling detailed measurements of the engine condition. A description of the methodology adopted to determine key experimental variables is described. These include the determination of maximum brake torque and minimum advance for best torque spark timing, where a simple 2nd order polynomial was found to represent the spark sweep accurately. An evaluation of different methods to determine AFR was carried out, both UEGO and emissions provide similar AFR measurements at stable operating conditions. At unstable operating conditions where partial burning/misfiring cycles are apparent, both the AFR calculated from the emissions and UEGO measure leaner than the actual supplied AFR. Previously developed experimental apparatus [62] was modified and successfully applied to the AJ27 to enable the measurement of in-cylinder residual gases (x_r). Increasing the valve overlap (VO) by advancing the intake valve opening substantially increases the x_r, although modelled results show that MAP is the most important variable in determining the x_r followed by VO and then rpm. Calculated values of x_r were found to under predict measured x_r, an empirical correction factor is applied allowing reasonable determination of x_r across the fully operating range. The traditional integral method for the calculation of *mep* was compared to an alternative method [65] for the full range of VO on the AJ27. The difference between the calculated values of the two methods was very small; the traditional method was therefore adopted throughout. Finally it was shown that COV_{IMEP} is influenced by sample size, for accurate representation of COV_{IMEP} over the entire operating range 500 samples are required.

CHAPTER 4

Determination of Mass Fraction Burned

4.1 Introduction

In this chapter, two methods of determining the mass fraction burn profiles are investigated. The merits of both approaches are examined and important considerations to be taken into account when applying either method are reviewed. In both cases the burned mass fraction is determined from the measured in-cylinder pressure and volume. There are two methods widely used for determining the mass fraction burn profile. Firstly the Rassweiler and Withrow method, secondly, the approach based on the first law of thermodynamics, which is applied to both SI and diesel engines. The main aim of the investigation is to apply both methods, evaluate the results and decide upon which method will be used throughout this work to determine the mass fraction burn profiles and related burn duration angles.

4.2 Rassweiler and Withrow Technique

The Rassweiler and Withrow method [67] is based on experimental observations of combustion in a constant volume bomb. It was found that the mass fraction burned was approximately equal to the fractional pressure rise.

$$X = \frac{m_x}{m_t} = \frac{p_x}{p_t} \tag{38}$$

where m is mass, p is pressure and the suffix t indicates the conditions at the end of combustion (EOC). For a given amount of energy release in a specific volume, the combustion pressure rise p_c is inversely proportional to the volume V

$$p_c \alpha \frac{1}{V} \qquad (39)$$

During combustion in an engine cylinder the pressure change is a result of two separate processes, pressure change due to combustion and the pressure change due to piston motion causing a change in volume, ΔV. The compression and expansion process before and after combustion were found to be well fitted by a polytropic relation:

$$pV^n = \text{constant} \qquad (40)$$

Therefore the pressure produced due to ΔV is given by:

$$p_p = p_{\theta - \Delta\theta} \left(\frac{V_{\theta - \Delta\theta}}{V_\theta} \right)^n \qquad (41)$$

where p_p is the pressure produced by the change in volume at a given crank angle (θ), $p_{\theta - \Delta\theta}$ is the pressure measured at the previous half crank position, n is the polytropic index. The pressure resulting from combustion is therefore given by

$$p_c = p_\theta - p_p \qquad (42)$$

The calculation of the pressure rise due to combustion can take place at all crank angle intervals from spark timing to exhaust valve opening. The calculated combustion pressures have been evaluated at different volumes, to maintain consistency with the constant volume experiments the pressure must be referenced to a specific volume, in this case the volume at top dead centre (TDC).

$$p_c^{'} = (p_\theta - p_p)\left(\frac{V_\theta}{V_{TDC}}\right) \tag{43}$$

The burned mass fraction at any given θ is therefore,

$$x_\theta = \frac{\sum\limits_{\theta=spark}^{\theta} p_c^{'}}{\sum\limits_{\theta=spark}^{EOC} p_c^{'}} \tag{44}$$

Apart from the required pressure and volume data, a value for the polytropic index (n) and end of combustion (EOC) are required. The gas temperature inside the cylinder during the compression and expansion is different. During compression the fuel-air mixture and wall temperatures are similar therefore heat flow can occur in either direction. The compression n will be near to a value of 1.3. Contrastingly the expansion process, where the gas temperature is significantly higher due to combustion, results in positive heat flow and normally the calculated expansion index is lower, although still remains 1.3 (± 0.05) [14]. This necessitates the calculation of individual compression and expansion polytropic indexes.

4.2.1 Calculation of the polytropic index for compression

Both polytropic indexes need to be calculated in regions of the pressure data that are free from combustion, the compression index (n_c) is therefore determined before spark discharge. The n_c is used in the calculation until TDC from then until the EOC the expansion index (n_e) is used. The method used to determine both the compression and expansion index is outlined in [68]. The n value is established on the basis of satisfying zero combustion pressure (δ). This uses the relationship between the n and the predicted δ over a small crank angle interval. A value of n is chosen to give δ equal to zero before combustion commences (spark discharge). The relationship between n and δ is approximately linear, as given by:

$$n \cong \frac{\{\ln(p_\theta / p_{\theta-\Delta\theta}) - \delta / (p_\theta(V_\theta / V^{'}))\}}{\ln(V_{\theta-\Delta\theta} / V_\theta)} \tag{45}$$

Therefore in each case n is identified by linearly interpolation over a range of trial values until the value of n is found that gives zero δ. As δ increases, the value of n decreases for a compression process and increases for an expansion process.

Due to the effect of signal noise on real data the value of δ will fluctuate with crank location. The number of points depends on the signal to noise level of the combustion pressure record. Previous work [68] calculated the average δ over a summation of 10 points at a resolution of 1°CA to suppress the effects of signal noise. This method was applied here. It was found that the calculated value of the n_c was dependent on spark timing as shown in Figure 20, where the index increases to values greater than 1.3 for spark timings within 10°CA of top dead centre (TDC), suggesting strong heat rejection from the gases to the cylinder walls. The influence of the high n_c index on key calculated mass fraction burned angles namely the flame development angle $(\Delta\theta_{0-10\%})$ and the rapid burn angle $(\Delta\theta_{10-90\%})$ is shown in Figure 21 and Figure 22 respectively. The calculated values are insensitive to changes in the n_c. This is attributed to the n_c only being used until TDC.

4.2.2 Calculation of the polytropic index for expansion and methods for determining the end of combustion

The calculation of the n_e is more complex. In certain cases, the EOC and therefore the point at which the n_e is calculated, is determined from the calculated combustion pressure which is a function of the n_e. Two of these methods [68] are, the 'first negative index' where the EOC is located when the first negative combustion pressure occurs. Secondly 'sum negative index' where the EOC is determined when 3 consecutive negative combustion pressures occur. The second method is seen as a more robust method for determining the EOC since it reduces the influence of signal noise. In both cases an iterative method is adopted whereby an initial EOC point is set as 10°CA before exhaust valve opening (EVO). The n_e is then calculated using the standard method. A new EOC is then determined using either method 1 or 2 along with a new n_e. The loop is exited once there is no change in the EOC location. Alternatively two different methods adopted by [68] 'tuned index' and [69] '$pV^{1.15}$ index' do not require such an iterative process. For the tuned index equation 45 is applied to point in the expansion stroke where under normally combusting cycles combustion will have ceased. The point selected was just before EVO. The final method $pV^{1.15}$ index simply uses the point where $pV^{1.15}$ reaches a maximum plus 10°CA to indicate the EOC. In all cases, as with the n_c the n_e is an average value calculated over 10°CA.

The distribution of the n_e calculated using the four methods is shown in Figure 23. The n_e should be approximately 1.3; therefore the distribution is produced by normalising the calculated n_e to 1.3. Both the first negative and the sum negative methods produce distributions that are biased towards higher values. This is more noticeable with the sum negative method than with the first negative method, where the average n_e is 1.52 and 1.45 respectively. The distribution produced by the $pV^{1.15}$ method is a very narrow band around the 1.3 value, which is a result of the method, where the average n_e is 1.29. The late polytropic index method produces a distribution that is significantly biased towards higher values of the n_e this is due to the relative lateness, compared to the other methods for determining the n_e. The

average n_e in this case is 1.58. The overall trend exhibited is that the n_e varies significantly with the point in the expansion stroke where it is calculated, with calculations late in the expansion stroke resulting in higher values of the n_e.

The sensitivity of the $\Delta\theta_{0-10\%}$ and the $\Delta\theta_{10-90\%}$ to the variation of the n_e from the four methods is investigated in Figure 24 and Figure 25 respectively. For convenience, as with the n_c variations in the burn parameters are compared to those calculated using a fixed, n_e of 1.3. The mass fraction burn parameters, particularly the $\Delta\theta_{10-90\%}$ are more sensitive to differences in the n_e than the n_c. The tuned index method for determining the n_e shows the greatest deviation from the fixed value, the effect is that the $\Delta\theta_{10-90\%}$ in some cases is over twice as long. This is due to the fact that larger n_e values suggest heat addition from the gases resulting in extended burn durations. The difference between all four methods reduces as the burn duration increases since the EOC point for all four methods converge to the same point. The $pV^{1.15}$ method is shown to be the most robust method for determining the EOC due to the resulting n_e being close to 1.3. Throughout this work the mass fraction burned profile is determined using $pV^{1.15}$ to locate the EOC.

4.2.3 Pressure Referencing

The in-cylinder pressure measurements are made using piezoelectric transducers. The piezoelectric transducers measure dynamic pressure rather than absolute and need to be referenced. It has been shown [70] that incorrect pressure referencing results in errors of pressure derived parameters such as the polytropic index. Two methods were investigated, inlet manifold pressure referencing (IMPR) and polytropic index pressure referencing (PIPR). The disadvantage of PIPR is that a polytropic index has to be specified and as has been shown the value varies with operating condition.

The dynamic pressure has therefore been referenced to absolute using IMPR. The pressure referencing is normally carried out at BDC during induction, taking the

average of several points to reduce the sensitivity to noise, typically 10° to 20° CA. It was found [70] that the correction value was dependent on crank angle and was suggested this would be engine dependent. This method was applied to measured data to minimise the inaccuracies associated with incorrect pressure referencing. The effect of changing the crank angle location of the pressure referencing is shown in Figure 26. The dynamic pressure averaged over 20°CA ($\pm 10^{\circ}$ CA either side of the reference point) are referenced to inlet manifold pressure, the datum point on the figure indicating referencing at BDC. Changing the position of the referencing has an insignificant effect on the absolute pressure, with a change in referencing point of $\pm 15^{\circ}$CA resulting in a change in absolute pressure of ± 0.01bar. Pressure referencing was therefore carried out at BDC.

4.3 Heat release approach

The heat release approach is a single zone model based on the first law of thermodynamics, where net heat release is given by [14]:

$$\frac{dQ_{net}}{d\theta} = \frac{\gamma}{\gamma - 1} p \frac{dV}{d\theta} + \frac{1}{\gamma - 1} V \frac{dp}{d\theta} \qquad (46)$$

where p and V are the instantaneous pressure and volume measurements and the value of gamma (γ) is calculated based on the mixture composition and temperature at each crank angle using equations developed by NASA [71]. The gross rate of heat release is calculated by adding the energy exchange to heat transfer and to blowby to the net rate of heat release as shown by:

$$\frac{dQ_{gross}}{d\theta} = \frac{\gamma}{\gamma - 1} p \frac{dV}{d\theta} + \frac{1}{\gamma - 1} V \frac{dp}{d\theta} + \frac{dQ_{ht}}{d\theta} + \frac{dQ_{bby}}{d\theta} \qquad (47)$$

Integration of the gross heat release from the start to the EOC should give the total heat released by combustion, where this value under normally combusting conditions should account for approximately 92 to 96% of the energy supplied in the fuel. The remainder is attributed to combustion inefficiency, fuel lost in the crevices, quench layers on the cylinder walls and fuel absorbed into the oil layers on the cylinder liner and any deposits [72]. The instantaneous heat release divided by the total provides the mass fraction burned profile from which both the $\Delta\theta_{0-10\%}$ and $\Delta\theta_{10-90\%}$ are determined.

4.3.1 Heat transfer

Heat transfer on average accounts for between 15 to 20% of the total energy release [14]. Convective heat transfer is responsible for the majority of the losses. Convective heat transfer is given by:

$$Q_{ht} = h_c A \Delta T \tag{48}$$

where h_c is heat transfer coefficient, A is the cylinder surface area and ΔT is the difference in temperature between the cylinder charge and the cylinder wall (T_w). Calculation of the heat transfer coefficient is complex and many uncertainties exist. The Woschni [73] correlation is used here,

$$h_c = 3.26 B^{-0.2} p^{0.8} T^{-0.55} w^{0.8} \tag{49}$$

where the units are h_c (W/m²K), bore B (m), pressure p (kPa), temperature T (K) and velocity w (m/s). The average cylinder velocity is determined from

motored (suffix m) and reference conditions, here taken as IVC and the mean piston speed $\overline{S}p$:

$$w = \left[c_1 \overline{S}_p + c_2 \frac{V_d T_{IVC}}{p_{IVC} V_{IVC}} (p - p_m) \right] \tag{50}$$

The constants c_1 and c_2 were taken as follows. During compression $c_1 = 2.28$ and $c_2 = 0$; during combustion and expansion $c_1 = 2.28$ and $c_2 = 3.24 \times 10^{-3}$, as used by Shayler et al [74]. The T_w was a function of equivalence ratio [75] where:

$$
\begin{aligned}
\phi &< 0.833, & T_w &= 400K \\
0.833 &< \phi < 0.9, & T_w &= 425K \\
\phi &> 0.9, & T_w &= 450K
\end{aligned}
\tag{51}
$$

Previous work by Cheung and Heywood [75] showed that the predicted mass fraction burn parameters are relatively insensitive to variations of T_w, c_1 and c_2. The largest discrepancies between predicted and expected peak mass fraction burned values occurred when the heat transfer per cycle was the greatest.

4.3.2 Blowby

Blowby typically accounts for 1 to 2% of the total energy release at high speed fully warm conditions [14]. Work by Irving [76] has shown that for a modern 4 cylinder diesel engine the blowby mass flow rate can be assumed to be constant, at approximately 0.1g/s per cylinder across a range of engine speeds from 1000rpm to 3000rpm. Therefore at lower engine speeds the energy loss to blowby will become more important. The model adopted here is the simplest and is outlined by Pugh [77], where the blowby flow is a flow through an orifice with an upstream pressure

equal to the cylinder pressure and a downstream pressure equal to crankcase pressure. This results in choked flow during the compression and expansion stroke of the cycle. Applying classical one-dimensional isentropic flow and assuming $\gamma = 1.4$ the blowby mass flow rate is given by:

$$\dot{m}_{bby} = 0.68 A_{ring} (\rho p)^{\frac{1}{2}} \tag{52}$$

where A_{ring} is the orifice area, in the absence of experimental data A_{ring} was fitted so that $\dot{m}_{bby}$ was a constant value of 0.1g/s at each operating condition. Applying this method it was found A_{ring} could be set as a constant of 2.71e-7m^2. The density of the cylinder charge is evaluated using the cylinder wall temperature and measured in-cylinder pressure. The rate of energy transfer to blowby can therefore be calculated using:

$$\frac{dQ_{bby}}{d\theta} = \frac{60\dot{m}_{bby}}{360N} \frac{pV}{m_{trapped}} \frac{\gamma+1}{\gamma-1} \tag{53}$$

where N is the engine speed and $m_{trapped}$ is the total trapped mass of air calculated from measured air and fuel mass flow rates and the modelled residual mass fraction given in Chapter 3.

4.3.3 Evaluation of the heat release approach

A set of experimental data was analysed using the heat release approach described above to investigate the robustness of the models used. Figure 27 shows the influence of relative spark timing on the percentage of fuel accounted for at three typical engine speeds. Examination of the proportion of fuel energy released which is

accounted for indicates accuracy is poor and a correction is required. The analysis does not account for as much fuel energy as would be expected, with a small dependence on engine speed. There is a marked reduction in fuel energy accounted for as the spark timing is retarded from MBT* in all cases. Figure 28 shows the influence of different AFR, there is a discrepancy between the different engine speeds where for the 1000 and 1500rpm an increasing amount of fuel energy is accounted for compared to 2000rpm. Although the influence of changes in AFR on fuel energy accounted for is less than those associated with dMBT. Analysis of the energy lost to heat transfer and blowby showed that the modelled heat transfer was lower than expected. A simple multiplication factor, described by equation 54 that was weighted with relative spark timing was applied to the Woschni heat transfer coefficient

$$W_{scale} = 2.3 + 0.175 dMBT \tag{54}$$

applying these correction factors (the multiplication factor of 2.3 applied to all conditions and the relative spark timing weighting factor) allowed on average 95% of the fuel energy supplied to be accounted for in the heat release analysis. Three distinct heat transfer models have therefore been created, firstly the reference heat transfer model, simply application of the Woschni model, secondly the Woschni model with a multiplication factor to enable more fuel energy to be accounted for and finally the addition of a multiplication factor to take into account changes in relative spark timing.

A comparison of the $\Delta\theta_{0-10\%}$ and $\Delta\theta_{10-90\%}$ calculated from the heat release approach using the three heat transfer models and the Rassweiler and Withrow is shown in Figure 29 and Figure 30 respectively. The value of $\Delta\theta_{0-10\%}$ calculated using the Rassweiler and Withrow and heat release approach including the three different heat transfer models is very similar. With the majority of the data encompassed within the 10% error bounds. This is relatively unsurprising since during the $\Delta\theta_{0-10\%}$ rate of heat transfer is minimal. The calculated values of the

$\Delta\theta_{10-90\%}$ vary significantly depending on the method used, changes to the heat transfer model also significantly influence the value of the $\Delta\theta_{10-90\%}$ calculated using the heat release approach. Generally the base Woschni model produces results that are most comparable to the Rassweiler and Withrow method although longer burn durations are predicted as the engine speed increases and spark timing is retarded. Introduction of the multiplication factor and then the weighting factor with dMBT to improve the heat release analysis ability to account for the fuel energy increases the difference between the Rassweiler and Withrow and the heat release approach in all cases.

These findings indicate that values of the $\Delta\theta_{10-90\%}$ are significantly influence by the analysis method. Although the heat release approach provides a breakdown of the energy flows, calibration of the heat transfer model to allow more accurate accounting of the fuel energy significantly affects the burn duration.

4.4 Discussion and Summary

Two methods of calculating the mass fraction burned from experimental data have been described and evaluated. In applying the Rassweiler and Withrow approach it was shown that the most robust method for determining the EOC was that proposed by Brunt and Emtage [69] since the calculated n_e was within a small distribution around the expected value of 1.3. If the calculation point is late in the expansion stroke the n_e becomes unrealistically large, resulting in increased burn durations. Variations of this sort cannot be caused by incorrect referencing of the pressure and volume since this would result in a linear error in the index value across the entire expansion period. Analysis, using the heat release approach with a blowby and heat transfer sub model did not account for the expected fraction of fuel energy delivered. The proportion of energy transferred through heat transfer was found to be lower than expected, weighting factors were applied to the heat transfer model allowing for a more representative proportion of the fuel energy to be taken into account. Comparison between the Rassweiler and Withrow method and the heat release approach indicated that the values of $\Delta\theta_{0-10\%}$ were very similar.

Significant differences were found between values of $\Delta\theta_{10-90\%}$ with in general the heat release approach producing values greater than the Rassweiler and Withrow method.

The choice of analysis method to determine the mass fraction burned by researchers varies and without detailed knowledge of the method used, comparison of results is impossible. Throughout this work the Rassweiler and Withrow method is adopted to calculated the mass fraction burned using the Brunt and Emtage [69] method for determining the ECO. Final consideration in this chapter is similar to the issues raised with the calculation COV_{IMEP} in Chapter 3, where it was shown calculated values were dependent on the number of cycles. Figure 31 shows the influence of different cycle numbers to calculate $COV_{\Delta\theta_{0-10\%}}$ and $COV_{\Delta\theta_{10-90\%}}$. At stable operating conditions both parameters for the three engine speeds shown have reached stable values with the minimum number of cycles (50) any increase in the number of cycles results in insignificant changes to the values calculated. The trend is repeated with the unstable operating conditions, the only exception being that the required number of cycles to calculate a representative value of $COV_{\Delta\theta_{10-90\%}}$, where it can be seen the number of cycles needs to be at least 200.

CHAPTER 5

Physical and Chemical limits of stable operation

5.1 Introduction

Considered in this chapter are the parameters which limit stable operation in a gasoline engine. Throughout the chapter COV_{IMEP} is used as the parameter to describe the transition from stable to unstable operating conditions. Initial work by Winborn [4] established that limits on stable operation of lean AFR mixtures at various operating conditions could be characterised as a function of GFR for both fully warm and cold operating conditions. The influence of spark timing was also investigated, no change in the limiting value of GFR was found. Lai [5] expanded on this work with the use of two diagrams, establishing both a rich AFR, x_b and GFR limits on stable operation. Only limited data was presented at spark timings retarded from MBT[*]. The work presented in this chapter further develops the diagrams presented by Lai [5]. Further understanding is provided as to the trends observed and clarification of the limits of stable operation is provided by adopting two testing methodologies. Finally, GFR as a parameter used to describe limits on stable operation is compared to the thermal dilution parameter (TDP) defined by [6] to rationalise stable operating range of a gasoline engine operating on different fuel mixtures.

5.2 The influence of chemical and physical parameters on cycle to cycle stability, initial testing

The results presented in this section were obtained using the test methodology described in [4,5]. Firstly a stable (AFR ≈ 14.6) steady state test point is achieved at a given throttle angle and valve timing. The fuel pulsewidth is then decreased to increase the AFR (and GFR) until an unstable operating point is achieved, unstable is defined as COV_{IMEP_n} greater than 10 (this test methodology is defined as 'constant air'). A discrepancy in the method of calculating COV_{IMEP_n} exists between [4] and [5]: misfiring and partial burning cycles[5] were removed from the calculation by [4] whereas [5] included all cycles, the implication being that at conditions where misfiring cycles exist COV_{IMEP_n} will be greater in the work presented by [5]. Here, in this initial analysis, all cycles are included and therefore the data processing is consistent with [5]. At each steady state condition a spark sweep is conducted to ascertain MBT[*] spark timing, where the first data set is taken. To establish the influence of spark retard on CCV two more data sets are taken with the spark timing retarded from MBT* by 10 and 20°CA respectively.

The influence of chemical parameters, AFR, x_b and relative spark timing was investigated in 2 combustion stability diagrams. These two diagrams show the boundaries of stable operation and show what parameters are involved in a way which is diagrammatically clear.

The first m_a / m_b plotted against m_f / m_b results in straight lines of constant GFR bounding regions of stability. From Chapter 3 equation 14.

$$GFR = \frac{m_a + m_f + m_b}{m_f}$$

---

[5] A misfiring cycle is defined as a cycle producing less than 5% IMEP_n than the average. A partial burn cycle is defined as producing less than 70% IMEP_n than the average.

$$GFR - 1 = \frac{m_a}{m_f} + \frac{m_b}{m_f}$$

$$GFR - 1 = \left(\frac{m_a}{m_b}\right)\left(\frac{m_b}{m_f}\right) + \frac{m_b}{m_f}$$

rearranging:

$$\frac{m_a}{m_b} = (GFR - 1)\frac{m_f}{m_b} - 1 \tag{55}$$

The burned gas in the unburned mixture during compression acts as a diluent, that dilutes the fuel and air mixture. Once the amount of burned gas reaches a certain limit, the air fuel mixture will become over diluted and combustion becomes unstable. The second diagram is used to establish the burned gas fraction limit over the range of AFRs tested. From equation 14, since

$$GFR = \frac{AFR + 1}{1 - x_b}$$

rearranging:

$$x_b = \frac{GFR - AFR - 1}{GFR}$$

$$= \left(1 - \frac{1}{GFR}\right) - \left(\frac{1}{GFR}\right)AFR \tag{56}$$

Plots of x_b against AFR as shown by equation 56 are straight lines provided GFR is a fixed value. A stable region is formed by equation 56, burned gas fraction limit and AFR limit. The two diagrams are used to represent data at three different spark timings, MBT*, dMBT*=10 and dMBT*=20. These are shown in Figure 32, Figure 33 and Figure 34. For a given relative spark timing there exists mixture ratio limits that are dependent on both AFR and GFR. At MBT* operating conditions the range of mixture ratios available for stable combustion are at a maximum, with the stable operating range being bounded by a constant line of GFR = 24 for lean

and dilute mixtures, and an AFR = 10 for the rich operating limit. The stability limits for high levels of dilution are better represented in Figure 33, which provides zoomed in views of these areas for each spark timing. The x_b limiting curve, derived from Figure 34 intersects the rich limit as the dilution is increased up to the maximum near to an AFR of 14, it is suggested that at high dilution levels, $x_b > 0.27$ and lean mixture ratios, AFR>14.6 the stability limit can no longer be described using GFR and that there is greater dependence on x_b. Although similar trends can be observed for both dMBT*=10 and dMBT*=20, the dilution and mixture ratio limits are significantly reduced, particularly for the latter. For dMBT*=10 the GFR limit is slightly reduced from 24 to 23, the rich limit remains the same as for MBT*, with a notable change in the dilution limit, again the maximum dilution for stable operation occurs at an AFR of 14. Significant reduction in the stable operating mixtures occurs for dMBT*=20, the GFR limit is reduced to 19 and the rich limit although not as affected by the spark retard moves from an AFR of 9 to 10. Again the most notable change is the dilution limit; the maximum tolerable dilution is reduced to 20 percent across a similar AFR range. Figure 35 provides an overview of the limiting curves highlighting the significantly reduced operating mixture ratios that can sustain stable combustion when MBT*=20.

Certain implications of the test method and analysis need to be raised, firstly, what is the influence of removing misfiring cycles on COV_{IMEP_n}, are these dominating the reason for increasing COV_{IMEP_n}? The test method involves maintaining constant air charge and reducing fuelling, therefore the average $IMEP_n$ reduces as the mixture becomes lean, would this test method therefore affect the stability limit? The influence of retarding spark timing could have a similar effect. Since the average $IMEP_n$ reduces as the spark timing is retarded, would this reduction affect the stability limit? Finally the use of COV_{IMEP_n}, although this variable is representative of variability of 'useful' work output from the engine, ultimately what the driver will notice, to what extent is variability in combustion contributing to COV_{IMEP_n}, since COV_{IMEP_n} takes into account variations in both combustion and the pumping work. It is thought that variations in pumping work would be small compared to those associated with combustion, but since the results come from a multi cylinder engine

and all the cylinders are not instrumented it is possible variations in pumping work could become substantial as the cyclic variations increase. To what extent, though, needs to be established.

To answer in part some of these questions another set of tests were conducted.

5.3 Evaluation of test methodology

The tests were not as expansive as previously shown, and the focus is the GFR ratio limit rather than the x_b or rich limit. In part the study was dictated by the fact the x_b limit could be reached only at low engine speeds, therefore providing insufficient comparable data and that much work in both research and commercially focus on lean burn technology. Three engine speeds were used 1000, 1500 and 2000rpm which were typically encountered during the NEDC for this engine type, VO was constant at each engine speed although varied between engine speeds to ensure different initial x_b. Effectively 3 operating conditions were investigated. MBT^* spark timing was established at each test point as described previously. To establish the influence of test method on the stability limit constant air testing was conducted, along with this method another method was used, instead of maintaining constant air and reducing the fuelling to reach the stability limit the fuelling was held constant and the throttle angle increased.

5.3.1 Influence of removing partial burning and misfiring cycles

from COV_{IMEP_n}

Figure 36 shows the difference in COV_{IMEP_n} for calculations involving all cycles and those which are deemed not to have misfired or partially burned. As would be expected when misfiring and partially burning cycles are removed the value of COV_{IMEP_n} and the rate of increase of COV_{IMEP_n} reduces compared to the all cycles case, this would in turn make it more difficult to determine the stability limit. Yet if

the limit was, as is here defined as where COV_{IMEP_n} is greater than 10 then as can be seen both figures indicate a similar GFR stability limit.

5.3.2 Comparison of stability limit from constant air and constant fuel tests operating at MBT* spark timing

The influence on $IMEP_n$ and COV_{IMEP_n} for the three engine speeds as the GFR is increased is shown on Figure 37. The influence of the two different test methods on $IMEP_n$ is apparent, where for constant fuelling $IMEP_n$ increases to a peak until the point at which stability decreases, indicated by the associated increase in COV_{IMEP_n} where from that point onwards COV_{IMEP_n} increases rapidly. As expected the stability limit from the three engine speeds is the same. The constant air charge results show that there is a linear decrease in $IMEP_n$ as the fuelling is decreased, where there is a slightly earlier upturn in COV_{IMEP_n} compared to the constant air method, therefore it could be argued the results from this method would indicate effectively a richer GFR stability limit. To further investigate this trend additional examination of the data is presented. An alternative is provided in Figure 38 where the data is re-plotted by removing the influence of changing $IMEP_n$ by looking only at the change in variability by plotting the standard deviation (stdev) in $IMEP_n$ as a function of GFR. Using the stdev in $IMEP_n$ the difference in the rate of deterioration in stability as GFR is increased between the two test methods is negligible. This suggests deficiencies in using the constant air method for understanding and establishing stability limits, since part of the increase in COV_{IMEP_n} could be caused by the reduction in average $IMEP_n$ therefore not being directly related to the presence of partial burning and misfiring cycles. Figure 39 shows when partially burning and misfiring cycles occurred for both test methods. It is interesting that the point where the increase in COV_{IMEP_n} occurs actually corresponds to the point where partial burning cycles begin to be detected for both test types and that for further increases misfiring cycles start to be detected. Although the constant air test method results in a reduction in average $IMEP_n$ the

reason for increasing measured instability is due to the CCV. These results show that when comparing results from the two different test methods, both result in the same stability limit, but more importantly the occurrence of the instability is a direct reflection of cycle to cycle variations and not a reflection of the change in operating condition.

5.3.3 Validity of using net work output to characterise combustion stability

As was raised earlier the combustion stability parameters shown have all been derived from net work output, which is dependent on both variations in combustion work and variations in the pumping work. The correlation between $IMEP_n$ and $IMEP_g$ is shown in Figure 40 a, where the data for both constant air and fuel are characterised by a single linear correlation, the correlation coefficients produce the expected trend whereby higher $IMEP_g$ results in a smaller difference between $IMEP_n$ and $IMEP_g$ due to reducing PMEP. Figure 40b shows the correlation between COV_{IMEP_n} and COV_{IMEP_g}. The gradient of the line of best fit indicates a proportional offset between both parameters, where overall the COV_{IMEP_n} is 25 percent greater than COV_{IMEP_g}. This has significant implications with the data presented since a substantial proportion of the measured variability arises during the pumping stroke and is not directly related to variations in combustion. As mentioned a reason for the difference could in part be attributed to variations in pumping work. An alternative is the influence of signal-to-noise ratio on in-cylinder pressure data.

The influence of signal-to-noise ratio will be unique to the rig and the method of signal filtering adopted. Filtering was used here, where the method adopted was as that of Shayler and Wiseman [68], where filtering is particularly necessary when deriving combustion parameters namely the end of combustion. The Savitzky-Golay filter used, effectively fits a polynomial through a segment of the unfiltered signal, in this case a 3 third order polynomial was fitted every 11 measurement points

(5.5ºCA), this smoothing period was chosen so as not to filter the high frequency part of the pressure trace namely the peak pressure region. Figure 41 shows an unfiltered and filtered pressure trace and the associated error ratio between the two. There is significant high frequency noise on the pumping loop which decreases during the power stroke, where the filtered data follows the unfiltered data with very good accuracy indicated by the average error being 1. For the data sets previously shown in this Chapter the difference in values of both COV_{IMEP_n} and COV_{IMEP_g} between unfiltered and filtered in-cylinder pressure data is significantly less than 1% indicating the signal filtering has not influenced the trend seen. It is thought the contribution of variability from the pumping work will be higher for a multi-cylinder engine due to the increased number of cylinder interactions occurring compared to a single cylinder engine, but it is important to quantify this difference to enable differentiation between combustion derived variability and that associated to pumping work.

5.3.4 Comparison of stability limit from constant air and constant fuel tests operating at spark timings retarded from MBT*

The two test methods investigated, constant air and fuel, were shown to produce similar stability limits when chemical parameters were changed. Figure 34 highlights the detrimental influence on stability when spark timing is retarded from the optimum, yet again the reason for the increase in COV needs to be established to ensure it is a reflection of combustion instability and not caused by the experimental method. Figure 42 shows the influence of spark retard on COV_{IMEP_g} whereby for a given GFR increasing spark retard increases COV_{IMEP_g} where as the limiting GFR is approached the increase in instability for a given spark retard becomes greater. Data at dMBT* of 15 and 20 were not captured at the last two GFRs since the engine stalled at these conditions. Retarding the spark timing reduces the average $IMEP_g$, to investigate to what extent this accounts for increases in COV_{IMEP_g} is shown in two further figures. Firstly, Figure 43 re-plots

the data shown in Figure 42 where COV_{IMEP_g} is replaced by stdev of $IMEP_g$, this indicates a similar trend as with Figure 42, although the increase in stdev of $IMEP_g$ compared to COV_{IMEP_g} with retarding spark timing is less at given GFRs, this is more apparent at the richer GFRs. The reason for this trend is explained in Figure 44. Increasing COV_{IMEP_g} is caused in the case of spark timing changes by increasing stdev of $IMEP_g$ and reduction in average $IMEP_g$, the contribution of both these factors to COV_{IMEP_g} is quantified by calculating COV_{IMEP_g} by assuming a constant value of average $IMEP_g$ defined by

$$COV^*_{IMEP_g} = \frac{stdevIMEP_g}{IMEP_{g\_MBT*}} \tag{57}$$

Figure 44 shows the percentage difference in COV_{IMEP_g} calculated using both approaches. The contribution of reducing $IMEP_g$ is significant, particularly at the maximum spark retard where approximately 35% of the value of COV_{IMEP_g} results from the associated reduction in average $IMEP_g$. As the chemical stability limit is approached this contribution reduces. This has an influence on COV_{IMEP_g} and affects the defined stability limits for the most retarded spark timings, where for example the stability limit for dMBT = 20 would increase by approximately 1 GFR. As a final comparison Figure 45 shows the change in stability limits with spark retard, although there is some scatter all the data at a given relative spark timing is characterised accurately with a single line where the reduction in stability limit with increasing spark retard is apparent.

5.4 Comparison of parameters used to define stability limits

Throughout this work GFR has been used to characterise stability limits, whereby data from different engine speeds, loads, valve timings collapsed on to a single GFR characteristic. Work by Tully and Heywood [6] investigated alternative parameters that were particularly applicable with an engine operating on different fuel mixtures. The first of two parameters was defined as the Volumetric Dilution Parameter, VDP, representing the heat value per unit volume of the air/fuel mixture. The second the Thermal Dilution Parameter, TDP, representing the heating value per unit heat capacity of the air/fuel mixture, where combustion and emissions parameters were found to correlate with TDP. For example, the parameter collapsed on to a single characteristic the point at which combustion became unstable for tests with different fuels and at different operating loads. The non dimensionless parameter is given by:

$$TDP = \frac{\Delta T_{fuel\_only, \phi=1}}{\Delta T} \qquad (58)$$

where

$$\Delta T = \frac{\sum_i m_f . LHV_f}{m_{tot} . \overline{c_v}} \qquad (59)$$

It is assumed the combustion process is modelled at constant volume and the change in combustion composition is ignored, therefore $\overline{c_v}$ = average heat capacity of the unburned mixture. Where the mass weighted average $\overline{c_v}$ was calculated from the heat capacity of the individual components of the mixture at a representative reference temperature. Figure 46 shows the performance of using TDP to define

stability limits. The data as with GFR collapses on to a single characteristic when plotted using TDP, where the stability limit occurs at an approximate TDP value of 1.55, similar to the 1.57 found by Tully [6].

5.5 Discussion and Summary

The initial set of tests covered a wide range of operating conditions with the aim of describing the chemical stability boundaries at 3 physical spark timings. The widest set of boundaries, GFR limit 24, x_b <0.27 and AFR > 9 was found at MBT* spark timings. Only a small reduction in the boundaries occurred at dMBT*=10, where the GFR limit was reduced to 23. When the spark timing was retarded by 20°CA from MBT* the stability boundaries significantly reduced with a GFR limit of 19, x_b <0.2 and AFR > 10. This testing was termed 'constant air' testing since it moved towards the stability limits by reducing fuelling while holding the throttle angle constant. Issues with the test method and therefore the results were raised, whereby the stability limit could be occurring early due to a combination of CCV and lowering average $IMEP_n$ resulting in higher COV_{IMEP_n}, hence a second set of tests was conducted to validate the results from the first experimental set. Constant air tests along with constant fuel tests were carried out, where constant fuel tests increased the throttle angle to reach the stability limit. The results showed that the stability limit was not influenced by the test method even though in the case of the constant air tests there was a linear reduction in average $IMEP_n$ towards the stability limit. It was found however that 25% of the COV_{IMEP_n} is occurring in the pumping stroke and therefore not directly related to CCV, where this difference will be engine/rig specific, but it is recommended that when investigating CCV COV_{IMEP_g} should be used. The influence of spark retard on COV_{IMEP_g} was rationalised, whereby 35% of the increase at dMBT*=20 is accounted for by the reduction in average $IMEP_g$, in effect the magnitude of the CCV became greater for a given $IMEP_g$, although as the chemical stability limit was approached this contribution reduced. As a comparison the results were plotted against TDP [6] this parameter as with GFR collapsed the data on to a single characteristic. Combustion

stability has been shown to be a function of chemical and physical parameters, inlet fuel/air/residual mixture fractions and spark timing respectively, a spark retard of 10ºCA from the optimum does not significantly influence the stability limits whereas a spark retard of 20ºCA causes a marked reduction in stability limits.

CHAPTER 6

The Cause of Stability Limits

6.1 Introduction

The limits on stable operation reported in Chapter 5 were explored through the study of variations in engine work output . $IMEP$ provides information from the entire cycle or only the combustion stroke if $IMEP_g$ is used, whereby variability from only the combustion process can be indicated. Yet because $IMEP$ is an integral value over the combustion period it cannot provide any information on which part of the combustion process is causing the variability, to establish this the cylinder pressure information needs to be analysed and the associated mass fraction burned calculated. In this Chapter, the aim is to establish the dominant part of the burn that contributes to CCV. Establishing this link is important since it provides valuable insight into which part of the burn is causing the variability in $IMEP$. To understand which portion of the burn is dominant the mass fraction burn is broken down into two sections, firstly the $\Delta\theta_{0-10\%}$ and the rapid burn angle $\Delta\theta_{10-90\%}$. The flame development angle encompasses the period when the flame develops from a small kernel initiated by the spark to the point at which it has become fully influenced by the turbulence within the cylinder, the fully turbulent flame then propagates burning the majority of the cylinder mass during the rapid burn period. The method adopted to determine the mass fraction burned was described in Chapter 4.

6.2 The change in flame development and rapid burn angle as stability limits are approached and exceeded at MBT* spark timing

At MBT* spark timing both the constant air and fuel testing showed the chemical limit was reached at a GFR of 24. The combined data is used here to investigate the influence on mass fraction burned durations. Figure 47 shows the change in mass fraction burn durations as GFR is increased for the three engine speeds investigated previously, all at MBT* spark timing. The shortest burn duration in both cases occurs at the minimum GFR (in this case this is equivalent to a stoichiometric AFR). As the GFR ratio is increased both the $\Delta\theta_{0-10\%}$ and the $\Delta\theta_{10-90\%}$ increase, whereby the $\Delta\theta_{0-10\%}$ increases at approximately a constant rate to the maximum GFR value, with the $\Delta\theta_{10-90\%}$ relatively unaffected with the initial increase in GFR but more rapidly increasing in duration once the GFR exceeds 21. Interestingly, the two burn durations increase from similar minimum values, 22°CA to maximums of 45°CA. The increase in mass fraction burn duration for these sets of tests is essentially caused by changes in the laminar burning velocity. Although the burning process within the cylinder is turbulent, the increase in GFR for the tests shown has no influence on turbulence since the engine speed and valve timing remain constant, hence there will be no change in turbulent burning velocity apart from the change embodied in the laminar burning velocity.

The laminar burning velocity is a function of temperature, pressure and mixture ratio. Work by Rhodes and Keck [78] found an empirical relationship describing the influence of all the parameters mentioned above, based on constant volume bomb experiments, whereby the laminar burning velocity (S_u) is given by;

$$S_u = S_{uo}\left(\frac{T_u}{T_o}\right)^\alpha\left(\frac{p}{p_o}\right)^\beta(1-2.06\tilde{x}_b^{0.733}) \tag{60}$$

where S_{uo} is the undiluted laminar flame speed, T_o the referenced temperature (298K), p_o reference pressure (1 atmosphere), T_u unburned gas temperature, p actual pressure and $\tilde{x}_b$ volume fraction of diluent.

An estimate of the change in laminar burning velocity as the GFR is increased is given in Figure 47. The calculation of S_u assumes the unburned gas undergoes adiabatic compression, whereby the calculated T_u is based on measured cylinder pressure with the initial cylinder temperature at the start of compression assumed to be that of the measured inlet manifold temperature. Mixture ratios are based on measured parameters, where the values are calculated from methods discussed in Chapter 3. The values plotted are the inverse of S_u normalised at nominally the same GFR. In both plots, a and b, S_u is an average value, whereby the calculated values are the mean average value during either the $\Delta\theta_{0-10\%}$ or $\Delta\theta_{10-90\%}$. The change in S_u in both cases is very similar. This is effectively caused by the dominant influence of the mixture fraction in these calculations, and also that the combustion process is phased to maintain MBT* spark timing. The second effect means that each part of the combustion process will see similar temperatures and pressures although the change in mixture fraction towards more lean regimes reduces the absolute values. Figure 47 provides an overview of the combustion process; as the mixture ratio moves towards and exceeds stability limits, both the $\Delta\theta_{0-10\%}$ and $\Delta\theta_{10-90\%}$ both increase, approximately doubling over the range shown (~20°CA to 40°CA 18-27GFR). This does not provide information on the cause of stability limits, however increasing combustion duration does not directly indicate the combustion process is likely to be more unstable, stability limits are caused by variability between combustion events, not simply by a longer burning process.

Understanding which part of the combustion process is responsible for stability limits in terms of work output, $IMEP$, the normalised variability in $\Delta\theta_{0-10\%}$ and $\Delta\theta_{10-90\%}$ are plotted in Figure 48. Figure 48a indicates that there is a relatively small change in $COV_{\Delta\theta_{0-10\%}}$ as the stability limit is reached and exceeded, where it could be argued that taking the scatter into account there is actually no change in the variability, it is also worth noting that the approximate value of $COV_{\Delta\theta_{0-10\%}}$ is

7% across the entire range of GFR. Both the magnitude and change in $COV_{\Delta\theta_{10-90\%}}$ are much more substantial than those seen for $COV_{\Delta\theta_{0-10\%}}$. Figure 48b indicates that not only is the variability of $COV_{\Delta\theta_{0-90\%}}$ greater than that associated with $COV_{\Delta\theta_{0-10\%}}$ the increase in variability is significant, nearly trebling as the stability limit is reached and surpassed. In Chapter 5 issues were raised relating to the use of COV, these are applicable here although the influence is the inverse, in both cases the average burn durations increases therefore the instability indicated by calculating COV will be lower than if the duration had remained constant. Figure 49a and b shows the change in standard deviation of the $\Delta\theta_{0-10\%}$ ($stdev\Delta\theta_{0-10\%}$) and $\Delta\theta_{10-90\%}$ ($stdev\Delta\theta_{10-90\%}$). There is a distinct difference between Figure 49a and Figure 48a, whereby there is a notable increase in the $stdev\Delta\theta_{0-10\%}$, there is a similar pattern between Figure 49b and Figure 48b indicating the increase in variability of the $\Delta\theta_{10-90\%}$ is still greater than that of $\Delta\theta_{0-10\%}$. The fact that Figure 49 suggests an apparent correlation between the variability of $\Delta\theta_{0-10\%}$ and $\Delta\theta_{10-90\%}$ is further investigated in Figure 50. The correlation between increasing variation in the $\Delta\theta_{10-90\%}$ and $\Delta\theta_{10-90\%}$ is significant, whereby the correlation coefficient is approximately 0.7, though this appears to break down at the same point when the stability limit is reached and exceeded (at $stdev\Delta\theta_{0-10\%} \simeq 4$). Yet, the general correlation suggests that the move towards less stable combusting cycles is manifested in changes in the $\Delta\theta_{0-10\%}$ where the instability is further magnified in the $\Delta\theta_{10-90\%}$, with approximately a 3 times increase in instability in the $\Delta\theta_{10-90\%}$ compared to the $\Delta\theta_{0-10\%}$. The source of CCV appears to lie in the variability of the $\Delta\theta_{0-10\%}$ phase and is magnified in the $\Delta\theta_{10-90\%}$.

Previous work [31,79,80] investigated the causes of cyclic variability, as with much of the research carried out in this field a number of different parameters were used, not just burn rates and the associated variations. All compared experimental results with models of differing complexities. In the case of [31] the simulations suggested that 25% of the standard deviation of combustion duration, IMEP, maximum pressure and maximum pressure location was caused by 'random walk' of the flame kernel operating at stoichiometric conditions. Although this value is less than that found from the experimental work presented here the order of magnitude is similar, although some caution should be used in comparing these results due to the

different factors used. The work presented by [79] concluded that displacement of the flame kernel during the early stages of combustion has a major part in the origination of cycle to cycle variations, again many factors were used to assess the variations, including $COV_{\Delta\theta_{0-10\%}}$ and $COV_{\Delta\theta_{10-90\%}}$. The modelled results from [80] provided a fundamental appreciation of the causes of the variability during early stages of flame development, whereby initially the flame burns with a rate close to laminar flame speed, yet as the flame grows the influence of turbulence increases until a point where the flame is a fully developed turbulent flame. The work showed that the flame development period is most susceptible to flame stretch, where excessive flame stretch can lead to unstable burning and eventually the flame will quench. Flame stretch is characterised by the Karlovitz number, representing the ratio of chemical to eddy lifetime. In effect a high Karlovitz number indicates high flame stretch, therefore a less stable flame. It was shown that for the initial flame development process flame stretch for lean mixtures can enter regions of partial quench therefore resulting in less robust initial flame propagation. It is likely a combination of the factors discussed above will increase the cyclic variations seen in the results shown but it does appear that variability in the initial flame development is magnified during the propagation phase.

6.3 The change in flame development and rapid burn angle as stability limits are approached and exceeded at dMBT* spark timing

An increase in instability was shown to occur as the spark timing was retarded, although the absolute level of instability was shown to be amplified when using COV parameters since there was a reduction in average work output not just an increase in CCV. The influence on burn rate parameters is initially shown in Figure 51, with the change in $\Delta\theta_{0-10\%}$ and $\Delta\theta_{10-90\%}$ duration plotted as a function of GFR for a range of spark retards (sub plots a and b are a repeat of Figure 47 and are

shown to ease comparison). Dealing with the $\Delta\theta_{0-10\%}$ first, the change in relative spark timing is shown to have an interesting trend, whereby if the spark timing is retarded from MBT* by 5 degrees there is a slight reduction in $\Delta\theta_{0-10\%}$ that becomes most notable at the highest GFR. There is a significant change in the $\Delta\theta_{0-10\%}$ when the dMBT*=10, with a reduction in $\Delta\theta_{0-10\%}$ of approximately 25% at the highest GFR. There is also a change in the shape of the curve with the gradient moving from an increasing duration as seen with MBT* and dMBT*=5 to a flat profile, whereby the changes in GFR no longer influence the $\Delta\theta_{0-10\%}$. For the final two spark timings dMBT*=15 and dMBT*=20 the trend is similar to that seen for dMBT*=10 although there is an increase in duration and a slight upturn in gradient the absolute burn durations are still lower than those seen at MBT* and dMBT*=5. This trend is predominantly caused by the relative location of the $\Delta\theta_{0-10\%}$ and the associated change in thermodynamic conditions. Spark retard results in the $\Delta\theta_{0-10\%}$ moving closer to TDC where the unburned gas temperature is higher than at MBT*, the result is that the associated S_u is greater manifesting in reduced $\Delta\theta_{0-10\%}$. The results suggest that a spark retard of 10 from MBT* results in cylinder thermodynamic conditions that produce the most rapid and consistently the most rapid $\Delta\theta_{0-10\%}$ across the wide range of GFR.

The results for the $\Delta\theta_{10-90\%}$ are contrary to those shown for $\Delta\theta_{0-10\%}$ and in many respects are more simple. Generally there is an increase in $\Delta\theta_{10-90\%}$ as the spark timing is reduced from MBT*, with the increase reaching a maximum with a spark retard of 20. The trend of increasing duration as GFR is moved to leaner conditions is maintained as the spark timing is retarded. Scatter in the data increases as the spark timing is retarded, this reflects the generally unstable nature of the combustion process at these conditions. The two types of tests, constant air and fuel indicate similar relationships with spark retard for both the $\Delta\theta_{0-10\%}$ and the $\Delta\theta_{10-90\%}$.

As with the MBT* data to understand which part of the combustion event is causing a reduction in cycle stability, plots of $COV_{\Delta\theta_{0-10\%}}$ and $COV_{\Delta\theta_{10-90\%}}$ are shown in Figure 52, for completeness the MTB* is re-plotted as a datum. As the spark timing is retarded from MBT* the change in $COV_{\Delta\theta_{0-10\%}}$ is marginal for a given GFR, it is

only once dMBT*=15 that there is a notable increase in $COV_{\Delta\theta_{0-10\%}}$, where for a given GFR the trendline suggests $COV_{\Delta\theta_{0-10\%}}$ is increased by ~30%. At dMBT*=20 there is a further ~30% increase in $COV_{\Delta\theta_{0-10\%}}$ compared back to dMBT*. It should be noted though that the scatter in the data increases at the extreme spark retards and therefore it could be suggested $COV_{\Delta\theta_{0-10\%}}$ is no longer a function of GFR. The influence of spark retard on $COV_{\Delta\theta_{10-90\%}}$ follows a more consistent trend whereby as the spark timing is retarded for a given GFR there is always (as shown by the trendline) an increase in $COV_{\Delta\theta_{10-90\%}}$, as with the $COV_{\Delta\theta_{0-10\%}}$ there is a reasonable amount of scatter in the data particularly at the maximum spark retard. For completeness the change in $stdev\Delta\theta_{0-10\%}$ and $stdev\Delta\theta_{10-90\%}$ is shown in Figure 53. The change in $stdev\Delta\theta_{0-10\%}$ is reasonably consistent, whereby with retarded spark timing at a given GFR there is an increase in $stdev\Delta\theta_{0-10\%}$, at the maximum spark retard, the data shows the $stdev\Delta\theta_{0-10\%}$ is insensitive to GFR whereby the level of variability is greater than that for all other spark timings but there is no increase as the GFR ratio is increased. The change in $stdev\Delta\theta_{10-90\%}$ follows a more expected trend, with a significant increase in $stdev\Delta\theta_{10-90\%}$ with GFR, whereby the absolute level of variability is increased as the spark timing is retarded from MBT*.

Figure 54 correlates $stdev\Delta\theta_{0-10\%}$ and $stdev\Delta\theta_{10-90\%}$. At MBT* spark timing the increase in variability of the $\Delta\theta_{0-10\%}$ is directly proportional with that of $\Delta\theta_{10-90\%}$, for retarded timings the same statement holds yet the correlation between the two is significantly reduced for the maximum retarded spark timings. At a spark retard of 10ºCA the $stdev\Delta\theta_{10-90\%}$ increases for a given $stdev\Delta\theta_{0-10\%}$ but once the spark timing is retarded by 10ºCA any additional spark retard results in the same $stdev\Delta\theta_{10-90\%}$ for a given $stdev\Delta\theta_{0-10\%}$, in effect the maximum level of $stdev\Delta\theta_{10-90\%}$ has been realised.

6.4 Discussion and Summary

Greater understanding of the causes of CCV have been established in this chapter by correlating combustion parameters $\Delta\theta_{0-10\%}$ and $\Delta\theta_{10-90\%}$ and the associated variations in these parameters with GFR. Increases in burn duration have been

shown to directly correlate with increases in CCV, this is predominantly caused by variability in $\Delta\theta_{0-10\%}$ which is translated into greater variability in the $\Delta\theta_{10-90\%}$, in effect the source of the variability is manifested in the $\Delta\theta_{0-10\%}$ and does not start occurring in the $\Delta\theta_{10-90\%}$. The influence of spark timing changes has been described, whereby the changes in $\Delta\theta_{0-10\%}$ are different to those of $\Delta\theta_{10-90\%}$ as the spark timing is retarded. The $\Delta\theta_{0-10\%}$ decreases significantly as the spark timing is retarded from MBT* to a minimum at dMBT*=10, caused predominantly by the more favourable thermodynamic conditions, since the $\Delta\theta_{0-10\%}$ is occurring closer to TDC where the unburned gas temperature is greater than if the spark timing is at MBT*. Although the $\Delta\theta_{0-10\%}$ reduces in duration the actual variability increases as the spark timing is retarded to a maximum at the maximum spark retard. The characteristics of the $\Delta\theta_{10-90\%}$ are much more straight forward, as the spark timing is retarded both the duration and variability increase again to a maximum at the maximum spark retard. The cause of combustion variability is similar between MBT* operating conditions and retarded spark timing cases, the combustion variability starts in the $\Delta\theta_{0-10\%}$ and is amplified during the $\Delta\theta_{10-90\%}$. Although for significant spark retards, >15ºCA the correlation reduces, indicating increased levels of instability occurring in the $\Delta\theta_{10-90\%}$.

CHAPTER 7

Emissions Characterisation

7.1 Introduction

Current European legislation on pollutant emissions from spark ignition engines sets limits on emissions of carbon monoxide (CO), unburned hydrocarbons (HC's) and oxides of nitrogen (NOx). The main reason to restrict, specifically these emissions is their toxicity and the detrimental impact they have on the environment [81]. Legislation restricts the emissions per kilometre (km), determined over a representative drive cycle, for example the NEDC, which all new vehicles must adhere to. The use of a vehicle model that predicts emissions flow rates accurately is therefore a very powerful tool that can be used to assess the required performance of the vehicle aftertreatment system.

The emissions work here focuses on the characterisation of engine out pollutant emissions in the exhaust gas stream of a PFI engine, not emissions formation in cylinder. The engine was operated with variable valve timing, at stable and unstable combusting conditions. The methodology uses the connections between exhaust emissions and engine global parameters such as AFR, x_b and spark timing relative to the optimum. Emissions are more sensitive to changes in operating conditions with for example a few degree changes in spark timing resulting in a small decrease in torque but a doubling of pollutant emissions. An alternative approach using NOx emissions to determine spark timing relative to MBT* is highlighted and evaluated. The impact of deteriorating combustion stability on emissions is investigated and decoupled from normally occurring emissions. Physical underpinning of forms of generic functions is deferred until Chapter 8.

7.2 Characterisation of Emissions and Previous Work

Exhaust emissions based on measurements of molar volumetric concentrations in the exhaust gases vary with engine speed, load, AFR, spark timing and EGR rate. Normalising values provides a useful comparison of data and aids the direct comparison of emissions from different engines. The normalised value is termed the emissions index, defined as:

$$EI_{gas} = \frac{\dot{m}_{gas}}{\dot{m}_{fuel}} \tag{61}$$

where $\dot{m}_{gas}$ refers to the particular emission in question, for this study CO, HC's and NOx.

Emissions concentrations are sensitive to a small set of particular engine parameters and have been shown to produce repeatable trends from one engine to the next. Shayler et al [7] developed a set of 'generic functions', based on a number of independent variables, namely AFR, spark timing relative to the optimum and the x_b. The functions were derived from analysis of a large database of experimental data from four-valve cylinder DOHC engines with typical pentroof, open chamber features. The functions were successfully used by Horn [82] to predict emissions accurately for a Mitsubishi DISI engine operating in homogenous charge mode. Although the emissions from the same engine operating under stratified mode were described using trained neural networks.

The trends characterised were found to be universal and adjustments where necessary were simple scaling factors of the original functions. The original functions derived by [7] and modified functions used to characterise the Jaguar AJ27 where necessary are shown in Table 4 referred to as Series 1 and Series 2 respectively. The form of the generic equations and values for the constants are provided in Table 5 and Table 6.

7.3 Generic Representation

7.3.1 CO Emissions Index

Carbon monoxide emissions are a function of equivalence ratio. Under lean operation there is sufficient oxygen to oxidise the CO to CO_2 but CO remains in the exhaust due to limiting chemical reaction rates as discussed in Chapter 8. CO is present in the exhaust gases during rich operation due to insufficient oxygen. Figure 55 shows the fit of Jaguar AJ27 data to both Series 1 and Series 2. The correlation when the engine operates rich is excellent, as found by Horn [82] Series 1 under predicts EI_{CO} for lean operating points, the alternative function Series 2 shows improved correlation with these points as highlighted by Figure 56. There is no noticeable change in EI_{CO} with varying intake cam timing. Siewert [83], made similar findings when operating a single cylinder engine with two extreme intake valve opening times. Although these findings are contrary to Leone et al [43] that stated the early intake valve opening intake turbulence decreases, increasing mixture charge inhomogeneity resulting in higher CO emissions.

The generic functions were previously fitted to data sets where there was no information about the combustion stability. Using COV_{IMEP_n} as a method of distinguishing between unstable and stable combustion operating points the contribution of 'normal' emissions and those resulting from unstable combustion can be decoupled. Figure 57 shows the effect of combustion instability on EI_{CO}, the trend in CO emissions remains the same as for the stable operating points. This is highlighted in Figure 58 by the comparison of the measured and predicted EI_{CO} at unstable and stable operating conditions, where it is shown that there is no significant deviation due to increasing instability.

7.3.2 HC Emissions Index

Hydrocarbon emissions index is a function of equivalence ratio and relative spark timing. The original generic function work found that EI_{HC} was approximately proportional to GFR which is used here as a starting point. The change in the relative emissions index (EI_{HC}/GFR) with equivalence ratio is shown in Figure 59. The data from the AJ27 comprises only experimental points where the VO was fixed to 15°CA and $COV_{IMEP_n} < 4.0$. These constraints are applied since this is a typical VO period for conventional SI engines [84] and combustion instability increases the hydrocarbon emissions (discussed later), thus ensuring the changes in hydrocarbon emissions are only a function of equivalence ratio. Although it is evident that there is a significant spread of data, due to experimental scatter and the limitations of a simple equivalence ratio function, the Jaguar AJ27 data is shown to follow the original function with no less accuracy than the original PFI engine data. The shape of the curve is dictated by oxygen availability and bulk gas temperature. Under rich operation $\phi = 1.4$ HC emissions account for only 3% of the fuel burned although there is 40% excess fuel, CO accounts for the significant proportion of excess fuel with H_2 the remainder. Lean combustion and therefore lower temperature causes an increase in HC emissions due to the reduced rate of HC oxidation to CO, this is further discussed in Chapter 8. The correlation between GFR and EI_{HC} is investigated in Figure 60 and Figure 61. The correlation between EI_{HC} and equivalence ratio is very similar to that shown for relative EI_{HC}, therefore a generic function was created to predict EI_{HC} as a function of equivalence ratio. Comparing measured and predicted error ratio for this generic function against GFR shows that under stable operating conditions the correlation is poor, $R^2 = 0.0542$.

The influence of VO on EI_{HC} is shown in Figure 62 by comparing the error ratio correlation of measured and predicted as a function of VO. Increasing VO produces a notable reduction in EI_{HC} with the maximum reduction of approximately 20% at the maximum VO. The reason for the reduction was hypothesized by [43] where the increased VO period causes gas to backflow into the intake port and is therefore drawn back into the cylinder during the intake stroke where the unburned

hydrocarbons are 're-burned'. A study by Seabrook et al [85] using a fast flame ionisation hydrocarbon detector placed in the exhaust port showed that due to the VO period, significant back flow occurs from the exhaust port into the intake port. The backflow significantly reduced the final hydrocarbon peak associated with the exhaust process.

The final part of the generic function for hydrocarbon emissions is the effect of spark timing. Altering the spark timing phases and changes the duration of the combustion process. Rationalisation of the influence of spark timing changes are achieved by referencing spark timing to the optimum values at MBT*. Figure 63 shows the influence of spark timing on normalised EI_{HC}. The correlation between the generic function and the data set is excellent. The influence of AFR is as was previously found; the effect of external EGR could not be evaluated since the engine did not have an external EGR system. The effect of EGR previously, was similar to reducing AFR, where the reduction in HC emissions due to retarded spark timing is less because of lower expansion and exhaust port temperatures. The combined performance of the HC generic function is shown in Figure 64, although each individual part of the generic function contributes errors, overall the predictions are within 30% of measured values.

Combustion instability is associated with poor driveability and an increase in HC emissions, due firstly to lower combustion temperatures reducing post flame HC oxidation both during expansion and in the exhaust port, followed by partial burn and then misfiring cycles. The effect of combustion instability is shown in Figure 65; the deviation from the generic function is significant with in some cases the EI_{HC} exceeding 100% of the predicted value. In these cases combustion stability limits were exceeded by operating the engine past the lean or dilution limits. Combustion instability limits can also be reached and exceeded by retarding the spark timing from the optimum, this effect is shown in Figure 66. Where under stable operating conditions spark retard reduces EI_{HC}, spark retard that results in reduced combustion stability increases the EI_{HC} from the minimum occurring at MBT*. Rationalisation of the influence of combustion instability on EI_{HC} is shown in Figure 67, where the increase in EI_{HC} due to both chemical and physical factors is

described by a single linear function of COV_{IMEP_n}. Determining the point at which EI_{HC} starts to increase due to combustion instability is hard to define due to scatter of experimental data. A reasonable approach to gaining some insight is to evaluate the point at which the equivalence ratio function and the COV_{IMEP_n} function intersect at a given equivalence ratio. At an equivalence ratio of 1.0 the intersection point is equivalent to a COV_{IMEP_n} of 2.5, although the spread of data about this point suggests COV_{IMEP_n} between the range of 2.5 - 4. The upper limit is chosen here.

Application of the EI_{HC} generic function falls into two parts, stable and unstable with the switching point between the two defined as COV_{IMEP_n} >4. In the stable region EI_{HC} is a function of equivalence ratio, relative spark timing and VO. For COV_{IMEP_n} >4 EI_{HC} is predicted using the base equivalence ratio function with the addition of the linear function of COV_{IMEP_n}. The overall performance of the HC generic function is shown in Figure 68 where again the majority of the predictions are within 30% of the measured values.

7.3.3 NOx Emissions Index

NOx emissions are predominantly a function of the burned gas temperature and oxygen availability, these factors can be described using AFR, GFR and relative spark timing. Figure 69 shows the agreement between the measured and the predicted NOx emissions index over a range of AFR and GFR at MBT[*]. The trends are consistent with previous work [7], although the overall prediction was approximately double the measured values across the entire operating range. A constant correction factor as shown in Table 4 is applied to all predictions. There is no noticeable direct effect of VO on EI_{NO_x} as shown in Figure 70, changes in VO have been shown to significantly influence the residual gas fraction, and these are accounted for in the generic function by GFR. As with EI_{HC}, EI_{NO_x} is substantially affected by changes in spark timing relative to the optimum as shown in Figure 71. The original function fitted to engine data by Shayler et al [7] is shown

to under predict EI_{NO_x} when the spark timing is advanced from MBT*, the reason for this is that the original function was fitted to experimental data with engines operating up to dMBT values of –10. For dMBT < 20 the generic function provides a very accurate prediction, if dMBT ≥ 20, EI_{NO_x} remains at a constant value of approximately 0.12. The influence of combustion instability on EI_{NO_x} at MBT* is shown in Figure 72. From Figure 73 it is apparent that reducing combustion stability leads to a reduction in EI_{NO_x}, the reduction is not predicted by the current generic function. There is a greater reduction in EI_{NO_x} due to increasing x_b than was previously found, essentially due to the increased data set at the unstable combustion conditions. The prediction of the generic function is improved at these conditions without reducing the accuracy at stable operating points by altering the x_b constant as shown by the comparison of Figure 73 and Figure 74. Reduction in EI_{NO_x} from spark retard that also results in reduced combustion stability follows the original generic function as shown in Figure 75. The predictions of EI_{NO_x} generally fall within the 30% error, with less scatter exhibited than with the EI_{HC} generic function, due essentially to the more simplistic formation mechanisms of EI_{NO_x} emissions than EI_{HC}.

7.4 Assessment of emissions models over the NEDC

The influence of the models developed in the previous sections have been assessed using NuSIM, a vehicle simulation model whereby the engine system has been modelled based on experimental data. The engine controller was defined based on a prototype production controller designed by Jaguar. Figure 76 shows a comparison between the original emissions models and those based on the measurements from the AJ27, both real emissions flow rate and cumulative emissions are shown. Figure 77 shows a difference plot whereby new minus old emissions predictions are presented highlighting more easily the differences. There is generally no difference in CO emissions due to the model predicting the engine running most of the drive cycle slightly rich of stoichiometric. Of particular note is the significant difference between

the models in relation to the HC emissions, whereby the new model indicates increased HC emissions during both transient and steady state operation. The increase is caused by the additional contribution of unsteady combustion HC emissions, where during the transients the COV_{IMEP_n} is increasing to values in excess of 25 with certain steady state periods the engine predicted to be operating with a COV_{IMEP_n} of approximately 15. The cause of the high COV_{IMEP_n} is predominantly due to the engine running with large valve overlaps increasing the x_b to levels that are exceeding the stability limit. The change in NOx emissions is small but generally lower than the old model due to the correction factor applied and the high levels of x_b during steady state operation.

It is unlikely that a production variant of an engine controller would result in engine excursions and steady state conditions causing such increases in HC emissions. The model does show the importance of accurate engine calibration to avoid unnecessary increases in HC emissions.

7.5 Alternative Approach to Determining MBT*

Typical engine management systems (EMS) are calibrated to maintain spark timing as close to MBT* as possible, since this timing corresponds to maximum brake power and minimum brake specific fuel consumption. The exact location of MBT* is often hard to determine due to the relative flatness of the torque curve. Further problems can arise when determining MBT* spark timing when spark sweeps are knock limited, the method described in Chapter 3 to determine MBT* can frequently result in over extrapolation of MBT* under these conditions as shown in Figure 78. Although advancing or retarding spark timing from MBT* adversely effects brake specific fuel consumption, there is much more of a notable effect on EI_{HC} and particularly EI_{NO_x}, for example retarding the spark timing by 4ºCA from MBT* increases the brake specific fuel consumption by 6% but reduces EI_{NO_x} by 23%. Therefore knowledge of spark timing relative to MBT* is much more

important from the emissions perspective. An alternative method for determining MBT* from EI_{NO_x} is investigated.

There are two possible methods for determining MBT* from EI_{NO_x}. Firstly using the EI_{NO_x} trend from a spark sweep, or applying the generic functions to a single data point whereby the expected error between torque and EI_{NO_x} derived MBT* would be 30%. The first method utilises the robust correlation between spark timing and EI_{NO_x} as shown in Figure 71. Investigating this correlation further for data only at stoichiometric conditions EI_{NO_x} exhibits a linear increase for dMBT < 16 as shown in Figure 79. The excellent linear correlation between dMBT < 16 and EI_{NO_x} is shown to apply over eight individual spark sweeps. The accuracy is increased if as would be the purpose of using this method, the correlation was applied only for one spark sweep. Application of this method requires a linear line of best fit through the data set, the most retarded spark timing EI_{NO_x} value is assigned the constant value line, where the straight line intersects the constant line the actual spark timing has a relative spark timing of 16 (MBTD = 16), an example is shown in Figure 80. This method has limitations, the spark sweep ideally should have data points retarded more than MBTD = 16 so that an accurate crossing point can be determined and as shown in Figure 80 and the method itself can only be applied to spark sweep data. The method has been shown to have an accuracy of predicting MBT* to within ±3ºCA from MBT* evaluated using the torque based method.

7.6 Combustion Efficiency

The development of the generic functions including unstable combustion data has lead to an investigation of combustion efficiency since it was likely that previously developed trends would no longer be applicable. Combustion efficiency is defined by Heywood [14]:

$$\eta_c = 1 - \left[\frac{\sum_i x_i Q_{LHV_i}}{[\dot{m}_f / (\dot{m}_a + \dot{m}_f)] Q_{LHV_f}} \right] \tag{62}$$

where the mass fractions (x_i) are CO, hydrogen (H_2), HCs and particulates (assumed to be zero in a SI engine) and Q_{LHV_i} are the lower heating values of these species. Where the heating values for CO is 10.1MJ/kg and H_2 is 120MJ/kg, the lower heating value for HCs is assumed to be the same as the fuel, 44MJ/kg. Shayler and Chick [86] modelled η_c using the data presented by Heywood [14] using the following functions

$$\eta_c = 0.98 \tag{63}$$

for ϕ less than one, and by

$$\eta_c = 2.662 - 2.26\phi + 0.577\phi^2 \tag{64}$$

for ϕ greater than one. Reducing combustion stability leads to increasing HC emissions and therefore reduced η_c, the AJ27 data was used to calculated the η_c, where H_2 was calculated from the water gas shift reactions based on the measured and determined exhaust gas concentrations of CO and CO_2 and H_2O. Figure 81 shows that η_c is significantly influenced by x_b. With the lowest levels of x_b the η_c follows the previously developed function, where a significant reduction in η_c occurs when the mixture becomes rich due to incomplete combustion and therefore the presence of CO. As the mixture becomes increasingly lean ($\phi < 0.73$) the combustion stability limits are reached and then exceeded, HC emissions increase rapidly, reducing the η_c. As the x_b is increased the lean limit where η_c reduces,

moving towards stoichiometric conditions where the combustion process is most robust, this trend continues until the $x_b > 0.25$ where across the entire equivalence ratio range η_c is offset from the fitted trend. Further increase in x_b leads to extremely unstable combustion, ultimately causing the engine to stall.

7.7 Discussion and Summary

Feedgas Emissions including combustion efficiency have been successfully described using generic functions where the functions have been further developed to include the influence of unstable operating conditions and valve overlap. CO emissions were shown to be accurately characterised by a single function, whereby there was no need to include functions for the influence of valve overlap and differentiating between stable and unstable operating conditions. HC emissions are more complex, due to the numerous contributory sources within the cylinder and the complex formation and consumption that occurs during the combusting stroke. Again the general form of the functions were applied, although the dependence on GFR was disregarded, it is thought the inclusion of GFR in the original function aided collapsing unstable combusting conditions on to the ϕ function, whereas in this case unstable combusting conditions were described separately. For stable operating conditions changes in valve overlap had a significant influence on HC emissions, where from the datum overlap of 15°CA to the maximum valve overlap of 42°CA HC emissions reduced by approximately 20%. The influence of relative spark timing was shown to follow previous trends. The influence of deteriorating combustion stability on HC emissions was established whereby there was a deviation from the predicted HC emissions when COV_{IMEP_n} was greater than 2.5-4, where the increase in HC emissions with COV_{IMEP_n} followed the same trend whether COV_{IMEP_n} was increased by chemical (x_b and AFR) or physical means (changes to relative spark timing). NOx emissions are described using the originally developed functions with minor changes to improve the predictions. There was no direct influence of valve overlap on NOx emissions. The reduction in NOx emissions with valve overlap was described by the increase in x_b. As with CO emissions the inclusion of unstable

operating conditions did not require additional functions. The robust correlation between relative spark timing and EI_{NO_x} was shown and a method for determining relative spark timing based on EI_{NO_x} rather than the traditional torque based approach, where the results showed both methods would produce MBT* spark timing within 3°CA from each other.

The final part of this chapter dealt with combustion efficiency determined from the emissions. The experimental data showed that with an engine with variable valve timing the traditional functional form of combustion efficiency as a function of ϕ no longer holds true. It is necessary to take into account the change in combustion efficiency with x_b and that for a given equivalence ratio combustion efficiency can be substantially reduced by high levels of x_b, this is a direct reflection of the results shown in Chapter 5.

CHAPTER 8

Emissions Generic Function Physical Underpinning

8.1 Introduction

The generic functions to describe the emissions from SI engines developed in Chapter 7 were based on measurable engine parameters such as AFR and x_b, with the specific application to predict emissions for a vehicle model. This chapter underpins the functions developed by comparing the results with more fundamentally based approaches, including literature reviews relating to each of the emissions. Typically these types of approaches are used with thermodynamic simulations of the cylinder, where the combustion process is modelled along with emission formation on a crank resolved basis, these methods can be used relatively successfully to predict CO and NO_x emissions, whereas the complexities involved with HC formation and consumption mean the models tend to be highly complex. Results from such simulations are compared with the generic functions providing underpinning of the form the functions have taken.

8.2 Calculation of cylinder temperature and gas species

The major species of combusted hydrocarbon fuels at low temperatures are N_2, H_2O, CO_2 and O_2 or CO and H_2. At higher temperatures, approximately greater than 2200K, these major species dissociate and react to form additional species. The concentration of each species given sufficient time will reach an equilibrium level, where the production and removal of each species is at equal rates. The second law of thermodynamics defines the criterion for chemical equilibrium, for complex chemical equilibrium compositions, such as required here, standardised computer methods are available [87], commonly known as the NASA-Lewis method. The method used to calculate flame temperatures and equilibrium species here is a simplified approach, as developed by Olikara and Borman [88].

8.3 CO Emissions

CO formation is one of the principle reaction steps in the hydrocarbon combustion mechanism, summarised by [14]

$$RH \rightarrow R \rightarrow RO_2 \rightarrow RCHO \rightarrow RCO \rightarrow CO \tag{65}$$

where R stands for the hydrocarbon radical. The CO formed in the combustion process is then oxidised to CO_2 at a slower rate. The principle reaction being

$$CO + OH \rightarrow CO_2 + H \tag{66}$$

Figure 82 shows the EI_{CO} generic function and equilibrium EI_{CO} at three points in the cycle. Firstly equilibrium EI_{CO} at average peak burned gas pressures and

temperatures, where the temperature is defined as adiabatic flame temperature evaluated at measure peak cylinder pressure. Secondly equilibrium EI_{CO} evaluated at the end of expansion temperatures, the temperature has been assumed to be constant, at 1800K [84], across the equivalence ratio range. Finally equilibrium EI_{CO} calculated at measured exhaust port temperatures. The measured concentration of EI_{CO} is lower than the peak cycle temperatures and pressures but is higher than equilibrium values for the exhaust port conditions near to stoichiometric and lean conditions. This indicates the formation and removal of CO in the exhaust, is kinetically controlled, the drop in temperature and pressure caused by the expansion process is at a faster rate than the time constants of the controlling reactions, therefore CO does not remain locally equilibrated.

A study by Newhall [89] investigated the oxidation of CO during the expansion stroke by carrying out a series of kinetic calculations assuming the burned gas at the time of the peak cylinder pressure was uniform and in equilibrium. The study found that although reaction (66) is slow compared to many of the precursor hydrocarbon reactions it is sufficiently fast enough to be continuously equilibrated throughout expansion, this indicates that reactions producing OH and H must be themselves involved in rate limited reactions. The reactions studied, firstly the bimolecular atom exchange reactions

$$OH + H \rightarrow H_2 + O \tag{67}$$

$$OH + O \rightarrow O_2 + H \tag{68}$$

$$OH + H_2 \rightarrow H_2O + H \tag{69}$$

$$OH + OH \rightarrow H_2O + O \tag{70}$$

secondly the three body recombination reactions

$$H + OH + M \rightarrow H_2O + M \tag{71}$$

$$H + H + M \rightarrow H_2 + M \tag{72}$$

$$O + O + M \rightarrow O_2 + M \tag{73}$$
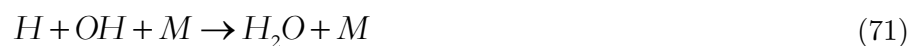
of these two sets of reactions studied, only the three body recombination reactions were found to be rate limiting. As shown in Figure 83 the prediction of EI_{CO} by Newhall [89] compared to the measured data across a range of equivalence ratios is reasonable with much improved accuracy compared to the equilibrium results near to stoichiometric. The reason for the inaccuracy can be attributed to the fact that Newhall based the expansion calculations on constant peak cycle temperature and pressure and that the burned gas was uniform.

Further investigations by [90,91] investigated the influence of non-uniform burned gas temperature during blow down and exhaust part of the cycle, it was found that a distinct CO concentration gradient exists. Exhaust gases that exited the cylinder first during blow down contained significantly higher concentrations of CO than the exhaust gases that left later, this was attributed to the early exhaust fraction cooling more rapidly. The conclusions from [90,91] were that, during fuel rich operation average exhaust CO concentrations are close to equilibrium concentrations in the burned gases during expansion. For close to stoichiometric operation the partial equilibrium calculations are shown to be in good agreement with the experimental data, the calculated equilibrium values of CO late in the expansion stroke and in the exhaust port are shown to be orders of magnitude lower. Under lean operation measured CO concentrations are significantly higher than those predicted by any of the kinetic models. A suggested reason for this discrepancy is that hydrocarbon emissions emerging during expansion such as those exhausted from the crevices are only partially oxidised to CO. A model developed by Lee and Morley [92] investigating the processes undergone by fuel that escapes the normal combustion event, using 84 kinetically controlled reactions during expansion found as before that under lean operation there was insignificant kinetic limitations in the bulk gas chemistry to produce the concentrations of CO observed in the exhaust

system. The introduction of two pulses of hydrocarbons entering the cylinder during expansion improved the prediction of CO emissions.

Figure 84 shows the EI_{CO} generic function broken down into three distinct areas, for equivalence ratios greater than 1.05, EI_{CO} is equivalent to equilibrium concentrations in the bulk burned gases near the end of expansion, in a close band around stoichiometric (0.95 – 1.05) the partial equilibrium models apply. For lean mixtures, EI_{CO} is attributed to partial oxidation of unburned hydrocarbons.

8.4 HC Emissions

The generic functions developed in Chapter 7 to describe EI_{HC} simplifies the complexities of HC emissions that arise from SI engines. An overview of the subject by Cheng et al [72] produced an HC flow chart for the fuel that escaped normal combustion, as shown in Figure 85.

The flow chart shows that approximately 1% of the fuel entering the cylinder is not involved in normal combustion because it is absorbed by the oil, this is equivalent to 16% of the HC feedgas emissions arising from oil layers. A further study, investigating the effect of oil layers on HC emissions by Linna et al [93] has suggested that oil layers account for less than 10 percent of total HC emissions. The deposits again were predicted to contribute 16% of the HC emissions, essentially they act as additional crevices within the combustion chamber absorbing fuel. An investigation by Haidar H A et al [94] suggested that the combustion chamber deposits could account for between 10 to 20 percent of the HC emissions, the study also found that the additional HC emissions from the combustion chamber deposits stabilised long before the combustion chamber thickness did. An added implication of combustion chamber deposits was studied experimentally by Kalghatgi [95] where volumetric efficiency was reduced by 2 – 3 percent due to the deposits heating the intake charge, the deposits were also found to promote knock (Knock Limited Spark Advance (KLSA) was reduced).

There have been many studies [96-98] since the paper by Cheng et al [72] investigating HC emissions due to liquid fuel, essentially these have investigated the effects of open and closed intake valve injection, different forms of injection, predominantly investigating the differences between fully prevaporised fuel injection and typical fuel injection, including changes in fuel impingement location. The findings by Landsberg et al [96] suggests that about 5% of the injected fuel enters the cylinder as liquid and this increases the HC emissions by approximately 11% above the fully vaporised gasoline HC emission level assuming half this liquid vaporises in the cylinder and does not impinge on the walls. This finding suggests that Cheng et al [72] overestimated the HC emissions due to liquid fuel, but this is a comparison with prevaporised fuel injection which will have HC emissions that have arisen from liquid fuel in the cylinder, one possible source of the liquid fuel arising from wall wetting. The HC emissions arising from the flame quench layer was established by LoRusso et al [99] which showed that the quench layer contributed no more than 3 to 12 percent to the hydrocarbons observed in the exhaust gases.

The largest source of HC emissions results from charge mixture being trapped in crevice regions, these regions where the flame cannot propagate can be equivalent to 1.6 percent of the clearance volume [100]. A model investigating HC emissions, only considering crevice and fuel absorption/desorption process from oil layers developed by Sodre and Yates [101] showed that the crevice contribution to HC emissions is between 70 to 85 percent with fuel contributions the remaining 15 to 30 percent. New piston designs have also been investigated recently, the findings by Bignion and Spicher [102] showed that a 30 percent decrease in HC emissions was achieved by increasing the piston top land crevice volume, facilitating greater flame intrusion into the piston top land region and allowing earlier scavenging with more effective post flame oxidation.

A widely investigated area since the overview by Cheng et al [72] is into the oxidation process the HC emissions undergo in the hot post flame combustion gases and in the exhaust port and runner. The study by Bian et al [103] found that post combustion oxidation depends on fuel structure, heat release rate, reaction rates and diffusion processes. Investigations [104-108] highlighted the importance of gas temperature in the oxidation process, the critical temperature suggested was

approximately 1400K below which no appreciable oxidation occurred. The study by Norris and Hochgreb [109] suggested that in-cylinder post combustion oxidation could reduce HCs escaping the main combustion event by between 50 – 90%. Although as suggested by Eng et al [105] the majority of HC oxidation occurs within the cylinder, experimental results by Caton et al [110] showed that between 2 and 70 percent of HC emissions exiting the cylinder oxidised in the exhaust port. The final part of the exhaust system that facilitates HC oxidation is the exhaust port runner, although as shown by Drobot et al [108] the reduction of HC emissions in the runner compared to the port was negligible reducing cylinder out HC emissions by only a further 2 percent.

It is apparent from these studies that feedgas HC emissions result from many sources the quantification of which in this study is impossible. It is possible to break the trend shown in Figure 86 into two distinct areas, where HC emissions result from bulk gas and normal mechanisms, as described above. Bulk gas HC emissions result from partial oxidation of the fuel and are most apparent when the mixture is rich of stoichiometric, the species that are known to represent bulk gas HC emissions are methane and acetylene. The work by [105,106] quantified the percentage of bulk gas HC emissions that were present across a range of ϕ. Although both these studies were conducted using hydrocarbon specific fuels the trends in the production of the bulk gases would be similar with gasoline, these findings are applied to the hydrocarbon generic function as shown in Figure 87. Although the bulk gas contribution does account for a significant proportion of the EI_{HC} as the mixture becomes increasingly rich there is still an increase in the normal EI_{HC}, this is accounted for by a reduced overall oxidation rate due to less oxygen availability. The same trend appears as the mixture becomes increasingly lean, in this case there is insignificant contribution of HCs from the bulk gases and the increase is associated with reduced oxidation due to lower combustion and expansion temperatures. It has been shown that EI_{HC} increase by orders of magnitude with reducing combustion stability. There is a critical ϕ where continued reduction in the fuel supplied rapidly reduces combustion stability and increases EI_{HC} where the critical ϕ depends on the x_b, as shown in Figure 88. The development of the EI_{HC} can therefore be broken down into three distinct

areas, bulk gas HC emissions, normal HC emissions and those attributed to combustion instability.

8.5 NOx Emissions

The generic function describing EI_{NO_x} is primarily a function of AFR and GFR. These findings were originally observed experimentally by [59,111,112]. The findings by Quader [111] showed that residual gases with higher specific heat capacity gave larger NOx reductions indicating the importance of temperature in the formation of NOx emissions.

The study of NOx emissions from internal combustion engines are extensive as listed previously, with particular emphasis being placed on NO (nitric oxide) emissions since in SI engines NO is the predominant oxide of nitrogen produced inside the engine cylinder. There are four established NO formation mechanisms: (a) thermal, (b) prompt, (c) nitrous oxide and (d) fuel nitrogen. The thermal mechanism dominates the formation of NO in SI engines with the prompt mechanism being significant during rich and highly diluted operation and the nitrous oxide mechanism being significant during lean operation. The thermal or extended Zeldovich mechanism as it is well known comprises three reactions:

$$O + N_2 \rightarrow NO + N \tag{74}$$

$$N + O_2 \rightarrow NO + O \tag{75}$$

$$N + OH \rightarrow NO + H \tag{76}$$
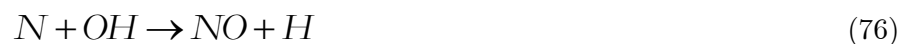
The rates of these reactions are generally slower than the combustion rate therefore combustion reactions can generally be assumed to be unaffected by the above reactions. This essentially means that the production of NO in the post flame gases almost always dominates any flame front produced NO. The concentrations of N_2,

O$_2$, O, OH and H in the post flame combustion gases may be assumed to be in equilibrium. The N atoms exist at low concentrations (~10^{-7} mol fraction) and a steady state approximation is valid for these species [14]. The reason for describing these reactions as 'thermal' is because the reactions involve breaking the strong triple bond of the N$_2$ molecule, which will only occur at high temperatures, for this reason reaction 74 is rate limiting and is so slow that NO does not achieve equilibrium concentrations [113].

An explicit expression may be derived for the changes in NO concentration, for the derivation, nitrogen atoms are assumed to be in steady state and the other species are assumed to be in equilibrium. For these conditions the formation rate for nitric oxide may be derived [14].

$$\frac{d[NO]}{dt} = \frac{2R_1(1-\beta^2)}{(1+\beta K)} \tag{77}$$

where the terms are:

$$R_1 = k_1^+[O]_e[N_2]_e = k_1^-[NO]_e[N]_e \tag{78}$$

$$R_2 = k_2^+[NO]_e[O_2]_e = k_2^-[NO]_e[O]_e \tag{79}$$

$$R_3 = k_3^+[N]_e[OH]_e = k_3^-[NO]_e[H]_e \tag{80}$$

$$\beta = \frac{[NO]_a}{[NO]_e} \tag{81}$$

$$K = \frac{R_1}{R_2 + R_3} \tag{82}$$

Where $[XX]_e$ is the equilibrium concentration for species XX, and $[NO]_a$ is the actual nitric oxide concentration. The use of equation 13 means that the rate coefficient of either the forward or the reverse reaction is sufficient and the steady state nitrogen atom is incorporated into the expression. The reaction coefficients used to calculate actual NO concentrations is shown in Table 7. Figure 89 shows the NO concentration as a function of time for five temperatures at 1000kPa and three equivalence ratios, the dashed lines representing the equilibrium NO concentrations for each given condition. As shown the NO concentration increases rapidly at first and then more slowly as it approaches its final equilibrium value. There is a significant influence of temperature and equivalence ratio where for a change in equivalence ratio from 0.9 to 1.1 at the highest temperature (2700K) equilibrium NO decreases almost 2.5 times. For the stoichiometric case, the highest temperature (2700K), NO has reached 90% of its equilibrium value in about 1.2ms. For the next temperature (2600K), 90% is reached in 2.6ms. For 2500K, 2400K and 2200K the time required to reach 90% of the equilibrium values are 6, 15.5 and >50ms. To put these into context the typical combustion duration of the AJ27 operating at MBT* over a range of loads and speeds is on average 62 ºCA which at 650, 1500 and 3000rpm is 16, 7 and 3.4ms. This means that within the time available for combustion NO concentration may not reach equilibrium, especially at the lower temperature periods and during the expansion stroke NO will be kinetically limited or 'frozen'.

The study of NO emissions using the Zeldovich mechanism is typically investigated using thermodynamic cycle simulations where pressure and temperature vary throughout the calculations, a crank based model [113 -117]. As has been shown to investigate the Zeldovich mechanism temperature and equilibrium species are required. A simple approach to investigate the trends exhibited by the generic function adopted here is to base the calculations on constant temperature, pressure and equilibrium species evaluated at the adiabatic flame temperature of the given mixture essentially a development of the results shown in Figure 89 (dependent on both the AFR and residual gas fraction). The adiabatic flame temperature and species equilibriums were determined from initial conditions of 1000kPa and a temperature of 700K. Figure 90 shows the EI_{NO} as a function of GFR, although in

this case GFR = AFR + 1, so there are no residuals in this calculation. The time required to reach equilibrium EI_{NO} for rich and stoichiometric cases is only 5ms, whereas for the lean cases, GFR >18.5 (AFR>17.5) equilibrium is reached after 16ms. The reason for this trend is the reduction in adiabatic flame temperature, once the temperature drops below 2350K the rate of formation of NO reduces significantly. The reduction in flame temperature when operating an engine at an AFR >17 primarily accounts for the reduction in NOx emissions, and although the adiabatic flame temperature continues to increase in the rich region the reduction in available oxygen reduces NO emissions as implied by the reduction in equilibrium NO. A major effect of burned gases is to increase the heat capacity of the charge, therefore reducing the adiabatic flame temperature at a given AFR as shown in Figure 91. An increase in the x_b from $0 - 25\%$ causes a reduction in adiabatic flame temperature from $2542 - 2175K$ at stoichiometric fuelling, the effect on EI_{NO} is shown in Figure 92. A comparison between the kinetic results (16ms) and the EI_{NO_x} generic function is shown in Figure 93. For rich and stoichiometric AFRs the generic function and the kinetic results produce very similar trends, for lean AFRs there is greater difference between the two, where the kinetic results suggest a greater reduction in EI_{NO} with increasing x_b. The comparison between the generic function and the model indicate that essentially the generic function can be described using the established extended Zeldovich mechanism for NO production.

8.6 Discussion and Summary

The form of all the generic functions has been investigated, with support from literature. CO is a principal species in the hydrocarbon oxidation process, the presence of which in the exhaust gases is a caused predominantly by slow precursor reactions when operating at stoichiometric conditions. When lean of stoichiometric the presence of CO is a result of partial oxidation of hydrocarbons being oxidised late in the expansion stroke, at rich conditions the CO is equivalent to equilibrium concentrations in the bulk burned gases near the end of expansion. HC emissions are caused by a variety of sources, the predominant source when the engine is operating

at stable combustion conditions are from the crevices. The generic function describing HC emissions has been broken down into 'normal' HC emissions caused by partial oxidation of HC during the combustion process. As the equivalence ratio is richened an additional source contributes to the overall measured HC level, bulk gas HC emissions are created and remain due to insufficient oxygen. As the mixture is weakened or diluted there is a rapid increase in HC emissions caused by longer/partial burning, or finally miss firing cycles, these sources are significantly greater than any of the others discussed. The NOx emissions generic function has been underpinned using the extensively researched thermal (extended Zeldovich) NO production mechanism. The combination of AFR and x_b effectively describes the changes in peak temperatures within the cylinder which is key in the NOx production.

<div align="right">

CHAPTER 9

</div>

Theoretical assessment of stability limits

9.1 Introduction

The investigations described in Chapter 6 raise questions about the role of burn parameters in the production of CCV. The results suggested that the cause of the CCVs could be attributed to variability in the $\Delta\theta_{0-10\%}$ which was magnified in the $\Delta\theta_{10-90\%}$. The data used to reach this conclusion was reasonably scattered. In this chapter, a theoretical approach is used to investigate the causes of CCVs. A finite heat release model is used to investigate the sensitivity of CCVs to variations in burn rate parameters.

9.2 Finite heat release model description

For a closed-system the differential energy equation per unit crank angle, assuming ideal gas behaviour is given by [14]:

$$\frac{dQ}{d\theta} - p\frac{dV}{d\theta} = \frac{c_v}{R}\left(p\frac{dV}{d\theta} + V\frac{dp}{d\theta} \right) \tag{83}$$

Rearranging for pressure, p,

$$\frac{dp}{d\theta} = -\gamma \frac{p}{V} \frac{dV}{d\theta} + \frac{\gamma - 1}{V} \left(\frac{dQ}{d\theta} \right) \tag{84}$$

The rate of heat release as a function of crank angle is obtained by differentiating the cumulative heat release and is given by:

$$\frac{dQ}{d\theta} = Q_s \frac{dx_b}{d\theta} \tag{85}$$

where Q_s is the total energy available at spark, determined from the mass of fuel, and fuel lower heating value. A typical cumulative heat release, burn fraction curve can be represented analytically by the Wiebe (although it is noted the correct spelling of the Wiebe is actually Vibe, as discussed in [118]) function:

$$x_b(\theta) = 1 - \exp\left[-a \left(\frac{\theta - \theta_s}{\theta_d} \right)^n \right] \tag{86}$$

where θ_d is the heat release duration (°CA), n is the Wiebe form factor and a is the Wiebe efficiency factor. Parameters a and n are adjustable and are used to fit experimental data, previous work has resulted with $a = 5$ and $n = 3$ [14]. θ_s, is the spark timing as set in the EMS, this differs from some research [119] whereby an ignition timing was preferred, with the ignition timing being established when the mass fraction burned was equal to one percent. The EMS spark timing is preferred since in spark ignition engines there is no such thing as an ignition delay, the flame starts to propagate outward immediately following the spark discharge. Previous experimental work [119] using a lean burn natural gas fuelled spark-ignition engine investigated the changes in n at different operating conditions with a fixed. A reasonable correlation between n and spark timing was established, whereby as the

spark timing was advanced n decreased indicating that as the spark timing was advanced the combustion rate increased. Changes in manifold pressure had no effect on the value of n. The spark timing correlation was only presented in absolute form, spark timing relative to the optimum, MBT* or MBT was not established. The influence of varying both a and n on the performance of a spark ignition engine has been investigated by Caton [120] using a thermodynamic cycle simulation. As a was increased it was shown that the start of combustion needed to be retarded to maintain maximum performance, a similar requirement was established when n was increased. Whereby parameters such as power and thermal efficiency increased modestly as a was increased from 3 to 7, with the effect of a small increase in n 1 to 3 resulting in a negligible increase.

9.3 Wiebe function investigation

The effect of changes in these parameters for a constant θ_d is shown in Figure 94. Increasing a results in an almost equal decrease in both the $\Delta\theta_{0-10\%}$ and the $\Delta\theta_{10-90\%}$ whereas increasing n results in only an increase in the $\Delta\theta_{0-10\%}$. The Wiebe function was fitted (minimising the sum of the square errors) to the measured mass fraction burn curves by manipulating both a and n. The sensitivity of a and n to different definitions of θ_d was investigated, whereby the θ_d was varied by adopting two different end of combustion locations, when x_b of the measured data equalled 90% and 99%. Figure 95 and Figure 96 indicate that values of a and n are insensitive to the two definitions of the θ_d, for this study 99% was used to indicate the end of combustion. The average correlation coefficient (R^2) between the measured and the fitted Wiebe function was >0.99, indicating an extremely good correlation and validating the applicability of using the function for this investigation. The influence of previously discussed parameters, namely relative spark timing and GFR on the values of a and n are shown in Figure 97a and b. At MBT* a is at a maximum value, this suggests that $\Delta\theta_{0-10\%}$ is at a minimum with MBT* spark timing, this is contrary to what the experimental data had shown previously, although the difference in the value of a would result in only a small

change in the $\Delta\theta_{0-10\%}$, approximately 1°CA. The trend for an increasing value of a with increasing GFR again is contrary to the experimental data, whereby it has been shown that as the GFR increases so does the $\Delta\theta_{0-10\%}$, as with the spark timing influence the magnitude of change in a results in only small change in the $\Delta\theta_{0-10\%}$. The effect on the $\Delta\theta_{10-90\%}$ as a increases is more consistent with those trends exhibited by the experimental data for changes in relative spark timing, whereby at MBT* the $\Delta\theta_{10-90\%}$ is at the shortest duration, with increasing duration as the spark timing is retarded. The proportional relationship between GFR and a is again contrary to the experimental data. This raises concerns as to the validity of using the Wiebe function for describing accurately the trends exhibited by the experimental data, yet as can be seen there is significant scatter about the trends established. The trends established for n reflect more those seen with the experimental data, as the spark timing is retarded from the optimum n reduces indicating a more rapid $\Delta\theta_{0-10\%}$, n also increases with GFR again this relationship was also apparent in the experimental data. It should also be noted that the experimental scatter is significantly less than that seen for a.

Although values of a and n can be adjusted to fit the experimental data, if the combustion duration is fixed as has been used here the value of a should also be fixed since

$$a = -\ln(1-0.99) = 4.6052 \tag{5}$$

The change in n as a function of relative spark timing and GFR is re-investigated with the value of a set to 4.6052, the results are shown in Figure 98. Fixing a changes the fitted values of n and more importantly the trend as GFR changes. Where previously as GFR had increased the value of n also increased which indicated an increase in the $\Delta\theta_{0-10\%}$ which was consistent with the experimental data, with a fixed the fitted values of n decrease, suggesting a decrease in $\Delta\theta_{0-10\%}$ with increasing GFR. The trend of a decrease in the value of n as the spark timing is retarded is maintained. It should be noted that the performance of the fit is

degraded, as would be expected when only n is being varied but the level of degradation is not significant, average R^2 changing reducing from 0.992 to 0.9969.

Generally the results suggest the Wiebe function is not ideal in modelling experimental burn data, particularly where the data covers a wide range of operating conditions and of relevance to this data set, the wide range of burn durations. Although it is not correct to vary both parameters, n and a, it has been shown that the results from this investigation provides values, particularly of n that are more representative of the trends shown by the experimental data. By varying a with a fixed duration, determined from the experimental data it is in effect introducing a method for varying the duration of the combustion. The range of fitted a values was between 3.454 and 8.301 which is equivalent to burn durations of 96.8% to 99.9%, this converts to no more than 6°CA increase in combustion duration, taking this into account it could be concluded that by varying a it allows errors in the experimentally derived burn rate to be accounted for.

9.4 Modelling methodology

A matrix of simulations was created adopting a single factorial approach. The parameters varied were a, n, θ_d and spark timing Table 8 shows the range of each parameter. The ranges encompassed values measured experimentally. Each simulation consisted of running the model 500 times while applying random variations to the mean value of each parameter, thus simulating CCV. The magnitude of the randomness was increased, for example all mean parameter values were fixed, including the variability of the parameter being investigated. Typically three runs were conducted, with the variability increasing for subsequent runs following the datum run, where typically the COV of the parameter resulted in variability that was consistent with stable engine operating conditions. Figure 99 provides an example of the output from the model, whereby the correlation between COV_{IMEP_g} and both $COV_{\Delta\theta_{0-10\%}}$ and $COV_{\Delta\theta_{10-90\%}}$ is shown. There is good correlation between $COV_{\Delta\theta_{0-10\%}}$ and COV_{IMEP_g}, as indicated by the R^2 value of 0.96,

interestingly the correlation between $COV_{\Delta\theta_{10-90\%}}$ and COV_{IMEP_g} is poor, suggesting CCV are particularly sensitive to variations in the $\Delta\theta_{0-10\%}$ and less so to those associated with the $\Delta\theta_{10-90\%}$. It should be noted though, that this is only an example of the output from the model and with a relatively fast total burn duration. To investigate the sensitivity of CCV to the varied parameters the results themselves were modelled using the MBC toolbox in MATLAB, the same tool that was used to model the cylinder residual gas fraction (see Chapter 3).

9.5 Modelling results

The key parameters, $COV_{\Delta\theta_{0-10\%}}$ and $COV_{\Delta\theta_{10-90\%}}$ were used as inputs to the model of COV_{IMEP_g}. The models created included only polynomial terms so as to establish the parameters that had the greatest influence on COV_{IMEP_g}. The polynomial order was also limited to a maximum of six since although increasing the order would improve the fit of the models to the data it would also mean establishing dominant factors would become increasingly difficult. The final restriction was to only model results that had $COV_{IMEP_g} > 5$, since values below this are within expected 'normal' operating variability. The results from the models using $COV_{\Delta\theta_{0-10\%}}$ and $COV_{\Delta\theta_{10-90\%}}$ as the only input factors did not provide satisfactory correlations as shown in Table 9. In an attempt to resolve the poor correlation an additional term was added. Along with $COV_{\Delta\theta_{0-10\%}}$ and $COV_{\Delta\theta_{10-90\%}}$, θ_d was added since typically increasing combustion variability is associated with increasing θ_d. Table 10 provides the new correlation coefficients with the additional input factor. In all cases the correlation coefficients have improved, although the 6th order model appears the best in terms of ability to model the trends a review of all models indicated the cubic model provided the most realistic trends.

The results of the model are presented in Figure 100. The modelled data presented is consistent with the measured results, whereby as the θ_d increases the effect of increasing $COV_{\Delta\theta_{10-90\%}}$ results in greater COV_{IMEP_g}. What the model does not reflect is a correlation between $COV_{\Delta\theta_{0-10\%}}$ and $COV_{\Delta\theta_{10-90\%}}$ that was suggested by the

measured data, in fact the model indicates maximum COV_{IMEP_g} with minimum $COV_{\Delta\theta_{0-10\%}}$. This is not fully unexpected, COV_{IMEP_g} is always going to be more sensitive to variations in $COV_{\Delta\theta_{10-90\%}}$ since it is over this burn duration that the largest proportion of $IMEP_g$ is produced. The investigation in this chapter has indicated that the model used here, or particularly the model used to simulate the burn profile does not have sufficient coupling between the $\Delta\theta_{0-10\%}$ and $\Delta\theta_{10-90\%}$. Importantly it also shows this kind of model is unlikely to provide sufficient detail to enable such a correlation to be found.

9.6 Discussion and Summary

A finite heat release model was used to investigate the correlations between $COV_{\Delta\theta_{0-10\%}}$ and $COV_{\Delta\theta_{10-90\%}}$ and COV_{IMEP_g}. An investigation of the Wiebe function indicated that by manipulating both a and n the function matched the measured data very well, although the trends developed for a did not generally support the experimental findings. The ability of such a simple function to predict the burn duration of such a wide range of operating conditions indicates the validity of using it for modelling purposes. The finite heat release model was used to investigate the effect of random variations in the burn rate. The results indicated that increasing variations in $COV_{\Delta\theta_{10-90\%}}$ lead to the greatest variations in COV_{IMEP_g}, there was no correlation with $COV_{\Delta\theta_{0-10\%}}$, to gain a reasonable such fit through the data θ_d was required. The results indicated that although such a model can be used to investigate influences on COV_{IMEP_g} the ability to understand causes of CCV and the propagation of early flame variations into later burn phases cannot be established. Work should be focused on flame surface imaging to understand better the transmission of early flame variability to later stages, this work along with a CFD based modelling approach could be used to better establish a link between variability in early flame development and whether that variation propagates and magnifies into the rapid burning phase.

CHAPTER 10

Discussions and Conclusions

10.1 Introduction

Accurate understanding of emissions and combustion variability over a wide range of operating conditions is key in understanding the robustness of the combustion system. Without this knowledge issues could arise with calibration and aftertreatment systems such as catalysts. A significant amount of research has been focused at understanding emissions and combustion variability. The knowledge of both has increased significantly with highly complex models providing detailed understanding of emissions formation and the combustion process. This research is key to providing a better understanding of both processes, but establishing stable operating limits and functions to describe emissions based on experimental engine data provides significant insight into the robustness of the combustion system.

This thesis focuses on developing and assessing stable operating limits for a typical modern PFI engine with variable intake valve timing and understanding the causes of unstable combustion. This work is presented alongside further developments of functions describing emissions across the entire operating envelope.

10.2 Discussion

The work in this thesis develops models to describe emissions across the entire engine operation and develops physical and chemical limits on stable combustion. Both investigations include further work to underpin the correlations based on theoretical approaches. The experimental work was carried out on a modern PFI SI engine with VVTi, the addition of VVTi was shown to have a significant influence

on the residual gas fraction. It was key to the investigation to establish accurate understanding of the residual gas fraction due to changes in valve overlap. This was achieved by the use of in cylinder gas sampling which provided the necessary information to calculate accurately the residual gas fraction. Although the in-cylinder sampling provides the most accurate method of determining the residual gas fraction NOx emissions have been shown to be highly sensitive to changes in residual gas fraction. Changes in NOx emissions could therefore be used in the future on engines with more complex valve timing/ phasing systems to indirectly calculate the residual gas fraction.

The determination of mass fraction burned profiles from experimental data was investigated thoroughly ensuring a robust method was adopted. The two commonly used methods Rassweiler and Withrow and the approach based on the first law of thermodynamics were evaluated. Both methods resulted in very similar initial burn periods but there was significant variations in the rapid burn period. In the current study, the Rassweiler and Withrow method was adopted. The differences found raises questions as to the ability to compare researchers results since variability in mass fraction burned will occur simply due to the calculation method.

Limits on stable combustion have been established that are defined using chemical terms namely AFR and GFR and relative spark timing. The GFR term takes into account variations in the residual gas fraction, which enables data to be collapsed on to a single characteristic. Although GFR is a robust parameter for standard gasoline operation an alternative parameter, TDP [6] has been shown to be applicable for different fuel operation since this parameter approximates the flame temperature of the mixture which GFR would not do. The widest range of stable operation occurs when spark timing is set to MBT* and although a slight reduction occurs as the spark timing is initially retarded a significant reduction occurs when the start timing is retarded by 20degs. During normal vehicle operation the engine is unlikely to be running at such significant spark retards due to the efficiency penalty associated with such spark timings. Times when this spark retard maybe used is during starting and the idle period post starting so as to achieve rapid catalyst light off times. The implication of the findings suggest care should be taken when using excessive spark retard since the potential for unstable combusting cycles to occur

increases significantly. The stable combustion island developed could be used as an initial go/ no go criteria for engine calibration since it will be generically similar for all port fuelled gasoline engines.

The limits on stable combustion was characterised using COV_{IMEP_g}, this parameter describes variations in work output from the engine. COV_{IMEP_g} only provides an understanding of variability in work output which is an integral parameter, it does not provide an understanding of the causes of the variation. Analysis of the burn rates and the key burn phases, the $\Delta\theta_{0-10\%}$ and the $\Delta\theta_{10-90\%}$ indicted that moving towards chemical stability limits resulted in increased variability and duration in both combustion phases. The variability in work output was manifested in the $\Delta\theta_{0-10\%}$ and magnified in the $\Delta\theta_{10-90\%}$. This is consistent with results presented by other researchers. It should be noted that although variations in the $\Delta\theta_{0-10\%}$ result in variations in $\Delta\theta_{10-90\%}$ it is the variations in the latter that directly influences the value of COV_{IMEP_g}. Moving towards the physical stability limit by retarding the spark timing resulted in a similar phenomenon as with the chemical limits, although the correlation between variability in $\Delta\theta_{0-10\%}$ and $\Delta\theta_{10-90\%}$ reduced as the spark timing was retarded. The reduced correlation is caused by the combustion being phased significantly into the exhaust stroke therefore increasing the susceptibility of the $\Delta\theta_{10-90\%}$ phase to partial burning which would not be reflected in the $\Delta\theta_{0-10\%}$.

Parameters affecting emissions were evaluated, CO and HC emissions could be described using equivalence ratio. The key to improving the accuracy of the HC emissions predictions was to add functions that take into account valve overlap and particularly unstable combustion. Increasing valve overlap was found to reduce HC emissions compared to the typical timings adopted, although this improved the predictive capability of the model, the key addition was to add HC contributions from unstable combustion. Over the NEDC drive cycle the additional unstable term was shown to result in significantly increased HC emissions during transient operation, essentially caused by the wide fluctuations in AFR/ GFR during the manoeuvres. NOx emissions were only influenced by AFR and x_b, there was no direct change in NOx emissions with valve timing. Theoretical evaluation of the

NOx function indicated the predictions were generally consistent with those from Zeldovich formation mechanism.

10.3 Further Work

Factors affecting emissions and combustion stability have been investigated in this thesis. Much of the work is experimental and although some theoretical assessments have been made more work could be conducted in this area. With increased focus on greater fuel economy and the use of different fuels to facilitate ultra lean combustion, research in this field with reference to the work presented here could be used to understand the benefits and limitations of different technologies.

Specific examples of areas that should be investigated further include:

- Comparisons of combustion stability of stratified SI combustion systems, does the combustion system exhibit the same characteristics in terms of how combustion stability degrades?

- Comparisons of combustion stability of direct injection compression ignition combustion systems, again can correlations and comparisons be made enabling more generic understanding of what limits stable combustion in all the reciprocating engine forms?

- The functions used to describe emissions for both NOx and CO were reasonable in the level of accuracy the predictions provided. HC emissions were more scattered. Further experimental work and modelling is recommended to be undertaken to understand the sources of variability. Operating the experimental engines on gaseous fuels would provide a good basis for removing some scatter from the data.

- The addition of unsteady combustion predictions in NuSIM could be coupled with an aftertreatment model to better understand the implications of unstable combustion events on catalyst efficiencies and therefore vehicle out emissions.

The experimental work presented here was conducted using an instrumented V8 engine. Although this engine was ideal for this work since it provided a production engine configuration further research work on both emissions and combustion benefit from utilising single cylinder engines. These provide a flexible tool for improving understanding and reducing experimental variability in terms of emissions and combustion measurements. Single cylinder engines can also be modified allowing optical access enabling an additional number of measurements to be taken facilitating better understanding of the combustion process.

10.4 Conclusions

Chapter 3 – Test facility and experimental variables

- AFR can be determined indirectly using sensors, such as UEGO or HEGO or directly from the air induced and fuel injected. For unstable combustion operating conditions significant errors in AFR occur from using the sensors.
- Increasing the VO by phasing the intake valve while the exhaust valve timing remains constant increases the x_r whereby the variables, in the order of greatest influence on x_r are MAP, VO and rpm.

Chapter 4 – Mass fraction burn determination

- Comparisons between the Rassweiler and Withrow approach and a heat release model including heat transfer and blowby terms to calculate the mass fraction burned profile indicated the rapid burn duration was greater using the heat release approach.
- The number of cycles required to establish variations in burn rates was 50 and 200 for stable and unstable operating conditions respectively.

Chapter 5 – Physical and chemical limits of stable operation

- Limits of stable combustion can be defined using GFR and AFR, whereby the rich limit is defined at a given AFR and lean limit at a constant GFR. A non linear function of AFR and GFR describes the stability limit between the rich and lean limit, where the most robust operating conditions are slightly rich of stoichiometric.

- Two different test methodologies were used to investigate the stability limits, both methods, constant air and fuel resulted in the same stability limits being establish. Indicating the parameters used are robust.
- The greatest range of stable combustion occurs at MBT* spark timing, a small decrease in the stable range occurs at dMBT*=10, where further spark retard, dMBT*=20 results in a significant reduction.
- COV_{IMEP_g} should be used for investigating combustion variability, significant variations in the pumping work causes COV_{IMEP_n} to not just reflect combustion variability.

Chapter 6 – The cause of stability limits

- The flame development time decreases to a minimum as the spark timing is retarded from MBT* (as the spark timing moves towards TDC), whereas the rapid burn time continuously increases.
- There is a reasonable correlation between the variability in the flame development time and rapid burn time, indicating cycle to cycle variability is predominantly caused in the flame development and magnified in the rapid burn time.

Chapter 7 – Emissions Characterisation

- CO emissions for both unstable and stable combusting conditions can be described as only a function of equivalence ratio.
- For stable combustion operation and typical valve timings and overlaps HC emissions can be described using only equivalence ratio. Additional functions are required to provide an accurate model of HC emissions, taking into account valve timing, relative spark timing and combustion stability.
- NOx emissions can be described using AFR, GFR and relative spark timing, no correction for unstable combustion conditions is required.
- Combustion efficiency traditionally described as a function of equivalence ratio is also a function of burned gas fraction whereby increasing burned gas fraction at a constant equivalence ratio reduces the combustion efficiency.

Chapter 8 – Emissions Generic Function Physical Underpinning

- HC emissions can be broken down into two sources, bulk and unstable combustion related. Under normal operation hydrocarbon emissions are predominantly caused by unburned fuel being trapped in the crevices. The greatest contribution though comes from unstable combustion.

- NOx emissions can be described using the extended Zeldovich thermal NOx mechanism the results are consistent with the NOx generic function developed.

Chapter 9 – Theoretical assessment of stability limits

- The Wiebe function can be used to accurately describe a wide range of experimental data including stable and unstable combusting operating conditions by manipulating both a and n.

- A theoretical assessment of the causes of COV_{IMEP_g} indicated $COV_{\Delta\theta_{0-10\%}}$, $COV_{\Delta\theta_{10-90\%}}$ and combustion duration are the key parameters. Where increasing $COV_{\Delta\theta_{10-90\%}}$ is the dominant factor in increasing COV_{IMEP_g}.

References

1. Colls, J, 'Air Pollution', E & FN Spon, 1997.

2. US Department of Energy: EERE (Energy Efficiency and Renewable Energy). http://www.eere.energy.gov/vehiclesandfuels/facts/2005/fcvt_fotw386.shtml accessed 9th of November 2005.

3. 'Directive 98/69/EC of the European Parliament and of the Council', Official Journal of the European Committees, October 1998.

4. Winborn L D, 'The Cold Operation of SI Engines and the Significance of Fuel Losses, Oil Dilution, and Mixture Gas/Fuel Ratio', PhD Thesis, University of Nottingham, 2001.

5. Lai W C, 'Valve Timing, Charge Dilution and Cycle-To-Cycle Stability of Work Output of a Spark Ignition Engine', PhD Thesis, University of Nottingham, 2004.

6. Tully E J, Heywood J B, 'Lean-Burn Characteristics of a Gasoline Engine Enriched with Hydrogen from a Plasmatron Fuel Reformer', SAE Paper 2003-01-0630, 2003.

7. Shayler P J, Chick J, Darnton N J, Eade D, 'Generic Functions for Fuel Consumption and Engine-out Emissions of HC,CO and NO_x of Spark-Ignition Engines', Proceedings of ImechE, Part D, Journal of Automobile Engineering, Vol 213, pp365-378, 1999.

8. Harbor N, 'The Development and Integration of Systems Models for the Simulation of V8 Engine Performance Attributes', PhD Thesis, University of Nottingham, 2004.

9. 'Directive 98/69/EC of the European Parliament and of the Council', Official Journal of the European Committees, October 1998.

10. Gupta V, 'The Modelling of Automotive Engines and Emissions Aftertreatment to Investigate Behaviour and Control', PhD Thesis, University of Nottingham, 2005.

11. Shiomoto G H, Sawyer R F and Kelly, 'Characterisation of the Lean Misfire Limit', SAE Paper 780235, 1978.

12. Brown A G, Stone C R and Beckwith P, 'Cycle-To-Cycle Variations in Spark Ignition Engine Combustion – Part I: Flame Speed and Combustion Measurements and a Simplified Turbulent Combustion Model, SAE Paper 960612, 1996.

13. Horie, K, et al, 'The Development of a High Fuel Economy and High Performance Four-Valve Lean Burn Engine', SAE Paper 920455, 1992.

14. Heywood J B, 'Internal Combustion Engine Fundamentals', McGraw-Hill, 1988.

15. Hillard J C and Springer G S, 'Fuel Economy in Road Vehicles Powered by Spark Ignition Engines', Plenum Press, New York & London, pp186, 1984.

16. Geiger J, Pischinger S, Bowing R, Kob H-J and Thiemann J, 'Ignition Systems for Highly Dilute Mixtures in SI-Engines', SAE Paper 1999-01-0799, 1999.

17. Goldwitz J A and Heywood J B, 'Combustion Optimization in a Hydrogen-Enhanced Lean Burn SI Engine', SAE Paper 2005-01-0251, 2005.

18. Hori T, Shibata M, Okabe S and Hashizume K, 'Super Ignition Spark Plug with Fine Centre & Ground Electrodes', SAE Paper 2003-01-0404, 2003.

19. Rivin B, Dulger M and Sher E, 'Extending Lean Misfire Limit of Methane-Air Mixtures by Means of an Enhanced Spark Discharge', SAE Paper 1999-01-0573, 1999.

20. Gillespie L, Lawes M, Sheppard C G W and Woolley R, 'Aspects of Laminar and Turbulent Burning Velocity Relevant to SI Engines', SAE Paper 2000-01-0192, 2000.

21. Inoue T, Matsushita S, Nakanishi K and Okano H, 'Toyota Lean Combustion System – The Third Generation System', SAE Paper 930873, 1993.

22. Johansson B and Soderberg F, 'The Effect of Valve Strategy on In-Cylinder Flow and Combustion', SAE Paper 960582, 1996.

23. Arcoumanis C, Bae C S and Hu Z, 'Flow and Combustion in a Four-Valve, Spark-Ignition Optical Engine', SAE Paper 940475, 1994.

24. Hires S D, Tabaczynski R J and Novak J M, 'The Prediction of Ignition Delay and Combustion Intervals for a Homogeneous Charge Spark Ignition Engine', SAE Paper 780232, 1978.

25. Young M B, 'Cyclic Dispersion – Some Quantitative Cause-and-Effect Relationships', SAE Paper 800459, 1980.

26. Hacohen J, Belmont M R and Ashcroft S J, 'Flame Speed in a Spark Ignition Engine', SAE Paper 942050, 1994.

27. Matekunas F A, 'Modes and Measures of Cyclic Combustion Variability', SAE Paper 830337, 1983.

28. Russ S, Lavoie G and Dai W, 'SI Engine Operation with Retarded Ignition: Part 1 – Cyclic Variations', SAE Paper 1999-01-3506, 1999.

29. Rousseau S, Lemoult B and Tazerout M, 'Combustion characterisation of Natural Gas in a Lean Burn-Ignition Engine', Proceedings of ImechE, Part D, Journal of Automobile Engineering, Vol. 213, pp481-489, 1999.

30. Johansson B, 'Influence of the Velocity near the Spark Plug on Early Flame Development', SAE Paper 930481, 1993.

31. Holmstrom Karin and Denbratt I, 'Cyclic Variations in an SI Engine Due to the Random Motion of the Flame Kernel', SAE Paper 961152, 1996.

32. Bradley D, Lawes M and Sheppard C G W, 'Combustion and the Thermodynamic Performance of Spark Ignition Engines', Proceedings of ImechE, Part C, Journal of Mechanical Engineering Science, Vol. 214, pp257-268, 2000.

33. Gatowski J A, Heywood J B and DeLeplace C, 'Flame Photographs in a Spark-Ignition Engine', Combustion and Flame, Vol. 56, pp.71-81, 1984.

34. Kuroda H, Nakajima Y, Sugihara K, Takagi Y and Muranaka S, 'The Fast Burn with Heavy EGR, New Approach for Low NO_x and improved Fuel Economy', SAE Paper 780006, 1978.

35. Harrington J, 'A Study of Carburation Effects on Power Emissions Lean Misfire Limit & EGR Tolerance of a Single Cylinder Engine', SAE Paper 760754, 1976.

36. Shiomoto G H, Sawyer R F and Kelly, 'Characterisation of the Lean Misfire Limit', SAE Paper 780235, 1978.

37. Quader A A, 'Lean Combustion & The Misfire Limit in Spark Ignition Engines, SAE Paper 741055, 1974.

38. Ryan T W, Lestz S S and Meyer W E, 'Extension of the Lean Misfire Limit and Reduction of Exhaust Emissions of an SI Engine by Modification of the Ignition and Intake System', SAE Paper 740105, 1974.

39. Hill M J, 'The Limits and Control of Mixture Leaness for Stable Engine Operation', PhD Thesis, University of Nottingham, 2001.

40. Ozdor N, Dulger M and Sher E, 'Cyclic Variability in Spark Ignition Engines: A Literature Survey', SAE Paper 940987, 1994.

41. Asmus T W, 'Fuel Economy in Road Vehicles Powered by Spark Ignition Engines', Plenum Press, 1984, pp149-181, Editors Hillard J C and Springer G S.

42. Moriya Y, Watanabe A, Uda H, Kawamura H, Yoshioka M and Adachi, M, 'A Newley Developed Intelligent Variable Valve Timing System – Continuously Controlled Cam Phasing as Applied to a New 3 Litre Inline 6 Engine', SAE Paper 960579, 1996.

43. Leone T G, Christenson E J and Stein R A, 'Comparison of Variable Camshaft Timing Strategies at Part Load', SAE Paper 960584, 1996.

44. Duckworth R F and Barker, L, 'A Comparative Study of Variable Camshaft Phasing and Port Throttling for Performance and Emissions', SAE Paper 960580, 1996.

45. Nagumo S and Hara S, 'Study of Fuel Economy Improvement Through Control of Intake Valve Closing Timing: Cause of Combustion Deterioration and Improvement', JSAE9439311, 1995.

46. Szczupak D, Brunson D, Carling J, Cooke J, Joyce M, Massey N and White C, 'The Jaguar AJ V8 Engine', SAE paper 970914, 1997.

47. Signal Group, 'MaxSys 900 System Data Manual', Issue 1.0, 1999.

48. Rai H S, Brunt M F J and Loader C P, 'Quantification and Reduction of IMEP Errors Resulting from Pressure Transducer Thermal Shock in an S.I. Engine', SAE Paper 1999-01-1329, 1999.

49. Brunt M F J and Emtage A L, 'Evaluation of IMEP Routines and Analysis Errors', SAE Paper 960609, 1996.

50. Nilsson Y and Eriksson L, 'Determining TDC Position Using Symmetry and Other Methods', SAE Paper 2004-01-1458, 2004.

51. Spindt R S, 'Air-Fuel Ratios from Exhaust Gas Analysis', SAE Paper 650494, 1965.

52. Fukui T, Tamura Y, Omori S and Saitoh S, 'Accuracy of A/F Calculation from Exhaust Gas Composition of SI Engine', SAE Paper 891971, 1989.

53. Uyehara O, 'A Method to Estimate H_2 in Engine Exhaust and Factors that Affect NO_x and Particulates in Diesel Engine Exhaust, SAE Paper 910732, 1991.

54. Urban C M and Sharp C A, 'Computing Air/Fuel Ratio from Exhaust Composition', ASME, Natural Gas and Alternative Fuels for Engines, ICE - Vol. 24, 1994.

55. Lynch D and Smith W, 'Comparison of AFR Calculation Methods Using Gas Analysis and Mass Flow Measurement', SAE Paper 971013, 1997.

56. SAE Recommended Practice, 'Instrumentation and Techniques for Exhaust Gas Emissions Measurement', SAE J254, 1984.

57. Horiba Ltd., 'A/F Analyser MEXA-700λ Instruction Manual', 2000.

58. Bosch, 'Gasoline-Engine Management', 2nd Edition, Professional Engineering Publishing Limited, UK, 2004.

59. Toda T, Nohira H and Kobashi K, 'Evaluation of Burned Gas Ratio (BGR) as a Predominant Factor to NOx', SAE Paper 760765, 1976.

60. Fallahzadeh F, Subranhmanyam J P and Babu M K G, 'A Variable Valve Timing Engine for the Improvement in Engine Performance and Emission Characteristics', SAE Paper 2000-01-1414, 2000.

61. Schirm E, De Jesus G A R and Valle R M, 'Performance Controlling of Spark Ignition Engine by the Variation of the Intake Valve Opening Angle', SAE Paper 2003-01-3720, 2003.

62. Alger L, 'The Advantages and Control of Variable Valve Timing Under Part-Load Operating Conditions', PhD Thesis, University of Nottingham, 2005.

63. Fox J W, Cheng W K and Heywood J B, 'A Model for Predicting Residual Gas Fraction in Spark-Ignition Engines', SAE Paper 931025, 1993.

64. Asmus T W, 'Valve Events and Engine Operation', SAE Paper 820749, 1982.

65. Shelby M H, Stein R A, Warren C C, 'A New Analysis Method for Accurate Accounting of IC Engine Pumping Work and Indicated Work', SAE Paper 2004-01-1262, 2004.

66. Shayler P J, Winborn L D and Hill M J, 'The Influence of Gas / Fuel Ratio on Combustion Stability and Misfire Limits of Spark Ignition Engine', SAE Paper 2000-01-1208, 2000.

67. Rassweiler G M and Withrow L, 'Motion Pictures of Engine Flame Propagation Model of SI Engines', SAE Journal (Trans.), Vol.42, pp185-204, 1938.

68. Shayler P J, Wiseman M W and Ma T, 'Improving the Determination of Mass Fraction Burnt', SAE Paper 900351, 1990.

69. Brunt M F J, and Emtage, A, 'Evaluation of Burn Rate Routines and Analysis Errors', SAE Paper 970037, 1997.

70. Brunt M F J, and Pond, C R, 'Evaluation of Techniques for Absolute Cylinder Pressure Correction', SAE Paper 970036, 1997.

71. Svehla, R A, and McBride, B J, 'Fortran IV Computer Program for Calculating of Thermodynamic and Transport Properties of Complex Chemical Systems', NASA Technical Note TND-7056, NASA Lewis Research Centre, 1973.

72. Cheng W K, Hamrin D, Heywood J B, Hochgreb S, Min K and Norris M, 'An Overview of Hydrocarbon Emissions Mechanisms in Spark-Ignition Engines', SAE Paper 932708, 1993.

73. Woschni G, 'A Universally Applicable Equation for Instantaneous Heat Transfer Coefficient in the Internal Combustion Engine', SAE Paper 670931, 1967.

74. Shayler P J, May S A and Ma T, 'Heat Transfer to the Combustion Chamber Walls in Spark Ignition Engines', SAE Paper 950686, 1995.

75. Cheung H M and Heywood J B, 'Evaluation of a One-Zone Burn-Rate Analysis Procedure Using Production SI Engine Pressure Data', SAE Paper 932749, 1993.

76. Irving R J, 'Applications of Cylinder Pressure Transducers as Low Cost Sensors for Diesel Engines', PhD Thesis, The University of Nottingham, 2008.

77. Pugh G J, 'The Analysis of Hest Release in the Investigation of Split-Main Fuel Injection in a Diesel Engine', PhD Thesis, The University of Nottingham, 2004.

78. Rhodes D B and Keck J C, 'Laminar Burning Speed Measurements of Indolene-Air-Dilutent Mixtures at High Pressures and Temperatures' SAE Paper 850047, 1985.

79. Stone, C R, Brown A G, and Beckwith P, 'Cycle-by-Cycle Variations in Spark Ignition Engine Combustion – Part II: Modelling of Flame Kernel Displacements as a Cause of Cycle-by-Cycle Variations, SAE Paper 960613, 1996.

80. Merdjani S, and Sheppard C G W, 'Gasoline Engine Cycle Simulation Using the Leeds Turbulent Burning Velocity Correlations', SAE Paper 932640, 1993.

81. Elsom D M, 'Atmospheric Pollution: A Global Problem', Blackwell, 1992.

82. Horn G, 'The Prediction of Fuel Economy and Pollutant Emissions to Assess the Benefits of Direct Injection Gasoline Engines', PhD Thesis, University of Nottingham, 2002.

83. Siewert R M, 'How Individual Valve Timing Events Affect Exhaust Emissions', SAE Paper 710609, 1971

84. Ferguson C R, Kirkpatrick A T, 'Internal Combustion Engines', 2nd Edition, John Wiley & Sons, Inc., 2001.

85. Seabrook J, Nightingale C, Richardson S H, 'The Effect of Variables on Hydrocarbon Emissions - An Investigation with Statistical Experiment Design and Fast Response FID Measurements', SAE Paper 961951, 1996.

86. Shayler P J, and Chick J, 'A Method of Predicting Brake Specific Fuel Consumption Maps', SAE Paper 1999-01-0556, 1999.

87. Svehla, R A, and McBride, B J, 'Fortran IV Computer Program for Calculating of Thermodynamic and Transport Properties of Complex Chemical Systems', NASA Technical Note TND-7056, NASA Lewis Research Centre, 1973.

88. Olikara, C, and Borman G L, 'A Computer Program for Calculating Properties of Equilibrium Combustion Products with Some Applications to I.C. Engines', SAE Paper 750468, 1975.

89. Newhall H K, 'Kinetics of Engine-Generated Nitrogen Oxides and Carbon Monoxide', Twelfth Symposium on Combustion, pp603-613, 1969.

90. Lavoie G A, 'Spectroscopic Measurement of Nitric Oxide in Spark Ignition Engines', Combustion and Flame, Vol. 15, pp97-108, 1970.

91. Johnson G L, Caretto L S, and Starkman, E S, 'The Kinetics of CO Oxidation in Reciprocating Engines', paper presented at the Western States Section, The Combustion Institute, Spring Meeting, April 1970.

92. Lee G R and Morley C, 'Chemical Modelling of Hydrocarbon Exhaust Emissions', SAE Paper 941958, 1994.

93. Linna J-R, Malberg H, Bennet P J, Palmer P J, Tian T and Cheng W K, 'Contribution of Oil Layer Mechanism to the Hydrocarbon Emissions from Spark-Ignition Engines', SAE Paper 972892, 1997.

94. Haidar H A and Heywood J B, 'Combustion Chamber Deposit Effects on Hydrocarbon Emissions from a Spark-Ignition Engine', SAE Paper 972887.

95. Kalghatgi G T, 'Effects on Combustion Chamber Deposits, Compression Ratio and Combustion Chamber Design on Power and Emissions in Spark-Ignition Engines', SAE Paper 972886, 1997.

96. Landsberg G B, Heywood J B and Cheng W K, 'Contribution of Liquid Fuel to Hydrocarbon Emissions in Spark Ignition Engines', SAE Paper 2002-02-3587.

97. Stanglmaier R H, Li J and Matthews R D, 'The Effects of In-Cylinder Wall Wetting Location on the HC Emissions from SI Engines', SAE Paper 199-01-0502.

98. Meyer R and Heywood J B, 'Effect of Engine and Fuel Variables on Liquid Fuel Transport into the Cylinder in Port-Injected SI Engines', SAE Paper 1999-01-0563.

99. LoRusso J A, Kaiser E W and Lavoie G A, 'In-Cylinder Measurements of Wall Layer Hydrocarbons in a Spark Ignited Engine', Combustion Science and Technology, Vol. 33, pp75-112, 1983.

100. Min K, Cheng W K and Heywood J B, 'The Effects of Crevices on the Engine-Out Hydrocarbon Emissions in SI Engines', SAE Paper 940306, 1994.

101. Sodre J R and Yates D A, 'An Improved Model for Spark Ignition Engine Exhaust Hydrocarbons', SAE Paper 971011, 1997.

102. Bignion E and Spicher U, 'Investigation of the Influence of Top Land Crevice Geometry on Hydrocarbon Emissions from SI Engine', SAE Paper 982560, 1998.

103. Bian X, Prabhu S K, Yang W, Miller D L and Cernansky N P, 'Tracer Fuel Injection Studies on Exhaust Port Hydrocarbon Oxidation', SAE Paper 982559, 1998.

104. Wu K-C and Hochgreb S, 'Numerical Simulation of Post-Flame Oxidation of Hydrocarbons in Spark Ignition Engines', SAE Paper 970886, 1997.

105. Eng J A, Leppard W R, Najt P M and Dryer F L, 'Experimental Hydrocarbon Consumption Rate Correlations from a Spark Ignition Engine', SAE Paper 972888, 1998.

106. Eng J A, Leppard W R, Najt P M and Dryer F L, 'The Interaction Between Nitric Oxide and Hydrocarbon Oxidation Chemistry in a Spark Ignition Engine', SAE Paper 972889, 1997.

107. Wu K-C, Hochgreb S and Norris M G, 'Chemical Kinetic Modelling of Exhaust Hydrocarbon Oxidation', Combustion and Flame, Vol.25, pp193-201, 1994.

108. Drobot K, Cheng W K, Trinker F H, Kaiser E W, Siegel W O, Cotton D F and Underwood J, 'Hydrocarbon Oxidation in the Exhaust Port and Runner of a Spark Ignition Engine', Combustion and Flame, Vol.25, pp422-430, 1994.

109. Norris M G and Hochgreb S, 'Extent of Oxidation of Hydrocarbons Desorbing from the Lubricant Oil in Spark Ignition Engines', SAE Paper 960069, 1996.

110. Caton J A, Heywood J B and Mendillo J V, 'Hydrocarbon Oxidation in a Spark Ignition Engine Exhaust Port', Combustion Science and Technology, Vol.37, pp153-169, 1984.

111. Quader A A, 'Why Intake Charge Dilution Decreases Nitric Oxide Emission from Spark Ignition Engines', SAE Paper 710009, 1971.

112. Benson J D and Stebar R F, 'Effects of Charge Dilution on Nitric Oxide Emission from a Single-Cylinder Engine', SAE Paper 710008, 1971.

113. Caton J A, 'Detailed Results for Nitric Oxide Emissions as Determined from a Multiple-Zone Cycle Simulation for a Spark-Ignition Engine', ASME, ICE-Vol. 39, ICEF2002-491, 2002.

114. Dean A M and Bozzelli, 'Combustion Chemistry of Nitrogen', in Gas-Phase Combustion Chemistry, ed. W C Gardiner, Jr., pp. 361-422, Springer-Verlag, 2000.

115. Rublewski M and Heywood J B, 'Modelling NO Formation in Spark Ignition Engines with a Layered Adiabatic Core and Combustion Inefficiency Routine', SAE Paper 2001-01-1011, 2001.

116. Miller R, Russ S, Weaver C, Kaiser E, Newman C, Davis G and Lavoie G, 'Comparison of Analytically and Experimentally Obtained Residual Fractions and NOx Emissions in Spark-Ignited Engines', SAE Paper 982562, 1998.

117. Miller R, Davis G, Lavoie C, Newman C and Gardner T, 'A Super-Extended Zel'dovich Mechanism for NOx Modelling and Engine Calibration', SAE Paper 980781, 1998.

118. Oppenheim, A K, and Kuhl, A L, 'Life of Fuel in Engine Cylinder', SAE Paper 980780, 1998.

119. Rousseau, S, Lemoult, B and Tazerout, M, 'Combustion Characterisation of Natural Gas in a Lean Burn Spark-Ignition Engine', Proceedings of ImechE, Part D, Journal of Automobile Engineering, Vol 213, pp481-489, 1999.

120. Caton, J A, 'The Effect of Burn Rate Parameters on The Operating Attributes of a Spark-Ignition Engine As Determined From The Second Law of Thermodynamics', 2000 Spring Engine Technology Conference of the ASME-ICED, 2000.

Tables

Jaguar V8 AJ27		
Cylinder arrangement	90 Degree, V8	
Displacement	3.996	litres
Bore		mm
Stroke		mm
Combustion chamber	Pent roof	-
Valve mechanism	DOHC 4 valve	-
Inlet valve diameter	35	mm
Inlet valve timing	IVO -15 to 32	^{o}CA BTDC
	IVC 65 to 18	^{o}CA ABDC
Inlet valve opening duration	230	^{o}CA
Exhaust valve diameter	29	mm
Exhaust valve timing	EVO 40	^{o}CA BBDC
	EVC 10	^{o}CA ATDC
Exhaust valve opening duration	230	^{o}CA
Block height	225	mm
Bore spacing	98	mm
Bank offset	18	mm
Compression ratio	10.75	-
Crank main bearing diameter	62	mm
Crank pin diameter	56	mm
Connecting rod length	151.75	mm
Peak power [DIN]	216 kW @ 6100 Rpm	-
Peak torque [DIN]	393 Nm @ 4250 Rpm	-
Weight	200	kg
Length	570	mm
Width	680	mm
Height	680	mm

Table 1
Engine specifications of the Jaguar V8 AJ27.

Property	Units	Quality requirements		Test method
		Minimum	**Maximum**	
Density @ 15°C	kg/m³	720	775	BS EN ISO 3675
				BS EN ISO 12185
Octane (RON)		95		BS EN25164: 1993
Octane (MON)		85		BS EN25163: 1993
Sulphur content	mg/kg		50	BS EN ISO 14596
Lead content	g/l		0.005	BS EN 237
Aromatics content	%V/V		35	BS 2000: 156
Olefins content	%V/V		18	BS 2000: 156
Benzene	%V/V		1	BS EN 12177
Ethers content	%V/V		10	BS EN 1601
Other oxygenates	%V/V		0.5	BS EN 1601
Oxygen content	%m/m		2.7	BS EN 1601
The product contains a multifunctional detergent gasoline additive				

Table 2
Specification and species components of the unleaded 'pump' gasoline.

	Variable	Description and location	Transducer type	Unit
	Engine Speed		Hohner optical shaft encoder	rpm
	Torque	-	(SP 10033)	Nm
	AFR bank A		Horiba MEXA-700□	-
	AFR bank B	-		-
	Inlet Manifold Pressure		Kulite PT2028-0X8-2	bar
	Exhaust Manifold Pressure	-		bar
Temperatures	T1	Ambient temperature		oC
	T2	Inlet coolant temperature		oC
	T3	Outlet coolant temperature		oC
	T4	Oil sump temperature		oC
	T5	Inlet manifold air temperature		oC
	T6	Bank B, manifold exhaust gas temperature by exhaust port for cylinder 2		oC
	T7	Bank B, manifold exhaust gas temperature by exhaust port for cylinder 4		oC
	T8	Bank A, manifold exhaust gas temperature by exhaust port cylinder 2	K type thermocouple	oC
	T9	Bank B, pre catalyst exhaust gas temperature		oC
	T10	Bank B, post catalyst exhaust gas temperature		oC
	T11	Bank B, tail pipe exhaust gas temperature		oC
	T12	Bank B exhaust manifold metal temperature		oC
	T13	Bank B, pre catalyst metal temperature		oC
	T14	Bank B, post catalyst metal temperature		oC
	T15	Bank B, tailpipe metal temperature		oC
Emissions	Nitrogen Oxides		4000 VM NOx	ppm
	Hydrocarbon (C3)		3000 HM THC	ppm
	Carbon monoxide	Engine feed gas or post catalyst emissions	7100 FM CO	%
	Carbon dioxide		7200 FM CO2	%
	Oxygen		8000 M O2	%

Table 3
Variables logged during time based data acquisition, including a summary of location and manufacturer of all relevant instrumentation.

Original functions as presented in [7] - Series 1	
CO	$EI_{CO} = fn1(\phi)$
HC	$EI_{HC} = GFR.fn2_a(\phi).fn4(\theta_{dMBT*})$
NOx	$EI_{NOx} = fn7(AFR, x_b).fn8(\theta_{dMBT*})$
Altered functions applied to Jaguar V8 4l - Series 2	
CO	$EI_{CO} = fn1(\phi)$
HC, COV_{IMEPn}<4	$EI_{HC} = fn2_b(\phi).fn3(VO).fn4(\theta_{dMBT*})$
HC, COV_{IMEPn}>4	$EI_{HC} = fn2_b(\phi) + fn7(COV_{IMEPn})$
NOx	$EI_{NOx} = fn8((AFR, x_b).C_{NOx}).fn9(\theta_{dMBT*})$

Engine	Correction factors for Series 2
	C_{NOx}
Jaguar V8 4l	0.52

Table 4
Generic functions used to characterise the emissions indices for conventional PFI engines.

	GENERIC EQUATION
CO	$\phi < 1$ $fn1_a(\phi) = \exp(a + b\phi^2)$ $fn1_b(\phi) = \exp(a + b\phi^2) + c$ * $\phi \geq 1$ $fn1_c(\phi) = a + b\phi$
HC **COV$_{IMEPn}$<4**	$fn2_{a\&b}(\phi) = a + b\phi + \dfrac{c}{\phi^2}$
	$fn3(VO) = a + b.VO + c.VO^2$
	$\theta_{DMBT} \leq 0$ $fn4_a(\theta_{DMBT}) = 1$ $\theta_{DMBT} > 0$ $fn4_b(\theta_{DMBT}) = 1 + fn5(\phi)\,fn6(EGR).\theta_{DMBT}^2$
	$fn5(\phi) = a + \dfrac{b}{\phi} + c\phi^2$
	$fn6(EGR) = a + b.EGR + c.EGR^2$
HC **COV$_{IMEPn}$>4**	$fn2_{a\&b}(\phi) + fn7(COV_{IMEPn})$
	$fn7(COV_{IMEPn}) = a * COV_{IMEPn} + b$
NO$_X$	$fn8(AFR, x_b) = \left(\dfrac{a + c.AFR + e.AFR^2}{1 + b.AFR + d.AFR^2} \right) \exp\left(\dfrac{-x_b}{x \text{ or } y} \right)$ $\begin{matrix} x=0.13 \\ y=0.11 \end{matrix}$
	$\theta_{DMBT} < 20$ $fn9(\theta_{DMBT}) = a + b.\theta_{DMBT} + c.\theta_{DMBT}^2$ $\theta_{DMBT} > 20$ $fn9(\theta_{DMBT}) = 0.12$

 *

Altered function as used by Horn [82] and on the AJ27 engine. x is the original value for fn7, y is the altered value fitted to AJ27 engine.

Table 5 Functional form of the generic equations.

	a	b	c	d	e
$fn1_a(\phi)$	-8.395	5.5181			
$fn1_b(\phi)$	-2.725	2.78	0.015		
$fn1_c(\phi)$	-2.725	2.78			
$fn2_a(\phi)$	-0.00484	0.004326	0.0013313		
$fn2_b(\phi)$	-0.07083	0.062996	0.0232		
$fn3(VO)$	1.072	-0.00299	-0.000127		
$fn4_a(\theta_{DMBT})$					
$fn4_b(\theta_{DMBT})$					
$fn5(\phi)$	-0.00326	2.134e-4	0.0016489		
$fn6(EGR)$	1	-0.016643	-0.002866		
$fn7(COV_{IMEPn})$	0.1266	0.6728			
$fn8(AFR, x_b)$	-0.00326	-0.12489	-7.41e-5	0.004	4.072e-5
$fn9(\theta_{DMBT})$	1	-0.021	-0.00051		
$fn9(\theta_{DMBT})^*$	1	-0.0505	0.00041		

* *Function remains in the same form but the constants were altered so as to predict experimental results more accurately (Jaguar V 8 4l only).*

Table 6
Values of required constants used in the generic equations.

Dean and Bozzelli [114]	Reaction	Rate Constant as Listed in the Reference (cc/gmol-s)
	$O + N_2 \rightarrow NO + N$	$1.95 \times 10^{14} \exp(-38660/T)$
	$N + O_2 \rightarrow NO + O$	$9.0 \times 10^{09} T \exp(-3270/T)$
	$N + OH \rightarrow NO + H$	$1.1 \times 10^{14} \exp(-565/T)$

Table 7
The reaction coefficients used to calculate actual NO concentrations.

Spark	a	n	θ_d
120, 130, 140, 150, 160, 170, 180	9.3, 6.4 3.5	6.5, 4.7, 3.0	40, 75, 110

Table 8
Range of parameters used to investigate the sensitivity of CCV.

Model type	R^2 value
Linear	0.2284
Squared	0.2795
Cubic	0.2840
Poly_4	0.2932
Poly_5	0.2977
Poly_6	0.2996

Table 9
Change in R^2 correlation coefficient as the model order is increased.

Model type	R^2 value
Linear	0.4376
Squared	0.5292
Cubic	0.5943
Poly_4	0.6221
Poly_5	0.6411
Poly_6	0.6784

Table 10
Change in R^2 correlation coefficient as the model order is increased, model input factors $COVx_b10$, $COVx_brap$ and θ_d.
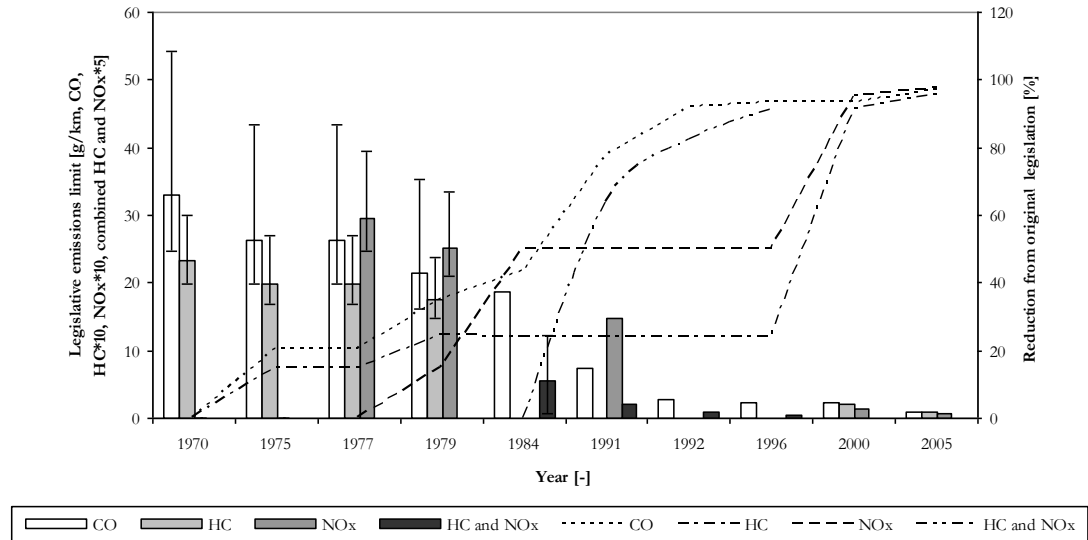
Figures

Figure 1
Change in legislative emissions from inception to current situation [3].
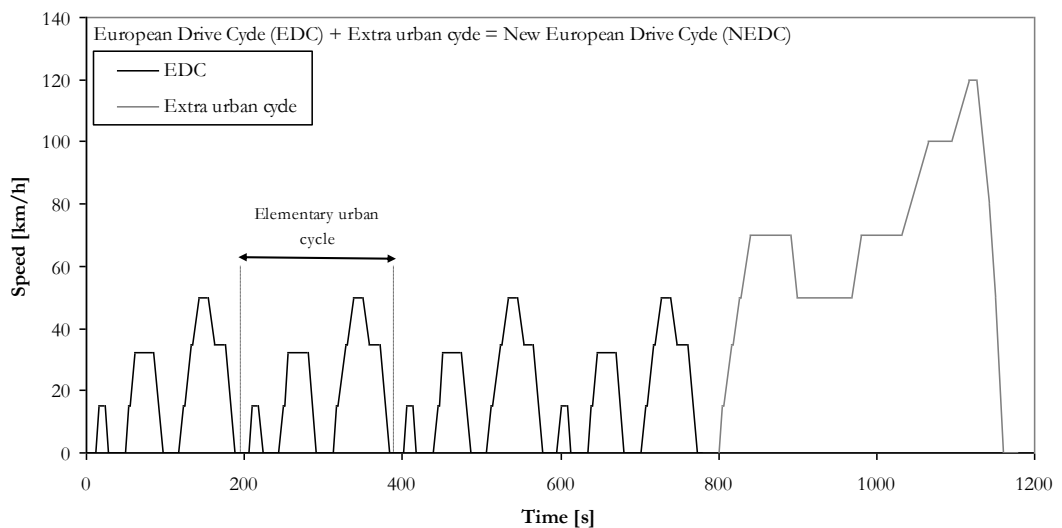
Figure 2
European legislative drive cycle.
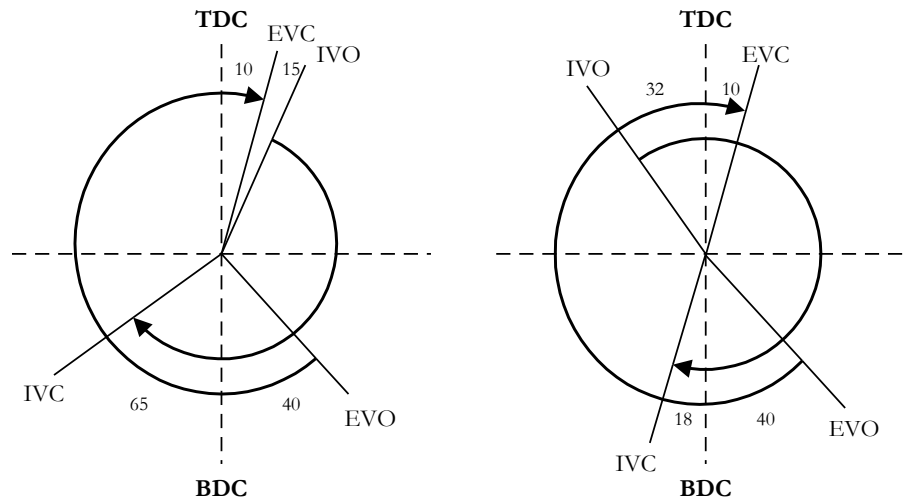
Figure 3
Minimum and maximum intake cam settings showing the associated intake valve timing changes.
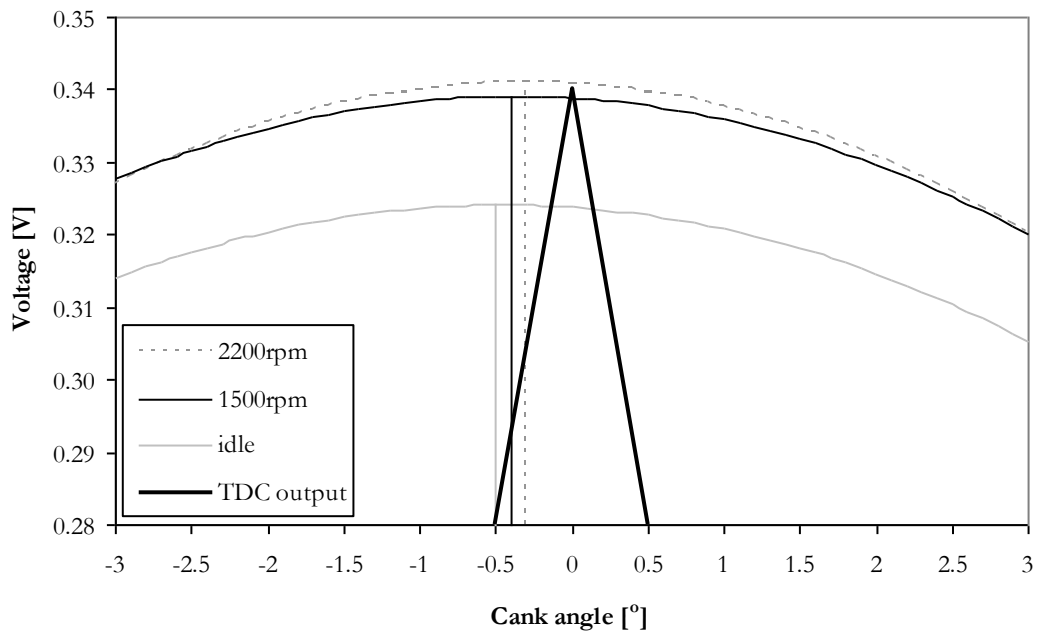
Figure 4
Comparison of the output of the AVL 428 capacitance probe and the shaft encoder TDC position, the standard deviation of TDC position over the speed range is ±0.1ºCA, with an average offset from the shaft encoder TDC of ±0.4ºCA.
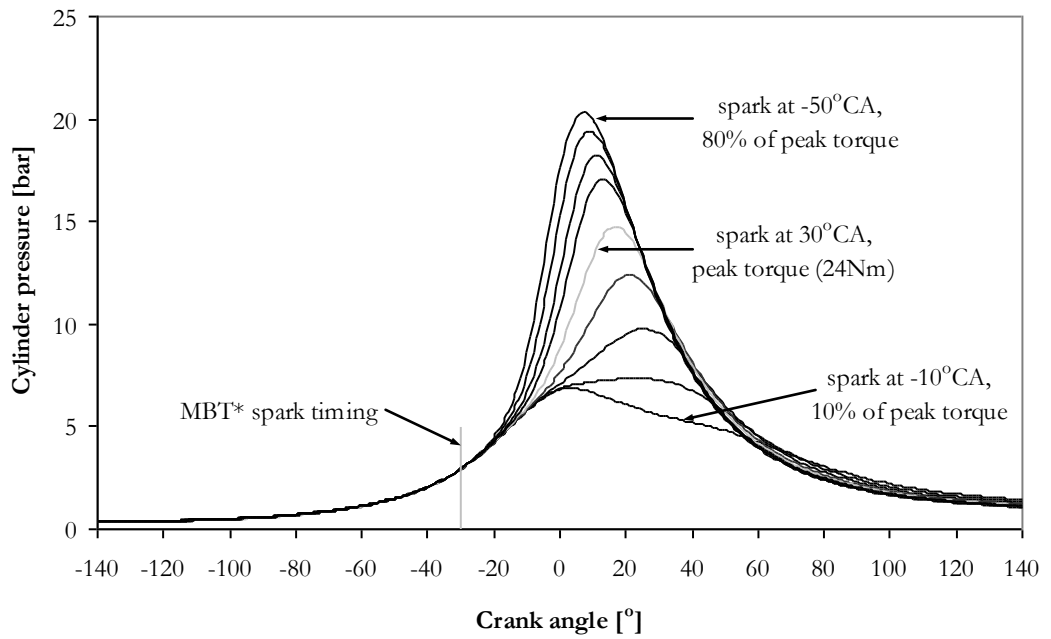
Figure 5
In cylinder pressure traces (ensemble averaged from 500 cycles at each spark timing). AJ27 operating at 1500rpm, light load, AFR = 14.6.
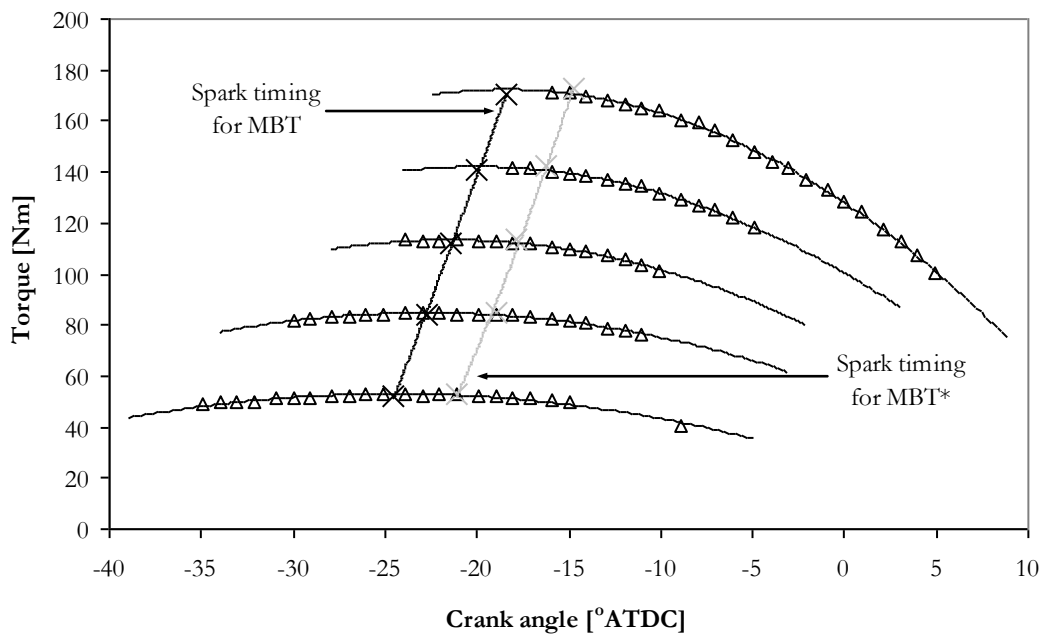
Figure 6
Change in brake torque with spark advance at 5 loads (0.41, 0.50, 0.57, 0.65 and 0.74 bar inlet manifold pressure) all at 1500rpm.
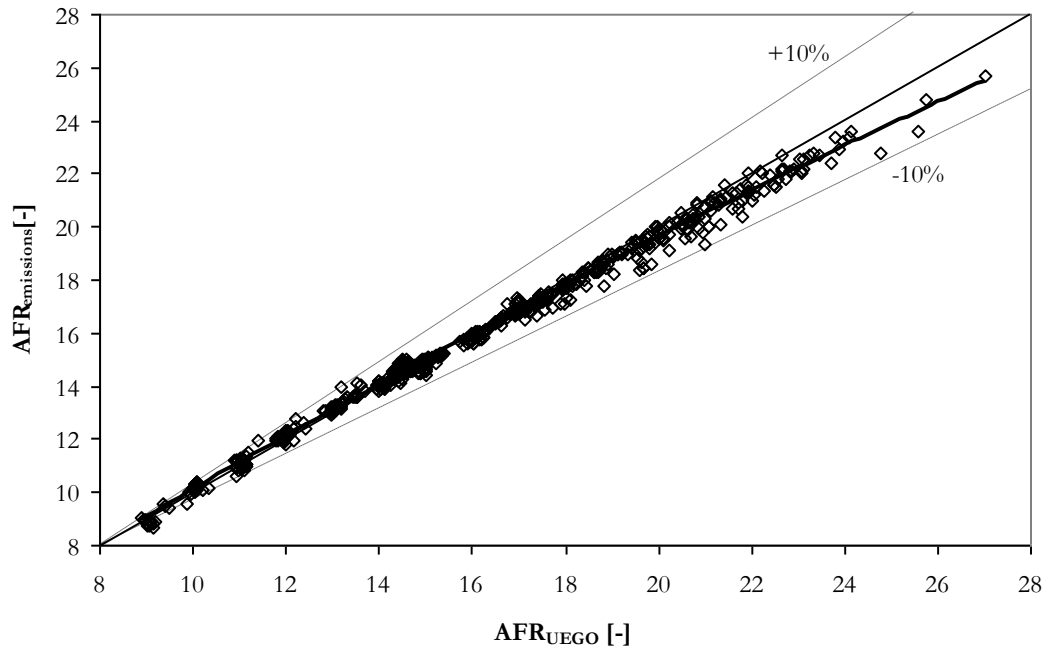
Figure 7
Comparison of AFR determined from the measured exhaust gas emissions and the UGEGO
sensor. Line of best fit through the data is shown, indicating a divergence from the y=x at
lean operating conditions. Data includes engine speeds from idle to 4000rpm WOT and the
full range of cam timings.
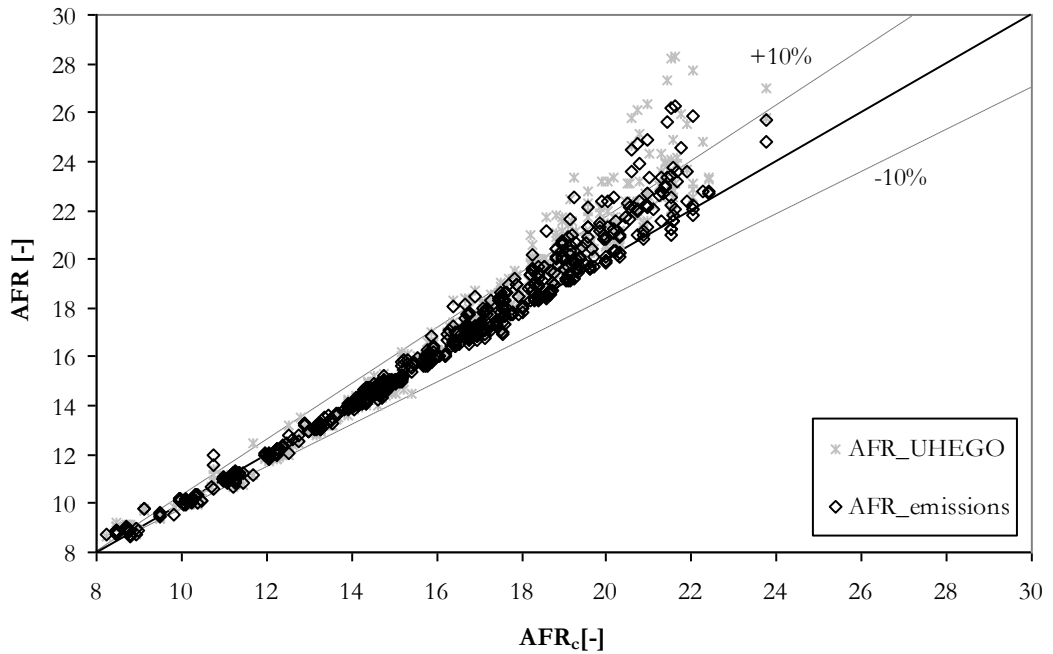
Figure 8
Relative inaccuracies of the AFR measured by the emissions and the UEGO sensor. AFR_c
is calculated from equation 9, directly from the measured fuel pulse width.
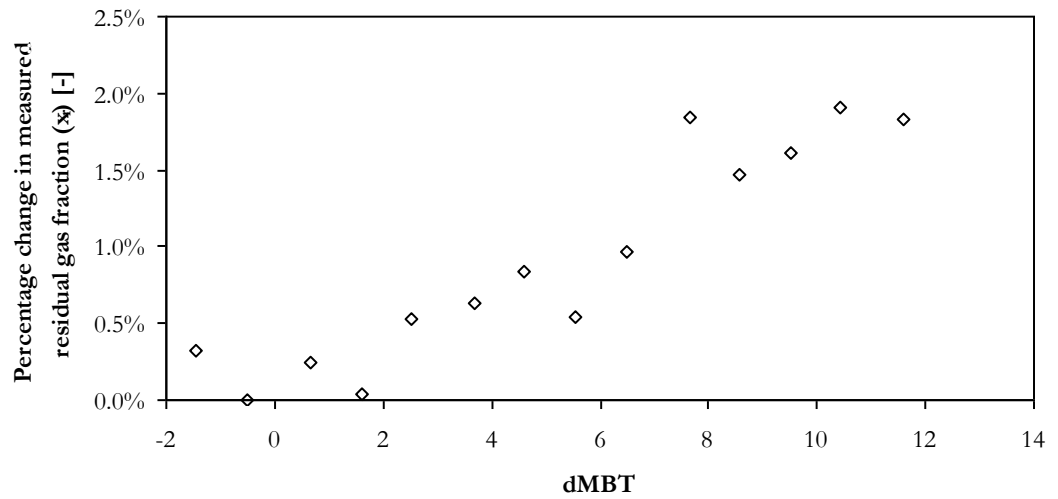
Figure 9
The effect of relative spark timing on measured x_r , operating condition:
1500rpm inlet manifold pressure 0.65 bar, -4°CA valve overlap, stoichiometric
AFR.
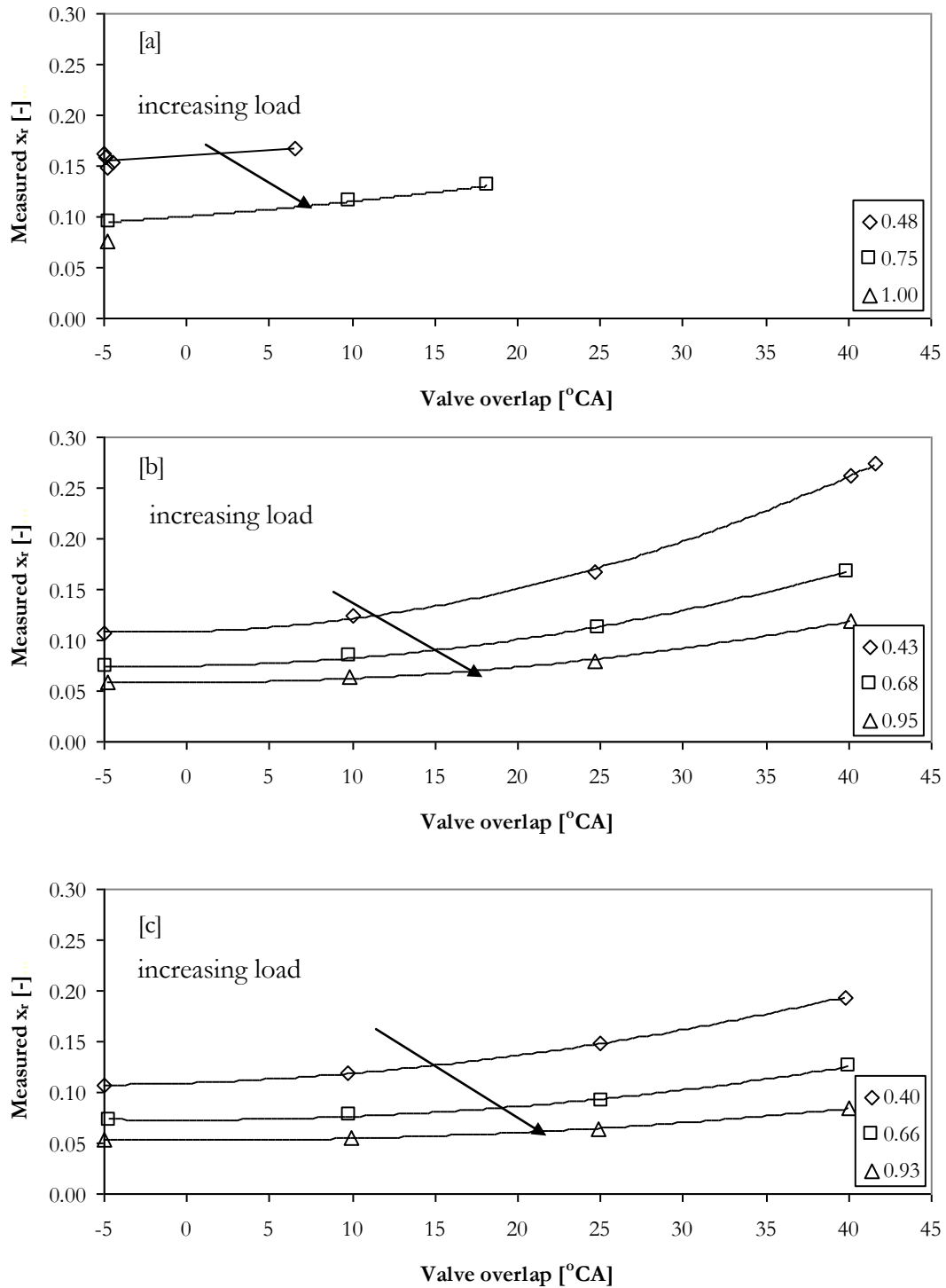
Figure 10
The effect of valve overlap (defined as the angle at which the intake valve opens in °CA to the °CA the exhaust valve closes, no minimum opening height applies) at three engine speeds: [a] 650rpm, [b] 1500rpm and [c] 2500rpm. The legend in all cases is inlet manifold pressure [bar].
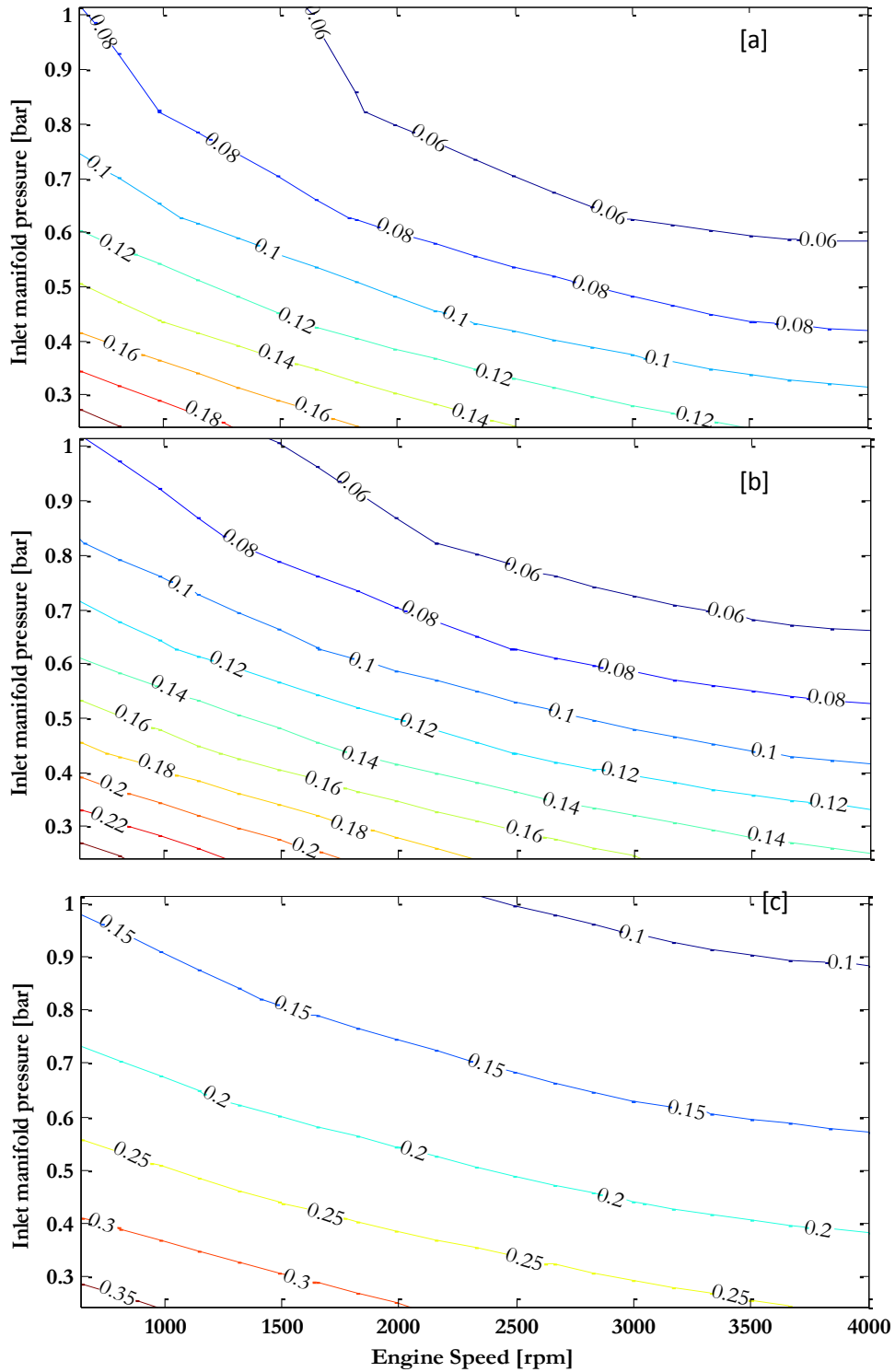
Figure 11

Modelled x_r over a wide range of engine speeds, loads and three valve overlaps [a] - 5°CA [b] 20°CA and [c] 42°CA. Contour plots created using the following equation:
0.096989 - 0.038673*rpm - 0.058202*MAP + 0.051956*VO + 0.017447*rpm^2 + 0.012772*rpm*MAP - 0.021327*rpm*VO - 0.026702*MAP*VO + 0.038794*VO^2. (where each variable is normalized to the range -1:1).
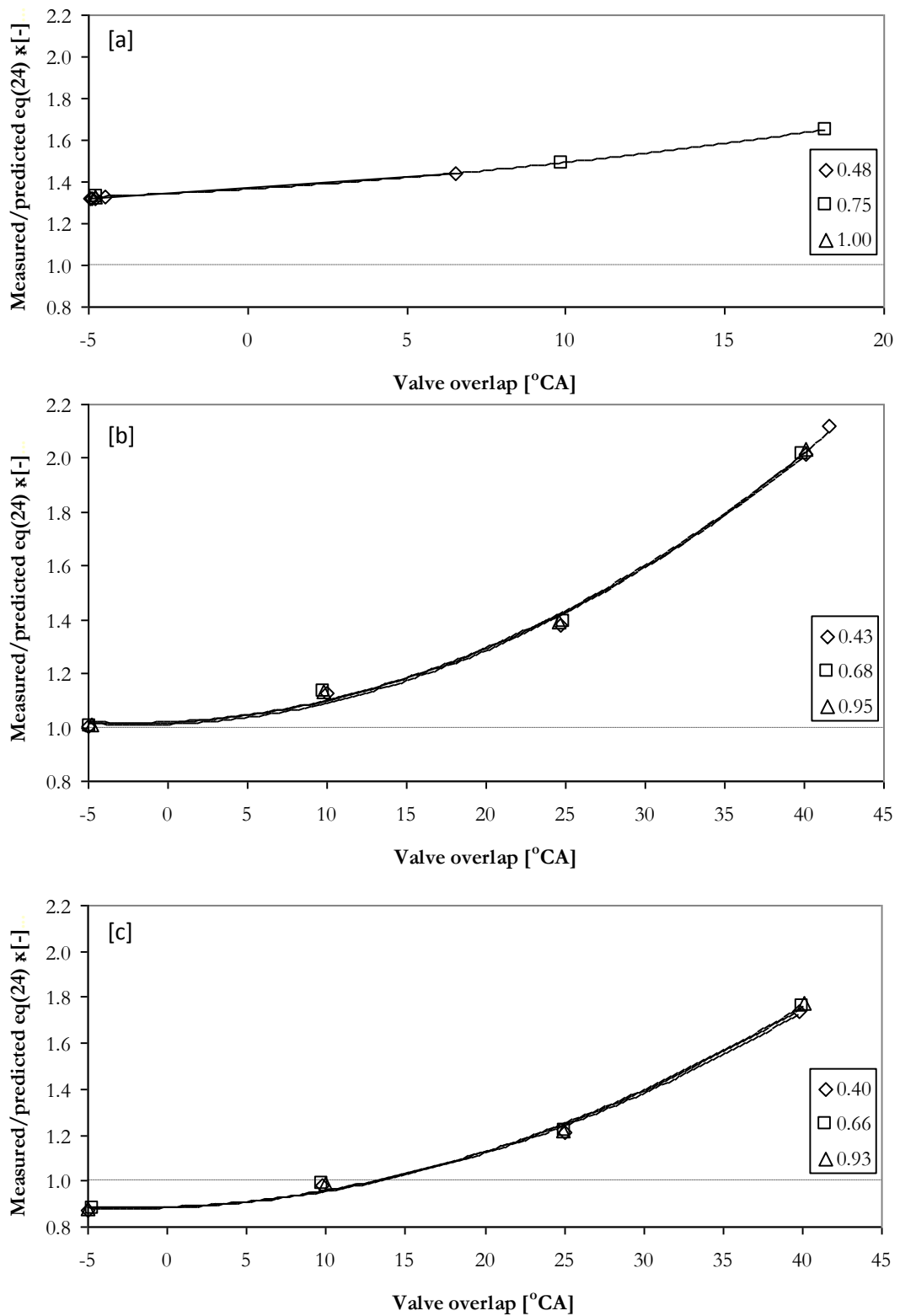
Figure 12

The error ratio of measured and predicted x_r at three engine speeds (measured data as shown in Figure 11) [a] 650rpm, [b] 1500rpm and [c] 2500rpm.
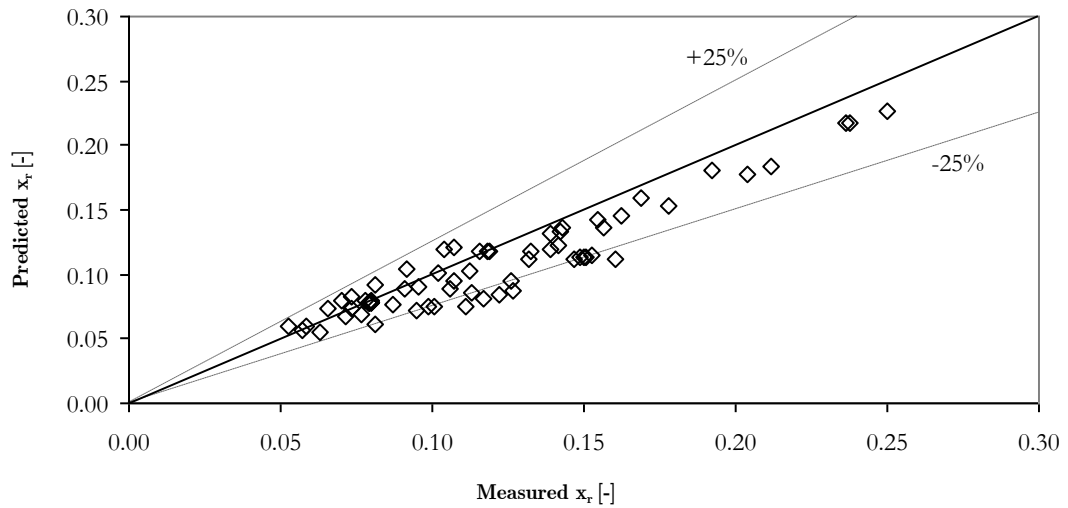
Figure 13
Comparison of the predicted x_r and the measured x_r. The predicted x_r is calculated from equation 27.
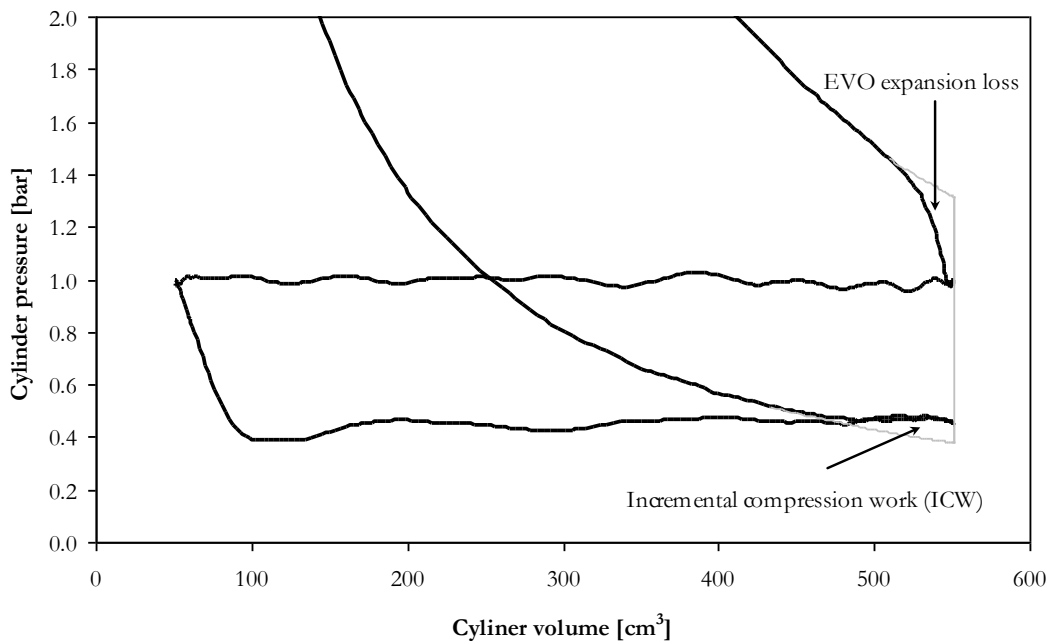
Figure 14
Example p vs. V diagram with extrapolated pressures allowing calculation of the EVO expansion loss and the incremental compression work. 1000rpm, IVC of 65°CA after BDC and EVO 40°CA BDC (equivalent to a -5°CA VO).
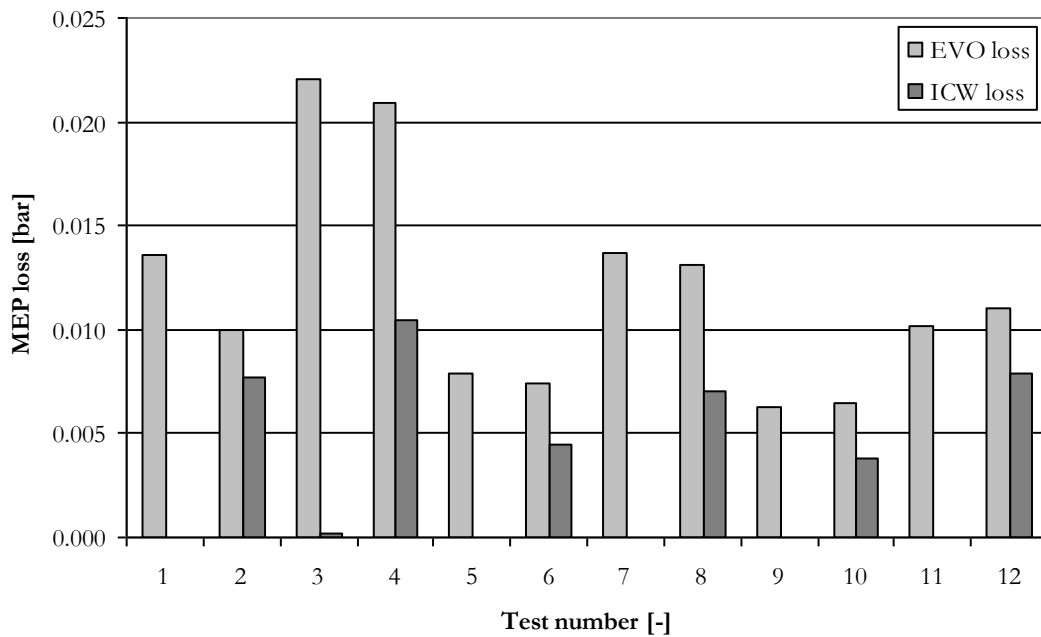
Figure 15
Difference in calculated EVO loss and ICW loss for fully retarded and advanced intake cam phasing.

Test number [-]	Engine speed [rpm]	Torque [Nm]	IVC [°CA ABDC]
1	1000	54	18
2	1000	53	64
3	1000	105	18
4	1000	106	64
5	2000	54	18
6	2000	53	64
7	2000	116	18
8	2000	113	64
9	3000	50	18
10	3000	50	64
11	3000	111	18
12	3000	111	64

Figure 15-Figure 19 Legend.
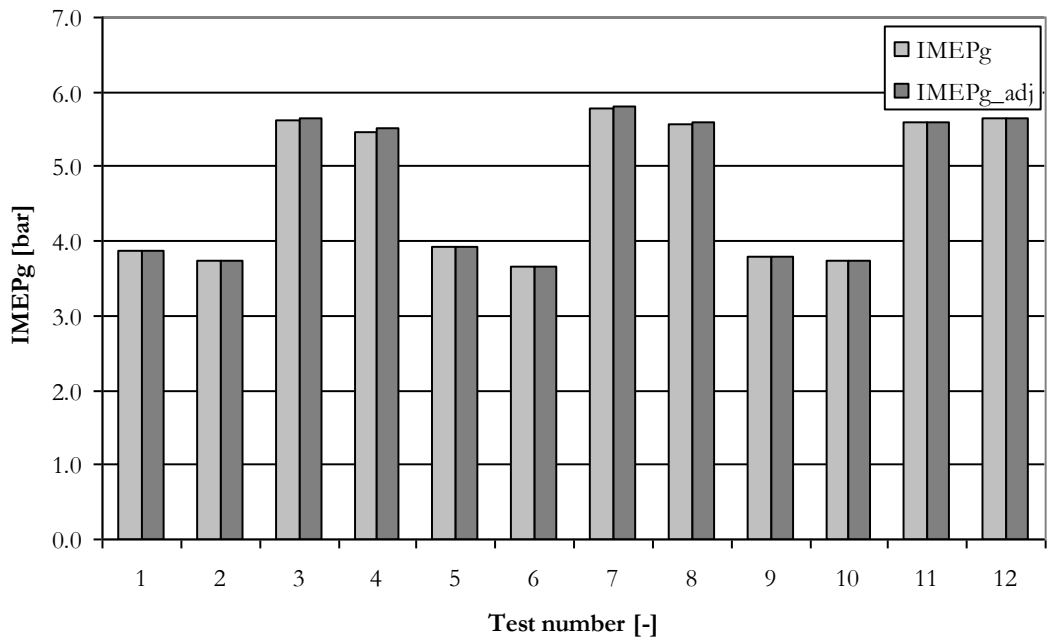
Figure 16
Difference in calculated IMEP$_g$ using the traditional integration method and
$IMEP_{g\_adj}$ **, that is corrected for** EVO_{loss} **and the** ICW_{loss} **.**
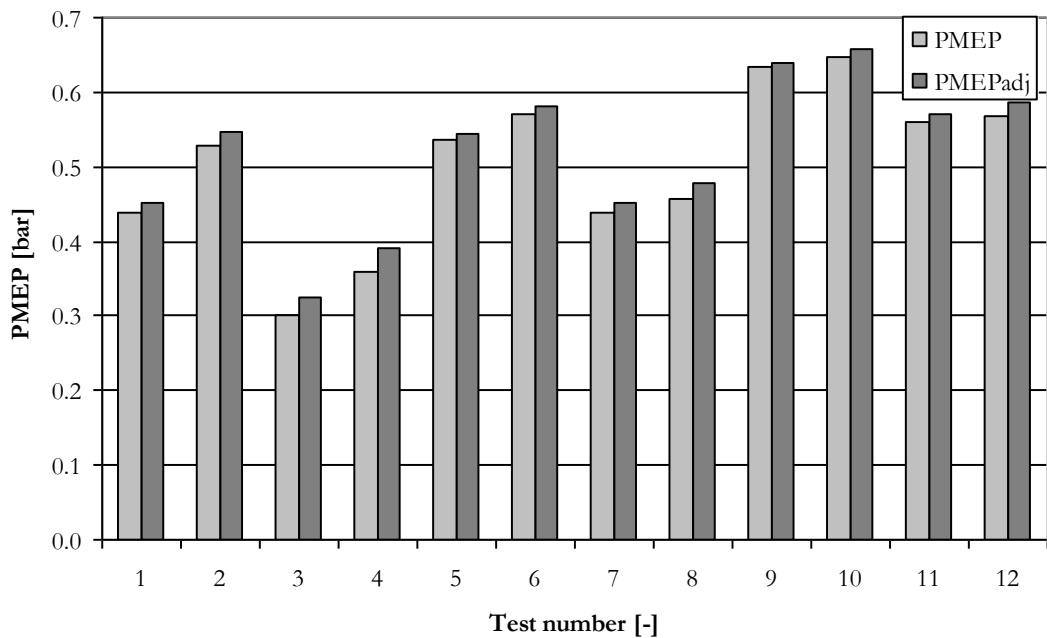
Figure 17
Difference in calculated PMEP using the traditional integration method and
$PMEP_{adj}$ **, that is corrected for** EVO_{loss} **and the** ICW_{loss} **.**
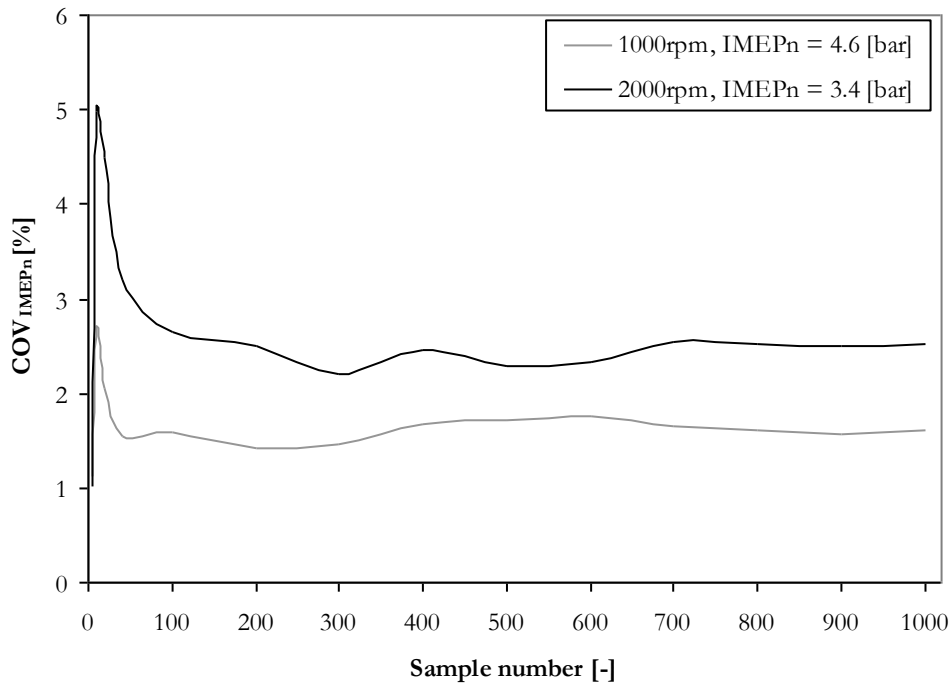
Figure 18

Influence of sample number on the calculated value of $IMEP_n$ during stable operating conditions for two engine speeds. (1 sample = 1 cycle).
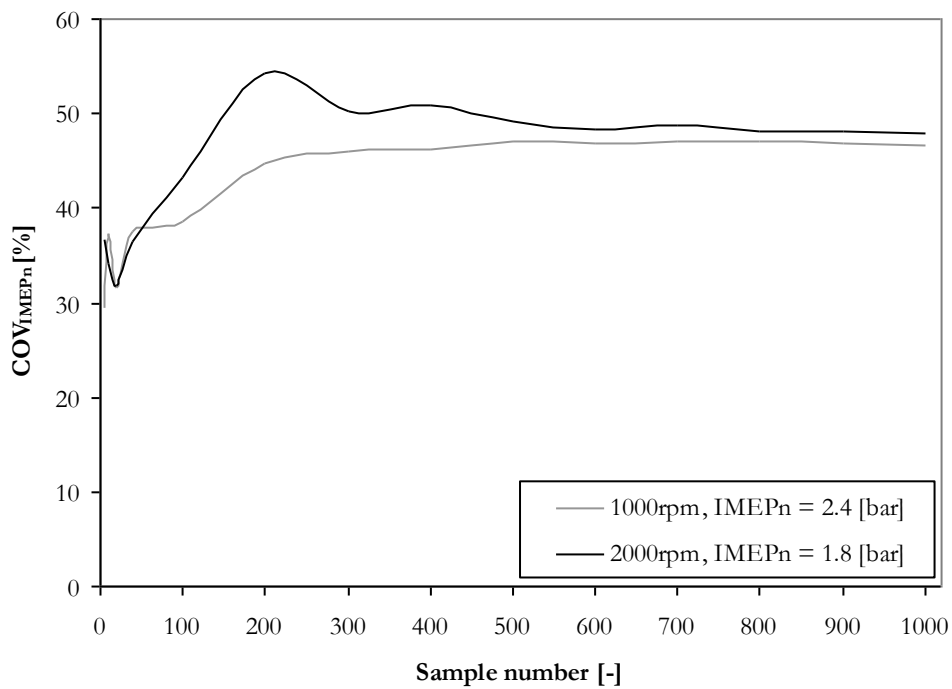
Figure 19

Influence of sample number on the calculated value of $IMEP_n$ during unstable operating conditions for two engine speeds.
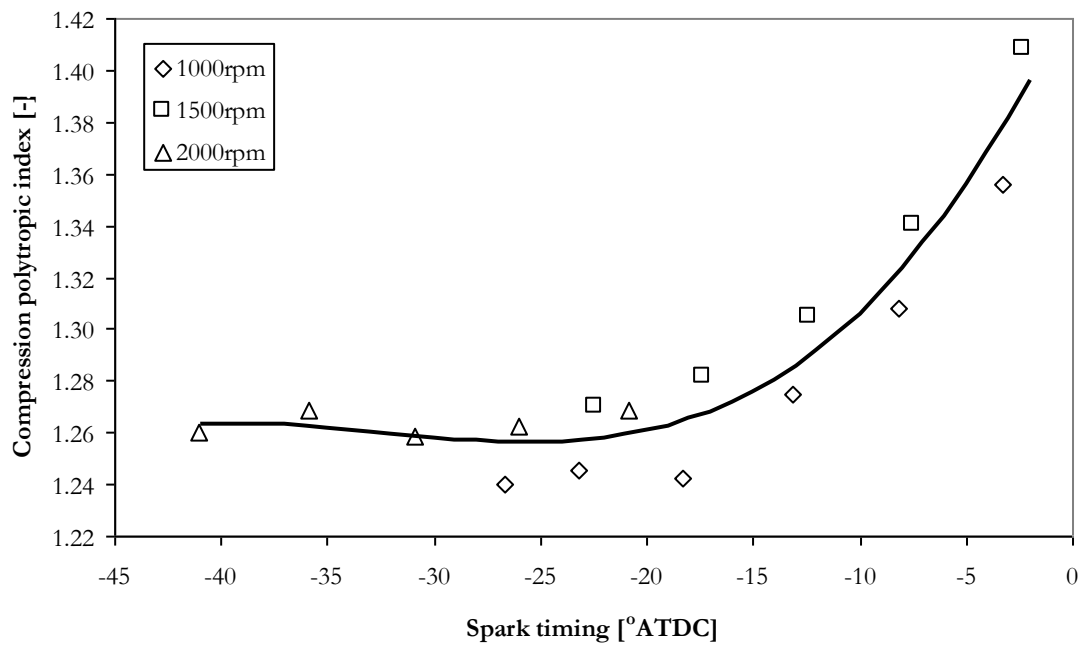
Figure 20

Influence of spark timing on calculated compression polytropic index $\left(n_{comp}\right)$ for three engine speeds (constant throttle angle and valve overlap (VO) for each engine speed).
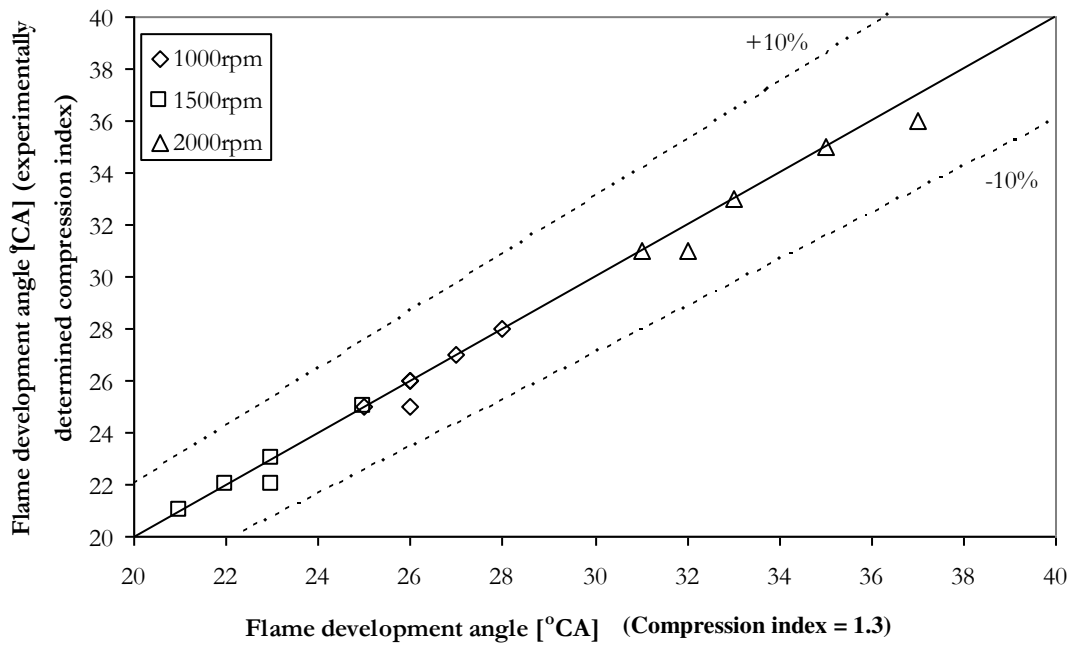
Figure 21

Difference in the flame development angle $\left(\Delta\theta_{0-10\%}\right)$ calculated from a fixed polytropic index (1.3) (x-axis) and experimentally determined polytropic index (y-axis). Expansion index $\left(n_{\exp an}\right)$ is fixed to 1.3.
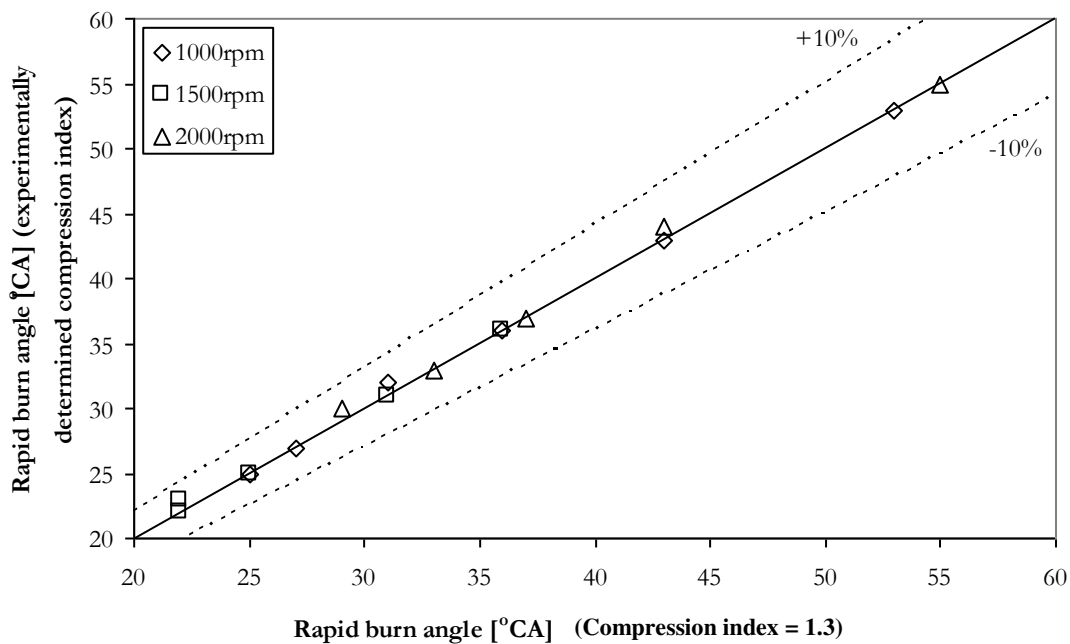
Figure 22

Difference in the rapid burn angle $\left(\Delta\theta_{10-90\%}\right)$ calculated from a fixed polytropic index (1.3) (x-axis) and experimentally determined polytropic index (y-axis). Expansion index $\left(n_{\exp an}\right)$ is fixed to 1.3. Mass fraction burn parameters calculated from an ensemble averaged pressure trace of 500 cycles.
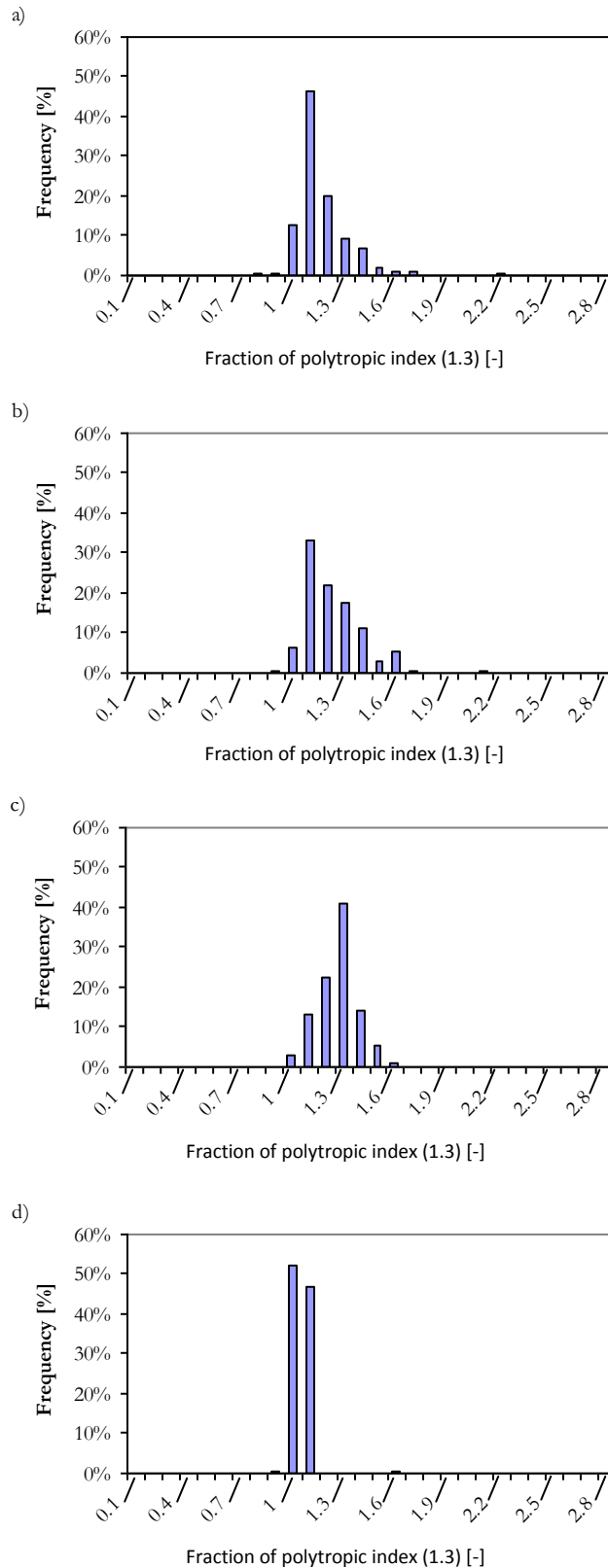
Figure 23
Expansion polytropic index frequency distribution for the four determination methods, (a)
first negative index, (b) sum negative index, (c) late polytropic index, (d) $pV^{1.15}$ index.
Operating conditions encompass engine speeds from 650 to 3000rpm, idle to **WOT** and, spark
timing 0°**BTDC** to 50°**BTDC** and VO from -5°**CA** to 42°**CA**.
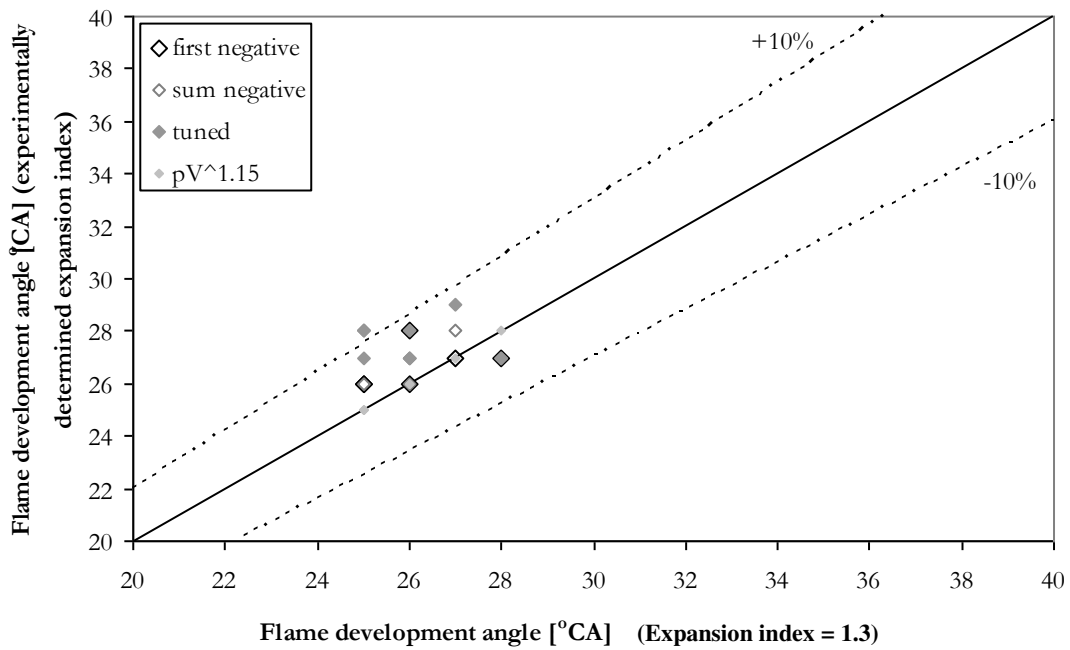
Figure 24

Difference in the flame development angle $\left(\Delta\theta_{0-10\%}\right)$ calculated from a fixed polytropic index (1.3) (x-axis) and experimentally determined polytropic index (y-axis). Compression index $\left(n_{comp}\right)$ is fixed to 1.3. 1000rpm set of data from Figure 21.
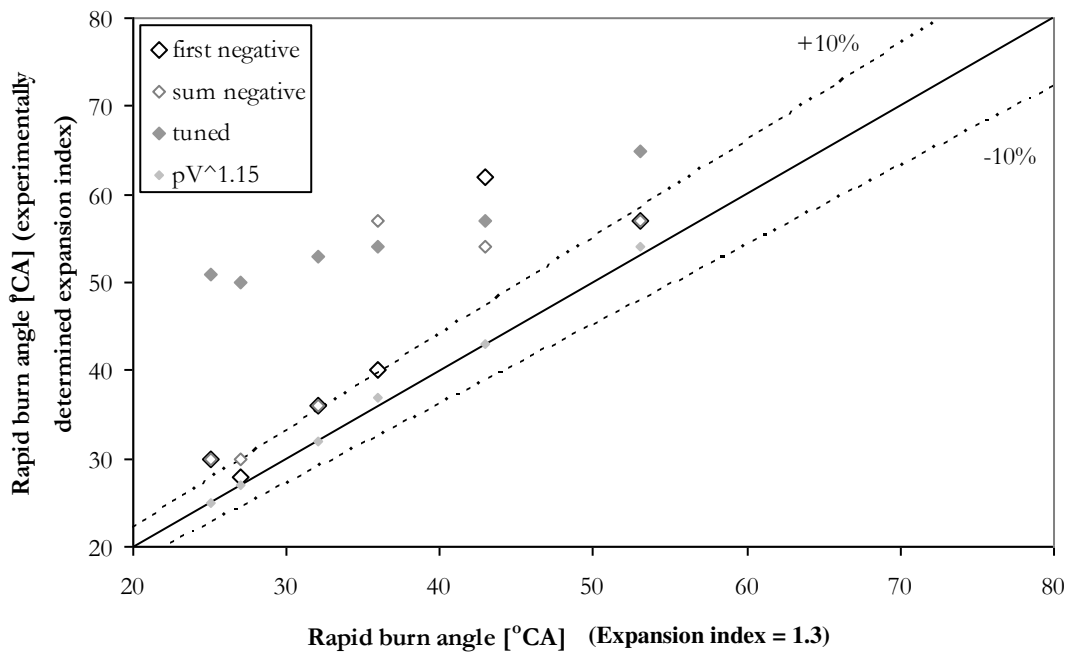
Figure 25

Difference in the rapid burn angle $\left(\Delta\theta_{10-90\%}\right)$ calculated from a fixed polytropic index (1.3) (x-axis) and experimentally determined polytropic index (y-axis). Compression index $\left(n_{comp}\right)$ is fixed to 1.3. 1000rpm set of data from Figure 22.
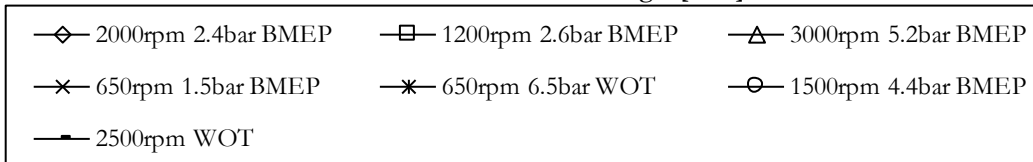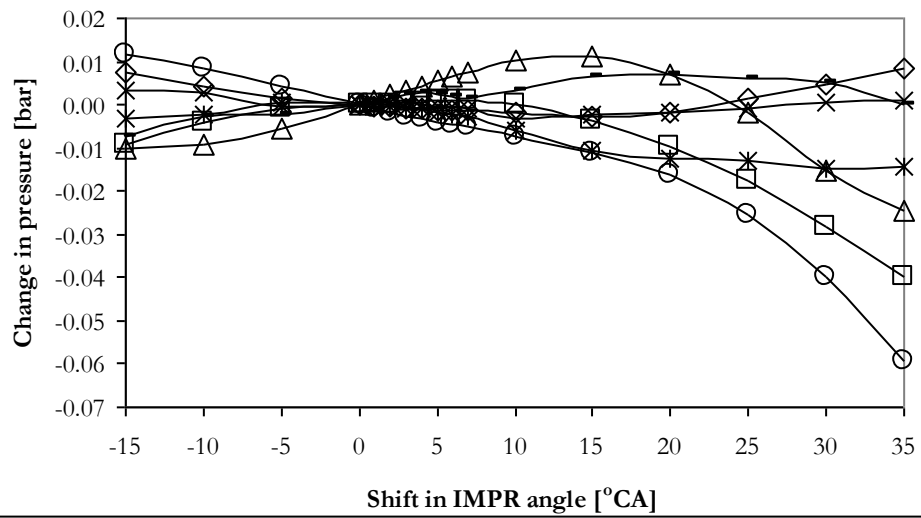
Figure 26
Change in the referenced pressure as the location of the referencing point is altered. Where the datum value is taken as bottom dead centre (the correction value is an average value calculated over 20°CA, with 10°CA either side of the referencing point).
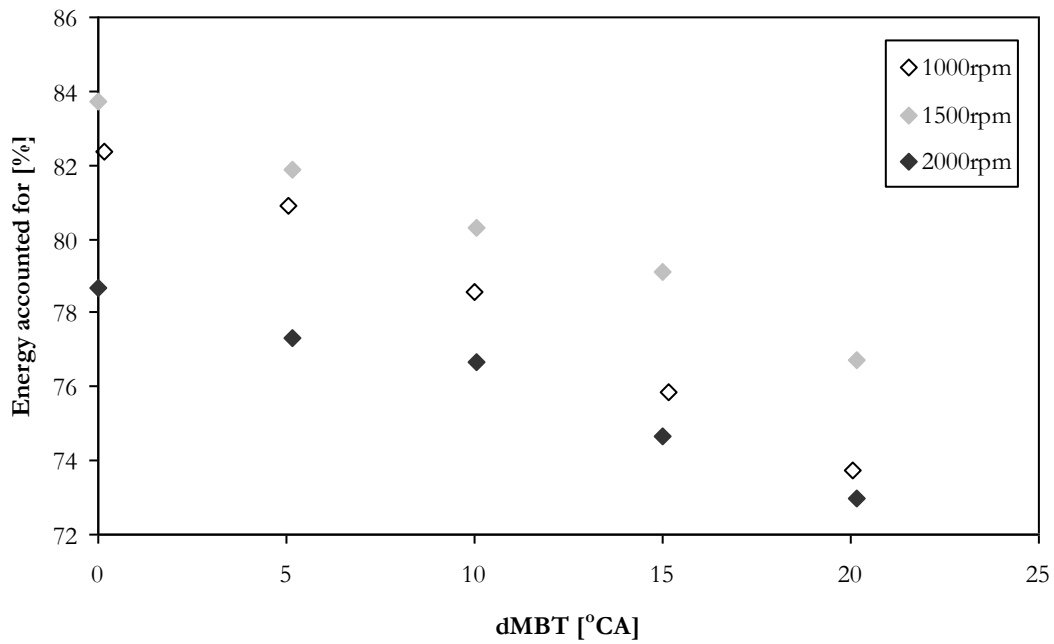
Figure 27
Change in the percentage of fuel accounted for at three engine speeds as a function of dMBT. (Values calculated from cycle averaged pressure. Ensemble averaged from 500 cycles).
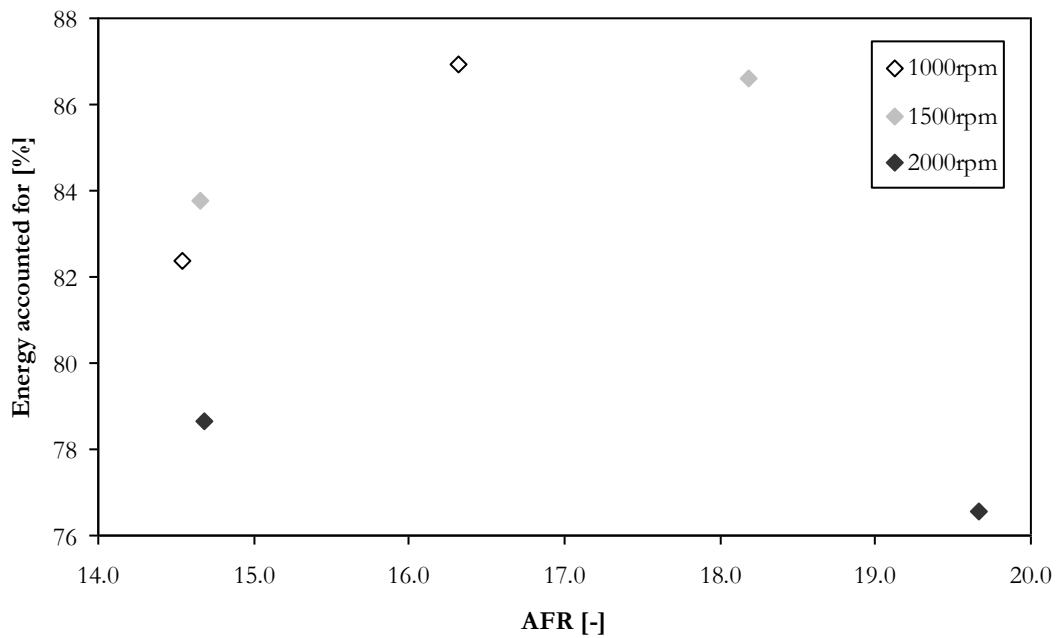
Figure 28
Change in the percentage of fuel accounted for at three engine speeds as a function of AFR, MBT* spark timing in all cases.
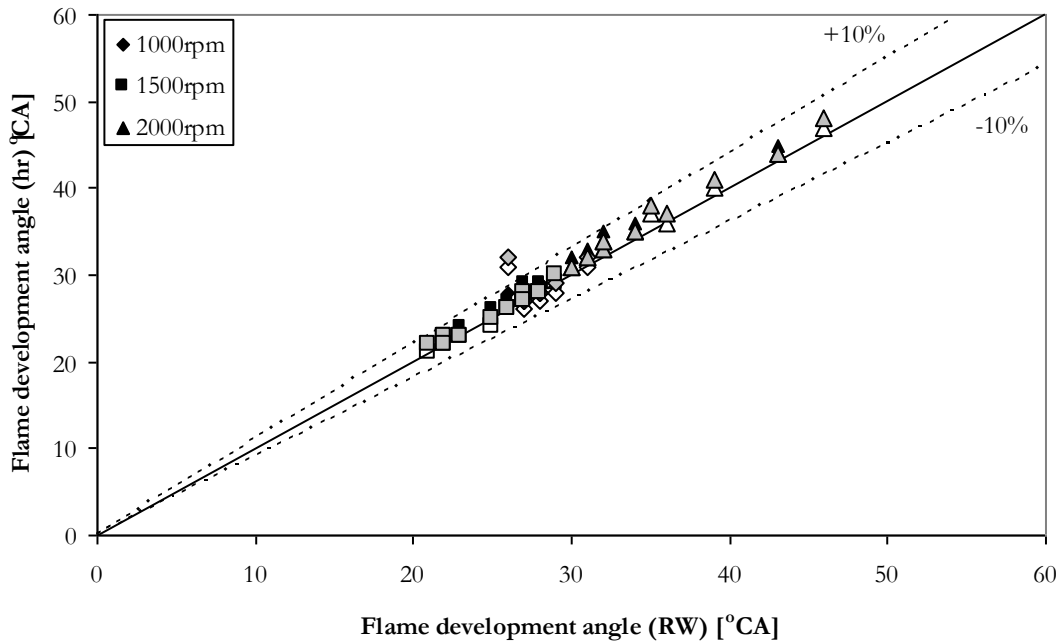
Figure 29

Comparison between the value of the $(\Delta\theta_{0-10\%})$ calculated using the Rassweiler and Withrow approach (RW, x-axis) and the heat release approach (hr, y-axis). Unfilled data points Woschni model, grey data points Woschni model with multiplication factor, black data points Woschni model with multiplication factor and dMBT weighting.
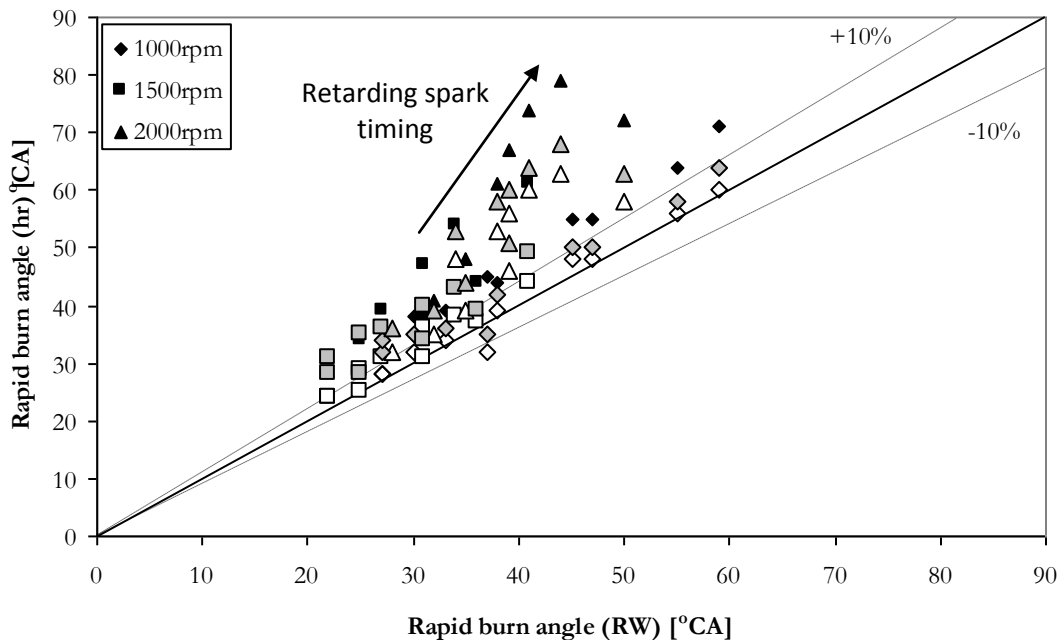
Figure 30

Comparison between the value of the $(\Delta\theta_{10-90\%})$ calculated using the Rassweiler and Withrow approach (RW, x-axis) and the heat release approach (hr, y-axis). Data points as described in Figure 29.

a)

b)
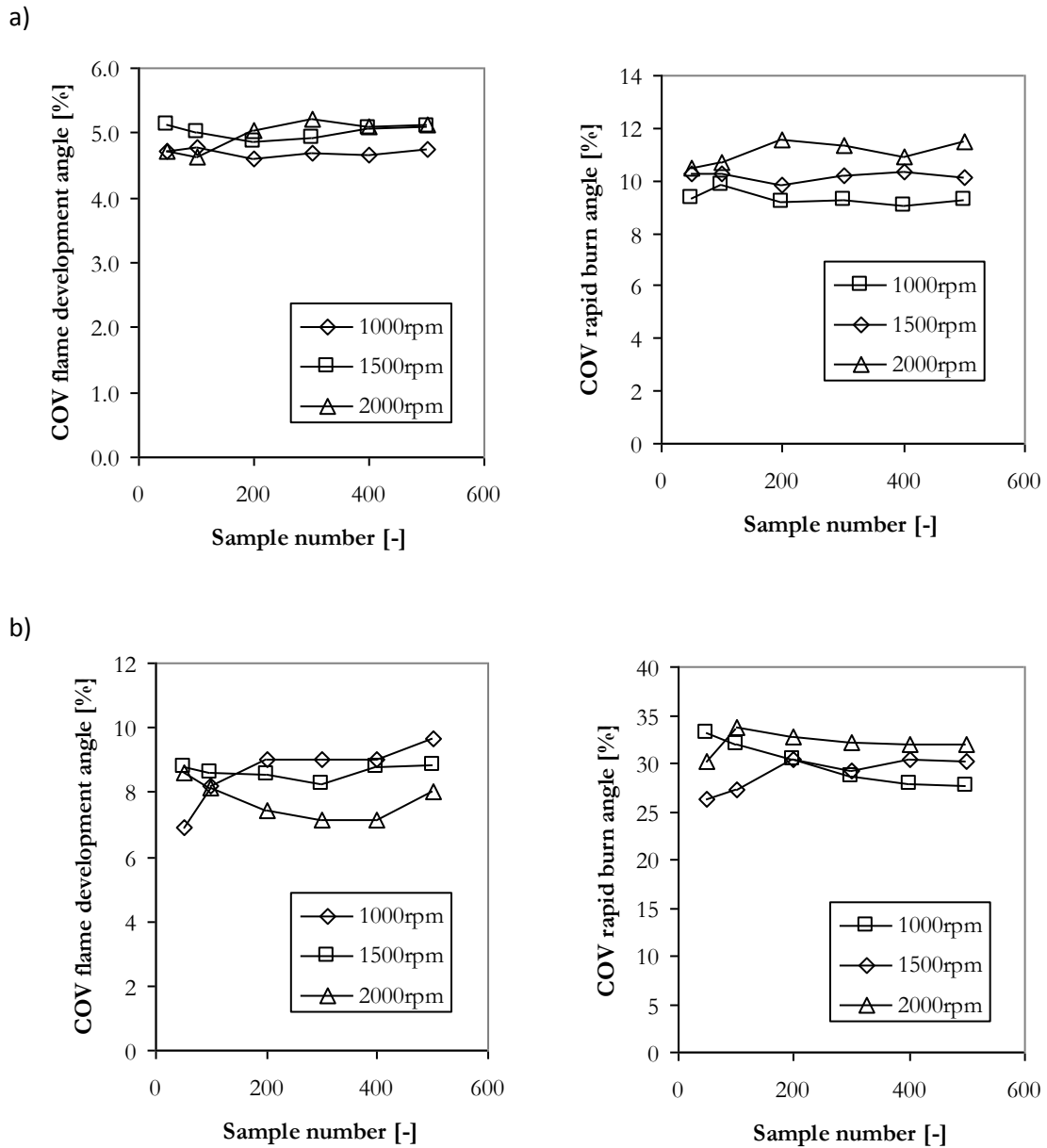
Figure 31

Influence of sample size on $COV_{\Delta\theta_{0-10\%}}$ and $COV_{\Delta\theta_{10-90\%}}$ at (a) stable operating conditions ($COV_{IMEP_n} < 10$) and (b) unstable operating conditions ($COV_{IMEP_n} > 10$).
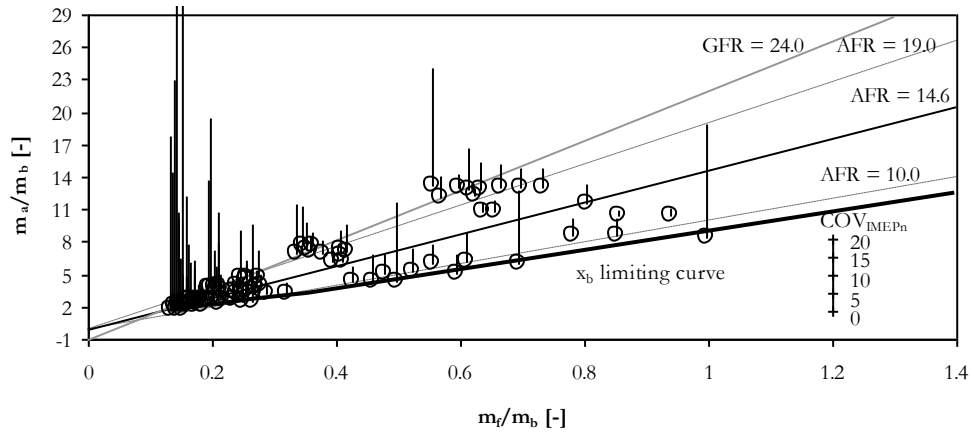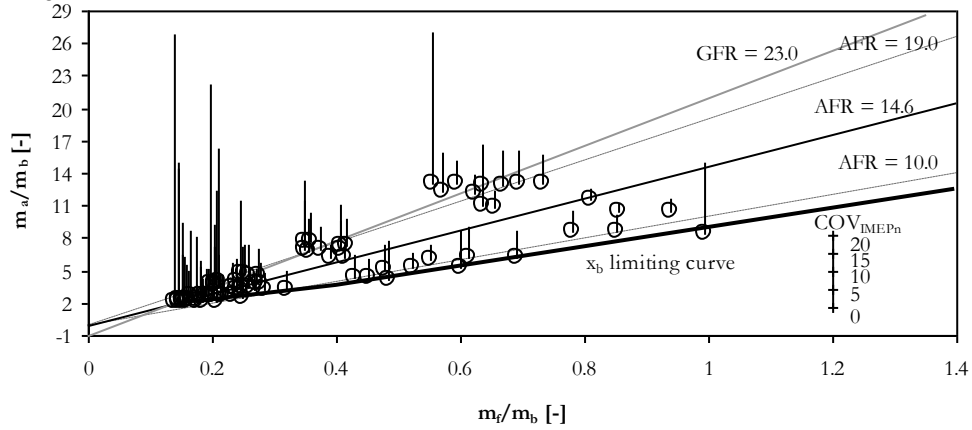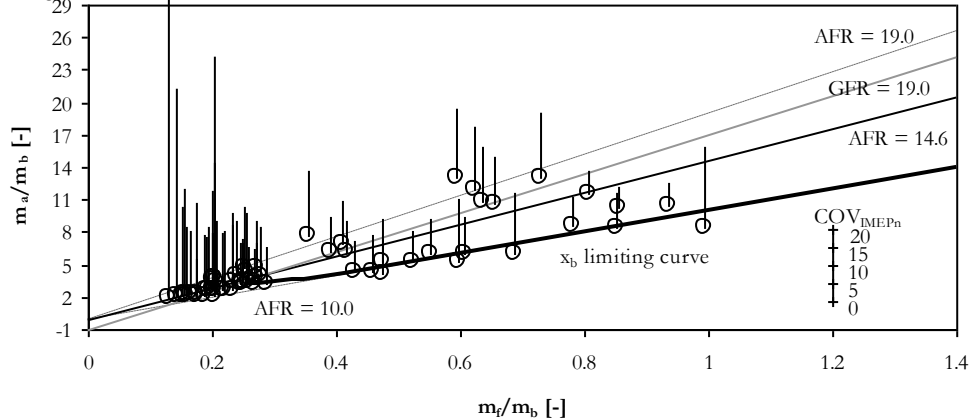
Figure 32

Combustion stability diagram, indicating limiting chemical constraints for three spark timings. Data taken at a variety of operating conditions: Engine speed 650 - 3000rpm, idle to WOT and no valve overlap to maximum valve overlap. Height of each bar at each test point indicates the level of COV_{IMEP_n}, higher the bar greater the level of instability.

MBT*
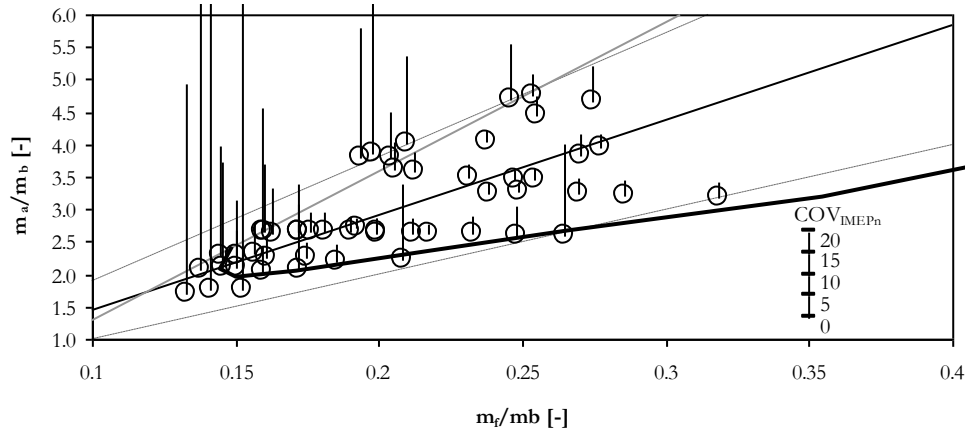
dMBT* = 10
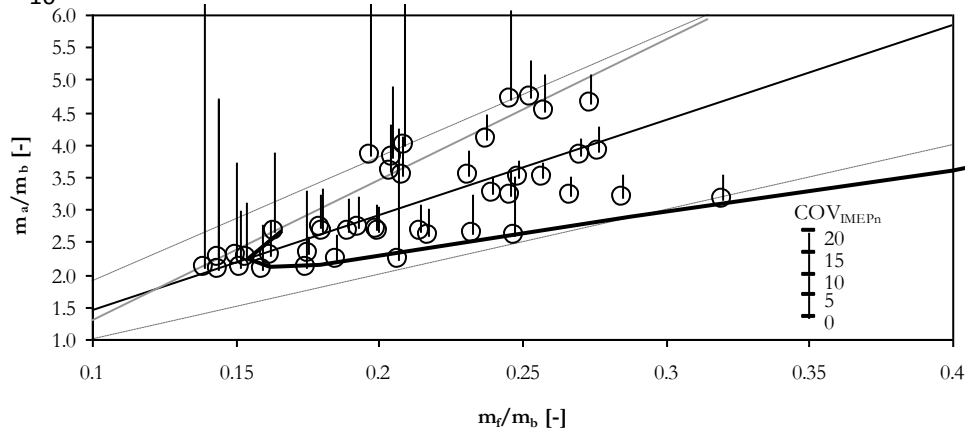
dMBT* = 20
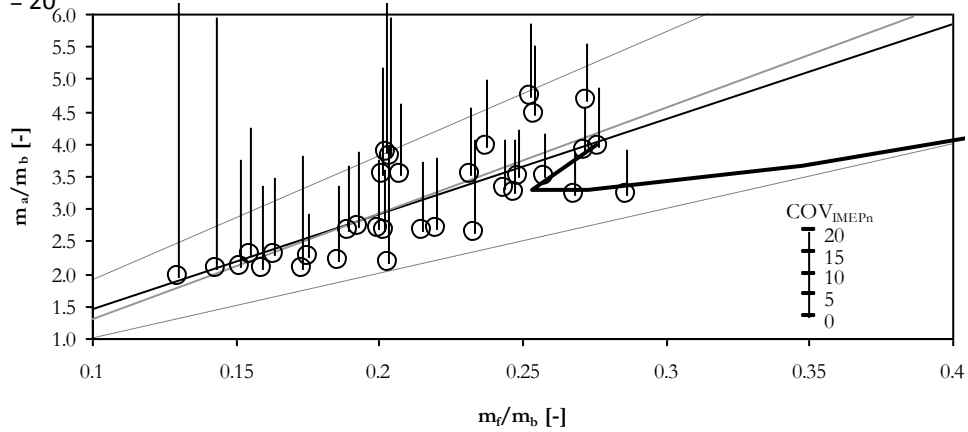
Figure 33
Zoomed combustion stability diagram, indicating limiting chemical constraints for three spark timings, focusing particularly on the region of high dilution.

MBT*
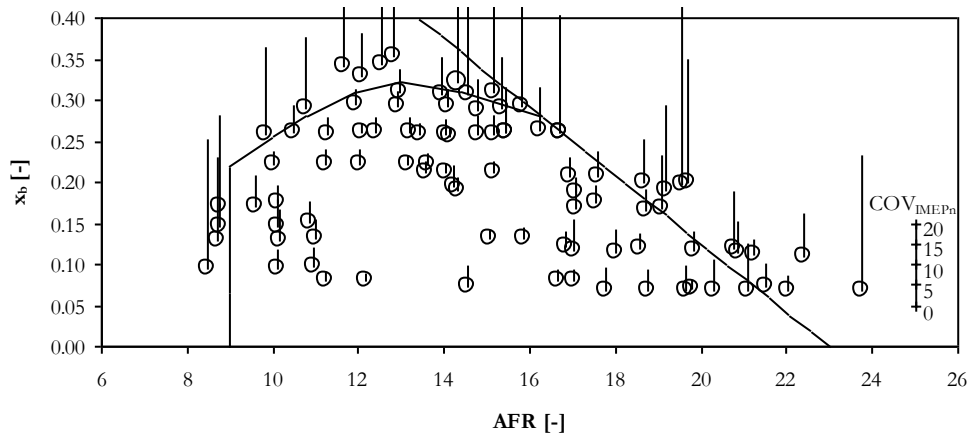
dMBT* = 10
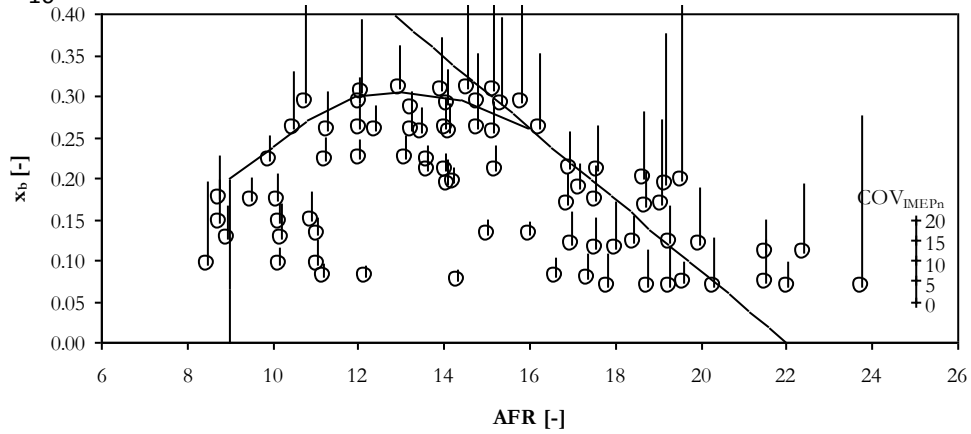
dMBT* = 20
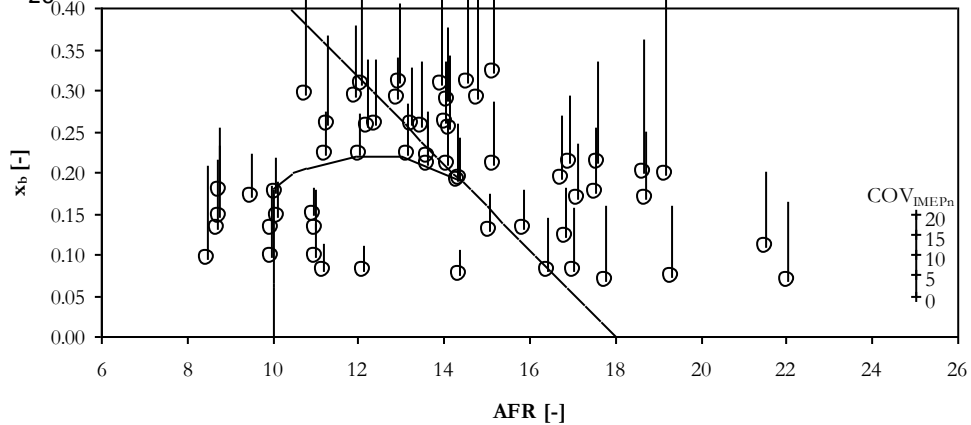
Figure 34

Combustion stability diagram used to determine the x_b limiting curve (based on experimental data), for three spark timings.
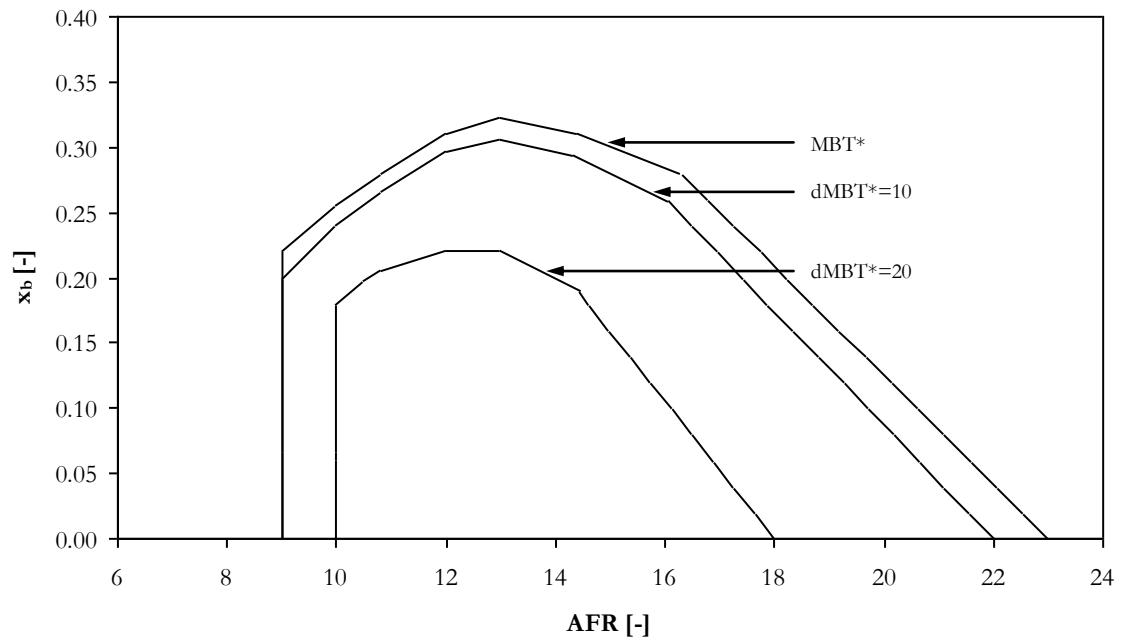
Figure 35
Overview of the mixture ratio stability limits for three spark timings. Showing the decreasing range of stable operating mixture ratios as the spark timing is retarded.

a)

b)

Figure 36
The influence of removing partial burning and misfiring cycles from the calculation of COV_{IMEP_n} . Where a) includes all cycles, b) has removed partial burning and misfiring cycles. Constant fuel data black points, constant air data grey data points.
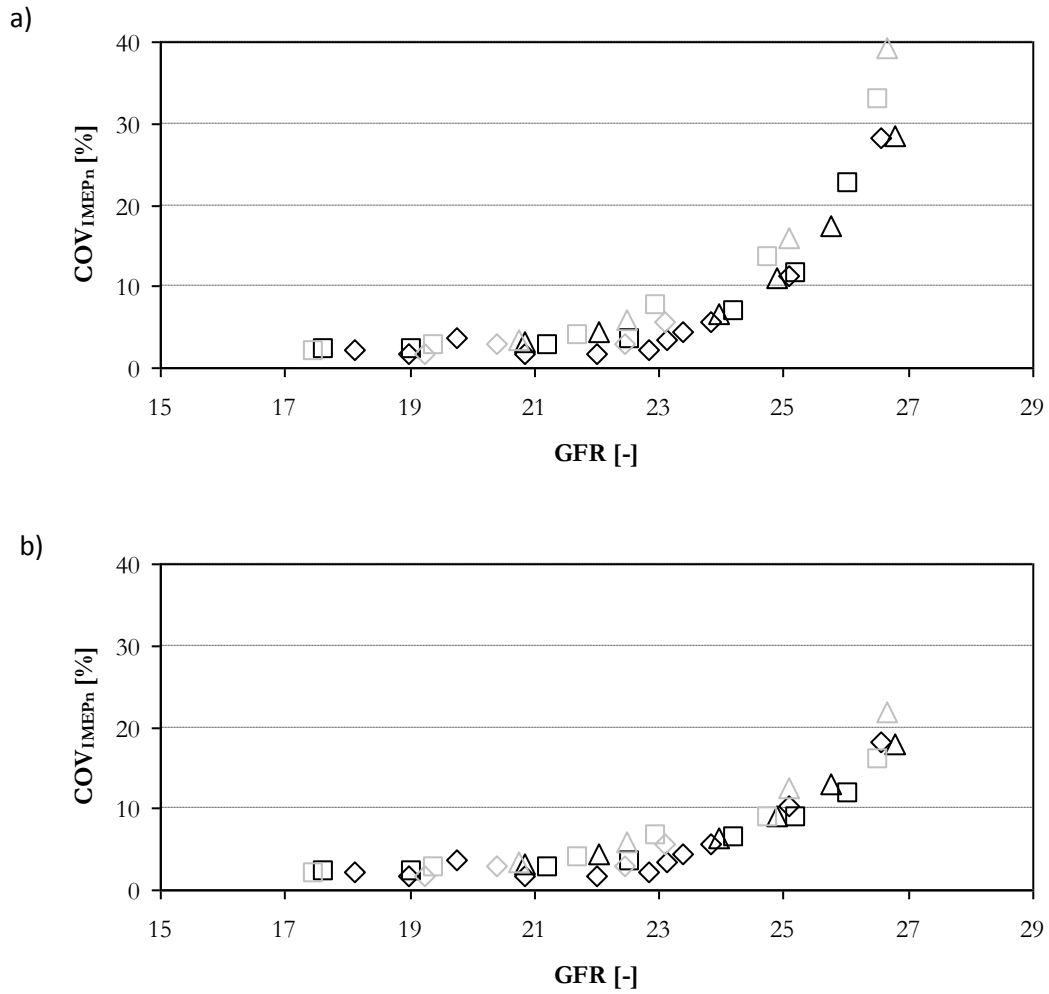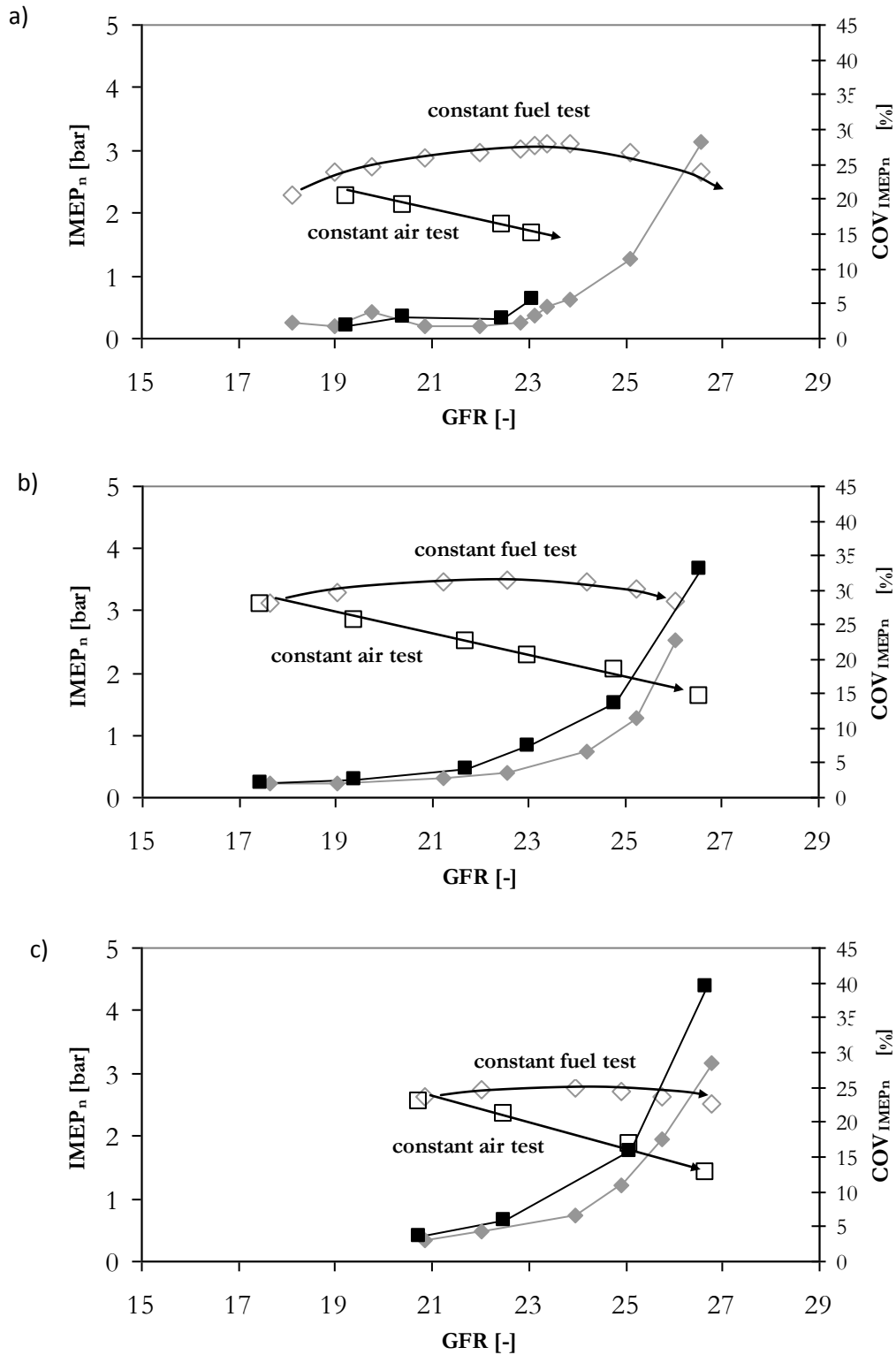
Figure 37
The change in IMEP$_n$ and COV$_{IMEPn}$ with GFR for two different test methods,
constant fuel tests indicated with diamonds and constant air tests indicated with
squares. Where a) is 1000rpm, b) is 1500rpm and c) 2000rpm.
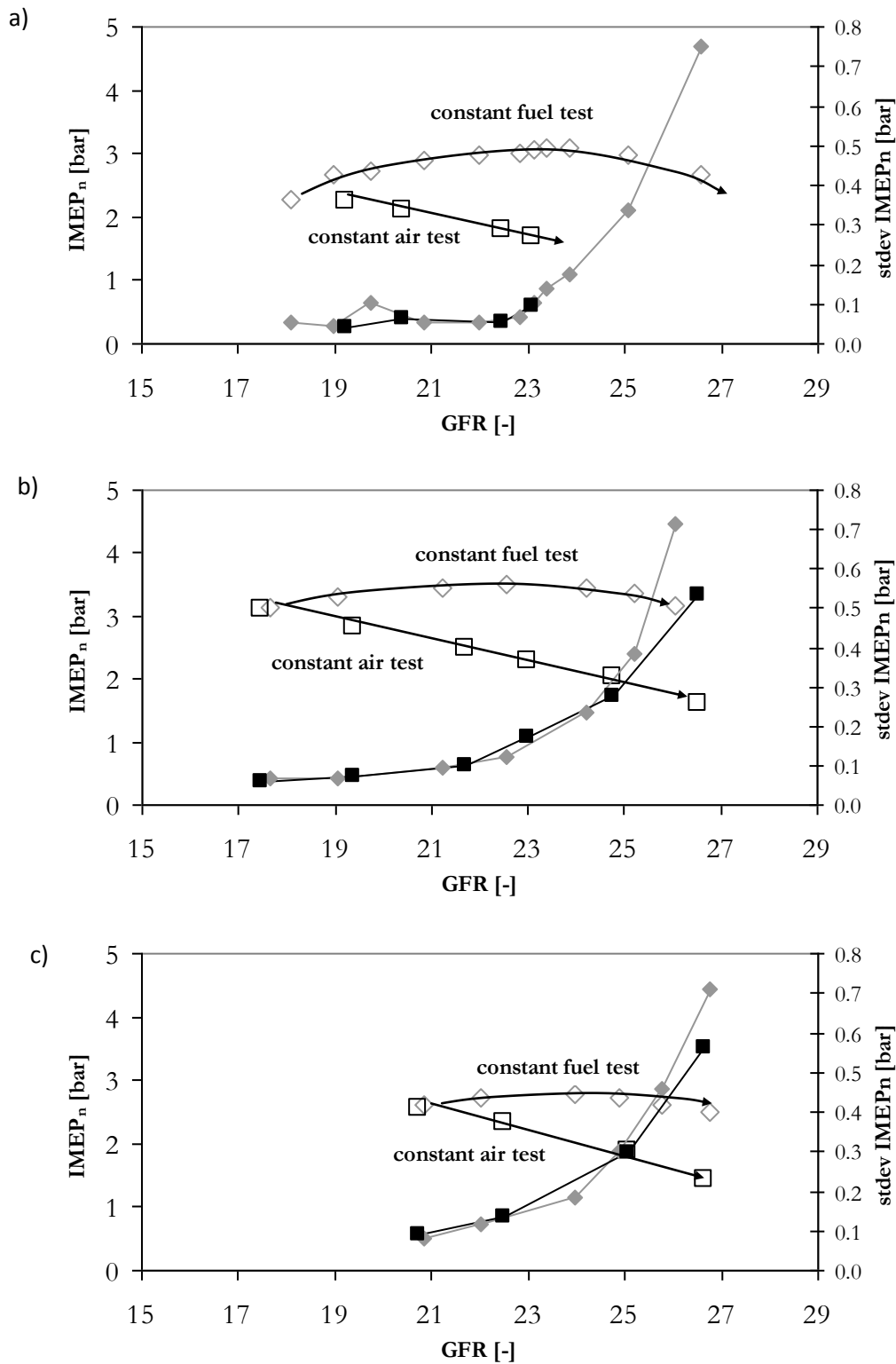
Figure 38
The change in IMEP_n and stdev IMEP_n with GFR for two different test methods, data as Figure 24. Constant fuel tests indicated with diamonds and constant air tests indicated with squares.
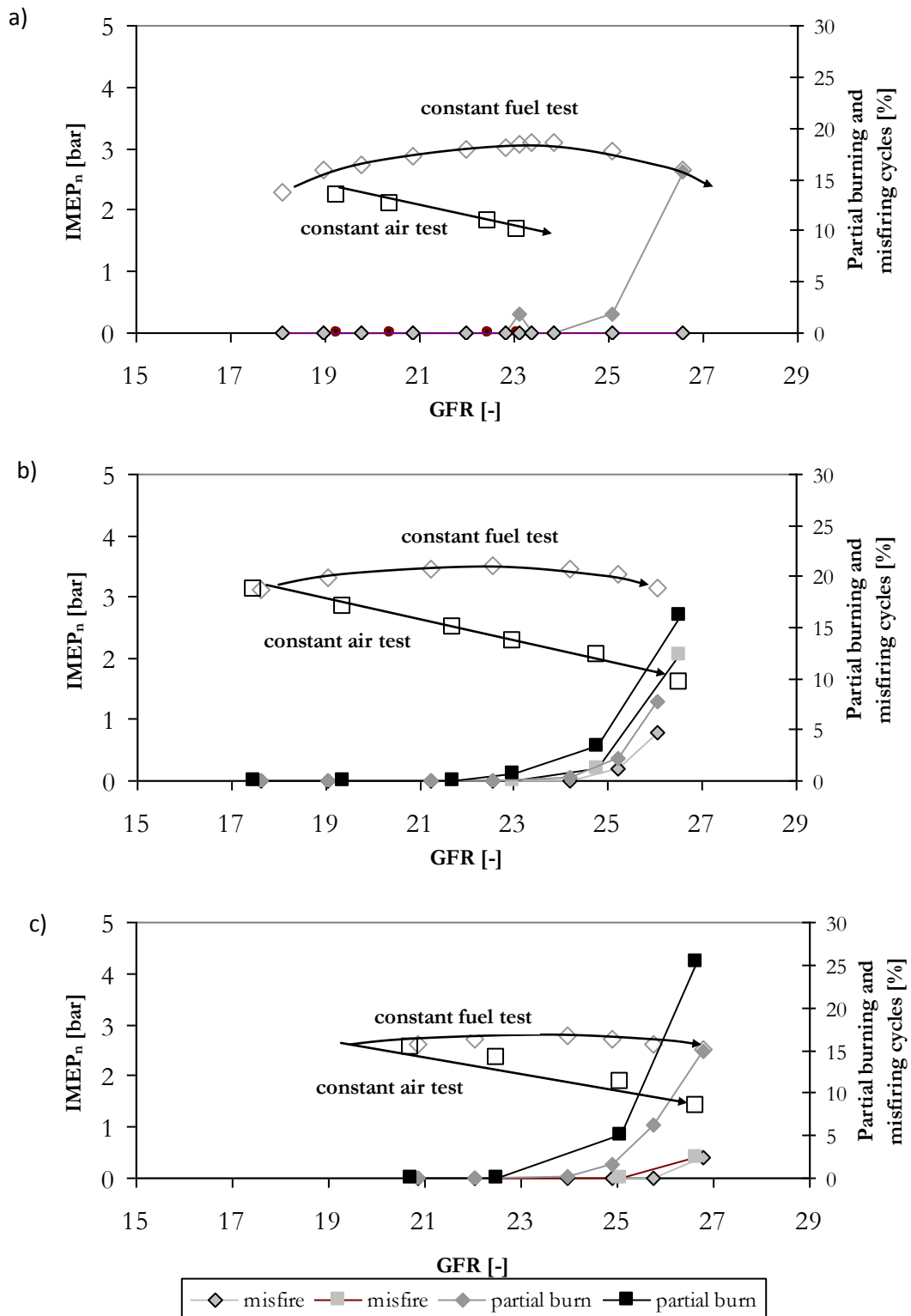
Figure 39
The change in IMEP$_n$ and % partial burning and misfiring cycles with GFR for two different test methods, data as Figure 24. Constant fuel tests indicated with diamonds and constant air tests indicated with squares.
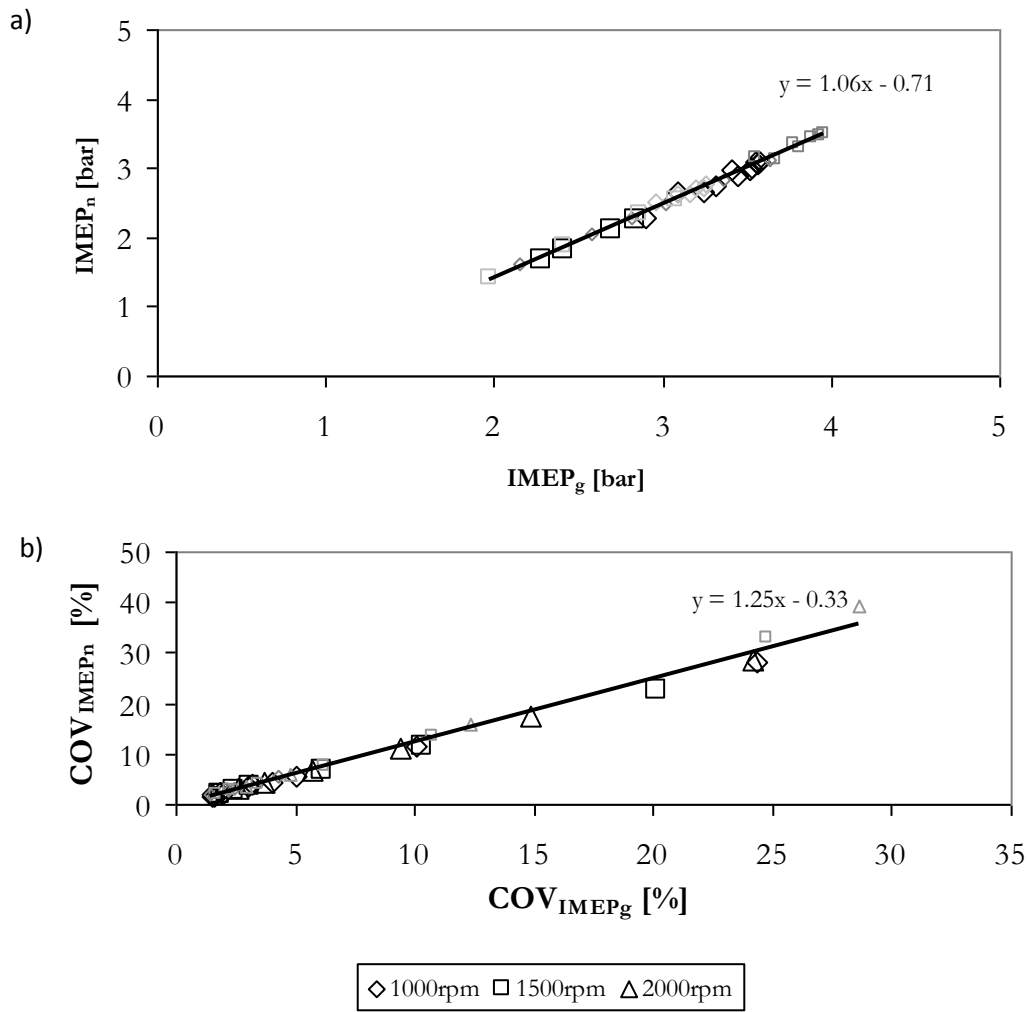
Figure 40
Correlation between net and (a) gross work output and (b) variability. Large symbols indicate constant air tests.
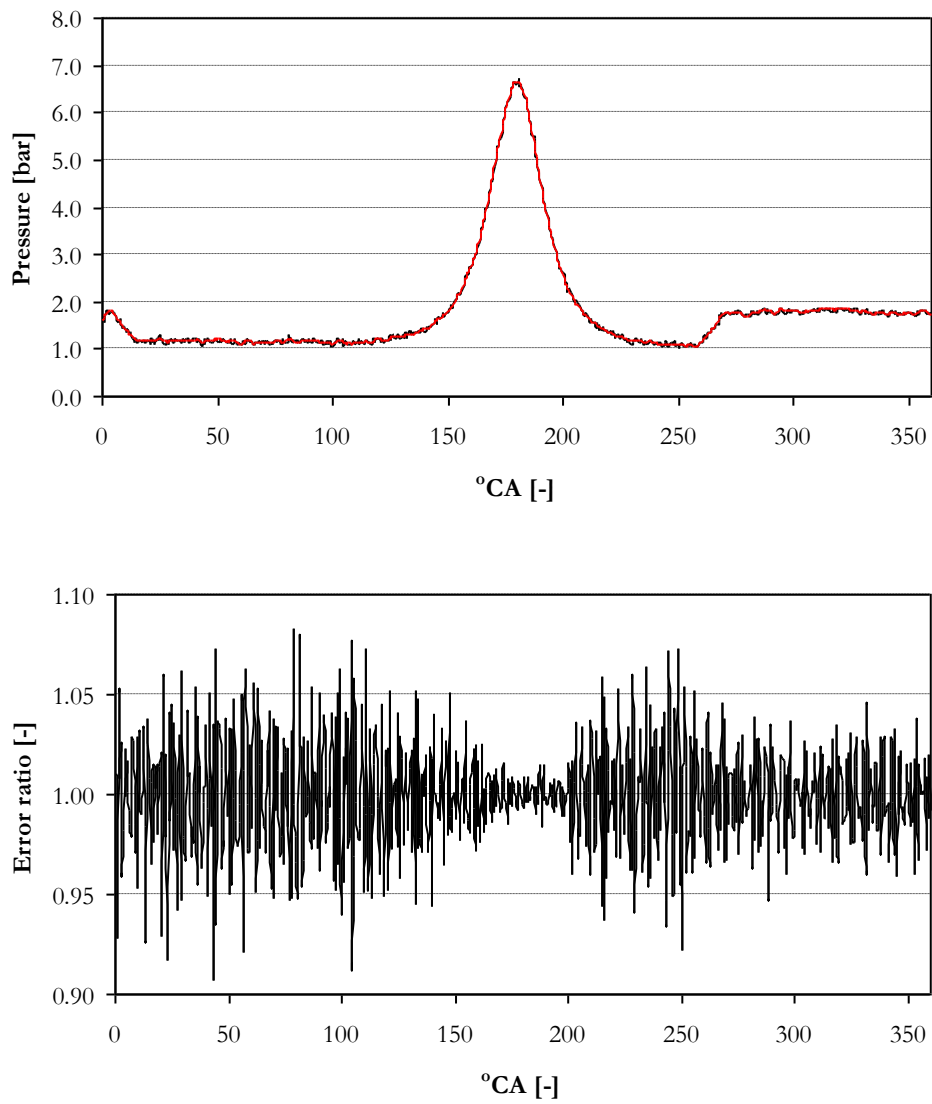
Figure 41
**Comparison of filtered and unfiltered motored pressure cycle data, and the error
ratio between the two (unfiltered/filtered), engine speed 1500rpm**
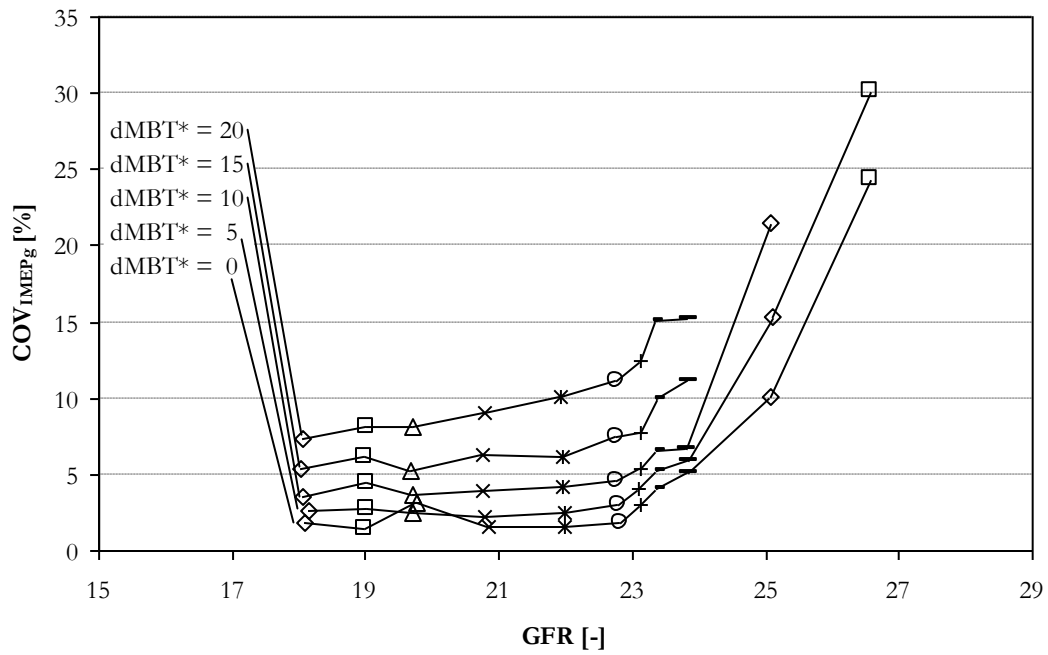
Figure 42

The influence of spark retard on COV_{IMEP_g} over a range of GFRs. Engine speed 1000rpm, constant fuel testing.
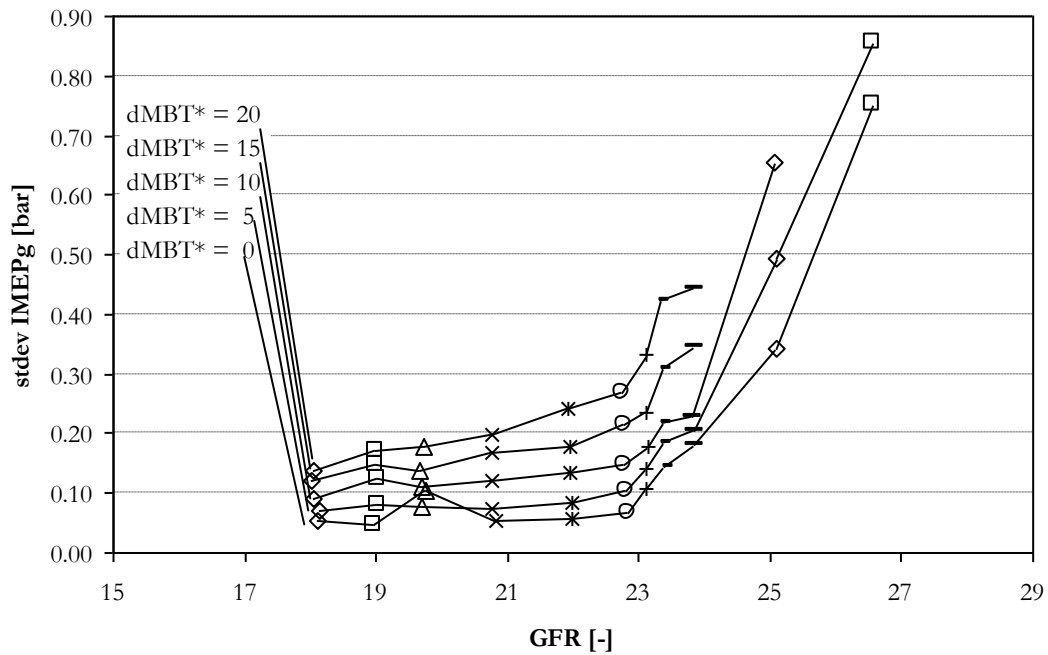
Figure 43

The influence of spark retard on stdev $IMEP_g$ over the same range of GFRs and engine conditions as shown in Figure 42.
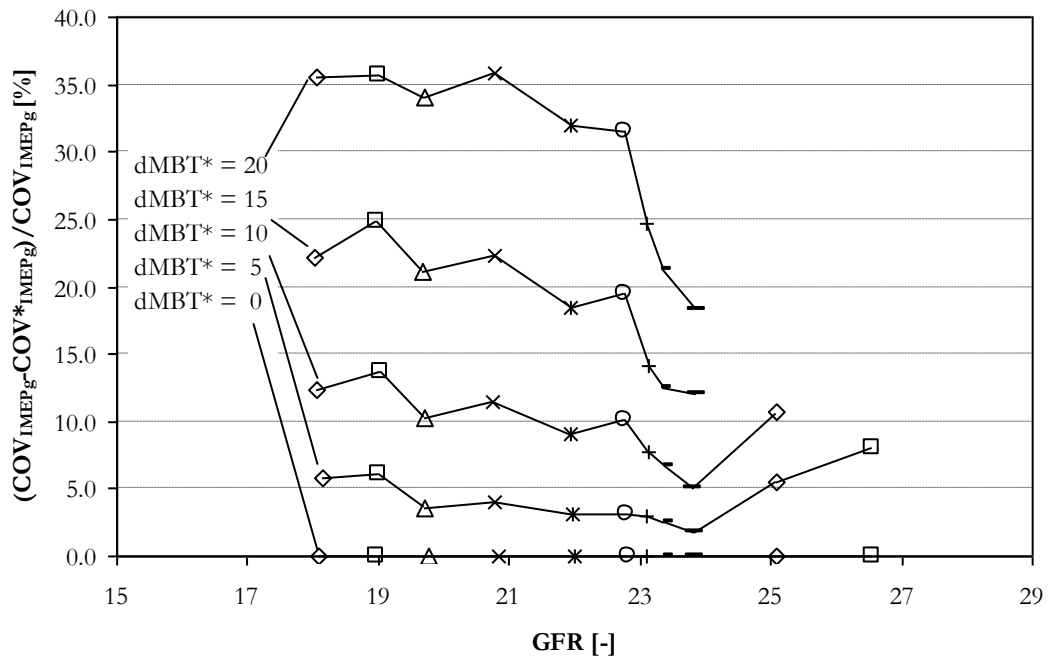
Figure 44

The % difference in COV_{IMEP_g} calculated using a constant value of mean $IMEP_g$ based on the value at dMBT* = 0 and the normally calculated value of COV_{IMEP_g}.
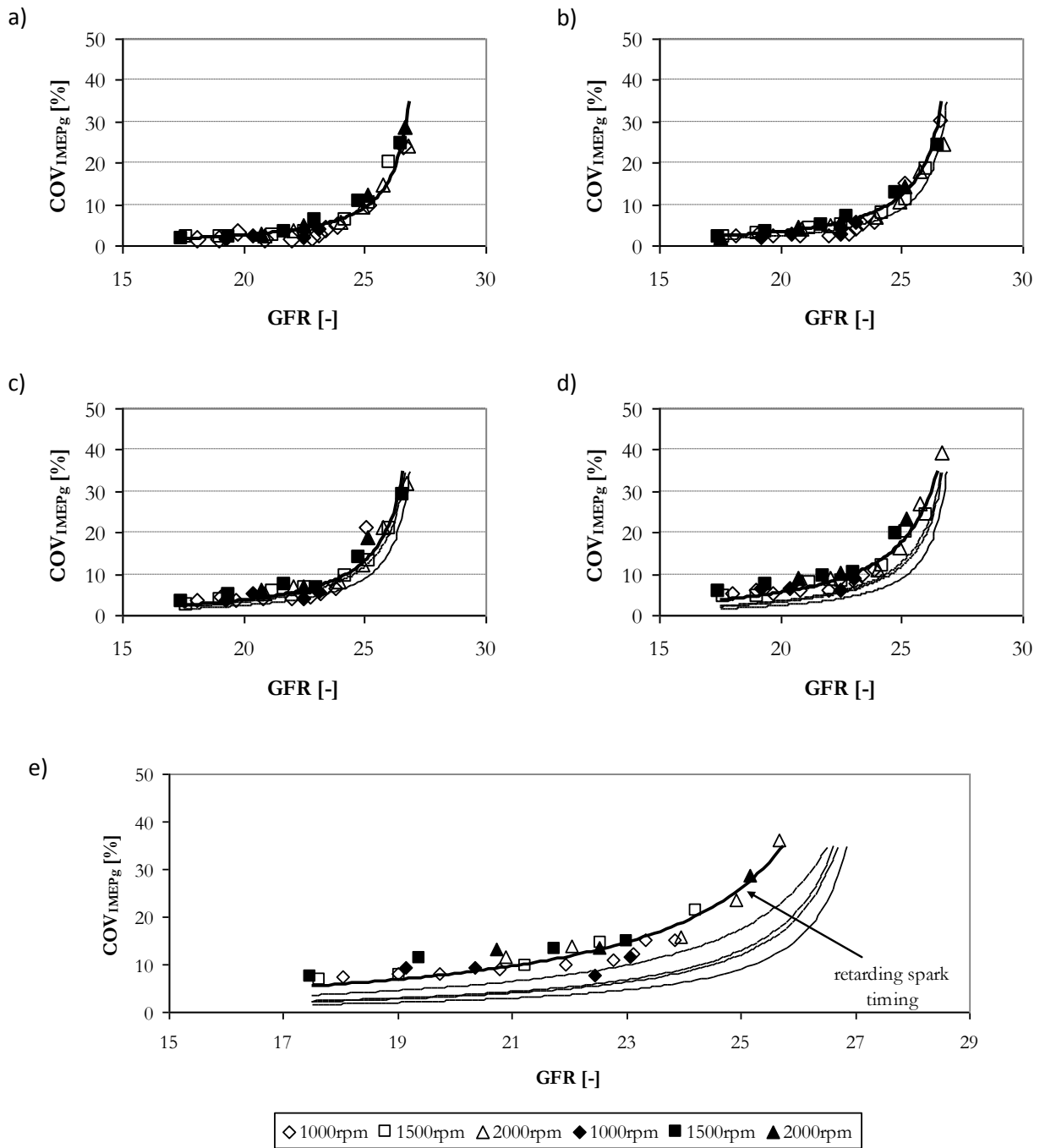
Figure 45

The change in COV_{IMEP_g} with GFR at different spark timings, a) MBT*, b) dMBT* = 5, c) dMBT* = 10, d) dMBT* = 15 and e) dMBT* = 20. Where the data for retarded spark timings is not corrected for the associated reduction in average $IMEP_g$. **Open symbols constant fuel test points, filled symbols constant air test points.**
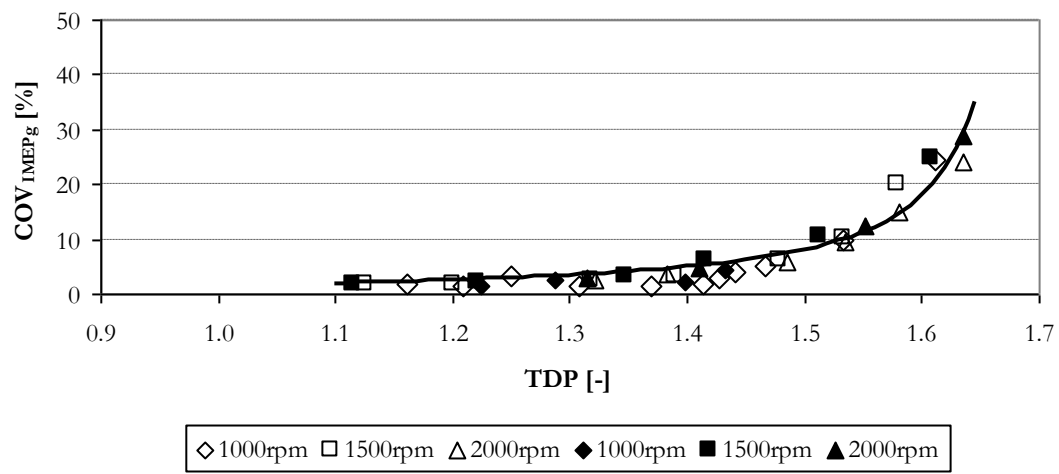
Figure 46
Change in COV_{IMEP_g} with TDP. Data as Figure 45 a).
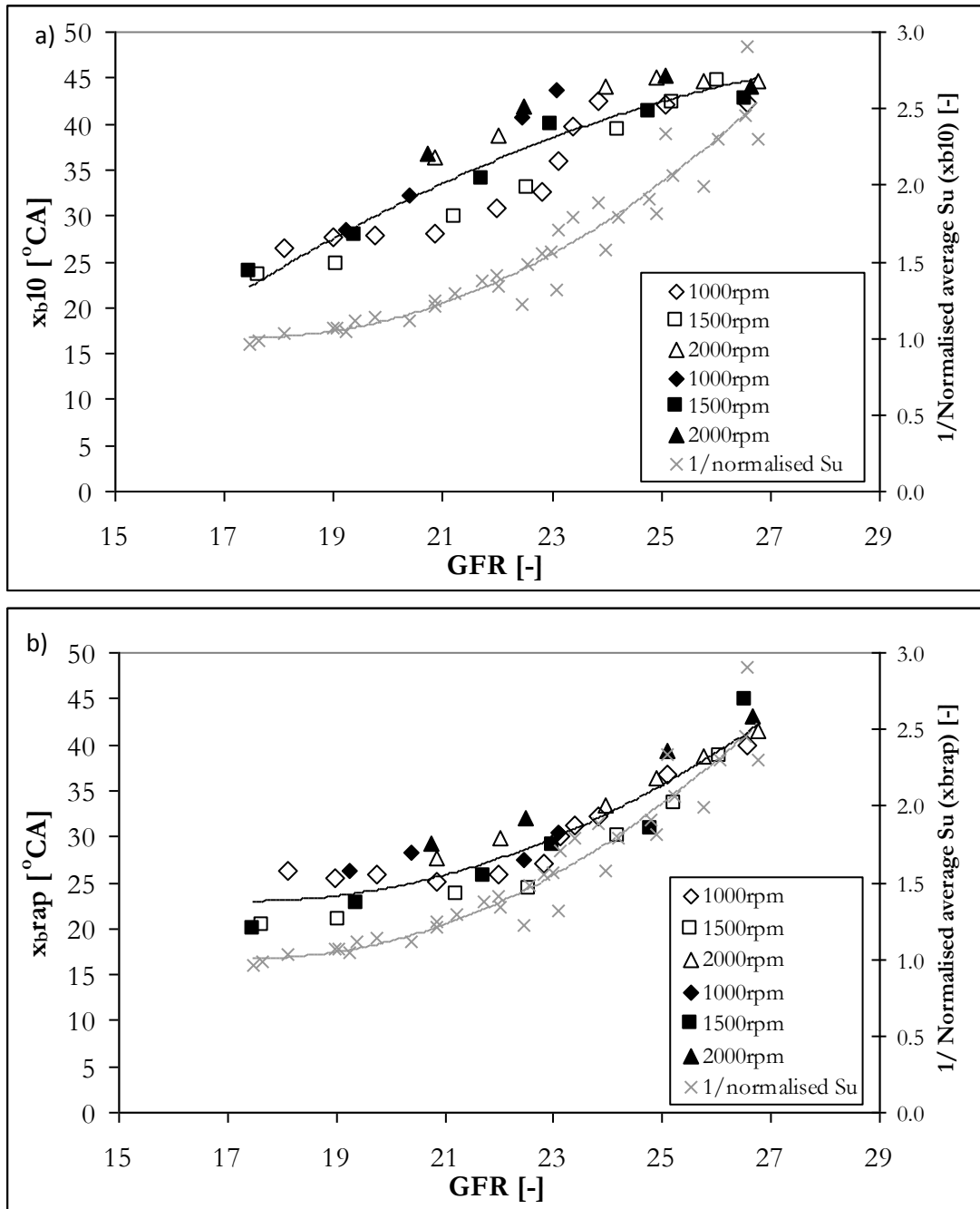
Figure 47

Change in (a) the flame development duration, $\Delta\theta_{0-10\%}$ and (b) the rapid burn duration, $\Delta\theta_{10-90\%}$ with increasing GFR. Open symbols constant fuel test points, filled symbols constant air test points. The laminar flame speed is described on the second y-axis. Where the values are 1/normalised S_u at a GFR of 18.0 extrapolated from the measured data. The S_u in both cases (a) and (b) is the average value calculated during the $\Delta\theta_{0-10\%}$ (xb10) and $\Delta\theta_{10-90\%}$ (xbrap).
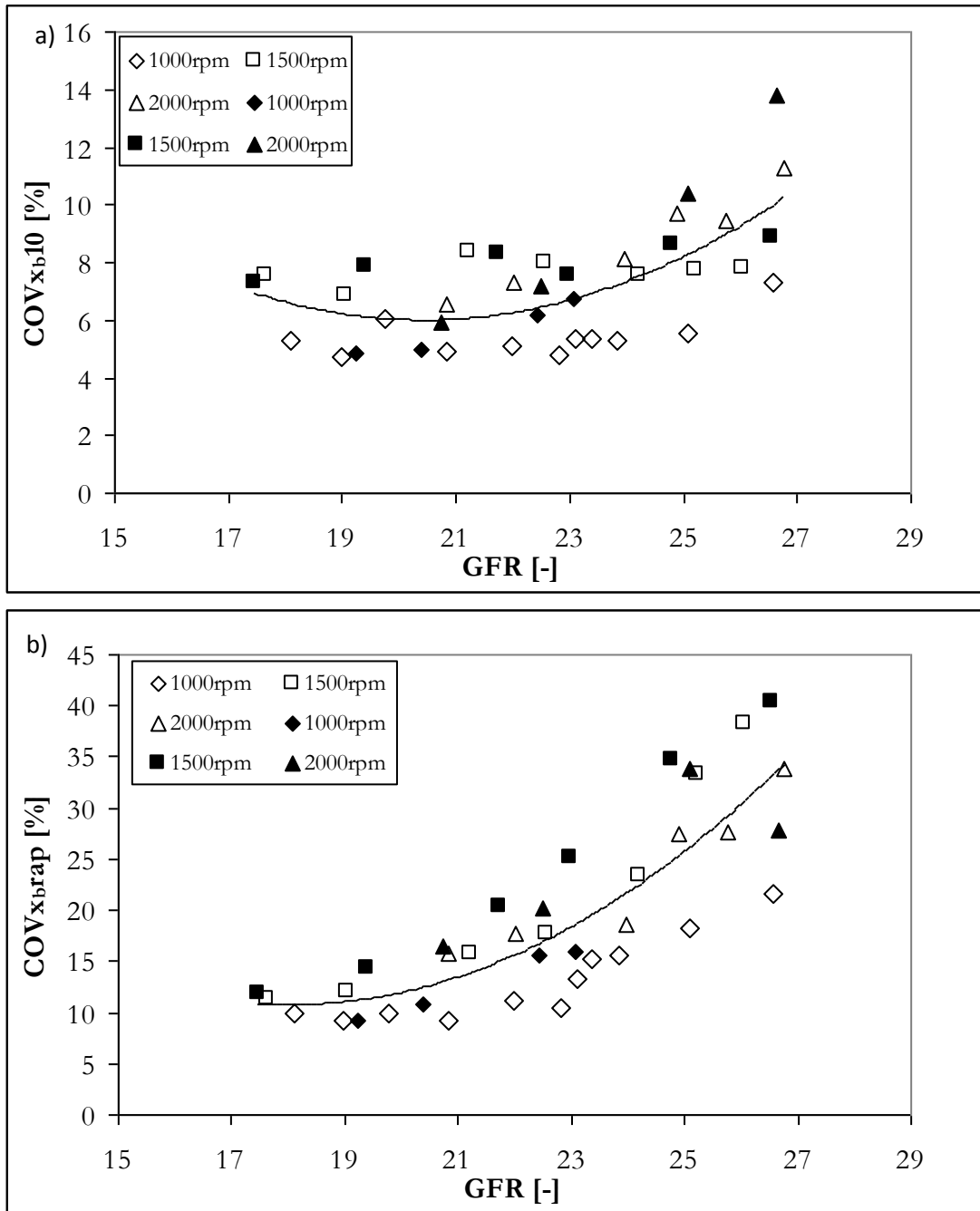
Figure 48
Change in (a) $COV_{\Delta\theta_{0-10\%}}$ and (b) the $COV_{\Delta\theta_{10-90\%}}$ with increasing GFR. Open symbols constant fuel test points, filled symbols constant air test points. Values calculated as stated in Chapter 3.
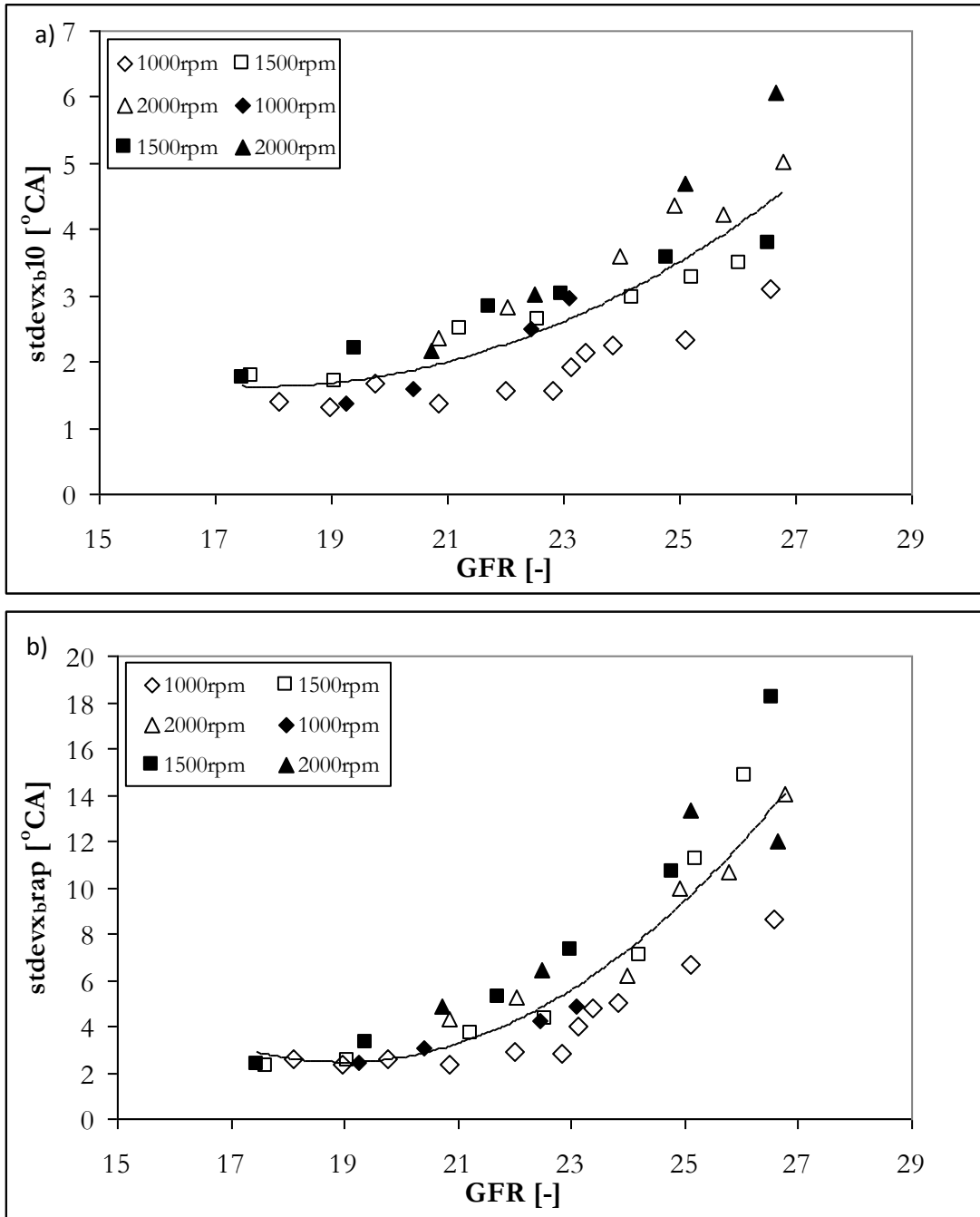
Figure 49

Change in (a) $stdev\Delta\theta_{0-10\%}$ and (b) the $stdev\Delta\theta_{10-90\%}$ with increasing GFR. Data shown as Figure 21.
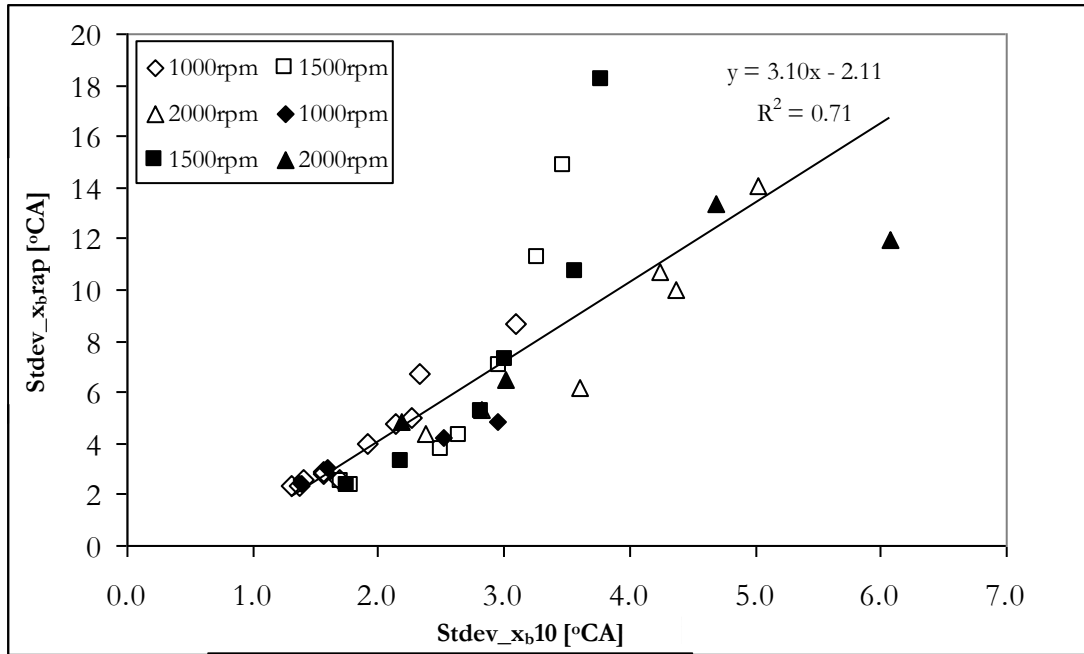
Figure 50
Correlation between $stdev\Delta\theta_{0-10\%}$ and $stdev\Delta\theta_{10-90\%}$. Data as Figure 21.
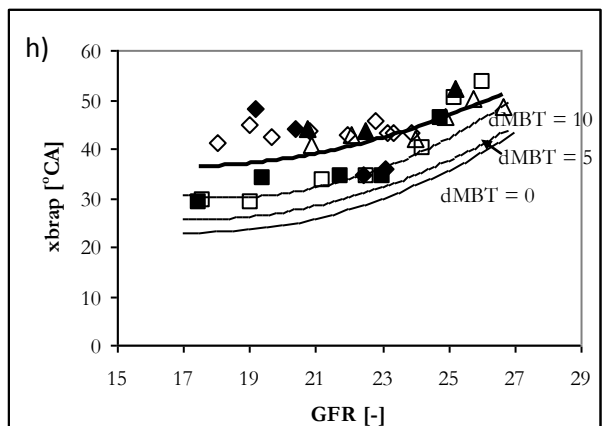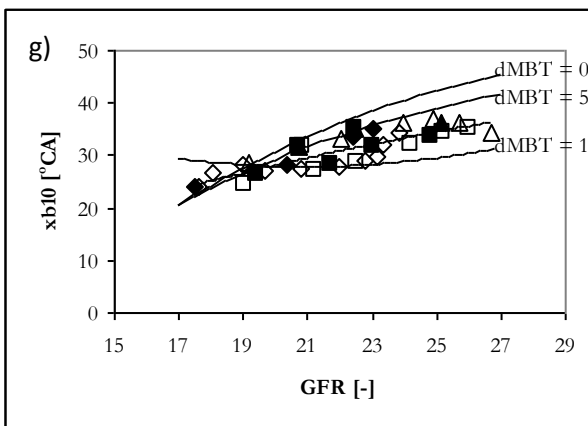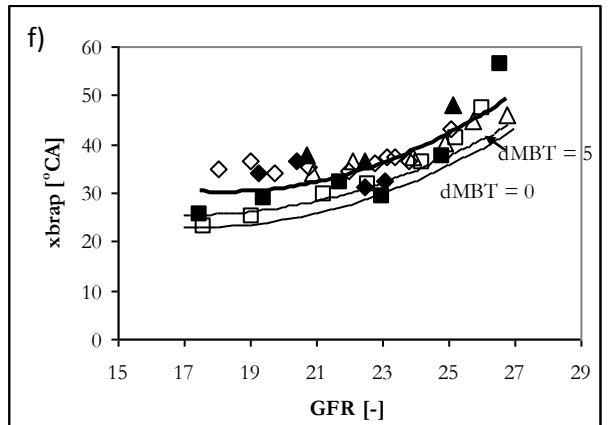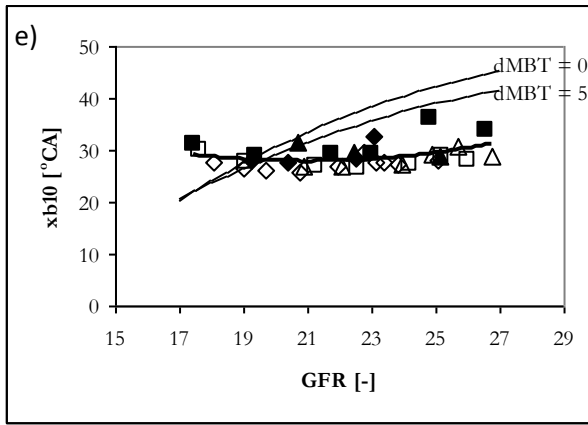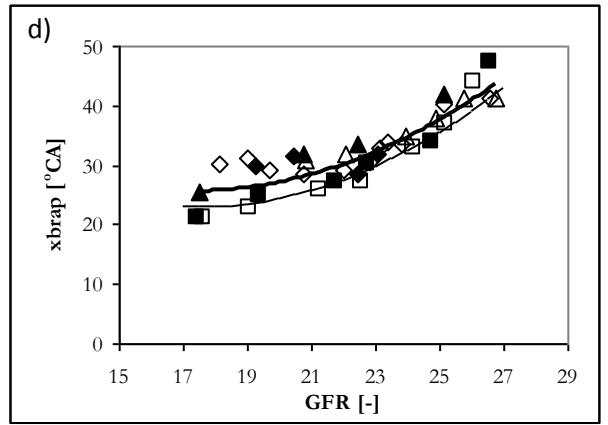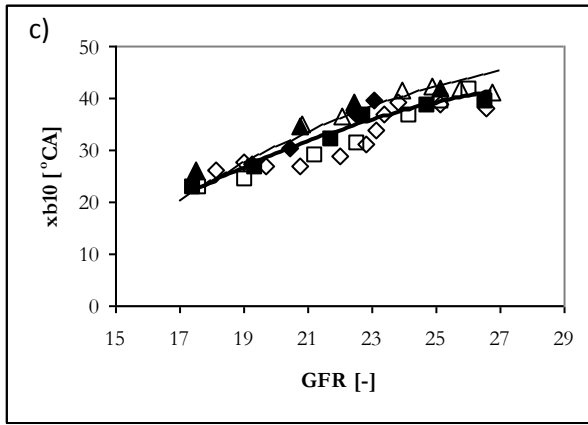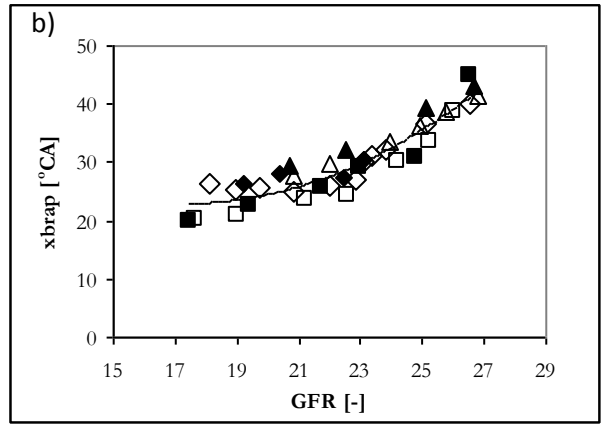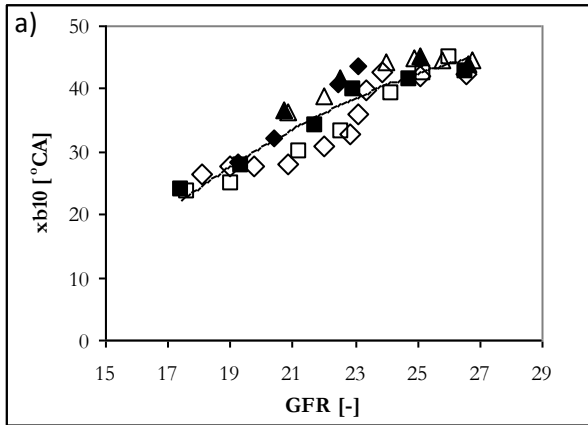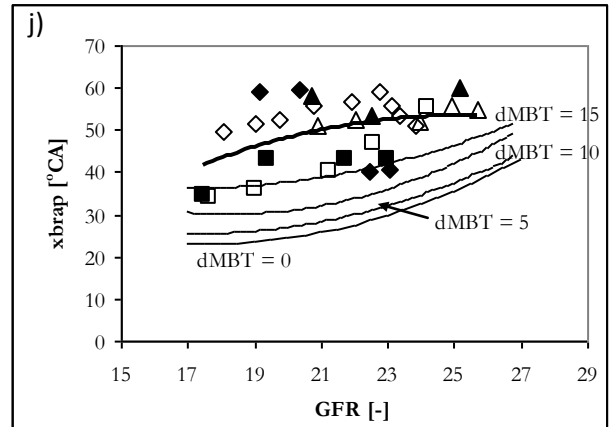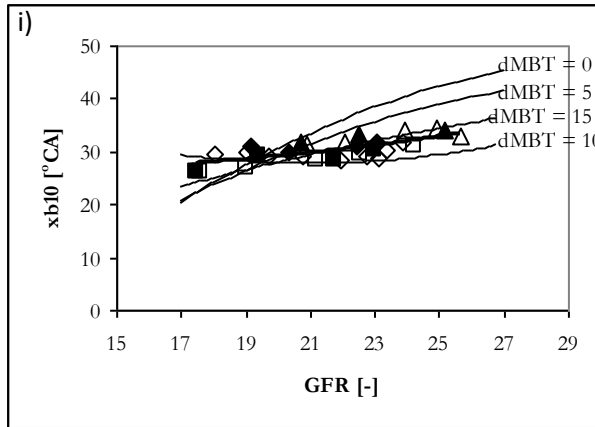
Figure 51

Change in $\Delta\theta_{0-10\%}$ and $\Delta\theta_{10-90\%}$ as the spark timing is retarded from MBT, where the maximum retard is 20, as a function of GFR. Where a and b are measured at MBT* spark timing, c and d dMBT*=5, e and f dMBT*=10, g and h dMBT*=15, i and j dMBT*=20. Data plotted as per legend in Figure 3.
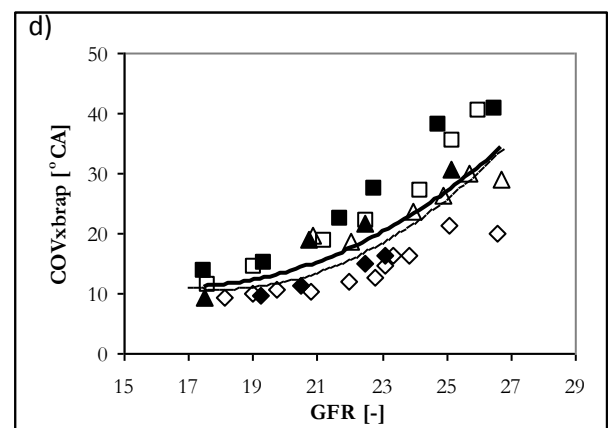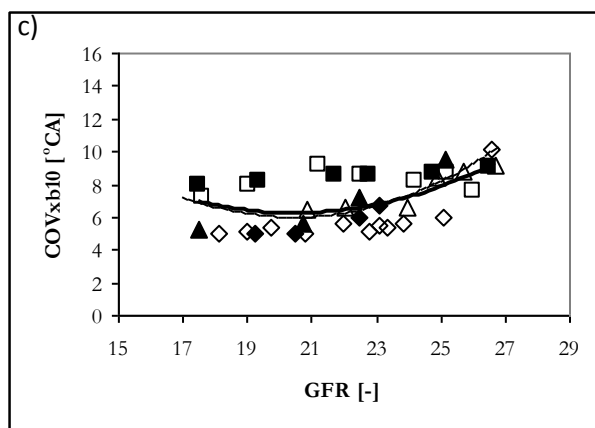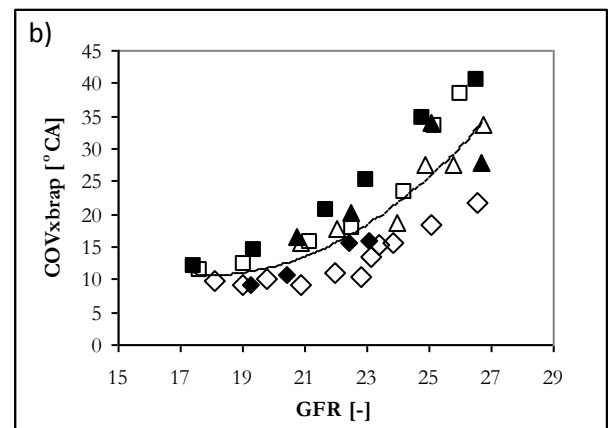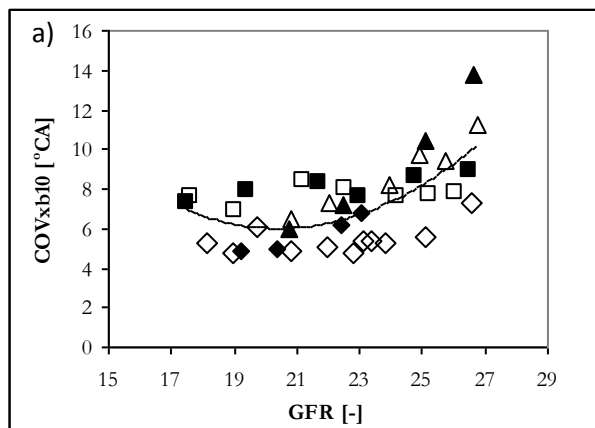
Note: Legend and continuation of figure on followng page
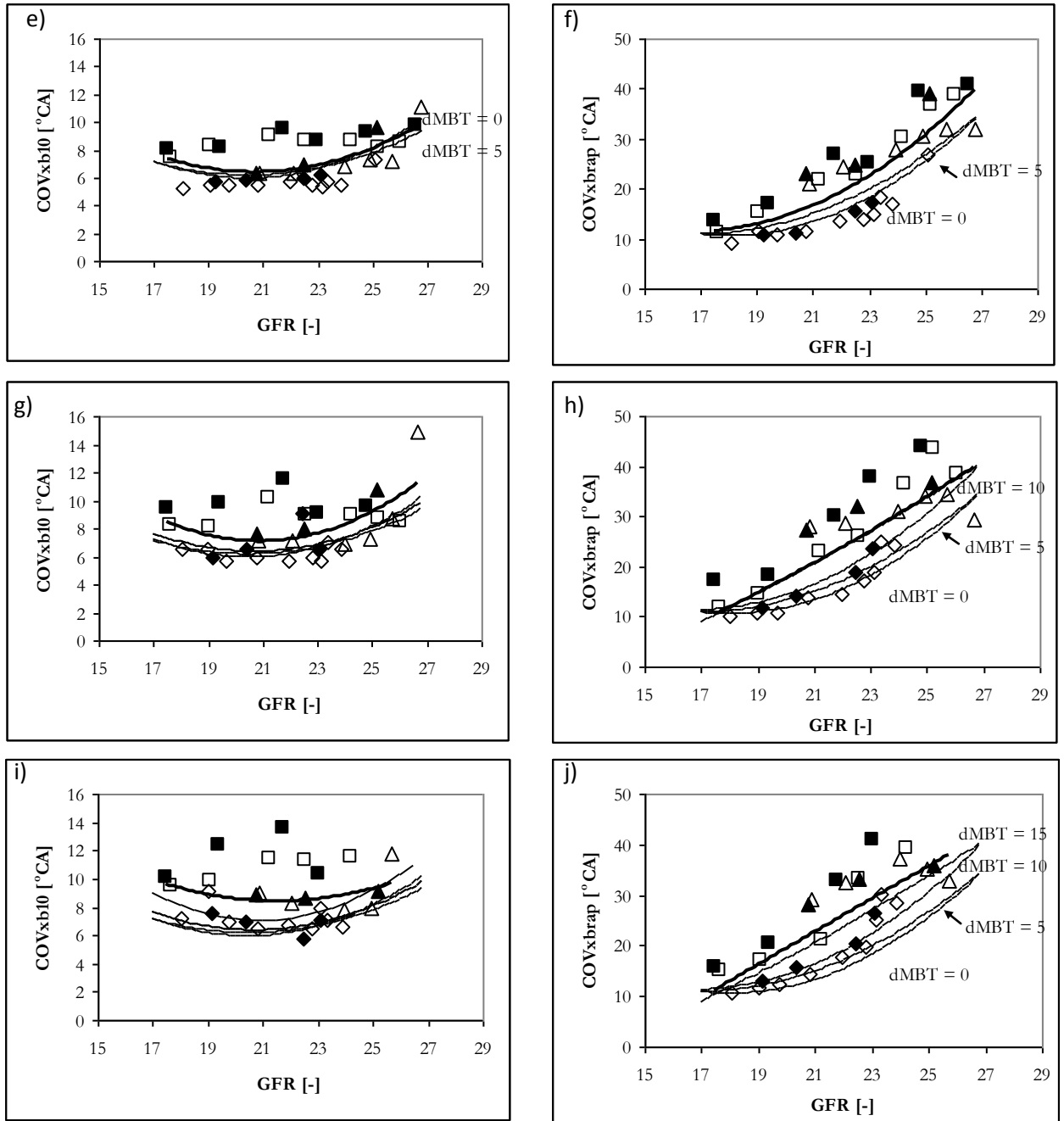
Figure 52

Change in $COV_{\Delta\theta_{0-10\%}}$ and $COV_{\Delta\theta_{10-90\%}}$ as the spark timing is retarded from MBT.
Data points as shown in Figure 36.
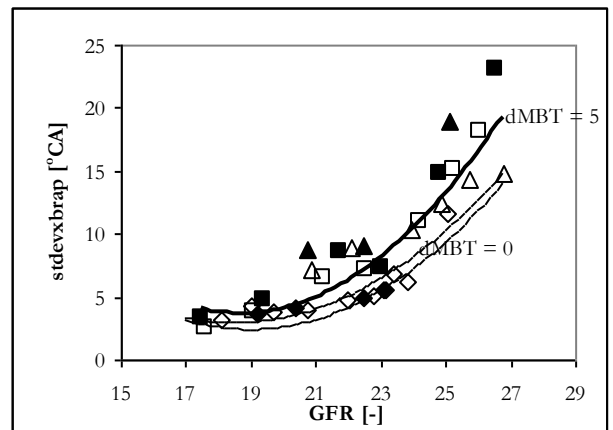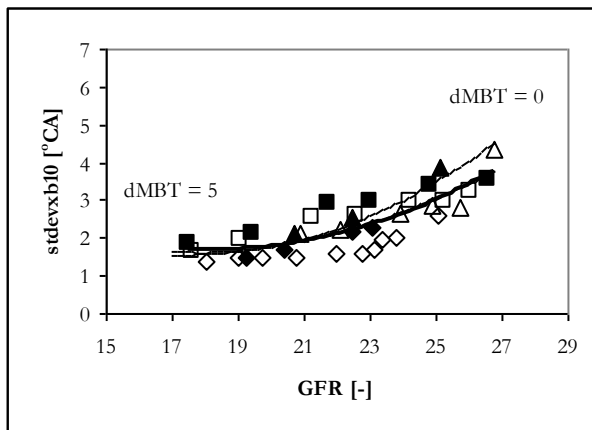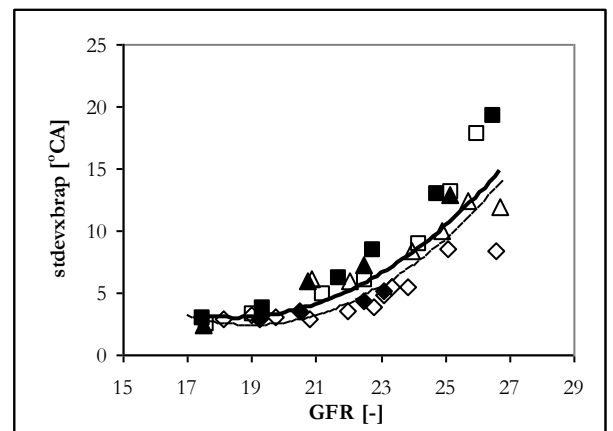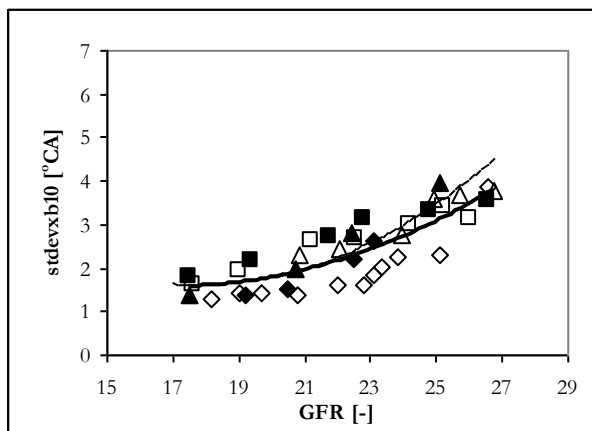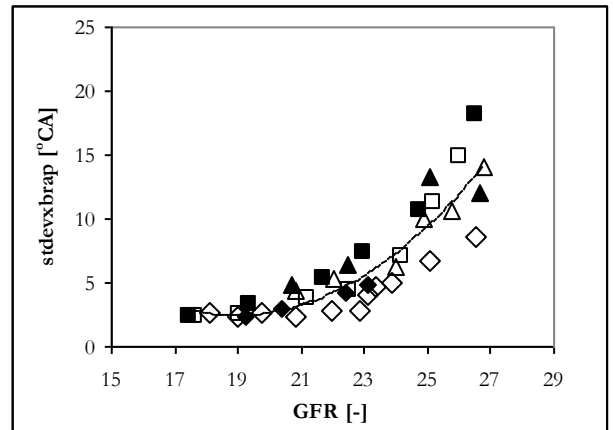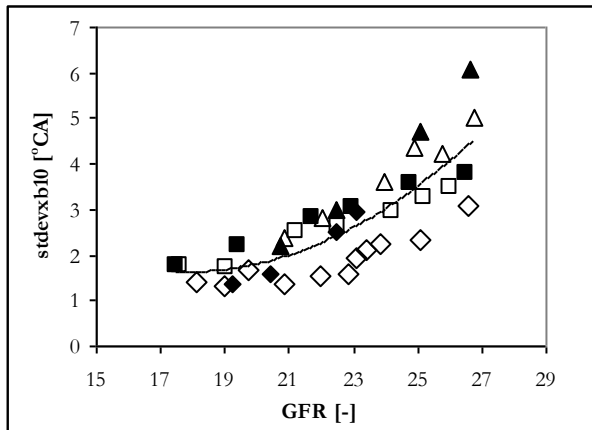
Note: Legend and continuation of figure on followng page
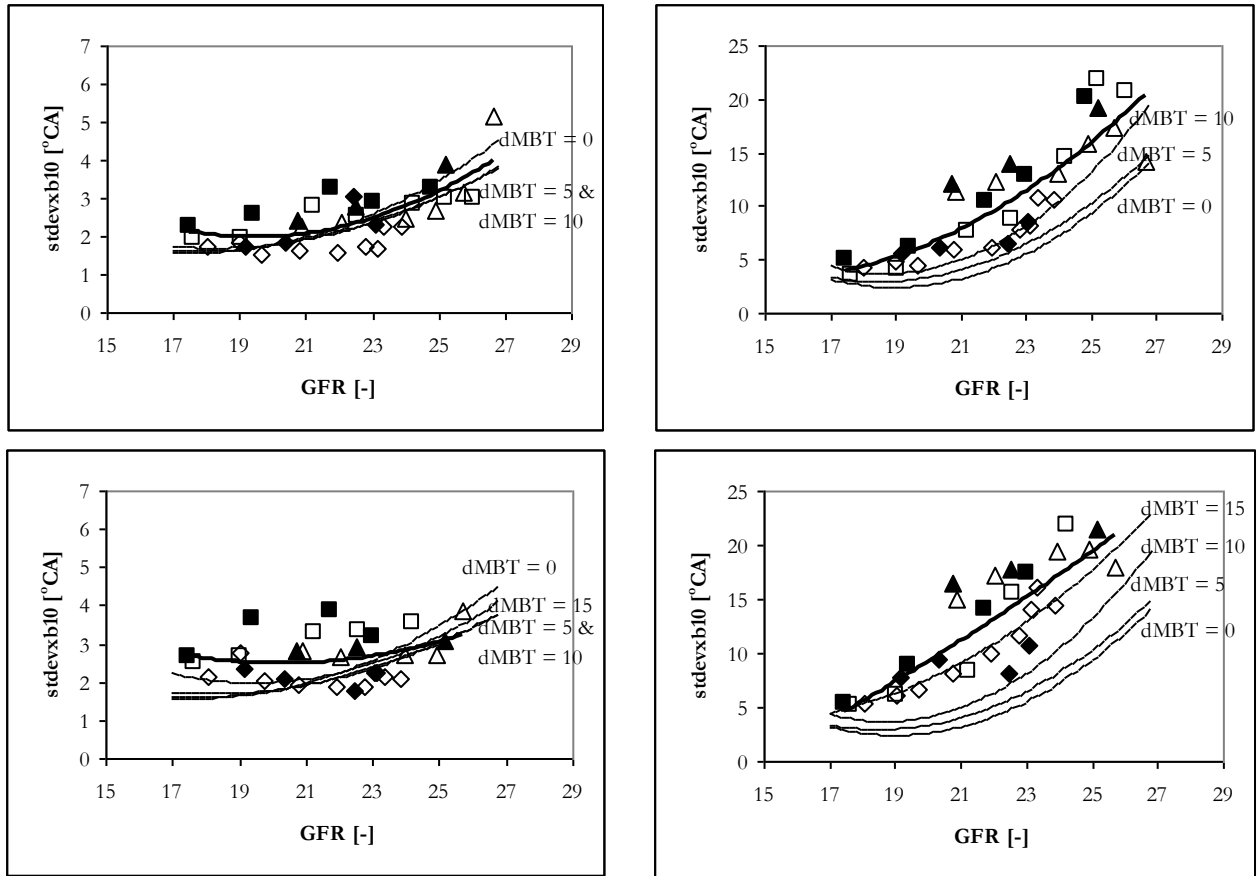
Figure 53

Change in $stdev\Delta\theta_{0-10\%}$ and $stdev\Delta\theta_{10-90\%}$ as the spark timing is retarded from MBT. Data points as shown in Figure 51.
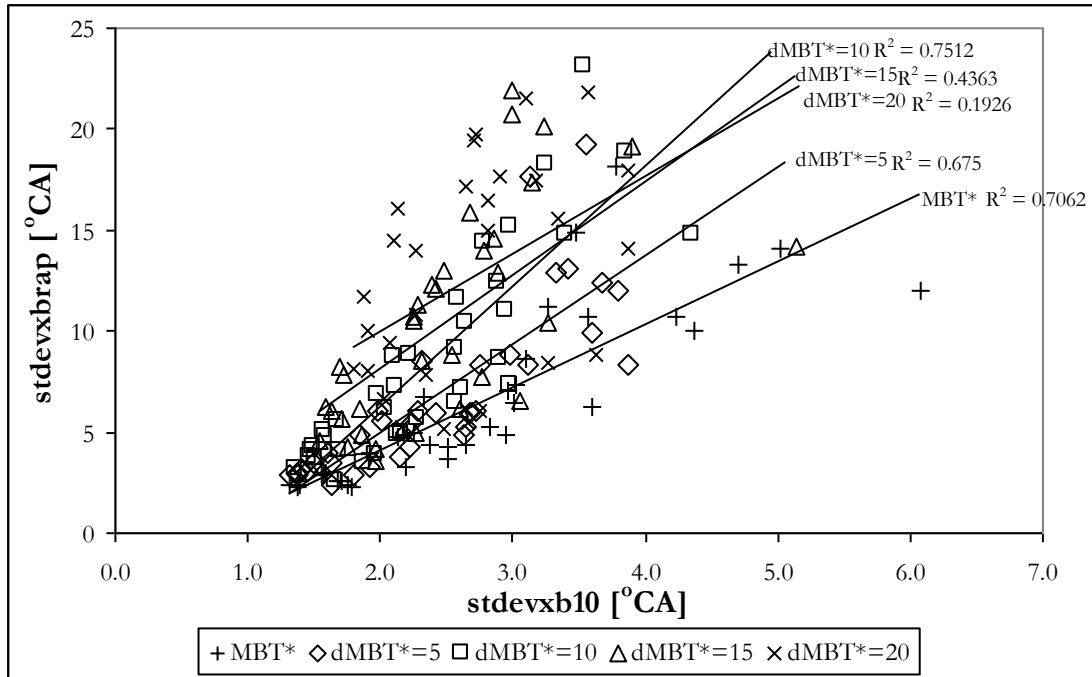
Figure 54

Correlation between $stdev\Delta\theta_{0-10\%}$ **and** $stdev\Delta\theta_{10-90\%}$ **for the four spark timing cases, MBT*, dMBT*=5, dMBT*=10, dMBT*=15 and dMBT*=20. Linear trendlines used in all cases**
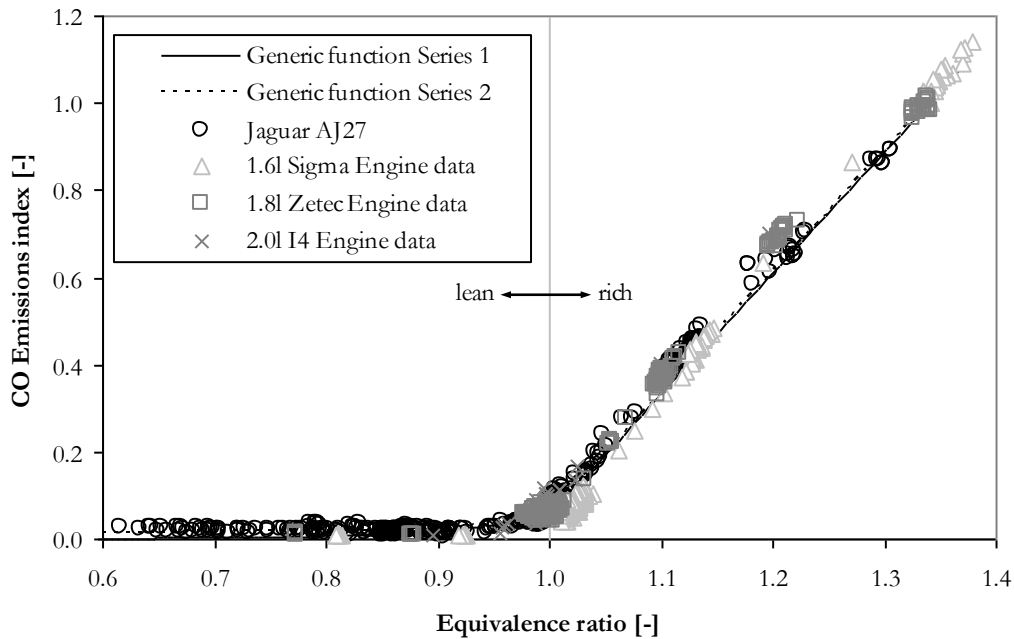
Figure 55

Carbon monoxide emission index as a function of equivalence ratio for four production engines (typical design, pentroof, four valve per cylinder), at a range of operating conditions. Specifically the AJ27 operating range is from idle (650rpm) to wide open throttle at 3500rpm, encompassing the full range of intake cam settings.
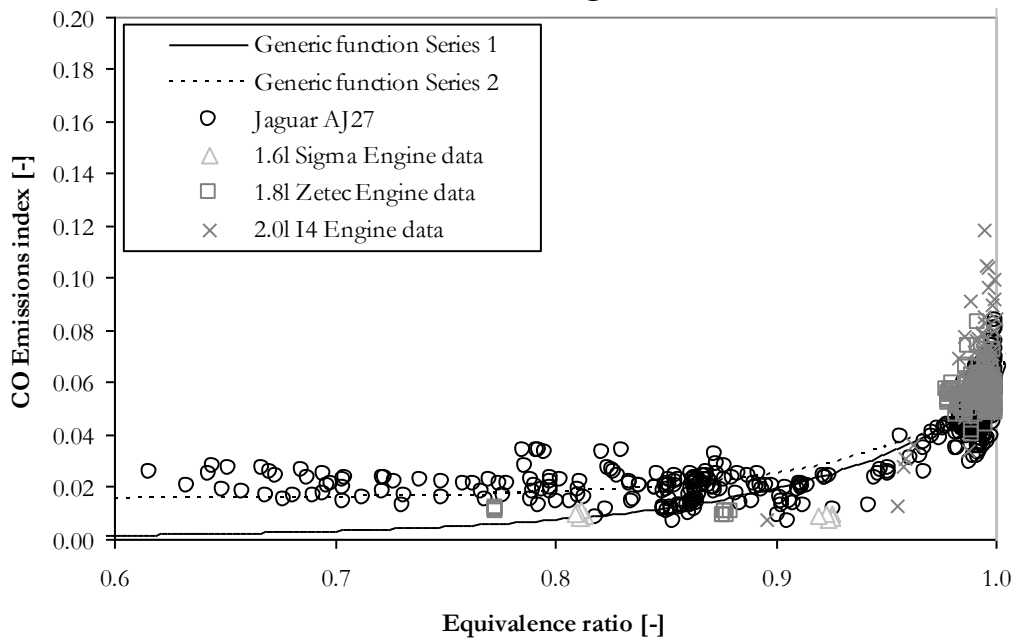
Figure 56

Highlighting the improved prediction of carbon monoxide emissions index by using generic function series 2.
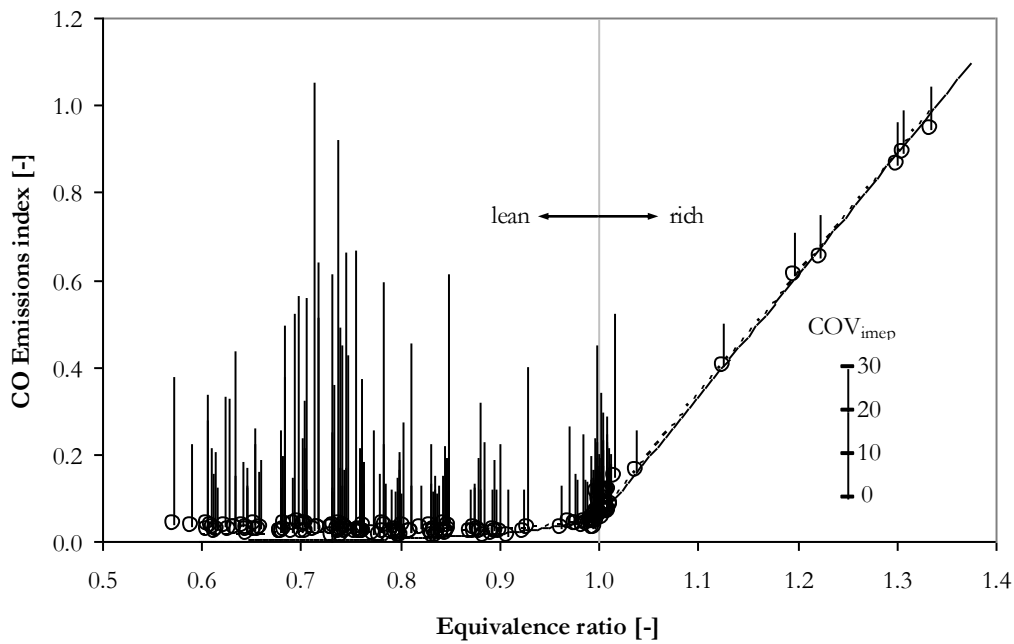
Figure 57
AJ27 carbon monoxide emissions index including operating point stability information (COV$_{IMEP}$). Height of each bar at each test point indicates the level of COV_{IMEP_n} **, higher the bar greater the level of instability.**
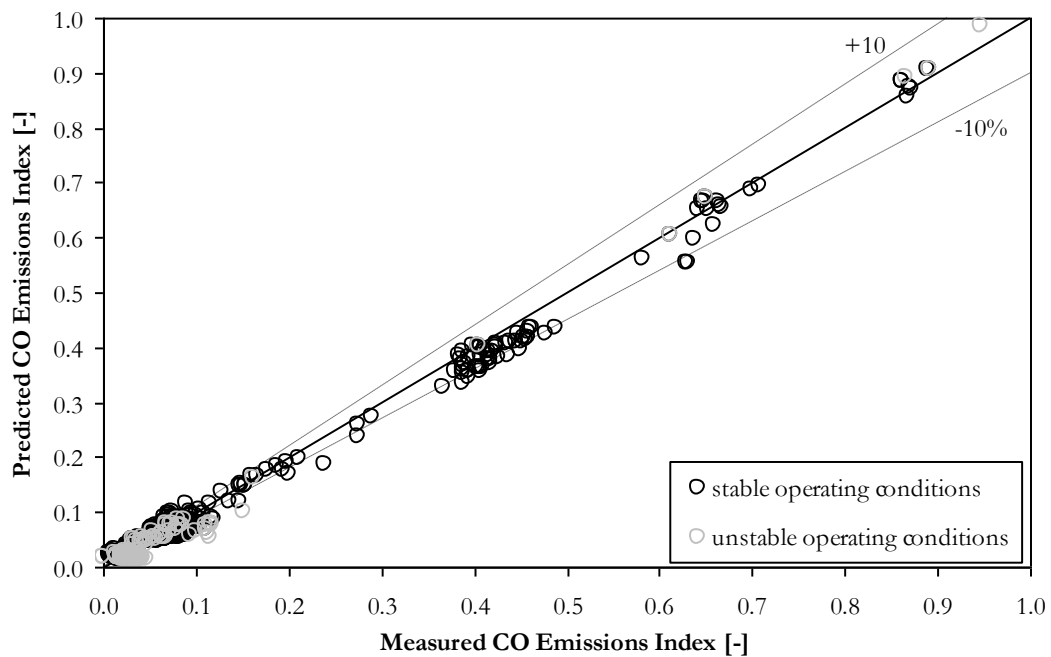
Figure 58
Performance of the carbon monoxide generic function for both unstable and stable operating points (where unstable is defined as COV_{IMEP_n} **>10).**
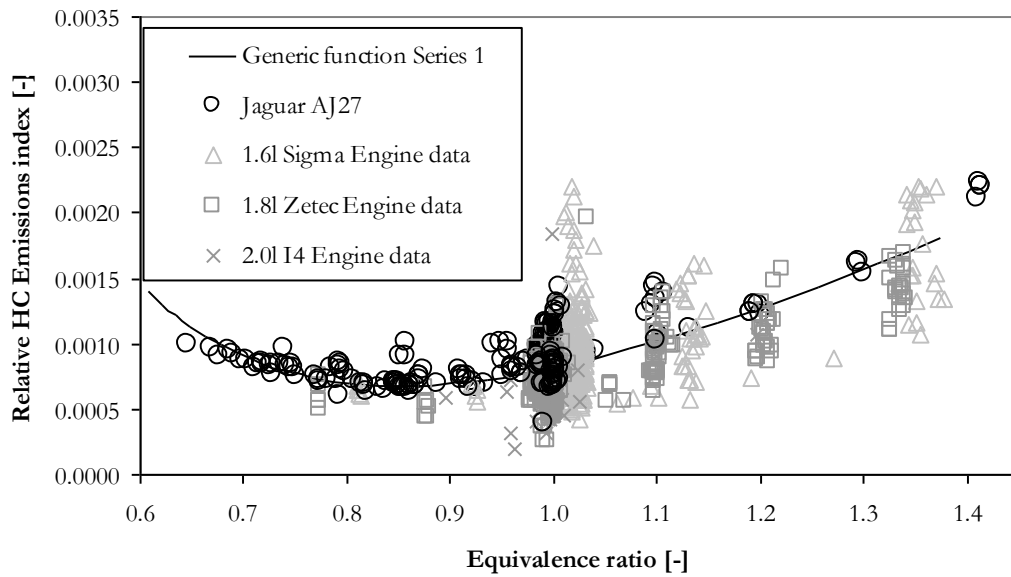
Figure 59
HC emissions index divided by GFR (relative HC emissions index) as a function of equivalence ratio. All data points are at MBT* spark timing, in the case of the AJ27 all the points shown COV$_{IMEP}$ <4.
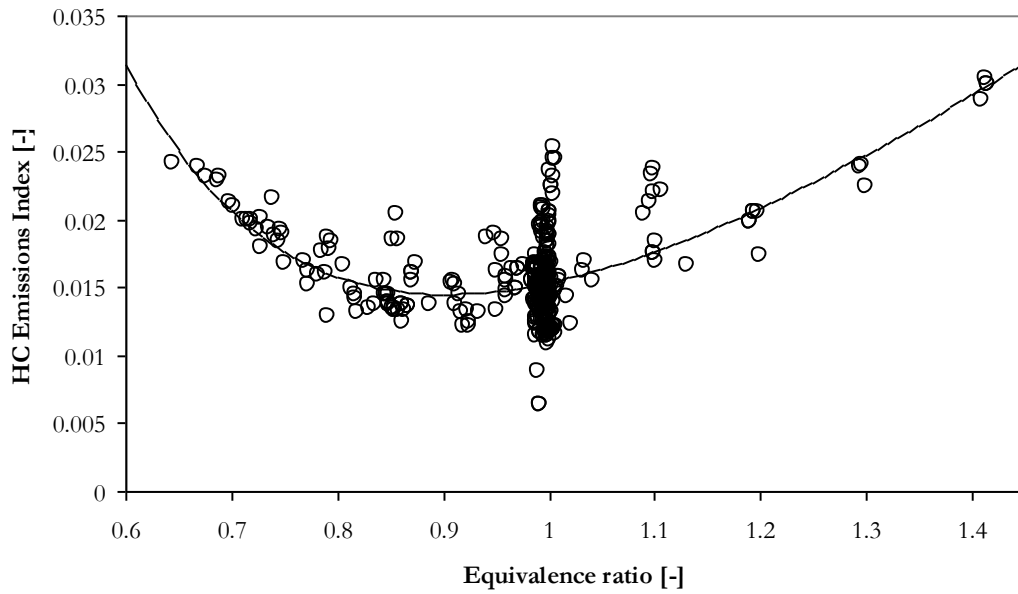
Figure 60
HC emissions index as a function of equivalence ratio, (AJ27 data as shown in Figure 59).
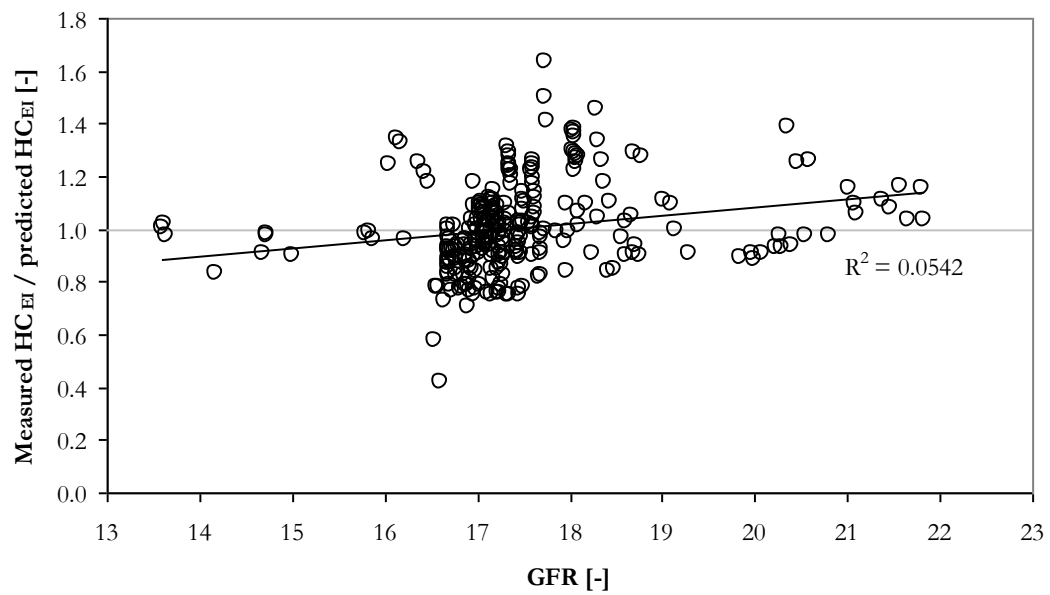
Figure 61
Correlation between HC emissions index and GFR.
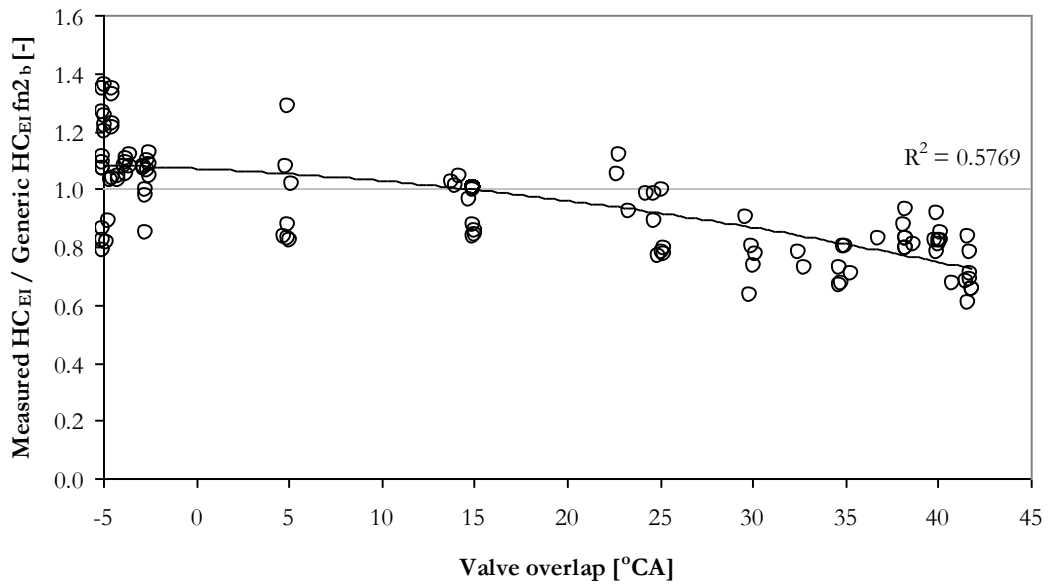
Figure 62

**The influence of valve overlap on the measured/predicted EI_{HC} error ratio.
Range of engine speeds, loads, and equivalence ratios**
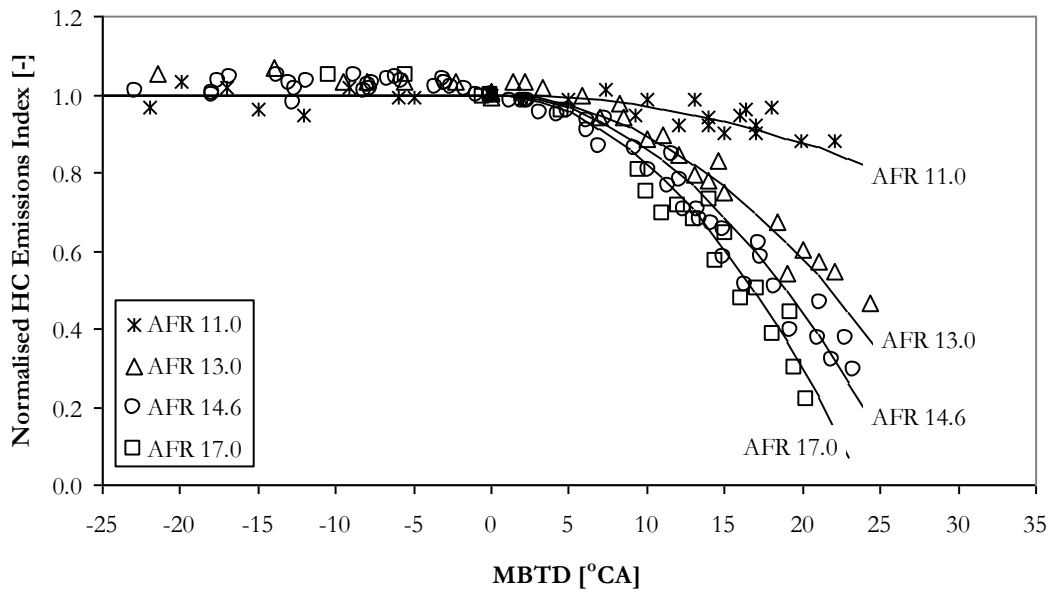
Figure 63
The effect of spark timing changes relative to the optimum for four different AFRs. The lines through the data are formed using the generic function 4b.
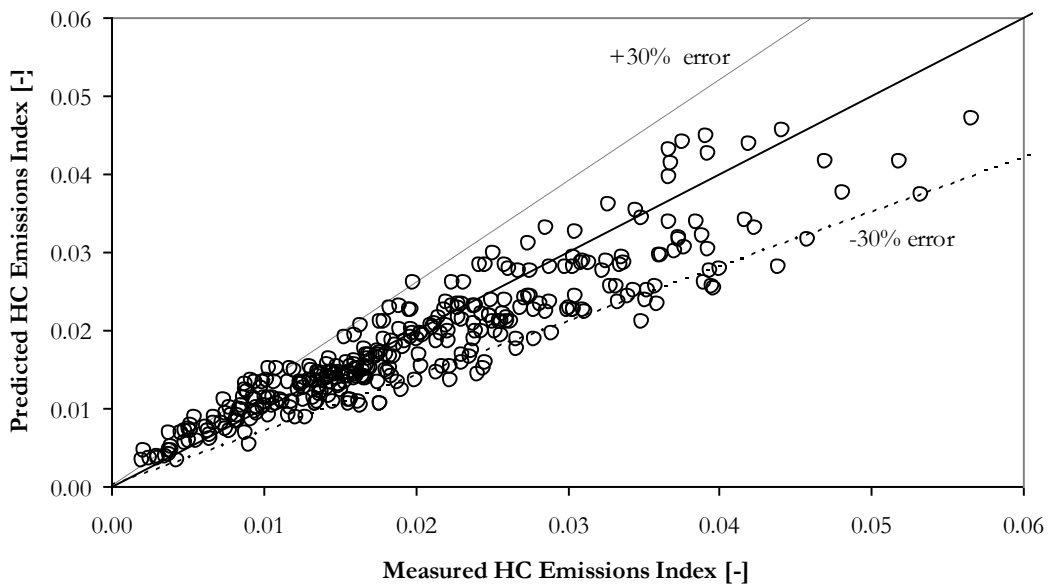
Figure 64
Overall performance of the HC generic function (equivalence ratio, valve overlap and dMBT). Idle to 3500rpm WOT, valve overlap from -5 to 42°CA and dMBT -15 to 20°CA.
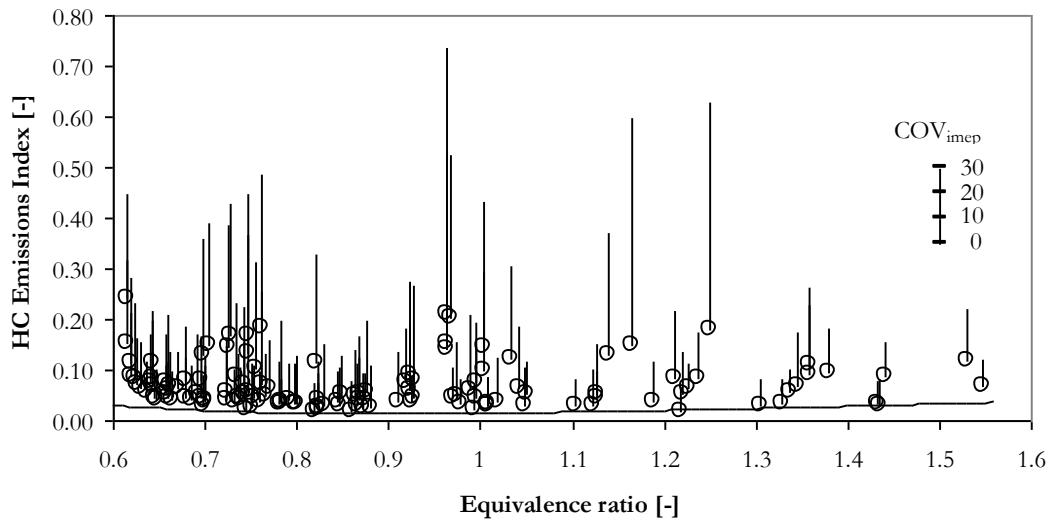
Figure 65
Effect of combustion instability on HC emissions index at MBT* operating conditions. The plotted line is generic function 2b. Height of each bar at each test point indicates the level of COV_{IMEP_n}, higher the bar greater the level of instability.
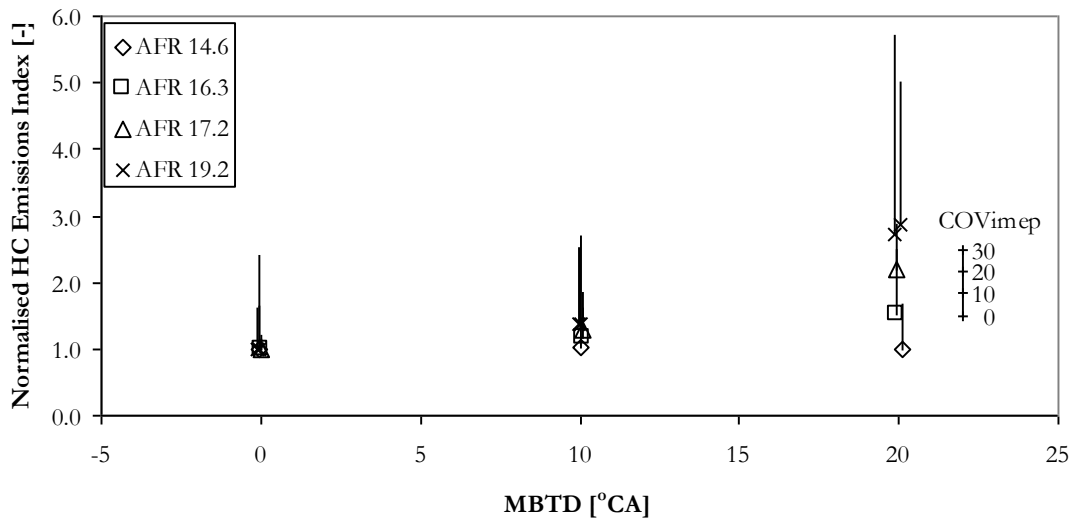
Figure 66
Effect of combustion instability reached by retarding the spark timing on HC emissions. Height of each bar at each test point indicates the level of COV_{IMEP_n}, higher the bar greater the level of instability.
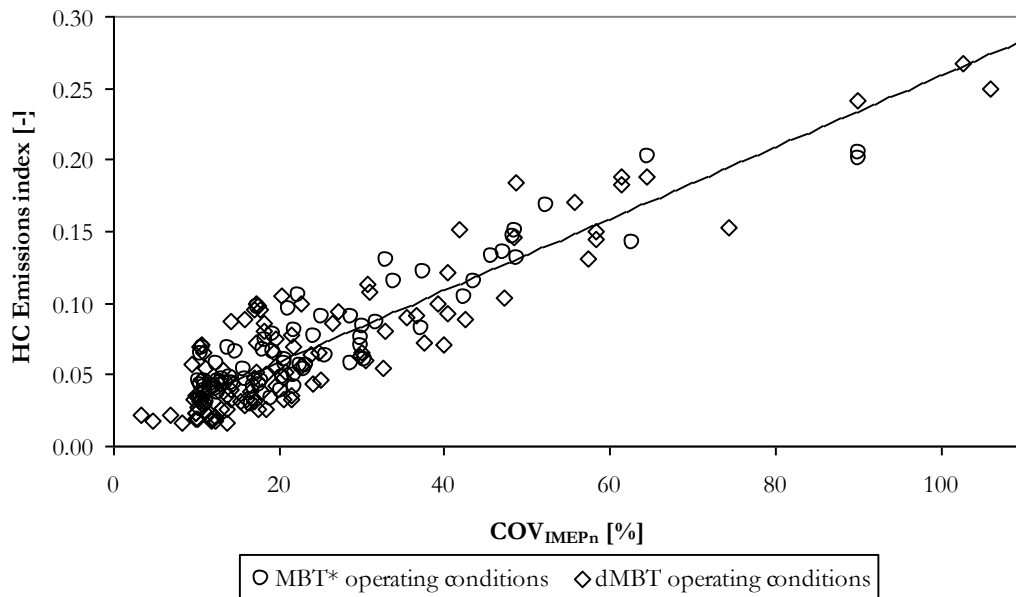
Figure 67
HC emissions index as a function of COV_{IMEPn}.
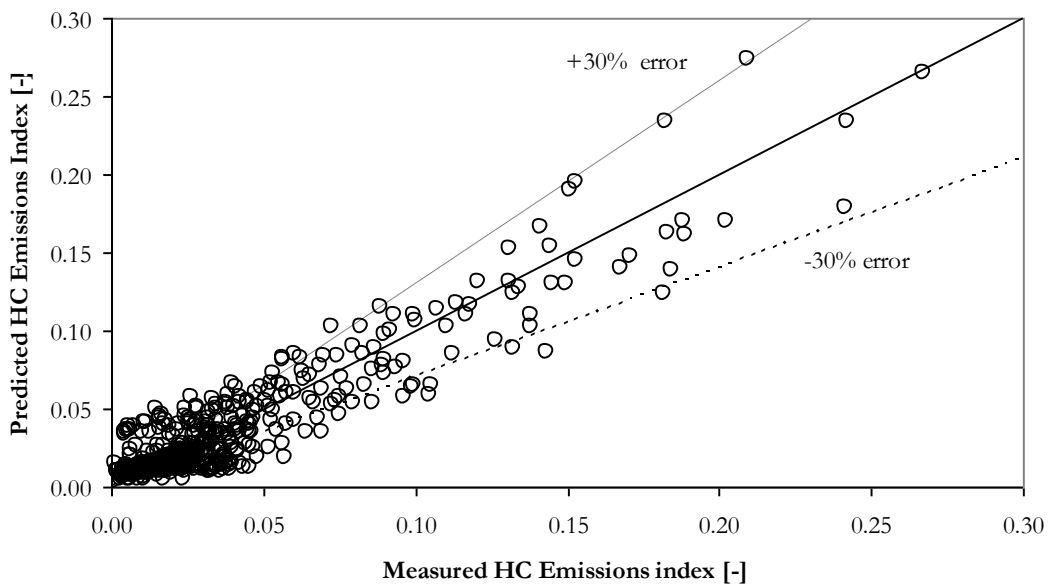
Figure 68
Performance of the HC generic function. Idle to 3500rpm WOT, valve overlap from -5 to 42°CA, dMBT -15 to 20°CA and COV_{IMEPn} from <1 to 106.
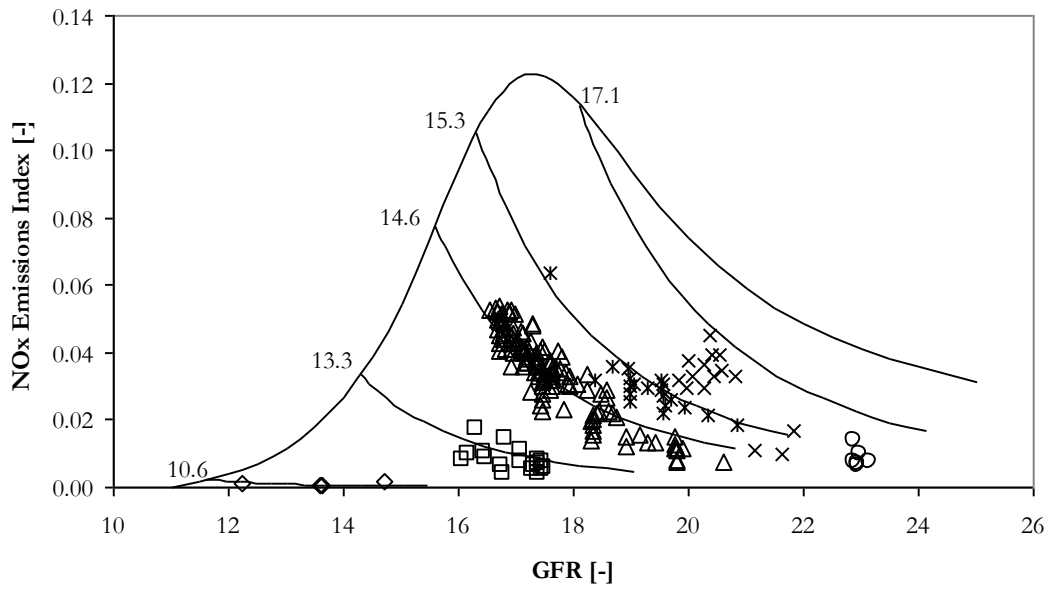
Figure 69
NOx emissions index as a function of GFR over a range of AFRs for the AJ27,
operating at MBT* spark timing. The range of GFR at a given AFR result from
variations in load and valve overlap.
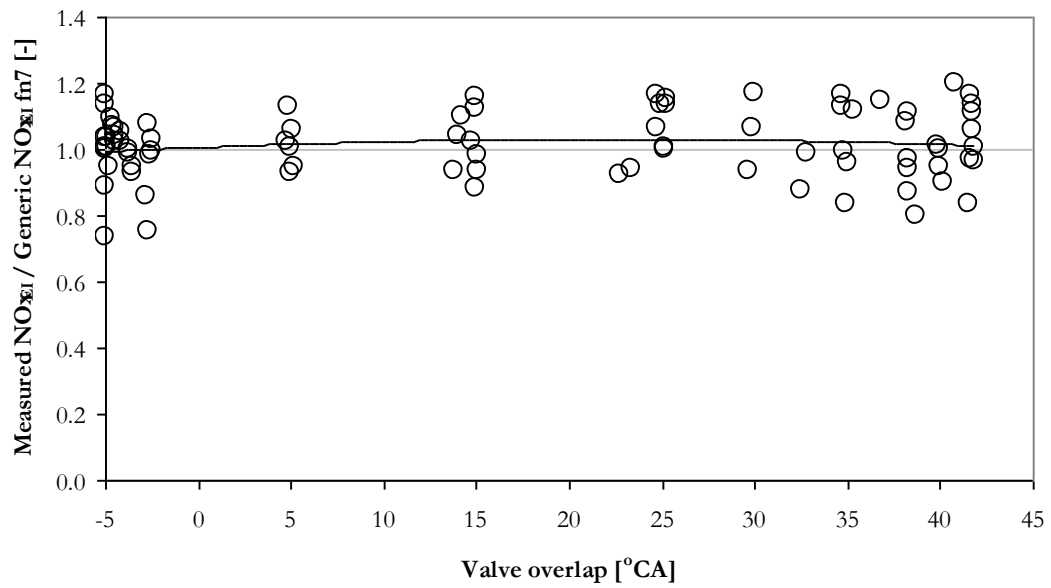
Figure 70
The influence of valve overlap on the measured/predicted EI_{NO_x} error ratio.
Range of engine speeds, loads, and AFRs at MBT* spark timing.
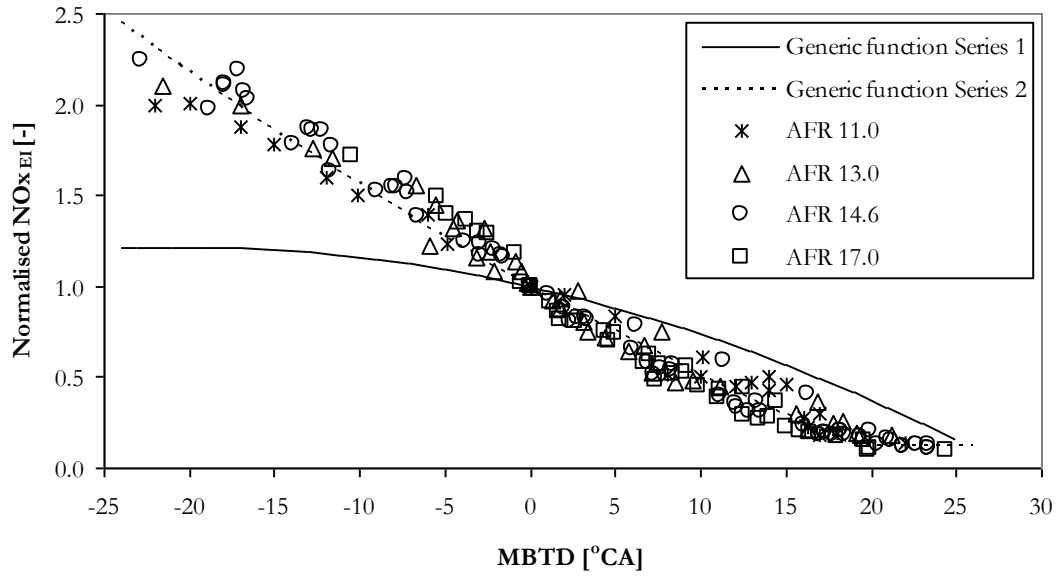
Figure 71

The effect of spark advance and retard from the optimum on EI_{NO_x} at a range of AFR's, engine speeds, loads and valve overlaps. Series 1 is the original generic function, series 2 is the modified generic function fitted to AJ27 data.
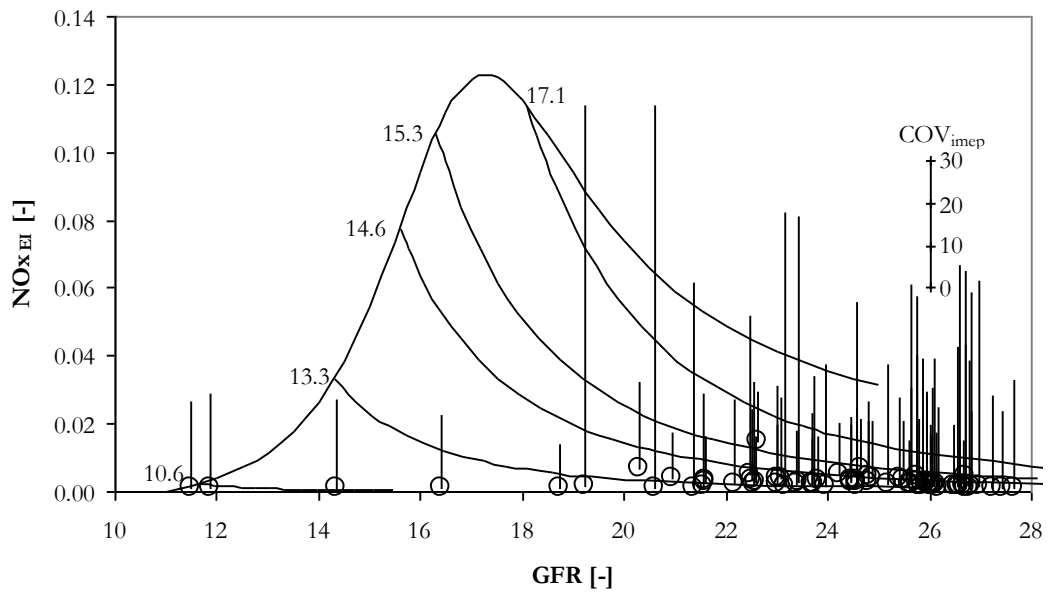
Figure 72

Effect of combustion instability on EI_{NO_x} at MBT* operating conditions at a range of AFR's, engine seeds, loads and valve overlaps.
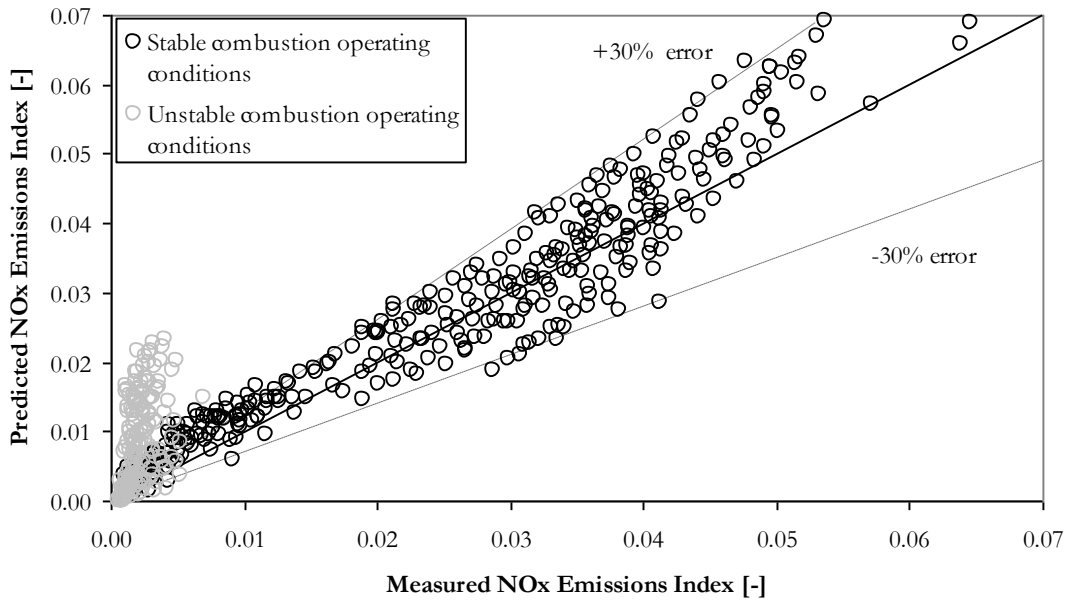
Figure 73
NOx Generic function performance for stable and unstable combustion operating conditions.
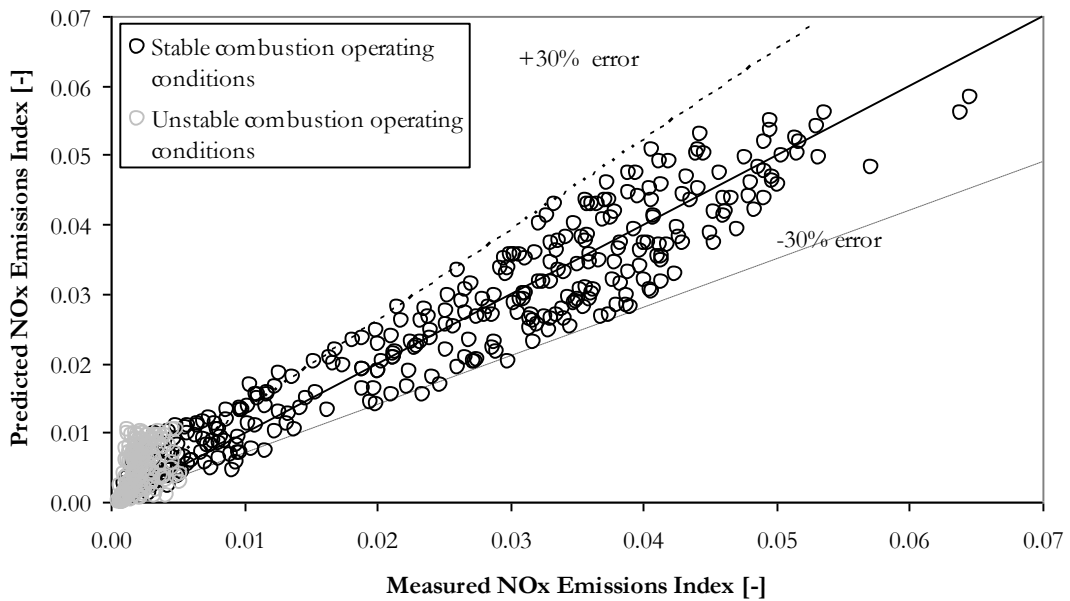
Figure 74
NOx Generic function performance for stable and unstable combustion operating conditions, with altered x_b dependence.
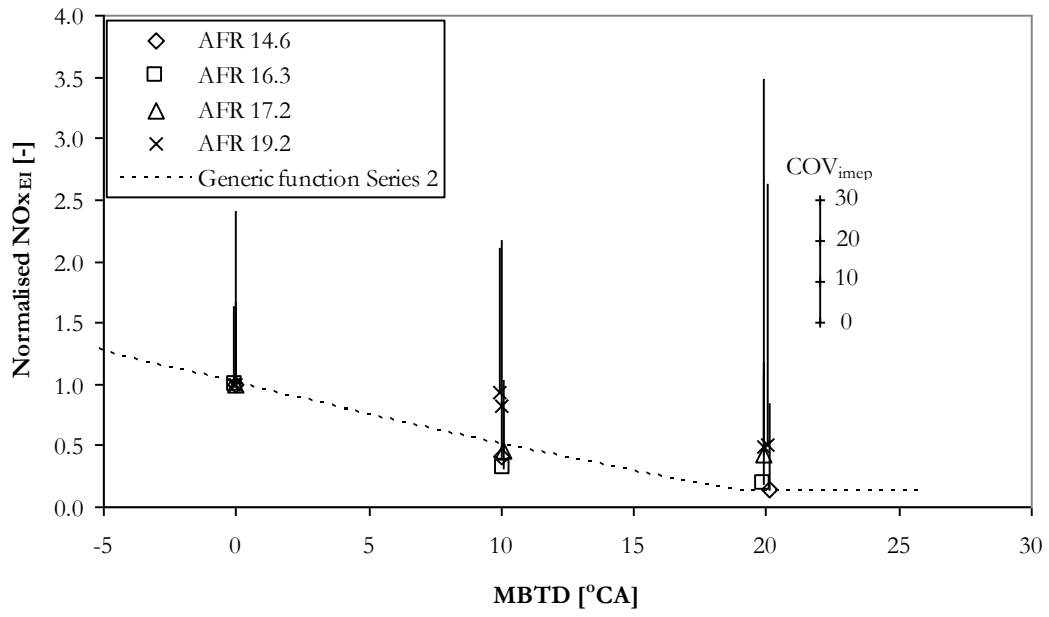
Figure 75

Effect of combustion instability reached by retarding the spark timing on EI_{NO_x} **.**

Figure 76
Influence of new emissions models over the NEDC. In all three cases the new model is shown before the original. (a) and (b) comparing CO emissions, (c) and (d) HC emissions, (e) and (f) NOx emissions

Figure 76
Influence of new emissions models over the NEDC. In all three cases the new model is shown before the original. (a) and (b) comparing CO emissions, (c) and (d) HC emissions, (e) and (f) NOx emissions
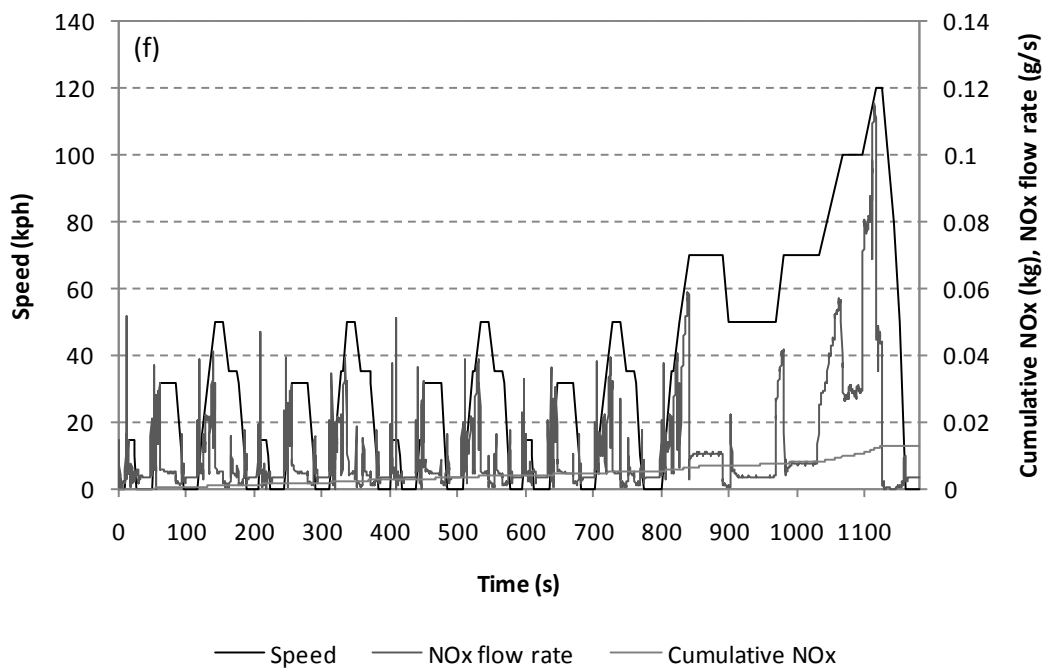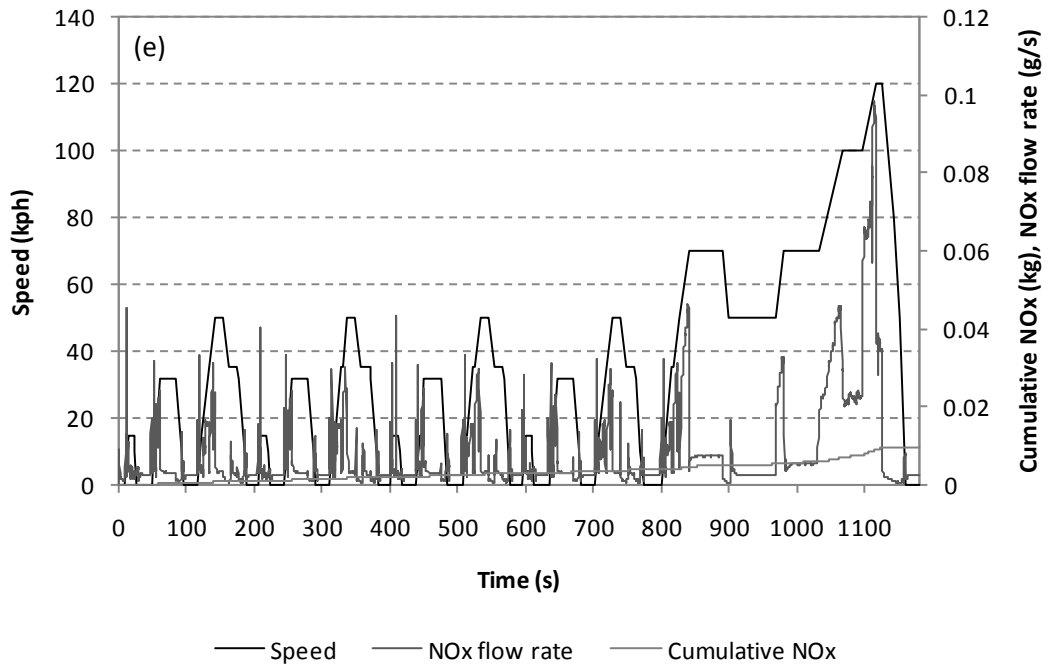
Figure 76
Influence of new emissions models over the NEDC. In all three cases the new model is shown before the original. (a) and (b) comparing CO emissions, (c) and (d) HC emissions, (e) and (f) NOx emissions

Figure 77
Difference plots (New emissions flow rate – Old emissions flow rate) over the NEDC. (note difference between old and new CO mostly 0, hence it appears no data plotted)
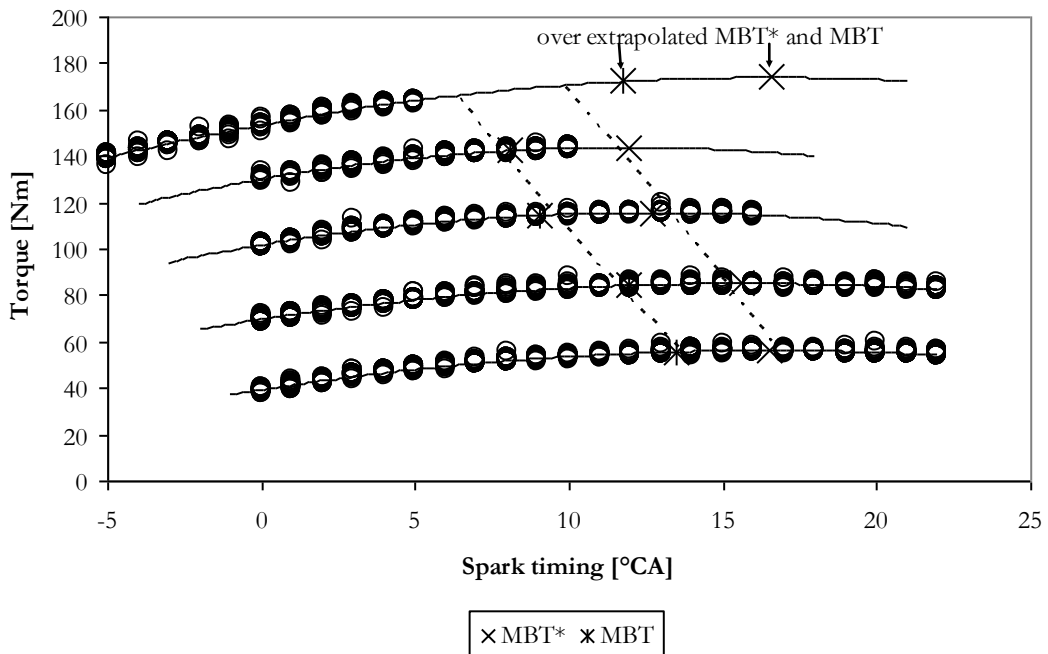
Figure 78
Knock limited spark sweep at high loads causing over extrapolation of MBT* and MBT spark timing.
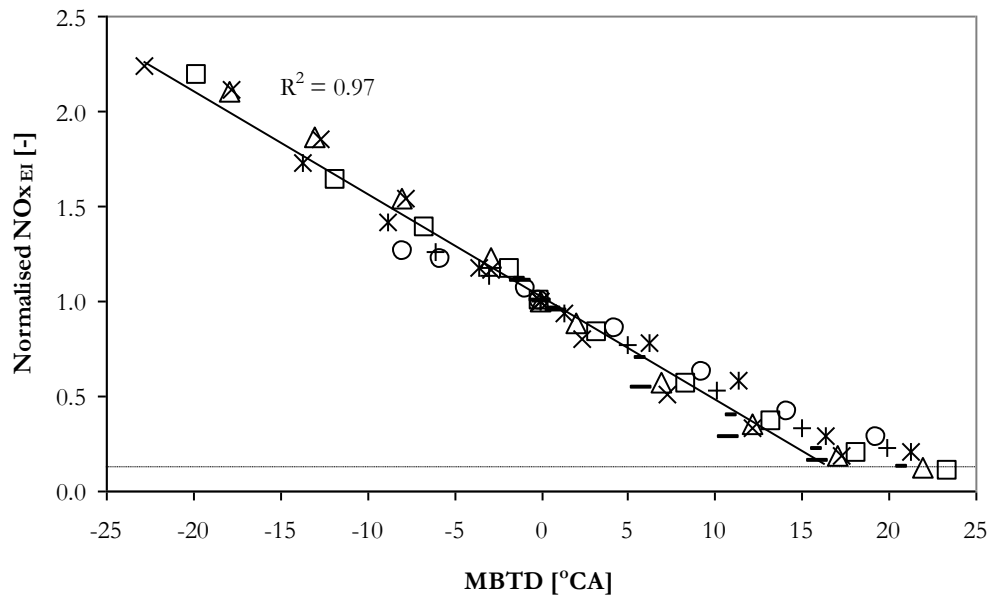
Figure 79
Linear relationship between relative spark timing (-23 to 16) and normalised EI_{NO_x}. Eight individual spark sweeps at 650rpm, 1500rpm, 2000rpm and 3000rpm, light and medium load. Baseline is 0.12 of MBT* EI_{NO_x}.
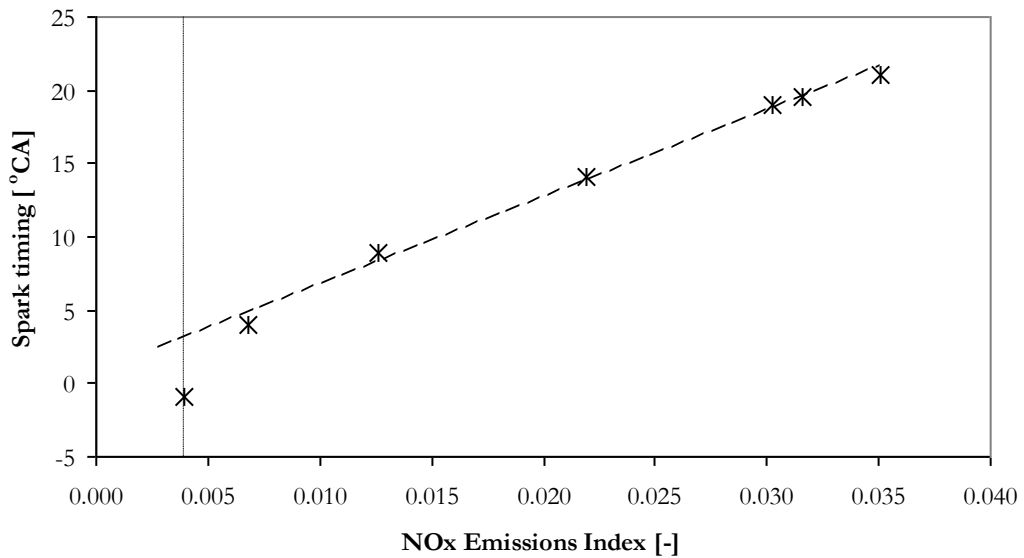
Figure 80
The application of the method to calculate relative spark timing from measured EI_{NO_x}.
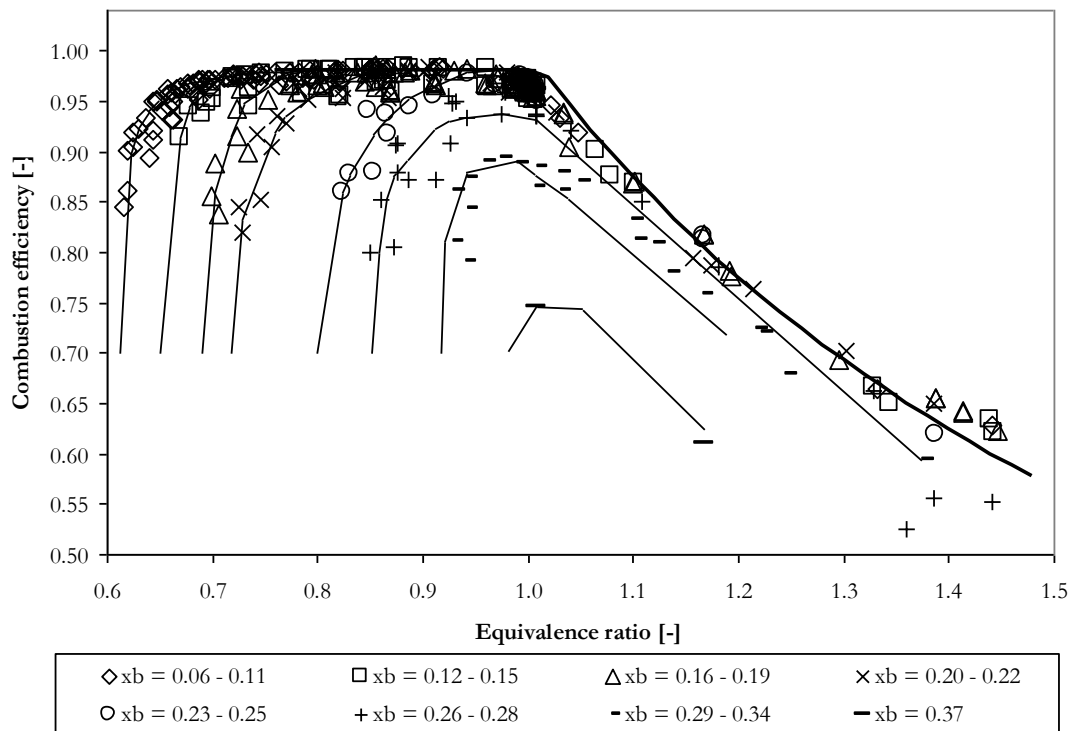
Figure 81

Variation in η_c with equivalence ratio and burned gas fraction, for measured data from the AJ27. Bold line is the fitted trend developed by Shayler and Chick [86], other lines are trend lines fitted to the data (minimising the sum of the square errors). Data at x_b = 0.37 was taken from a V6 DISI engine operating with homogenous fuelling, external EGR and standard valve timings.
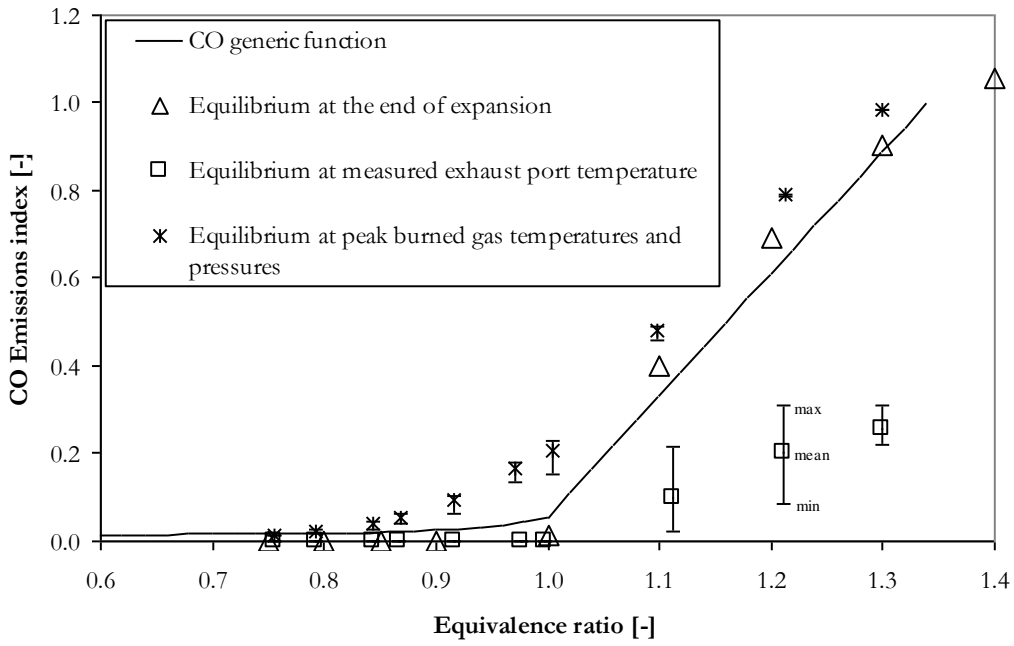
Figure 82

EI_{CO} **, generic function and calculated at points throughout the cycle.**
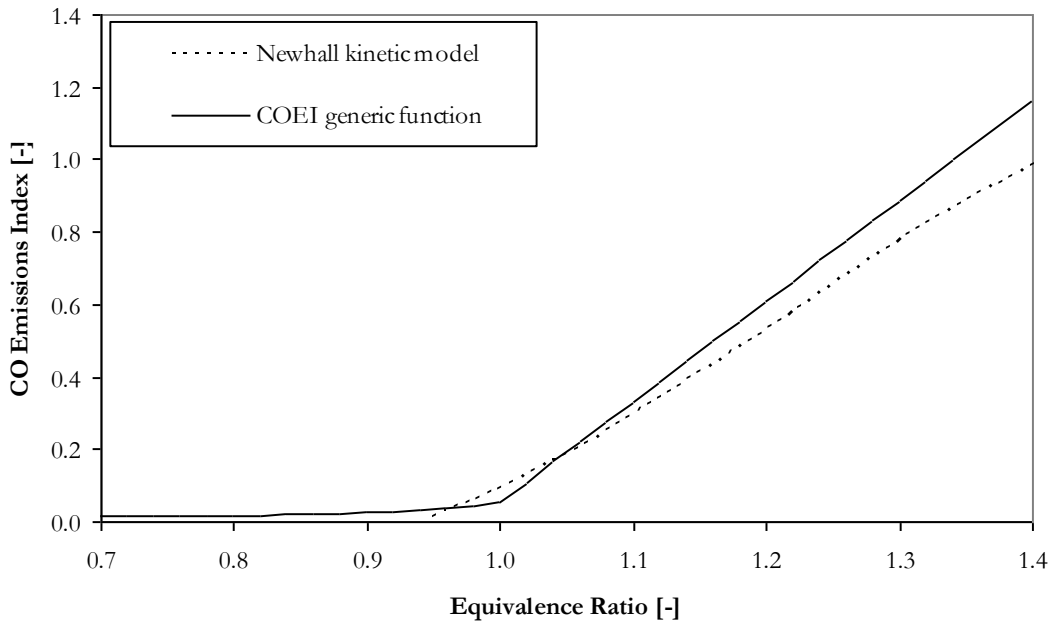
Figure 83

Comparison between the Newhall [89] kinetic model used to predict EI_{CO} **and the** EI_{CO} **generic function.**
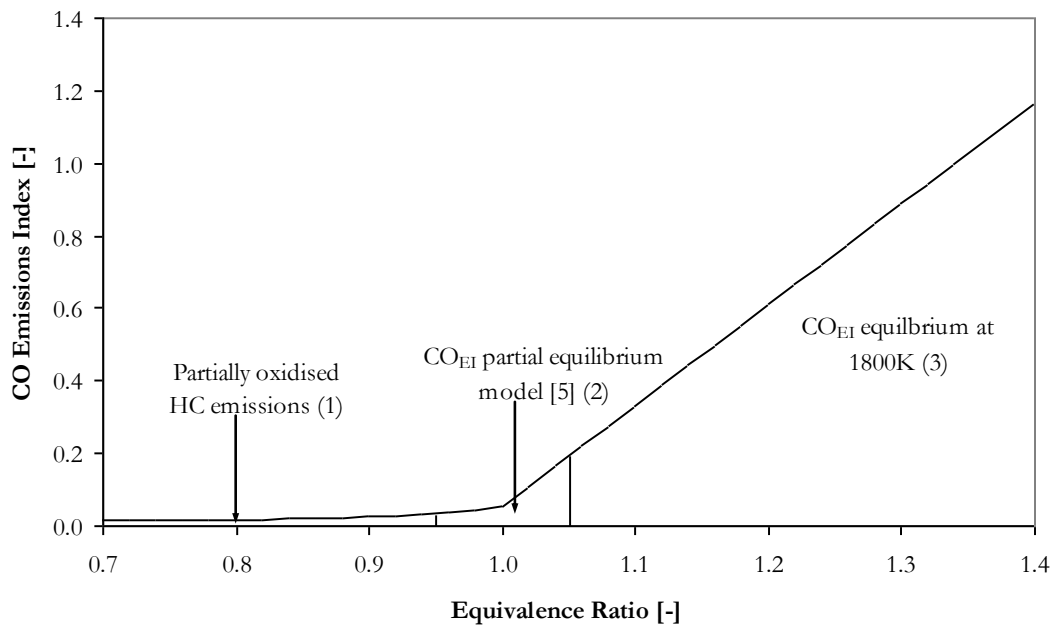
Figure 84
The EI_{CO} generic function, highlighting the production mechanisms of CO.
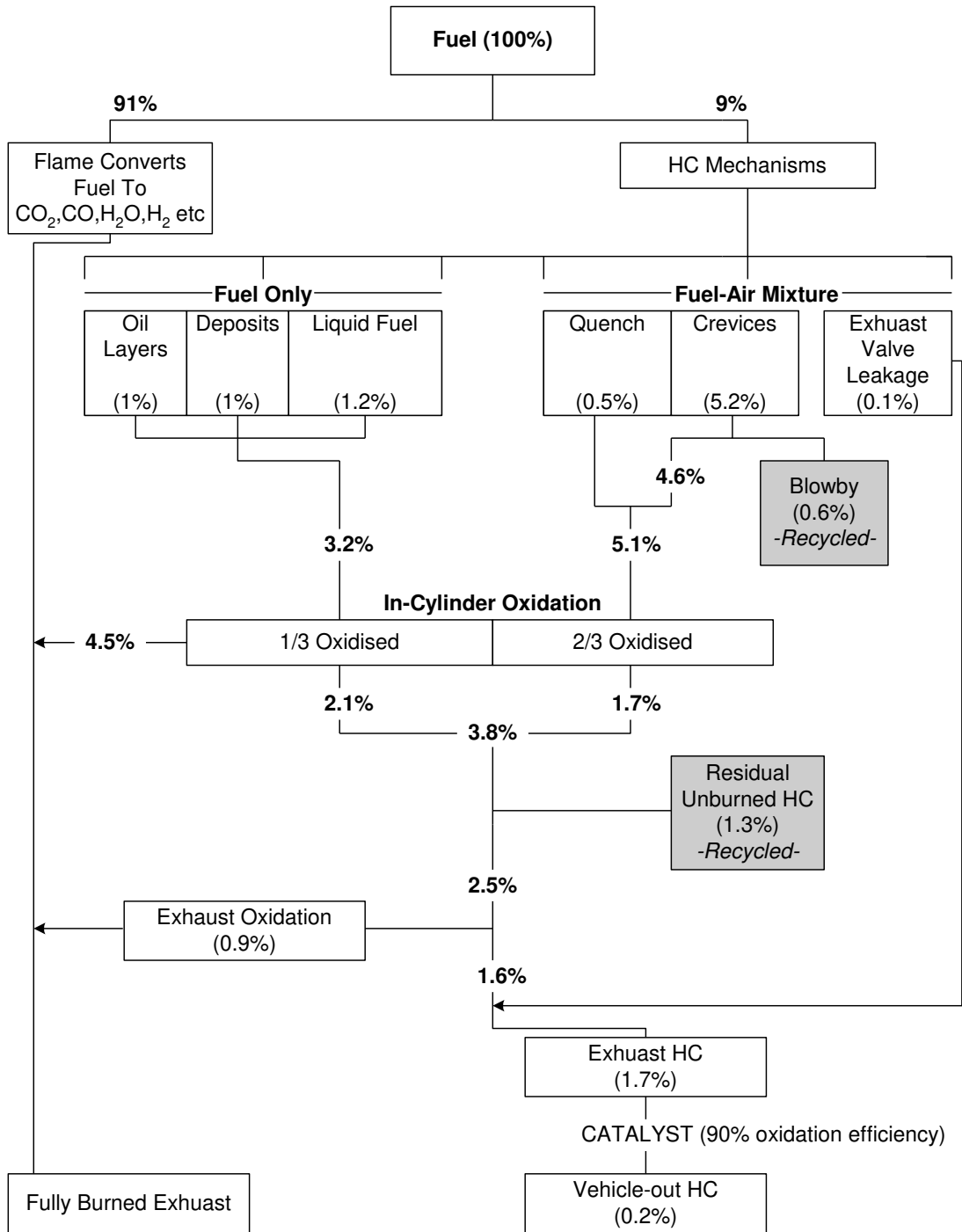
Figure 85
Gasoline flow chart developed by Cheng et al [72], proposed for an engine operating at steady state conditions (approximately equivalence ratio = 1).
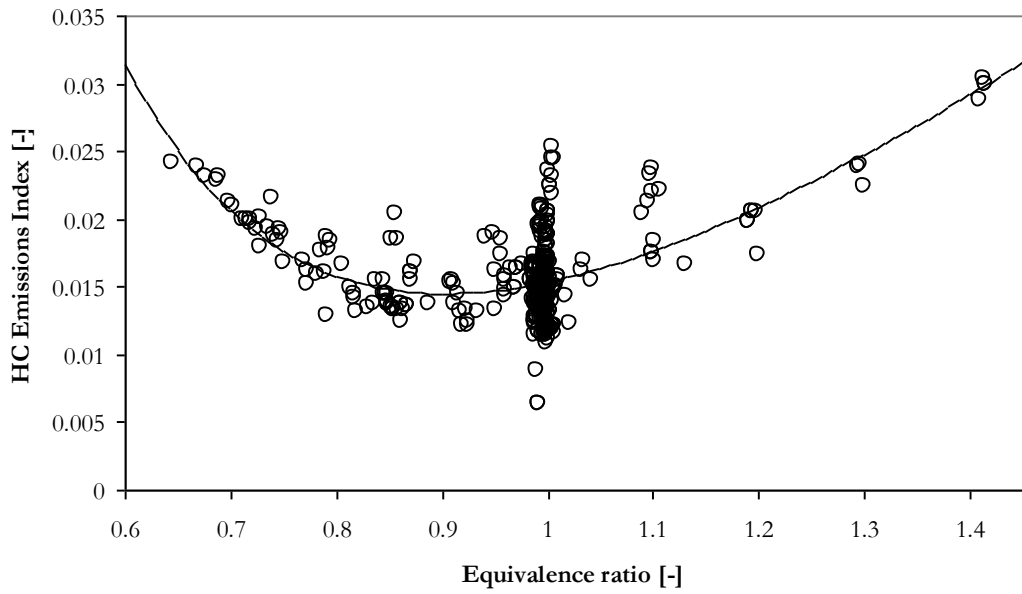
Figure 86
HC emissions index as a function of equivalence ratio
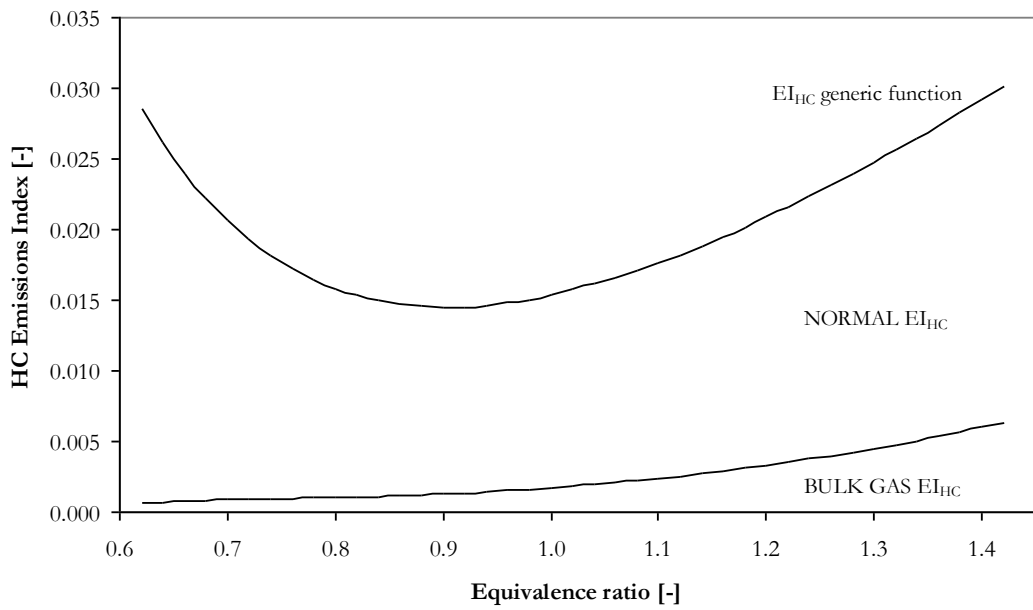
Figure 87
HC emissions index as a function of equivalence ratio
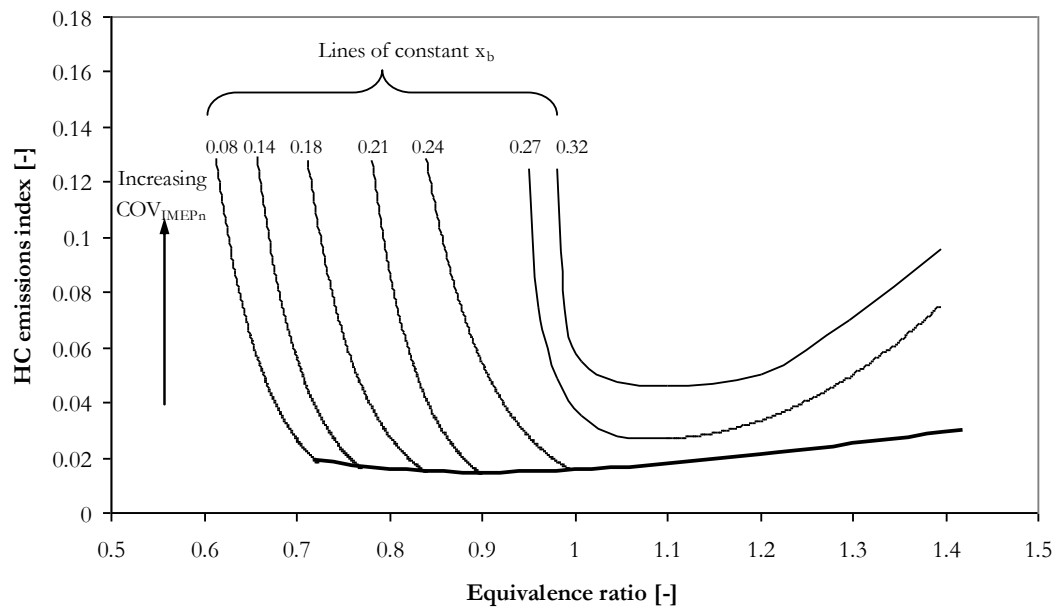
Figure 88

Influence of increasing combustion instability on EI_{HC}. The lower line is the EI_{HC} generic function, with each line of constant x_b derived from AJ27 data. Indicating mixture operating constraints.
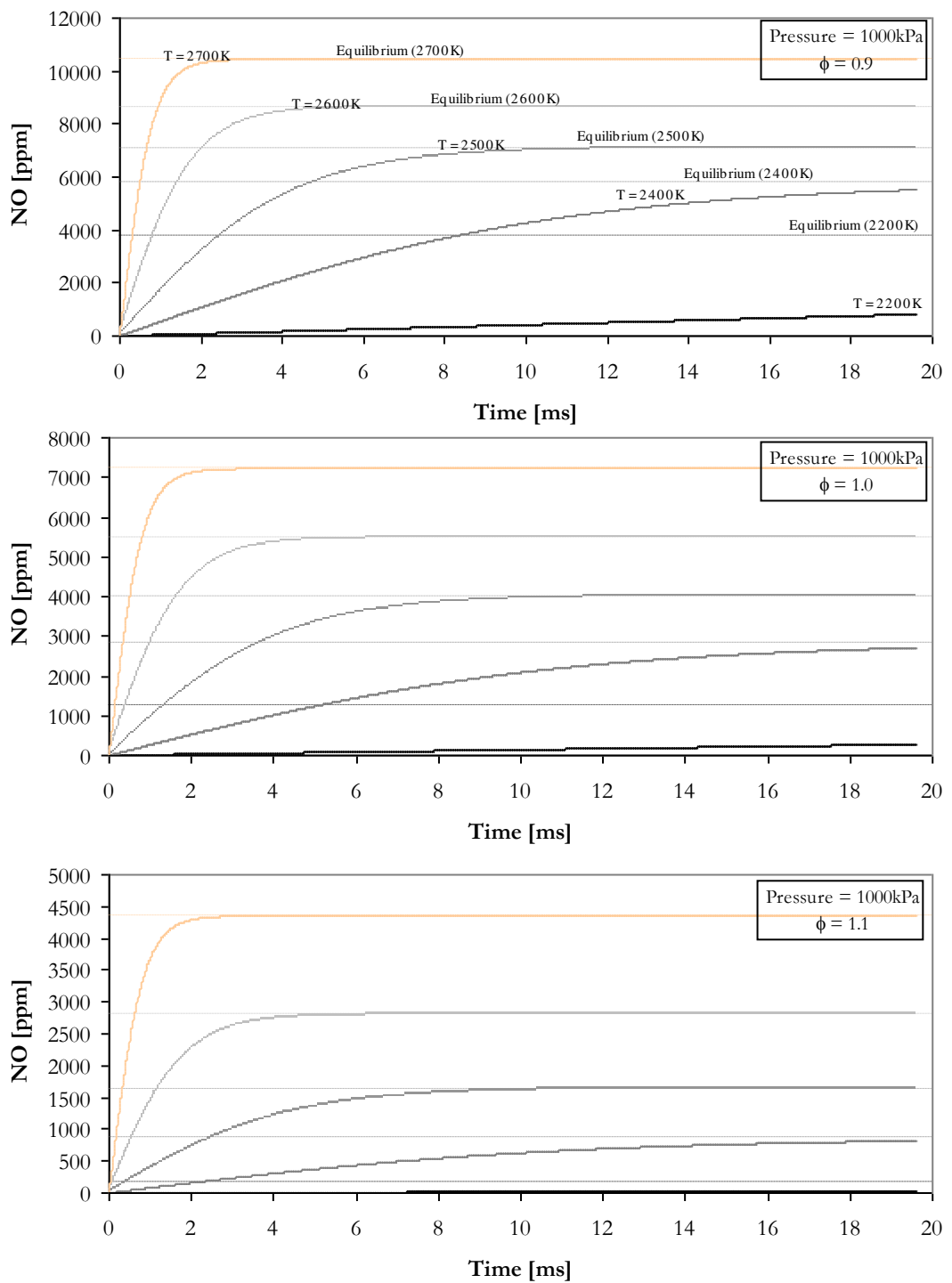
Figure 89
NO concentration as a function of time for five temperatures at 1000kPa and three equivalence ratios.
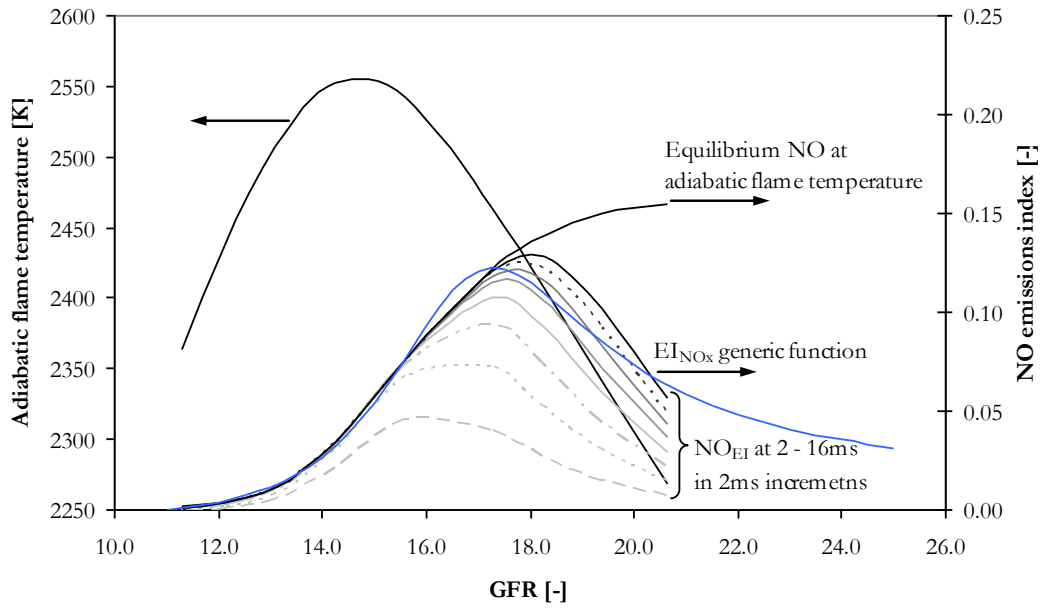
Figure 90
EI_{NO} **as a function of GFR (where GFR = AFR+1, x_b=0), adiabatic flame temperature as a function of GFR and the** EI_{NO_x} **generic function (as modified for the AJ27). (All modelled calculations were based on iso-octane and have been offset to account for the difference in stoichiometric AFR compared to gasoline).**
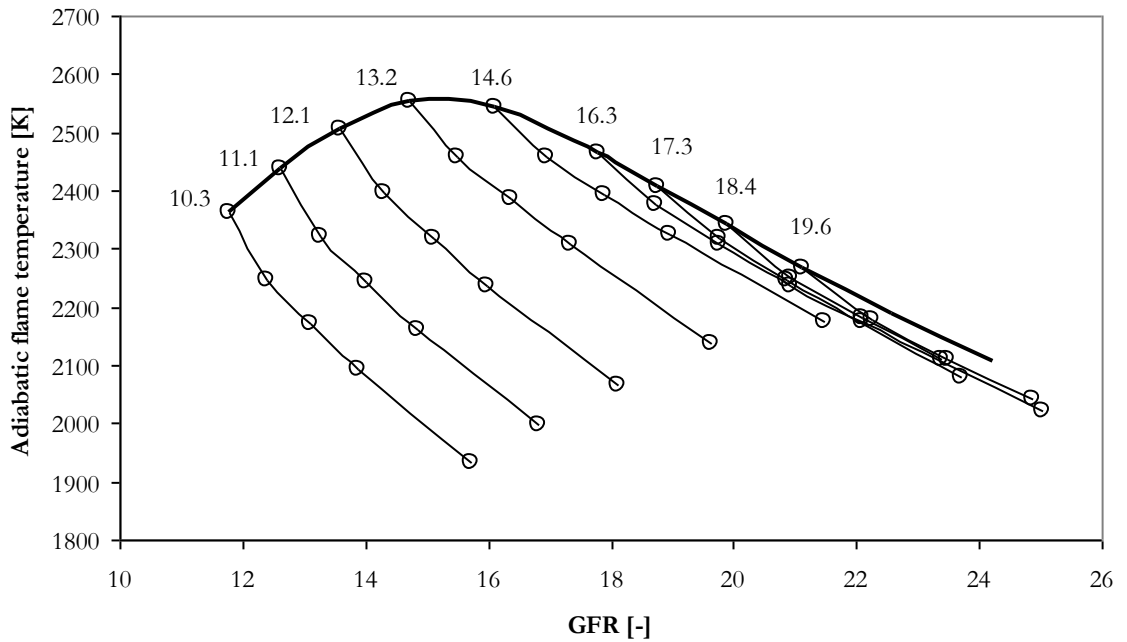
Figure 91
Adiabatic flame temperature as a function of GFR for lines of constant AFR. The upper curve is the locus point where x_b is zero, moving down the constant AFR curve x_b increases from 0:0.05:0.25.
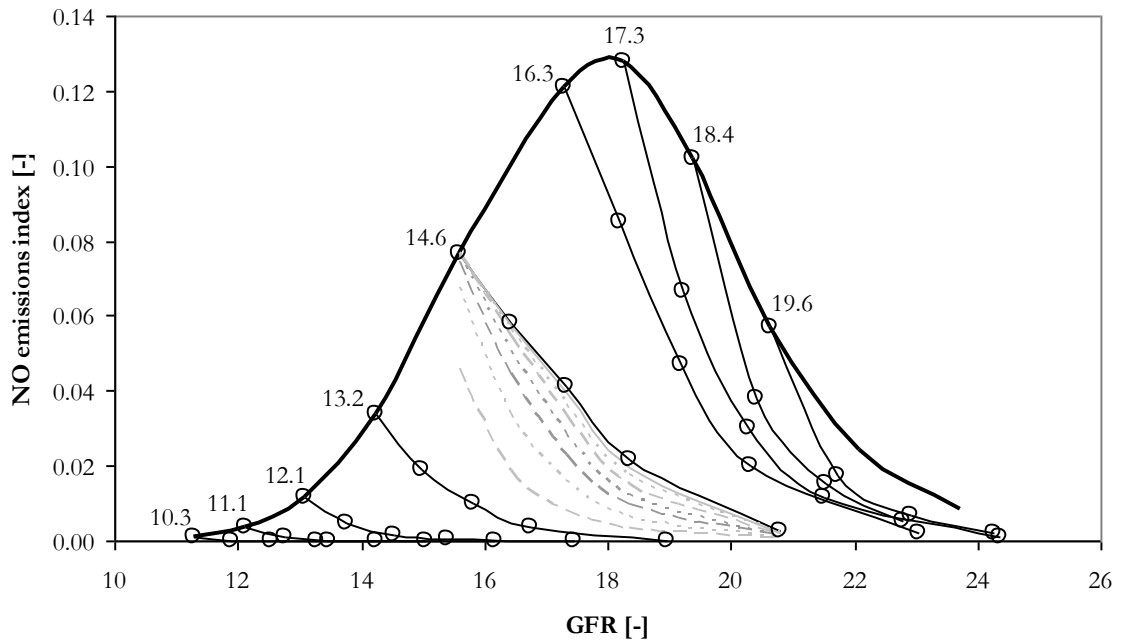
Figure 92

EI_{NO} **as a function of GFR for a range of constant AFR, solid lines represent** EI_{NO} **after 16ms, dashed lines show progressive increases of** EI_{NO} **(2-16ms in 2ms increments).**
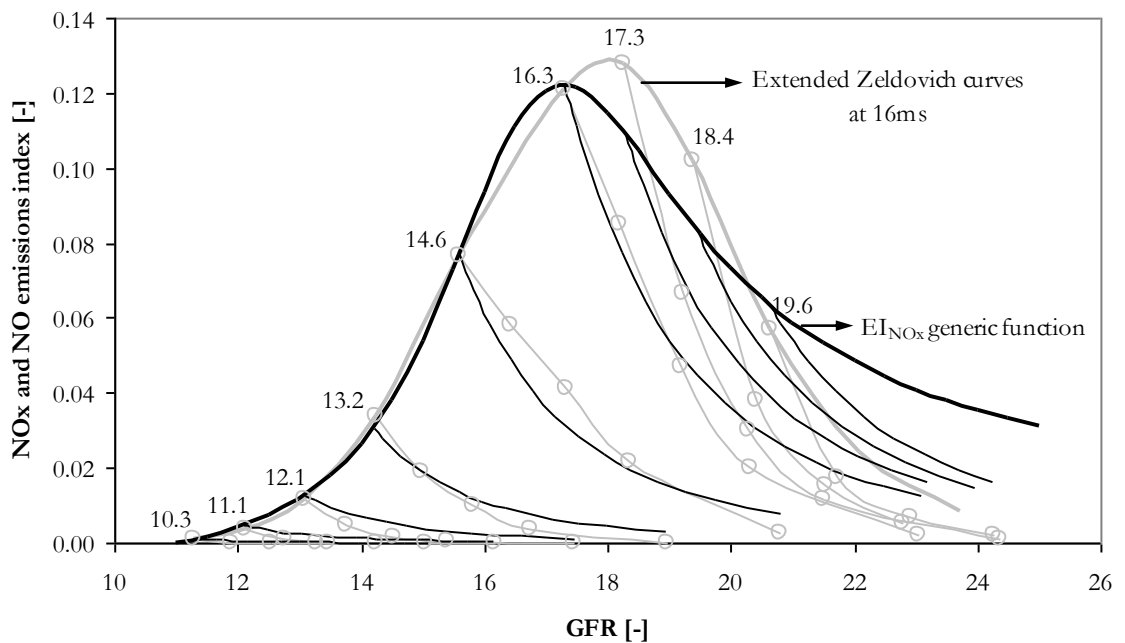
Figure 93

Comparison between the extended Zeldovich results at 16ms and the EI_{NO_x} **generic function, generic function is the altered version fitted to the AJ27.**
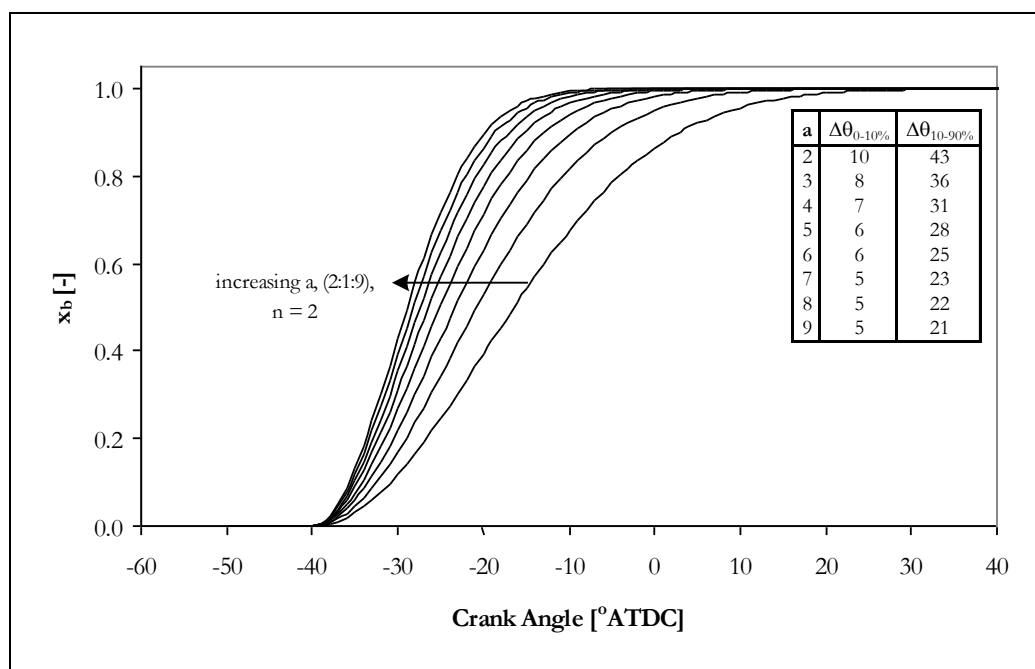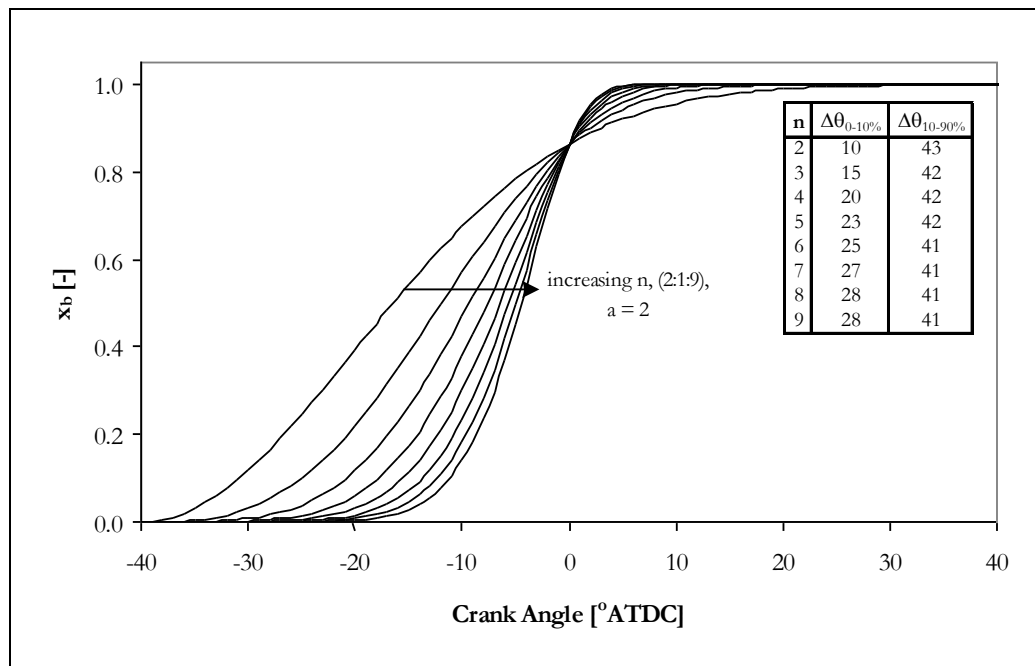
Figure 94
The effect of increasing a (efficiency factor) and n (form factor) on the shape of the burned mass fraction curve produced from the Wiebe function and the related changes in the $x_b 10$ and $x_b rap$.
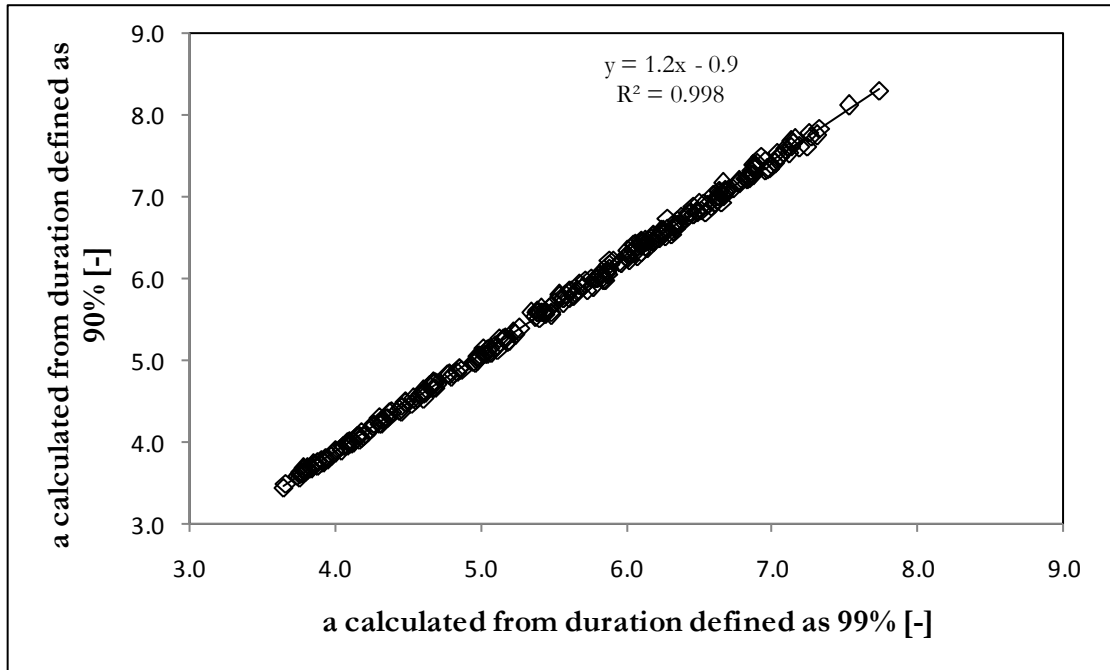
Figure 95

Correlation between a calculated from the θ_d defined as 99% and 90%.
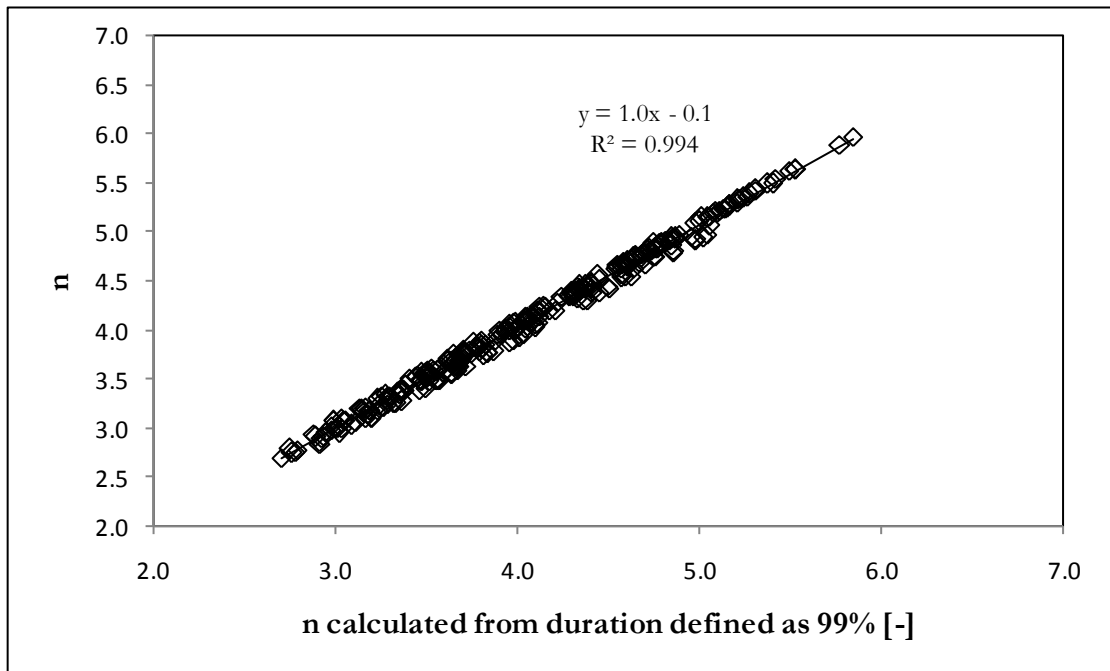
Figure 96

Correlation between n calculated from the θ_d defined as 99% and 90%.
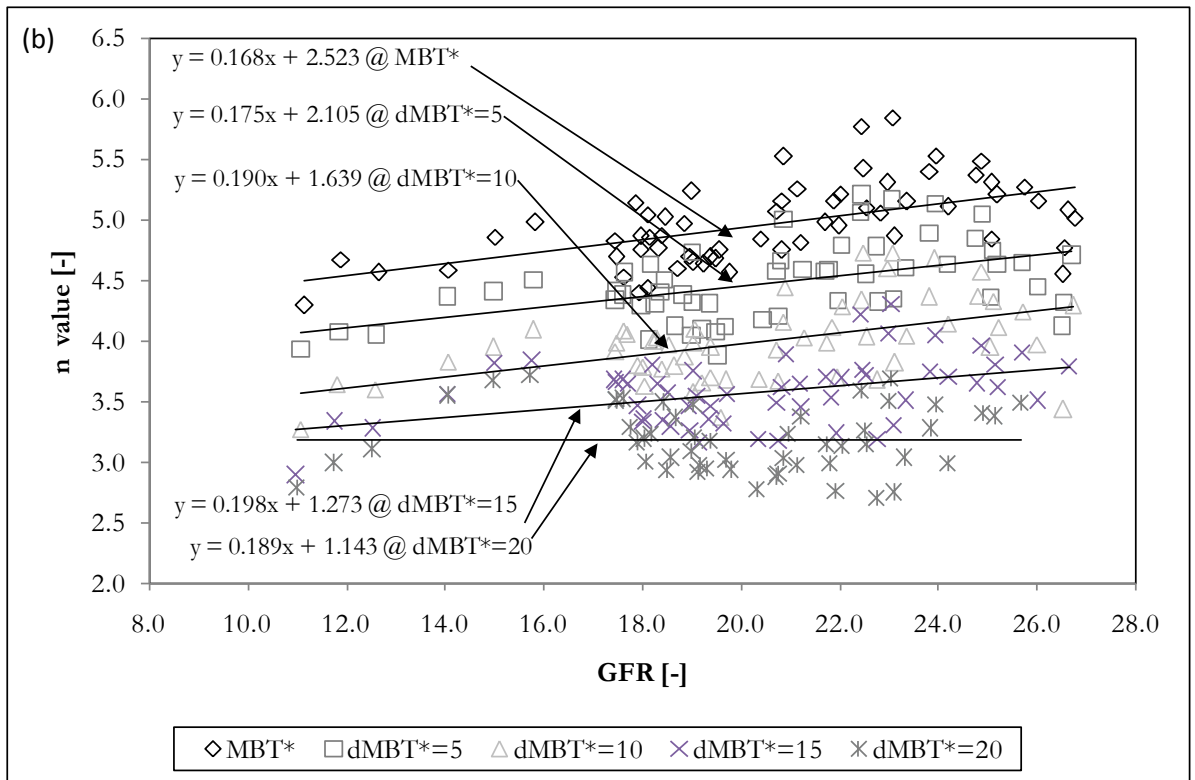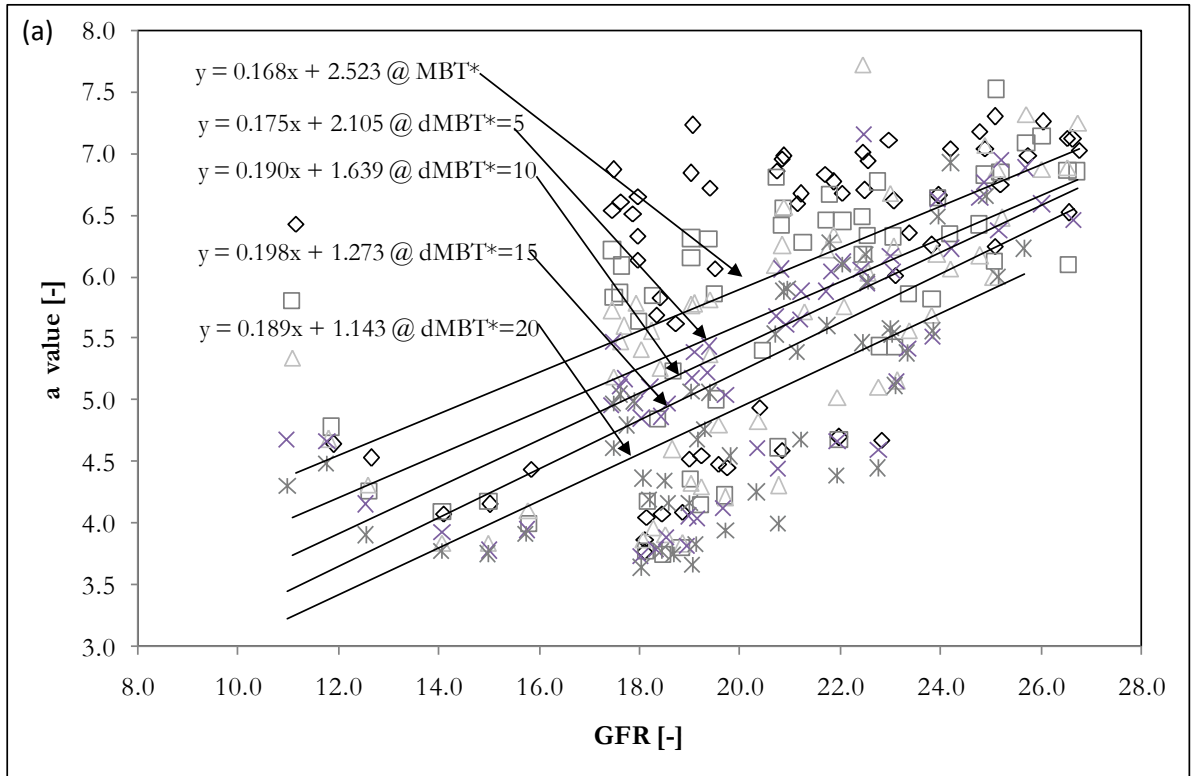
Figure 97
Change in the values of Wiebe parameters *a* **(plot (a)) and** *n* **(plot (b)) as a**
function of relative spark timing and GFR.
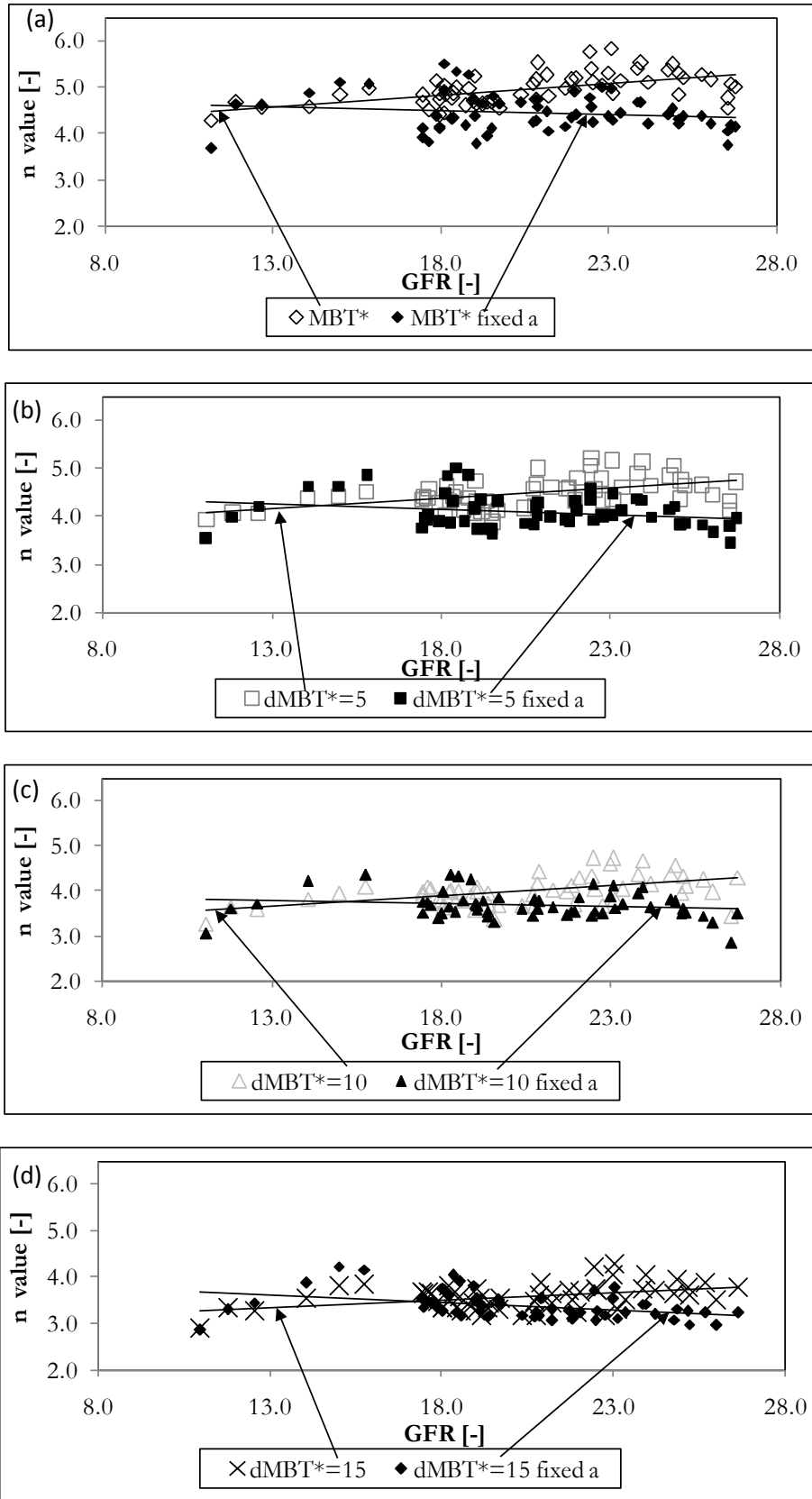
Figure 98
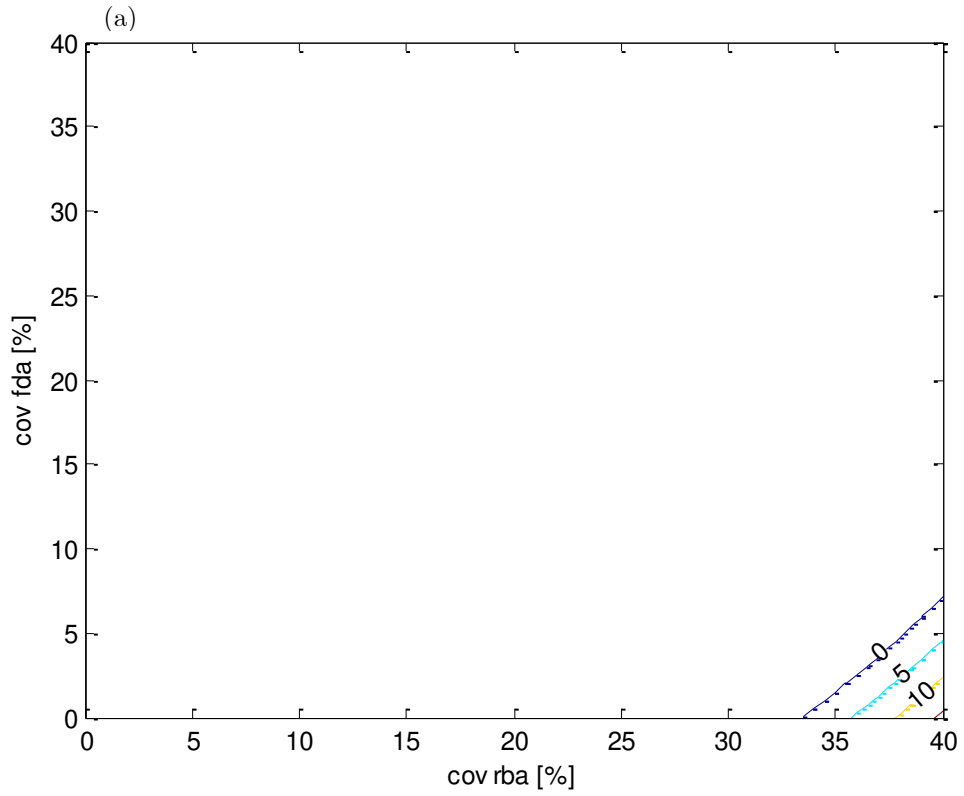**Effect of using a fixed value of a on the fitted value of n, data used as per Figure 97, a = 4.6052.**
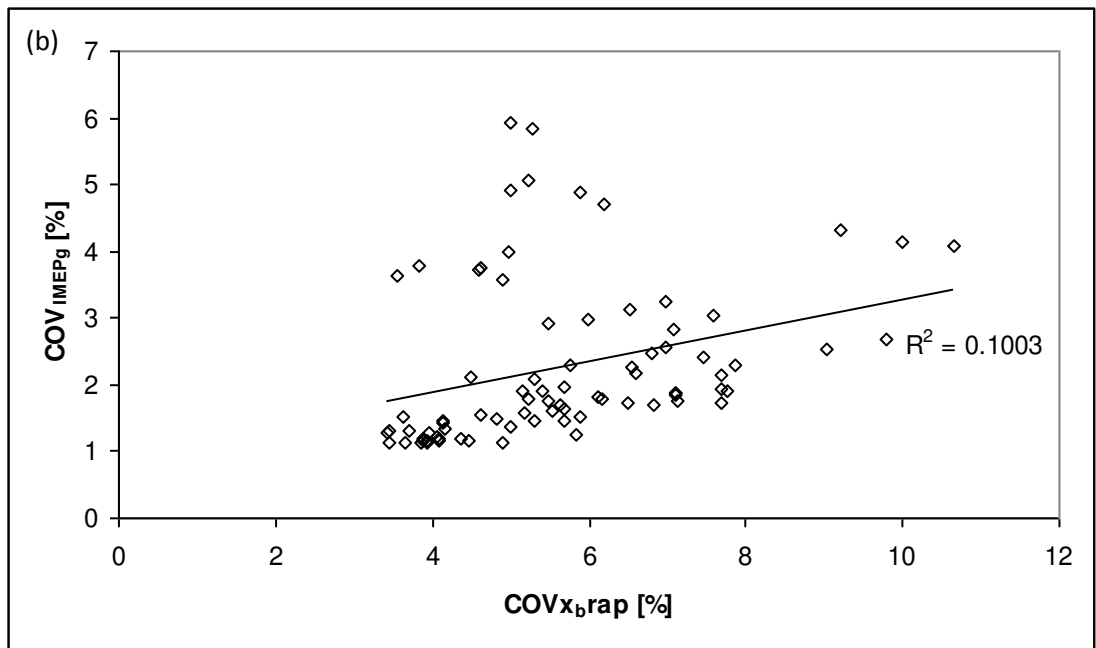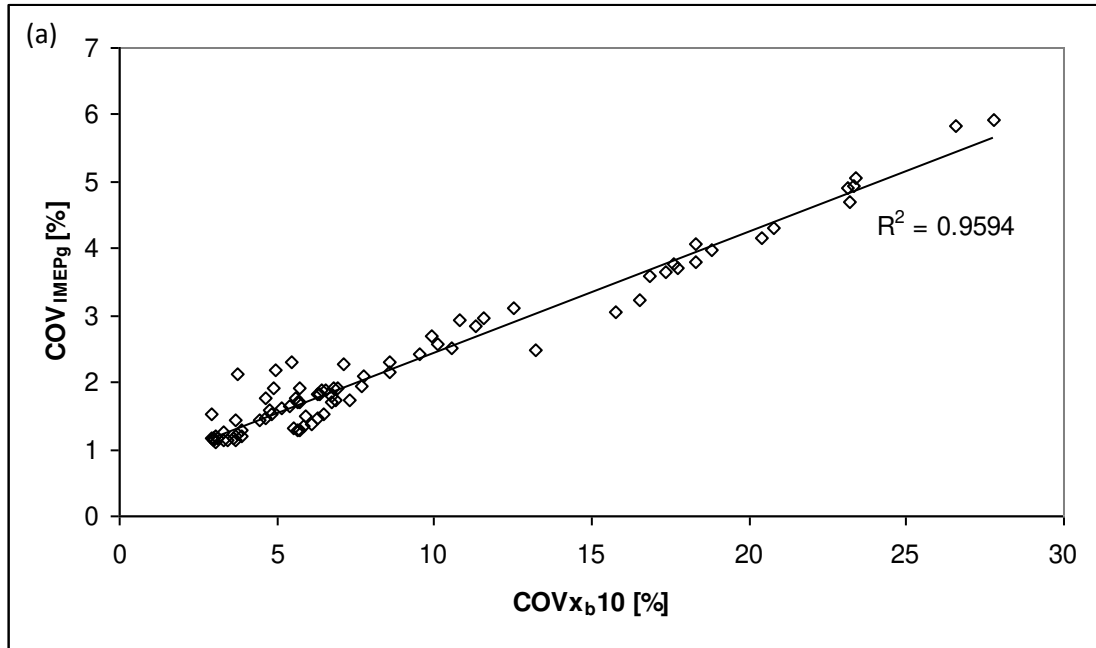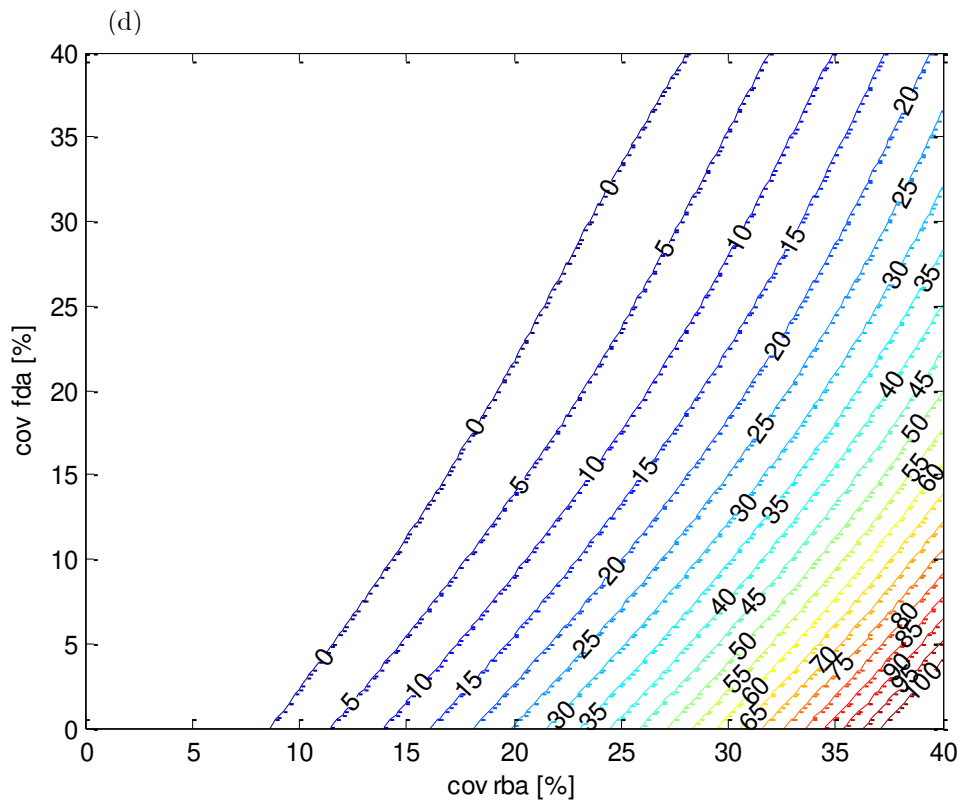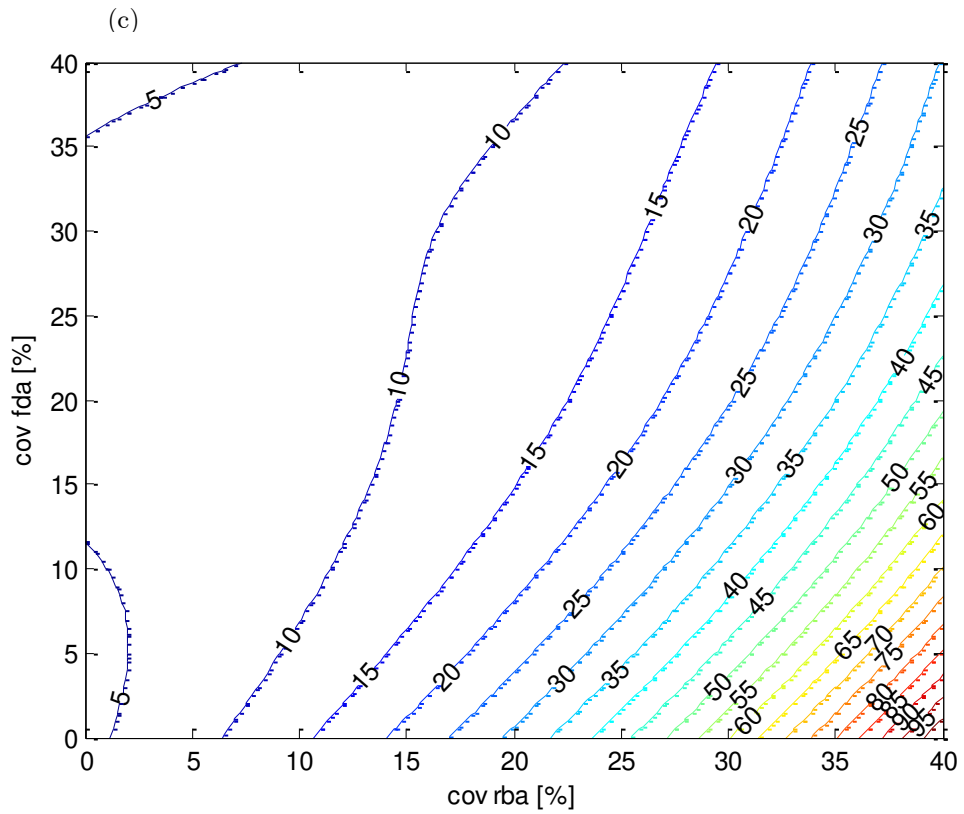
Figure 99

Correlation between COV_{IMEP_g} as function of (a) $COV_{\Delta\theta_{0-10\%}}$ and (b) $COV_{\Delta\theta_{10-90\%}}$.

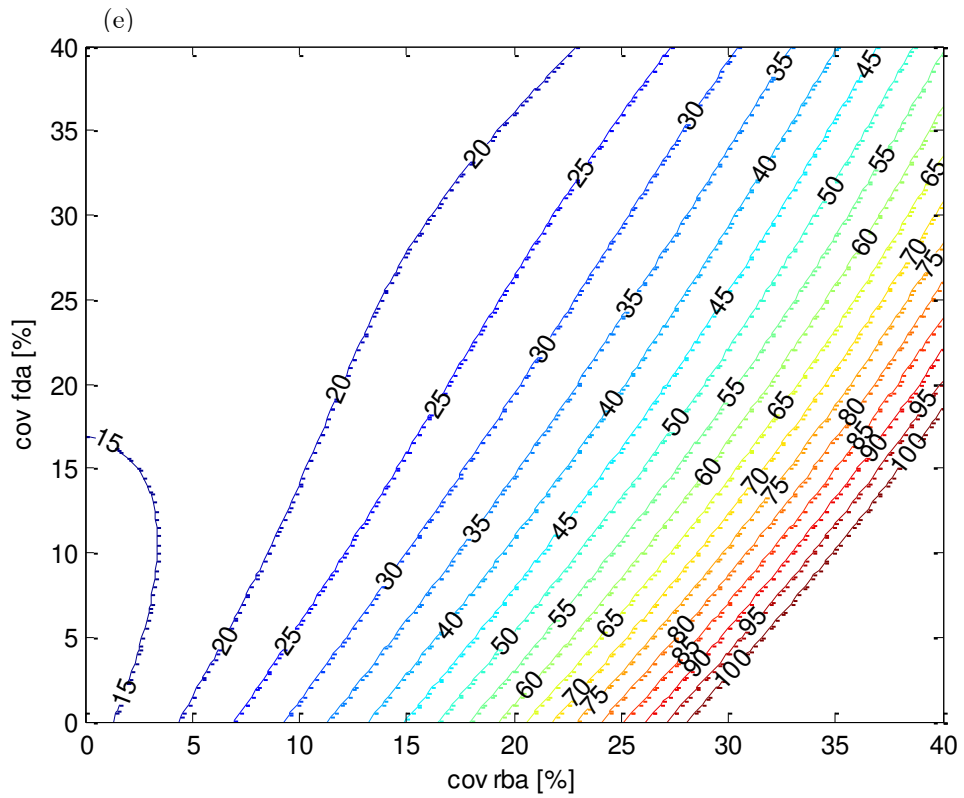Spark timing 120° BTDC, full range of a and n, θ_d fixed at 40°CA.
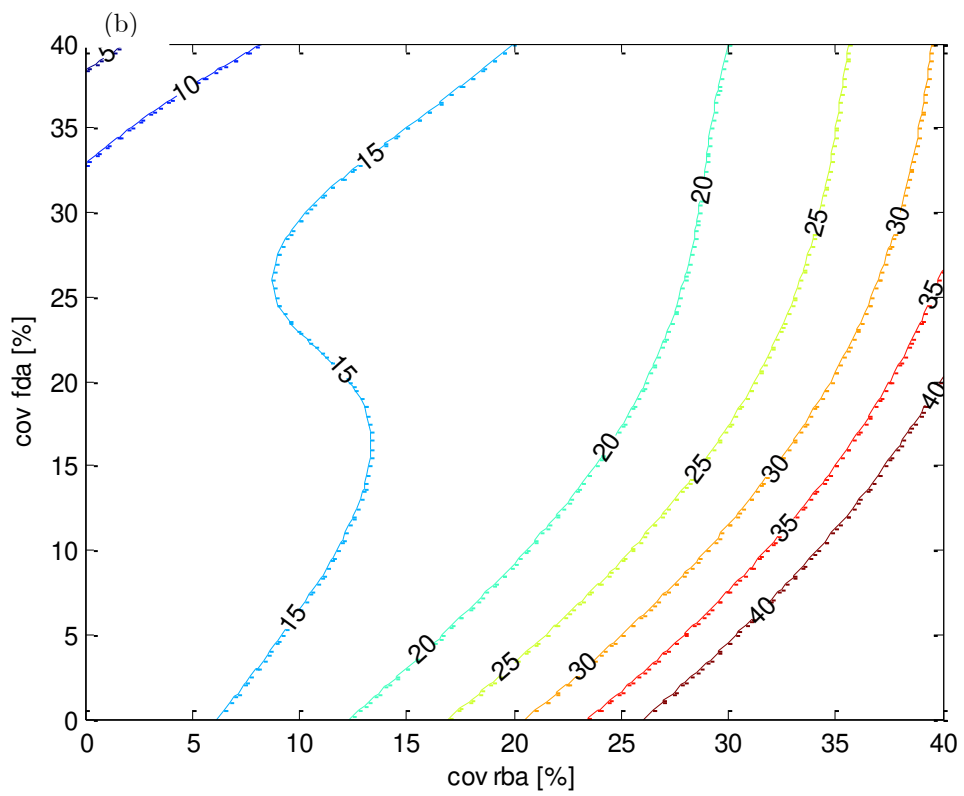
The effect of changes of $COV_{\Delta\theta_{0-10\%}}$ and $COV_{\Delta\theta_{10-90\%}}$ on COV_{IMEP_g} at five increasing θ_d:
(a) 30, (b) 50, (c) 70, (d) 90, (e) 115.

(c)

(d)

The effect of changes of $COV_{\Delta\theta_{0-10\%}}$ and $COV_{\Delta\theta_{10-90\%}}$ on COV_{IMEP_g} at five increasing θ_d:
(a) 30, (b) 50, (c) 70, (d) 90, (e) 115.

Figure 100

The effect of changes of $COVx_b10$ and $COV_{\Delta\theta_{10-90\%}}$ on COV_{IMEP_g} at five increasing θ_d: (a) 30, (b) 50, (c) 70, (d) 90, (e) 115.